THE UNIVERSITY OF CHICAGO

CONTEXT-DEPENDENT RNA DEMETHYLATION BY FAT MASS AND OBESITY-ASSOCIATED (FTO) PROTEIN

A DISSERTATION SUBMITTED TO

THE FACULTY OF THE DIVISION OF THE PHYSICAL SCIENCES

IN CANDIDACY FOR THE DEGREE OF

DOCTOR OF PHILOSOPHY

DEPARTMENT OF CHEMISTRY

BY

JIANGBO WEI

CHICAGO, ILLINOIS

MARCH 2021

Table of Contents

LIST OF FIGURES

ACKNOWLEDGEMENTS

First and foremost, I would like to express my heartfelt gratitude to my doctoral advisor, Professor Chuan He. I was deeply attracted by his knowledge, vision, as well as personality when I first met him as an undergraduate student, and inspired a lot by the fantastic research done in his lab. I am benefited tremendously that I have been trained in accordance with my aptitude all the time. I barely had any biology background as I majored in organic chemistry during my undergraduate years. Professor Chuan He was extremely considerate and assured me a very smooth transition. I was assigned to work closely with Dr. Kathy Liu, a senior postdoc, at the beginning, which laid a solid foundation for my subsequent projects. Shortly after, I got the opportunity to do my own research and I really appreciate the chance to work on the projects concerning FTO, the first RNA demethylase ever identified. I was also provided with lots of opportunities to collaborate with labs of diverse expertise and attending academic conferences to expand my horizon. Throughout my doctoral career, Professor Chuan He has always been patient, encouraging, and inspiring, especially when I encountered difficulties. It was a memorable experience to prepare for graduation and finalize the dissertation during the COVID-19 pandemic. Professor Chuan He has been a model advisor while chaperoning me and the entire lab through this unusual time. I could not be more grateful for his candor, advanced planning, thoughtful provisions, and for helping me to stay positive and still focused on science during my final year. This dissertation would not be possible without his insightful mentorship, intuitive guidance, and comprehensive supports.

I also wish to acknowledge my thesis committee members, Professor Joseph Piccirilli and Professor Tao Pan, for their valuable time and suggestions. Professor Piccirilli also served on my candidacy committee, and the first project of my own was benefited a lot from his advice. Professor

Tao pan jointly supervised the project I worked on with Kathy and his insights in tRNA biology helped a lot in my subsequent research.

I would also like to thank my research collaborators. Professor Yawei Gao and Lei Yang from Tongji University provided essential help on the project to investigate the physiological substrate and role of FTO in mammals. I had a long-term collaboration with Professor Yu-Ying He from the Department of Medicine. Our work expanded the understanding of context-dependent function and regulation of FTO in melanoma and skin cancers. Professor Jianjun Chen and Dr. Rui Su from City of Hope collaborated with us on systematically exploring the function and regulation of gene-region-specific m^6A on mRNA. In collaboration with Professor Zhijian Qian from the University of Florida and Professor Haojie Huang from Mayo Clinic, we further demonstrated the roles of context-dependent m^6A demethylation in different cancers. Professor Federica Accornero from the Ohio State College of Medicine worked with us on profiling the m^6A landscape in human heart failure. I am also grateful to Dr. Qin Jin, Dr. Pieter Faber, and other staff in the facilities of mass spectrometry and NGS sequencing.

It was my great fortune to work with members in Professor Chuan He's group for the past five years. Special thanks to Dr. Kathy Liu, who taught me all kinds of techniques in biochemistry as well as RNA biology and helped me a lot to get started with my independent project. I also want to thank Dr. Xiao-long Cui. Not only did we work together but also worked out and hung out together. He generously shared all his knowledge and experience in bioinformatics with me and offered help every time I needed it. I am also grateful to Dr. Li-Sheng Zhang. We have been working in the same lab since undergraduate years, and it was nice to have someone accompanied for nearly a decade in my early research career. Thanks also go to Dr. Xianbin Yu, Huanyu Wang, Boyang Gao, Cody He, Dr. Jun Liu, Zhike Lu, Dr. Ziyang Hao, Yuxi Ai, Xueyang Dong, and

Caraline Sepich for their help with my projects; Dr. Hailing Shi, Dr. Zijie Zhang, Dr. Xiaoyang Dou, and Zhongyu Zou for valuable discussions, especially Dr. Hailing Shi—I am extremely fortunate that our desks were close to each other, and I learned a lot from her about how to be a productive graduate researcher. Dr. Honghui Ma and Dr. Qili Fei provided me valuable suggestions for both my research and career development even after they left the lab. I sincerely thank all other members.

Finally, I would not have come this far without all the love and support from my family and friends. I am grateful to my father, a great chemist, who introduced me to the world of science when I was a child. I may have a higher starting point compared to him at the same age, but I truly wish I could be as tough and determined as he is in my future career. This dissertation is also for my mother and grandparents, who have always cared for me and supported me. I am also grateful to my college roommate, Dr. Yaocheng Shi, who was always available to take my complaints during my hard time. Lastly, I would like to thank all my childhood friends. They were not familiar with my profession, but their overpraise always pushed me to try my best during my path to graduation.

ABSTRACT

N^6-methyladenosine (m^6A) is the most abundant internal modification in mammalian messenger RNA (mRNA). It is deposited by writer proteins and can be reversed by erasers. Fat mass and obesity-associated (FTO) protein was the first RNA demethylase shown to catalyze the oxidative demethylation of m^6A in mRNA. This discovery reignited investigations of m^6A biology. FTO was later shown to demethylate m^6A_m near mRNA 5' cap (cap-m^6A_m). To address the question of which substrate on mRNA is the preferentially cellular substrate of FTO, I comprehensively characterized the substrate spectrum of FTO inside cells, and clarified internal m^6A as the main substrate contributing to FTO-mediated mRNA stability regulation. In terms of *in vivo* physiological significance of FTO, *Fto* knockout (KO) mice exhibit severe developmental defects, yet the primary physiological substrates of FTO and the related functional pathways during mammalian development and in mammalian tissues remained elusive. A major part of my doctoral work showed for the first time that FTO mediates m^6A demethylation of repeat RNAs in mouse embryonic stem cells (mESCs), especially the long-interspersed element-1 family (LINE1) RNAs, thereby regulating their abundance to affect chromatin state. Our analysis further revealed FTO-mediated LINE1 RNA m^6A demethylation associated with chromatin state regulation as a prevalent process in mammalian tissues, which also plays critical roles during early development. Additionally, in two collaborative studies, we investigated the context-dependent functions of FTO and demonstrated how FTO is regulated depending on the cellular stress in cancers. Collectively, these findings reveal RNA m^6A-mediated chromatin and transcriptional regulation as an additional layer to gene expression regulation by reversible RNA methylations, and expand the understanding of the context-dependent regulations and functions of FTO and RNA m^6A demethylation.

LIST OF PUBLICATIONS PRESENTED IN THIS THESIS[†]

1. **J. Wei**[#], X. Yu[#], L. Yang[#], X.-L. Cui, J. Liu, B. Gao, P. C. He, L.-S. Zhang, X. Liu, J. Chen, X. Dong, H. Wang, C. Chen, Y. Wu, Z. Hao, X. Dou, C. Sepich-Poore, Y.-Y. He, X. Li, Y. Gao*, C. He*. FTO mediates LINE1 m^6A demethylation and chromatin regulation in mESCs and mouse tissues. *Science* in revision.
2. Y.-H. Cui[#], S. Yang[#], **J. Wei**[#], C. R. Shea, W. Zhong, F. Wang, P. Shah, M. G. Kibriya, X.-L. Cui, H. Ahsan, C. He, Y.-Y. He*. Autophagy of the m^6A mRNA demethylase FTO is impaired by low arsenic exposure to promote tumorigenesis. *Nat. Commun*. in revision.
3. **J. Wei**, C. He*. Chromatin and transcriptional regulation by reversible RNA methylation. *Curr. Opin. Cell Biol.* in press. [Invited Review]
4. S. A. Hinger[#], **J. Wei**[#], L. E. Dorn, B. A. Whiston, P. M. L. Jassen, C. He, F. Accornero*. Remodeling of the m^6A landscape in the heart reveals few conserved post-transcriptional events underlying cardio-myocyte hypertrophy. *J. Mol. Cell. Cardiol.* **2021**, *151*, 46-55.
5. **J. Wei**, C. He*. Site-specific m^6A editing. *Nat. Chem. Biol.* **2019**, *15*, 848–849. [News & views]
6. S. Yang[#], **J. Wei**[#], Y.-H. Cui[#], G. Park, P. Shah, Y. Deng, A. Aplin, Z. Lu, S. Hwang, C. He*, Y.-Y. He*. m^6A mRNA demethylase FTO regulates melanoma tumorigenicity and response to anti-PD-1 blockade. *Nat. Commun.* **2019**, *10*, 2782-2796.
7. H. Shi[#], **J. Wei**[#], C. He*. Where, when and how: context-dependent functions of RNA methylation writers, readers, and erasers. *Mol. Cell* **2019**, *74*, 640-650. [Invited Review]

[†]The following chapters of this dissertation contain sections and figures adapted from the listed publications with modifications. Chapter **1**: publications 3 and 7; Chapter **2**: publication 9; Chapter **3**: publication 1; Chapter **4**: publications 1, 2, 4, and 6; Chapter **5**: publications 3, 5, and 7. [#]These authors contributed equally. *These authors jointly supervised the work.

8. Y. Huang[#], R. Su[#], Y. Sheng[#], L. Dong[#], Z. Dong[#], H. Xu, T. Ni, Z. S. Zhang, T. Zhang, C. Li, L. Han, Z. Zhu, F. Lian, **J. Wei**, Q. Deng, Y. Wang, M. Wunderlich, Z. Gao, G. Pan, D. Zhong, H. Zhou, N. Zhang, J. Gan, H. Jiang, J. C Mulloy, Z. Qian*, J. Chen*, C.-G. Yang*. Small-molecule targeting of oncogenic FTO demethylase in acute myeloid leukemia. *Cancer Cell* **2019**, *35*, 677-691.
9. **J. Wei**[#], F. Liu[#], Z. Lu, Q. Fei, Y. Ai, P. Cody. He, H. Shi, X.-L. Cui, R. Su, A. Klungland, G. Jia, J. Chen, C. He*. Differential m^6A, m^6A_m, and m^1A Demethylation Mediated by FTO in Cell Nucleus and Cytoplasm. *Mol. Cell* **2018**, *71*, 973-985.
10. F. Liu, W. Clark, G. Luo, X. Wang, Y. Fu, **J. Wei**, X. Wang, Z. Hao, Q. Dai, G. Zheng, H. Ma, D. Han, M. Evans, A. Klungland, T. Pan*, C. He*. ALKBH1-mediated tRNA demethylation regulates translation. *Cell* **2016**, *167*, 816-828.

Chapter 1

Introduction

1.1 Epigenetics and epitranscriptomics

As described by the central dogma of molecular biology, genetic information flows from deoxyribonucleic acid (DNA) to ribonucleic acid (RNA) and then to protein through the process of transcription and translation, respectively. What is Epigenetics? At the 2008 Cold Spring Harbor meeting, scientists reached a consensus definition as "an epigenetic trait is a stably heritable phenotype resulting from changes in a chromosome without alterations in the DNA sequence"[1].

Reversible chemical modifications on DNA and histones represent two well-known epigenetic paradigms. 5-methylcytosine (5mC), the "5th base" of DNA, is the most common form of DNA modification, which is installed by DNA methyltransferases (DNMTs) and undergoes oxidative demethylation by ten-eleven translocation (TET) enzymes[2-4]. 5mC has been shown to play a vital role in the epigenetic control of gene expression and a wide range of cellular processes. Histones, the proteins packing DNA of eukaryotic cell nuclei into the nucleosome, carry covalent post-translational modifications (PTM) as well. Histone modifications can be dynamically regulated by histone modifiers and subsequently modulate chromatin state and gene expression. Histone modifications can be roughly categorized into transcriptional activators, including H3K4Me3, H3K9Ac, and H3K27Ac, or transcriptional suppressors such as H3K27Me3[5,6].

Analogous to DNA and histones, chemical modifications have been known to exist on RNAs for decades[7]. So far, over 170 chemical modifications existing on multiple RNA species have been identified[8]. Therein, transfer RNA (tRNA) and ribosomal RNA were long known to be heavily modified and regulated by modifications[9,10]. However, whether these post-transcriptional

RNA modifications, especially the internal modifications on messenger RNA (mRNA) can be reversible and play critical regulatory roles in gene expression had been neglected until the term "RNA epigenetics" (also known as epitranscriptomics) was proposed in 2010[11]. One year later, this hypothesis was prompted by the discovery of the first RNA modification eraser, mRNA N^6-methyladenosine (m^6A) demethylase fat mass and obesity-associated (FTO) protein[12], which suggests that RNA modifications are not just passive marks—they can be actively controlled. This pioneering work by our group stimulated a renaissance in the study of the reversible RNA modifications and since then, dynamic RNA modifications in gene expression regulation have been a burgeoning area (**Figure 1.1**).

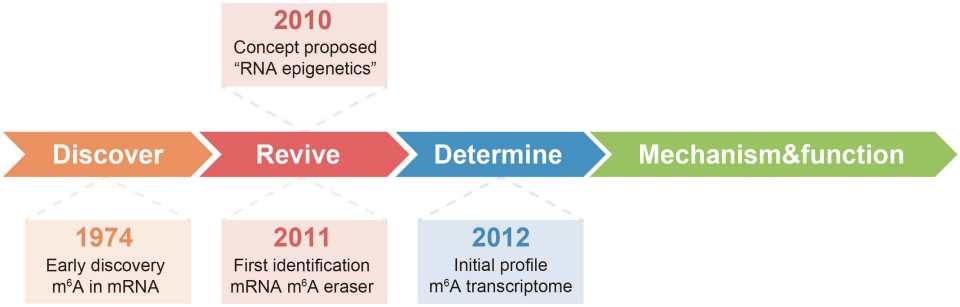

Figure 1.1 Schematic summary of milestones in early studies of epitranscriptomics

1.2 N^6-methyladenosine (m^6A): methylome and effectors

m^6A is the most prevalent and well-characterized internal mRNA modification in higher eukaryotes, first found in 1974, occurring in a sequence context as (G/A)(m^6A)C[13,14]. The amount of m^6A in mammalian mRNA is around 0.1-0.4% *versus* adenosine (that is, ~3–5 m^6A sites per mRNA). Transcriptome-wide mapping of m^6A *via* methylated RNA immunoprecipitation followed by high-throughput sequencing (MeRIP–seq) revealed its genome-wide distributions in mammalian cells, furnishing an initial view of the mammalian m^6A landscape[15,16]. These early mapping efforts revealed the prevalence of m^6A sites in thousands of mRNA and hundreds of non-coding RNA transcripts. The localization of m^6A peaks in mRNA is highly conservative in the

transcriptome of humans and mice with a distribution preferentially centered around the stop codons and enriched at 3' untranslated regions (3' UTRs).

From then on, diverse high-throughput mapping methods of m^6A with higher resolution have been developed, including the photo-crosslinking-assisted m^6A sequencing (PA-m^6A-seq)[17], m^6A individual-nucleotide-resolution crosslinking and immunoprecipitation combined with deep sequencing (miCLIP-seq)[18], MAZTER-seq based on an RNA endoribonuclease recognizing ACA motif[19] (also reported independently as m^6A-REF-seq, m^6A-sensitive RNA-Endoribonuclease–Facilitated sequencing[20]), and the sequencing of the deamination adjacent to RNA modification targets (DART-seq) enabled by m^6A reader YTH binding domain[21]. These improved mapping techniques have pellucidly illustrated the widespread presence of m^6A, other than in mRNA, in ribosomal RNAs (rRNAs), long non-coding RNAs (lncRNAs), microRNAs (miRNAs), small nuclear RNAs (snRNAs), and circular RNAs (circRNAs).

"Writers", "erasers", and "readers", which respectively deposit, remove, and recognize the m^6A are collectively known as m^6A effecters[22] (**Figure 1.2**). A large portion of mRNA m^6A is installed co-transcriptionally by a methyltransferase complex (MTC) composed of the core formed by methyltransferase-like 3 (METTL3) and methyltransferase-like 14 (METTL14)[23-27]. MTC is associated with additional subunits, including Wilms tumor 1-associating protein (WTAP)[28], Vir like m^6A methyltransferase associated (VIRMA)[29], Cbl proto-oncogene-like protein 1 (CBLL1) (also known as Hakai)[29,30], zinc finger CCCH-type containing 13 (ZC3H13)[30], and RNA binding motif protein 15/15B (RBM15/15B)[31]. More recently, methyltransferase-like 16 (METTL16)[32-36], methyltransferase-like 5 (METTL5)[37], and Zinc finger CCHC-type-containing 4 (ZCCHC4)[38] have been identified as m^6A methyltransferases that can install internal m^6A on some RNA species possessing certain structures, such as some small nucleolar RNAs, pre-mRNAs, and rRNA.

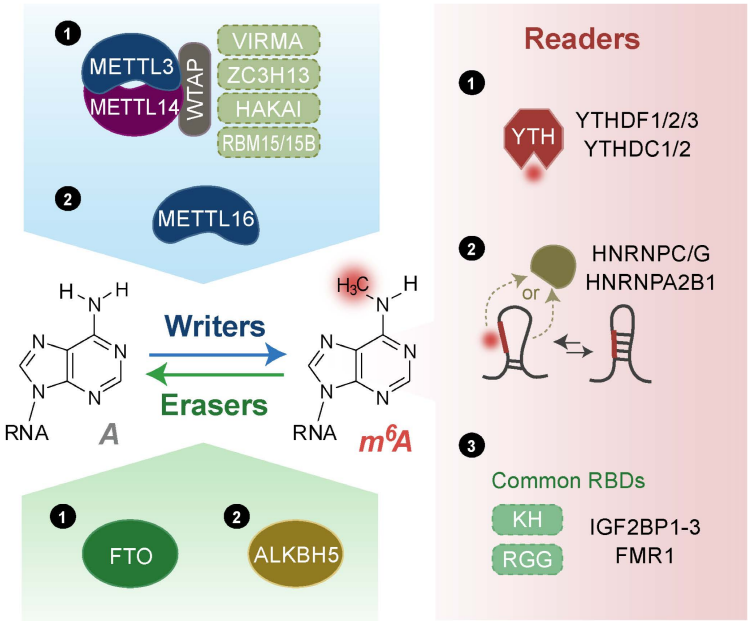

Figure 1.2 Schematic summary of mRNA m^{6}A effectors
mRNA m^{6}A is deposited by the methyltransferase complex MTC, removed by the demethylases, and recognized by reader proteins which also mediates its function.

FTO[12] and AlkB homolog 5 (ALKBH5)[39] are the only two known demethylases that can actively remove the m^{6}A, endorsing the dynamic nature of RNA modifications. FTO was later reported to be able to remove m^{6}A$_m$ adjacent to the 5' cap (cap-m^{6}A$_m$) in a portion of mRNAs[40], which was claimed to be a major contributor to the gene expression regulation role of FTO[40,41], while extensive studies so far have indicated a range of biological processes are predominantly affected by the internal mRNA m^{6}A demethylation of FTO[42-62]. Part of my doctoral work focused on characterizing the cellular substrate spectrum of FTO and clarifying its functionally relevant substrate on mRNA[63].

Numerous m^{6}A readers have been reported since the identification of YTH domain family proteins (YTHDF1-3)[64-66], including YTH domain-containing proteins (YTHDC1-2)[35,67-70], insulin-like growth factor 2 mRNA-binding proteins (IGF2BP1-3)[71], heterogeneous nuclear ribonucleoproteins (HNRNPs)[72-76], Fragile X mental retardation 1 (FMR1)[77-79], and Proline rich coiled-coil 2 A (Prrc2a)[80]. The list of potential m^{6}A readers is still growing. m^{6}A can be selectively

"read" by three essential mechanisms: (i) m^6A directly recruits readers and associated regulatory machinery, including YTHDF1-3[64-66] and YTHDC1-2[35,67-70]; (ii) m^6A repels certain RNA binding proteins (RBPs) that prefer unmodified A over m^6A, represented by G3PB1[81]; (iii) m^6A disrupts the local structure, termed "m^6A-switch", to alter the protein-RNA interactions, such as HNRNPs[72-76].

1.3 Gene expression regulation by m^6A

In parallel to the well-known reversible epigenetic modifications of histone and DNA, studies have demonstrated the dynamic regulatory roles of m^6A on mRNA, adding a new layer to the evolving perspective of the post-transcriptional regulation of gene expression.

1.3.1 Molecular mechanisms and cellular processes

Splicing—m^6A has been shown to play important roles in splicing regulation, which was elucidated by the transient m^6A transcriptome sequencing[82]. Multiple readers such as YTHDC1, hnRNPA2B1, hnRNPC, and hnRNPG are involved *via* divergent mechanisms. YTHDC1 recognizes and binds to m^6A site on precursor mRNAs (pre-mRNAs), recruiting SRSF3 while driving away SRSF10 to promote exon inclusion. HNRNPA2B1 binds m^6A sites in nuclear transcripts and elicits effects on alternative splicing events by mediating m^6A-dependent primary microRNA processing[70]. In addtion, m^6A-switch promotes the binding of splicing factors hnRNPC and hnRNPG[72,74,75]. In terms of the writers, METTL3 plays critical roles in both intron retention[83] and alternative intron/exon inclusion[84] depending on the cell line. METTL16 has been reported to induce efficient splicing of Methionine Adenosyltransferase 2A (*MAT2A*) by controlling intron retention[34]. Deficiency of m^6A demethylases, FTO and ALKBH5, both leads to aberrant RNA splicing due to the m^6A erasure failure near splice sites[53,85]. Regardless of the notion that *Fto*

knockout (KO) cells display splicing defects is owing to the snRNA m^6A_m demethylation[86], more direct evidence is required. On the other hand, FTO has been shown to preferentially binds and demethylates the intronic m^6A on pre-mRNAs, thereby changing pre-mRNA splicing with a prevalence of exon skipping events[50].

Nuclear export—in addition to the splicing regulation, YTHDC1 expedites nuclear to cytoplasmic transport of methylated mRNA by interacting with nuclear export adaptors and the mRNA export receptor machinery NXF1[69]. In neural differentiation, FMRP reads m^6A and cooperates with the nuclear export protein CRM1 to facilitate nuclear export of target mRNA nuclear export[77,79]. Likewise, MTC recruits the TREX mRNA export complex and stimulates its binding to mRNA to assist the efficient export of methylated mRNAs[87]. Moreover, knockdown of ALKBH5[39] and METTL3[69,87] respectively accelerates and delays the nuclear export in an m^6A-dependent manner further supports an emerging paradigm of m^6A as a distinct biomarker for mRNA export pathways.

Stability—as the first identified m^6A reader, the in-depth survey of YTHDF2 defined the earliest m^6A mediated molecular pathway. YTHDF2 recognizes m^6A sites and promotes the rapid degradation of target transcripts through deadenylation by recruiting the CCR4-NOT deadenylase complex[65,88]. Alternatively, by recruiting HRSP12 to the target mRNA, the degradation is triggered by endoribonucleolytic cleavage *via* the YTHDF2-HRSP12-RNase P/MRP complex[89]. YTHDF3 functions cooperatively with YTHDF2 in the cytosol to affect m^6A-dependent mRNA decay[64]. During mammalian spermatogenesis, YTHDC2 mediates target mRNA decay through recruiting the 5'-3' exoribonuclease Xrn1[68,90]. The convoluted destabilizing role of these YTH proteins may partially explain the more prominent increase in target mRNA abundance and half-lives upon METTL3 depletion[91]. In contrast, IGF2BP1-3 stabilize m^6A-methylated mRNAs through

cofactors ELAVL1 (also known as HuR), MATR3, and PABPC1[71]. FMRP has also been reported to maintain the stability of its mRNA targets, despite its direct association with YTHDF2[78]. Moreover, though repelled by m^{6}A, G3BP1 positively regulates mRNA stability in an m^{6}A-dependent manner[81]. It is noteworthy that despite YTHDF2-3 and IGF2BP1-3 exhibit a similar transcriptome-wide binding pattern, these two families oppositely impact the stability of target mRNAs. One plausible explanation is that on certain transcripts, different readers could preferentially recognize the m^{6}A sites localized at distinct regions and lead to the regional specific stabilizing or destabilizing effects on the target mRNA.

Translation—the other YTH family protein, YTHDF1, has been reported to promote translation of m^{6}A methylated transcripts in synergy with YTHDF3[64,65]. YTHDF1 recruits eukaryotic translation eIF3 to facilitate translation initiation through the cap-dependent translation mechanism by forming an eIF4G-dependent loop[65]. Notably, while m^{6}A-YTHDF1 dependent translation enhancement could be canonical in certain cancer cell lines, in other cells such as neuronal cells, this regulation may be stimulation-triggered[64,65,92]. METTL3 has also been shown to interact with eIF3 to enhance the cap-dependent translation of a subset of m^{6}A methylated transcripts by forming a similar loop[93]. Surprisingly, this translation-promoting role is independent of its enzymatic activity or YTHDF1-eIF3 interactions. In addition to the mRNA circularization model, m^{6}A residing in the 5' UTR is linked to the cap-independent translation by directly binding to eIF3[94]. eIF4F-independent mRNA translation can be facilitated by the coordination of METTL3 with ABCF1 in an m^{6}A-dependent manner[95]. Upon heat shock stress, nuclear YTHDF2 could protect 5' UTR m^{6}A of stress-induced transcripts from demethylation by FTO, thereby promoting cap-independent translation initiation[54]. This provides an intuitional example of the competition between m^{6}A reader and eraser during certain cellular responses. 5' UTR m^{6}A controls ribosome

scanning and subsequent start codon selection to guide mRNA alternative translation during the integrated stress response[45]. Besides translation initiation, m^{6}A in mRNA coding regions can be recognized by YTHDC2 to promote translation elongation by resolving mRNA secondary structures[96]. During translation elongation, the codon context of m^{6}A could disrupt the accommodation of selected tRNAs, resulting in the perturbation of translation elongation dynamics in mRNA decoding[97].

Phase separation—m^{6}A methylated mRNA has been known to be enriched in stress granules. Recently, YTHDF1-3 were shown to possess low complexity domains at the *N*-termini and could undergo concentration-dependent liquid-liquid phase separation (LLPS) in the absence of RNA, which can be stimulated by m^{6}A, especially clustered m^{6}As[98,99]. G3BP1 has also been shown to be a switch to trigger and tune phase separation[100,101]. Together, these findings provide new insights of the crosstalk between LLPS and m^{6}A.

1.3.2 Implications in diseases and development

A wealth of studies has demonstrated that the aberrant m^{6}A abundance and the dysregulated m^{6}A effectors are associated with various human diseases, especially in human cancers[102,103]. m^{6}A effectors have been mostly well studied and shown to play critical roles in acute myeloid leukemia (AML)[59-62,104-106], a common hematopoietic malignancy associated with high mortality. The study of FTO built up the first connection that mRNA m^{6}A affects leukemia pathogenesis. FTO is upregulated in some subtypes of AML and plays an oncogenic role by negatively regulating the gene expression of critical oncogenes, *ASB2* and *RARA*, through m^{6}A demethylation[60]. Inhibition of FTO by R-2-hydroxyglutarate (R-2HG) reduces leukemogenesis through destabilizing *MYC via* YTHDF2-mediated degradation in R-2HG sensitive AML cells[59]. METTL3 and METTL14 are also highly expressed in AML, positively impacting the initiation

and maintenance of AML, as well as the self-renewal of leukemia stem cells (LSCs) by introducing m^6A to certain fatal oncogenes to enhance their translation or expression[104]. The overexpression of both m^6A writers and eraser in AML indicates distinct pathways are involved and the m^6A-dependent regulation can be sophisticated.

In multiple studies of hepatocellular carcinoma (HCC), upregulated METTL3 has been observed, which promotes cancer progression by elevating the m^6A (i) on a tumor suppressor, *SOCS2*, to expedite its YTHDF2-dependent degradation[107]; (ii) on an oncogene, *SRF*, to impair its miRNA-directed decay in an IGF2BP1 dependent manner[108]; (iii) on a transcription factor of EMT, *Snail*, to trigger its YTHDF1-mediated translation[109]. However, METTL14 was shown to be downregulated in HCC, which modulates primary miRNA processing through reduced miRNA m^6A to suppress the metastatic potential of HCC[110]. These complexities make HCC a good system to study the mechanisms of how crosstalk occurs among writers and readers in cancer progression.

The upregulation and oncogenic roles of writers have also been reported in many other types of cancer[102,103]. In contrast, hypomethylated m^6A is also associated with a variety of cancers. For instance, in glioblastoma, highly expressed ALKBH5 upregulates *FOXM1* through the m^6A demethylation on its nascent transcript and consequently promotes proliferation and tumorigenesis of glioblastoma stem-like cells (GSCs), whereas FTO inhibition or METTL3 overexpression suppresses GSC growth and self-renewal[111]. In breast cancer, the hypoxia-induced upregulation of ALKBH5 and ZNF217, stabilizing *Nanog* by reducing m^6A on it to prompt breast cancer stem cell phenotype[112]. In endometrial cancer, reductions in m^6A methylation promote cell proliferation and tumorigenicity through dysregulation of key factors in AKT signaling[113]. Part of my doctoral work contributed to the collaborative study in melanoma[55] and skin cancers (in revision) to demonstrate the context-dependent function and regulation of FTO in these cancers.

As summarized above, m^{6}A has profound impacts on cell differentiation and proliferation to drive cancer progression. Such a role is also critical during development[114]. Initial evidence links m^{6}A to the development revealed m^{6}A as a mark of transcriptome flexibility to regulate pluripotency through facilitating mRNA turnovers core pluripotency factors[83,115,116]. Depletion of METTL3 or METTL14 enhances ESC self-renewal and impairs differentiation[116]. However, opposite pluripotency regulation of writers was reported at the same time, likely due to the differential control of cell fate transition through m^{6}A in naïve and prime stem cells[83], indicating the regulatory roles of m^{6}A could be cell state-specific. METTL16 was shown to be essential for mouse embryonic development[32]. In zebrafish, m^{6}A-dependent RNA degradation mediated by YTHDF2 promotes the clearance of methylated maternal mRNA and thereby plays a critical role in transcriptome switching during the maternal-to-zygotic transition[117]. YTHDC1[118] and YTHDC2[67,68] are respectively required for oogenesis and spermatogenesis by binding and facilitating the process of key methylated transcripts. Such a role of YTHDC2 is consistent with the METTL3-mediated regulation in meiosis initiation[119].

In addition to the fertility defects associated with the deprivation of multiple m^{6}A effectors, m^{6}A also impacts somatic cell differentiation in mammals. Loss of METTL3 in naïve T cells impedes the transcript decay of SOCS family proteins, thereby disrupting T cell homeostatic proliferation and differentiation[120]. Decreased m^{6}A upon *Mettl14* KO or METTL3 knockdown slows the decay of neurogenesis-related transcripts, leading to prolonged cell cycle of cortical neural stem cells and delayed cortical neurogenesis[121]. Depletion of YTHDF2 delays degradation of methylated neuron differentiation-related transcripts, thus impairs proliferation and differentiation of neural stem and progenitor cells[122]. Of note, despite FTO have been long proved to be associated with severe developmental defects of mice[44,123-125], it remained elusive whether

its m^6A demethylase activity is involved. A major part of my doctoral work was committed to investigating the physiological substrate of FTO in normal mammalian tissues and during development (under review).

1.4 Scope of this dissertation

My dissertation will focus on an emerging topic in the field of epitranscriptomics: the context-dependent regulation and function of RNA m^6A demethylation, as highlighted by the study of the specificity and multifunctionality of FTO in cancers, mammalian tissues, and during development.

Chapter **2** presents a comprehensive characterization of the cellular substrate spectrum of FTO, demonstrating the specific substrates contributing to the roles of FTO in mRNA stability and translation.

Chapter **3** presents the physiological substrates and functions of FTO in normal mammalian tissues and during development, addressing the question of the presence and functional relevance of RNA m^6A demethylation in mammals.

Chapter **4** presents the context-dependent regulation and function of FTO depending on the different types of cancers and environmental stresses.

Chapter **5** summarizes recent advances related to the findings presented in Chapter **2-4**, and discusses the potential future directions in the field.

Chapter 2

RNA m^6A, m^6A_m, and m^1A Demethylation by FTO

2.1 Introduction: FTO as the first identified RNA demethylase

FTO was the first discovered RNA demethylase, which exhibited a varies intriguing phenotypes in mammalian development[44,123-125] and human developmental diseases[43,126-129]. Our lab devoted extensive efforts to identify the substrates and to understand the biological functions of FTO. FTO was reported to catalyze the demethylation of 3-methylthymine (3meT) in single-stranded DNA[130] and 3-methyluracil (3meU) in RNA[131] as an iron(II)- and αKG-dependent dioxygenase. Later, FTO was identified as an RNA demethylase catalyzing reversal of the internal *N*^{6}-methyladenosine (m^6A) methylation in mRNA *in vitro* and inside cells[12,132], which revived the broad interest in gene regulation by reversible RNA methylation.

In addition to internal mRNA m^6A, adjacent to the 5' cap, the second base in many mRNAs can be 2'-*O*-methylated, with a portion of these bases also bearing m^6A methylation to form cap-m^6A_m[133-135]. The m^6A portion of cap-m^6A_m is known to be an *in vitro* substrate of FTO[136], with a recent study showing that cap-m^6A_m stabilizes mRNA by preventing DCP2-mediated decapping and microRNA-mediated mRNA degradation[40], whereas the functional relevance of the m^6A_m removal by FTO has yet to be fully explored. However, this study also suggested that internal mRNA m^6As may not be relevant substrates of FTO[40,41], despite recent reports of a range of biological processes affected by the demethylation of internal m^6A in the last several years[42-62].

We aim to investigate the demethylation preference of FTO towards internal m^6A and cap-m^6A_m and provide a systematic study of the substrate spectrum of FTO inside cells.

2.2 Results

2.2.1 Internal m^{6}A is the preferential substrate of FTO on mRNA

2.2.1.1 FTO demethylates more internal m^{6}A based on absolute modification amount

FTO has been shown to demethylate both m^{6}A and cap-m^{6}A$_m$. To further validate the previous reports and identify the preferential substrates with biological relevance, we first established the standard curves calibrated by using synthetic nucleoside standards on Ultra-high-performance liquid chromatography-tandem mass spectrometry (UHPLC-MS/MS) to quantify the levels of m^{6}A and cap-m^{6}A$_m$ (**Figure 2.1A**).

We then isolated polyadenylated RNAs possessing both naturally occurring m^{6}A and cap-m^{6}A$_m$ from human cells and performed *in vitro* demethylation using purified human FTO (**Figure 2.1B**). FTO (2 μM in 20 ul) is capable of almost complete demethylation of all cap-m^{6}A$_m$ and 81.4% of m^{6}A in 200 ng polyadenylated RNAs within 1 hour under the standard reaction condition. Using EDTA in the same reaction system, which chelates the essential iron cofactor, serves as a control. We further lowered the concentration of FTO to achieve incomplete demethylation of cap-m^{6}A$_m$ in polyadenylated RNAs and then compared the global changes of m^{6}A and cap-m^{6}A$_m$. We found that 0.2 μM of FTO (20 ul reaction volume) can demethylate 81.9% of cap-m^{6}A$_m$ and 20.3% m^{6}A in the purified polyadenylated RNAs. Our results unequivocally show that FTO demethylates both m^{6}A and cap-m^{6}A$_m$ in purified polyadenylated RNAs *in vitro* (**Figure 2.1C**). FTO exhibits a higher demethylation percentage towards cap-m^{6}A$_m$ *in vitro*; however, it should be noted that because the total amount of m^{6}A is around 10-fold to 15-fold higher than that of cap-m^{6}A$_m$ in mammalian polyadenylated RNAs (**Figure 2.1D**), more m^{6}A is demethylated compared to cap-m^{6}A$_m$ in purified polyadenylated RNAs in terms of the absolute number of modifications. Next, we evaluated the effects of FTO perturbation on the cellular m^{6}A and cap-m^{6}A$_m$ levels of

polyadenylated RNAs. We measured the levels of m^6A and cap-m^6A_m upon similar knockdown efficiency (**Figure 2.1E**) of FTO in comparison with the control. A 19.2%, 11.8%, and 8.8% increase of the m^6A/A ratio was observed in the polyadenylated RNAs in the knockdown samples compared to the control in HeLa, HEK293T, and 3T3-L1 cells, respectively, whereas a 13.7%, 20.6%, and 30.1% increase of the cap-m^6A_m/A ratio was observed (**Figure 2.1F**).

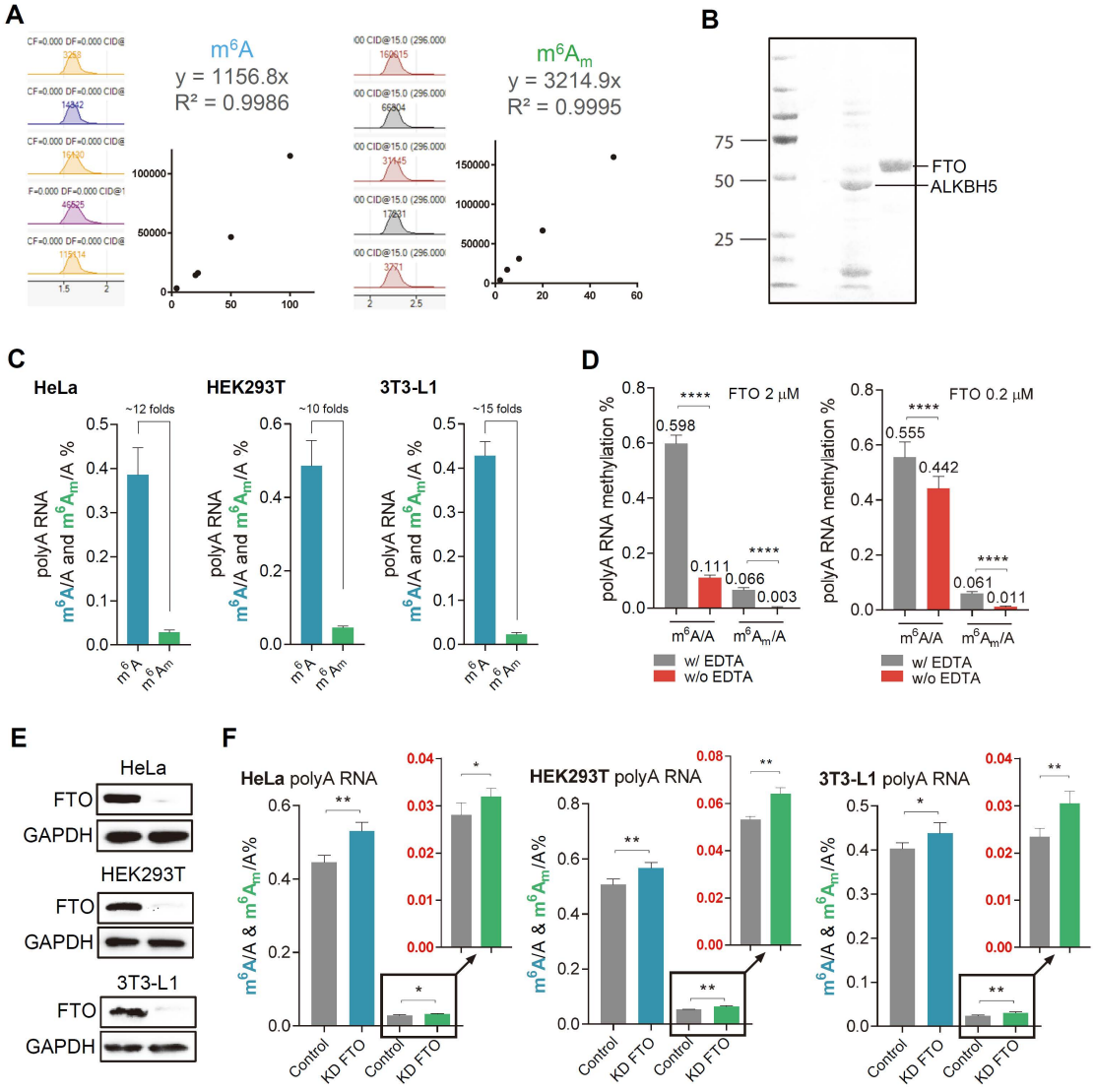

Figure 2.1 FTO mediates more m^6A demethylation based on the modification amount on mRNA

(**A**) Peak area and standard curve for m^6A and cap-m^6A_m. (**B**) Coomassie blue analysis of purified mammalian FTO. (**C**) Quantification of m^6A/cap-m^6A_m ratios in HeLa, HEK293T, and 3T3-L1 cells by UHPLC-MS/MS. (**D**) Quantification of remaining m^6A/A and cap-m^6A_m/A by UHPLC-MS/MS in the *in vitro* demethylation assay. (**E**) Western blot showing the knockdown efficiency

(**Figure 2.1, continued**) of FTO in HeLa, HEK293T, and 3T3-L1 cells. (**F**) Quantification of the m^6A and cap-m^6A_m ratios in polyadenylated RNA by UHPLC-MS/MS upon FTO knockdown compared to control in HeLa, HEK293T and 3T3-L1 cells. *p* values were determined using Student's unpaired *t*-test. **p* < 0.05, ***p* < 0.01. Error bars, mean ± SD for *n* = 4 experiments in (C), (D), and (F).

These results showed both m^6A and cap-m^6A_m demethylation by FTO inside different cell lines. Again, because the level of internal m^6A is 10-fold higher than that of cap-m^6A_m in these cells, 5-10 times more internal m^6A based on modification amount are subjected to FTO-mediated demethylation compared with m^6A_m inside cells.

2.2.1.2 Spatial regulation of FTO mediates its substrate preference

We were intrigued by the opposite pattern of demethylation percentage of m^6A and cap-m^6A_m by FTO across HeLa, HEK293T, and 3T3-L1 cells. We sought to investigate how FTO mediates differential m^6A *versus* m^6A_m demethylation in different cell lines and why FTO exhibits much higher m^6A demethylation (over ~10-fold) *versus* m^6A_m inside certain cells despite m^6A_m shows higher demethylation percentage *in vitro*. We reasoned that as almost all mRNA caps are bound by cap-binding proteins inside the cell nucleus[137], the lack of cap-m^6A_m demethylation in certain cells might reflect substrate accessibility by FTO.

FTO was first reported to be a nuclear protein, but it was later shown to exist in both cell nucleus and cytoplasm in different mammalian cell lines[138,139]. We asked whether the spatial regulation of FTO plays a crucial role in gaining access to its cellular substrate(s). We performed confocal immunofluorescence (IF) imaging with an anti-FTO specific antibody to investigate the cellular localization of FTO in several mammalian cell lines. We found that FTO predominantly accumulated in the cell nucleus in HeLa, Mel624, and HepG2 cells. However, FTO was located in both cell nucleus and cytoplasm in HEK293T cells and 3T3-L1 cells, with more notably cytoplasmic distribution in 3T3-L1 cells (**Figure 2.2A**). Consistent with our hypothesis, the

increasing proportions of cytoplasmic FTO from HeLa, HEK293T, to 3T3-L1 cells, correlate with the corresponding increased demethylation percentage towards cap-m^6A_m and reduced m^6A demethylation percentage in these cells.

We used HEK293T cells as a model to further study how cellular distribution of FTO affects its demethylation and substrate preference. We separated the nuclear and cytoplasmic fractions of HEK293T cells (**Figure 2.2B**) and then measured FTO-mediated demethylation of m^6A and cap-m^6A_m in polyadenylated RNAs in each fraction. We found that knockdown of FTO led to more than a 30% increase of the m^6A level in cell nucleus, but only a slight increase of the m^6A level in cytoplasmic polyadenylated RNAs. In contrast, cap-m^6A_m in cytoplasmic but not nuclear polyadenylated RNAs was significantly increased upon FTO knockdown (**Figure 2.2C**).

We next expressed an FTO mutant lacking the nuclear localization signal (ΔNLS-FTO)[138,140] in HEK293T cell lines. We found that overexpression of ΔNLS-FTO, which was directed to the cytoplasm, led to decreased cap-m^6A_m but not m^6A in polyadenylated RNA from HEK293T cells. This result contrasts with the effects caused by wild-type (WT) FTO overexpression mostly within the nucleus (**Figure 2.2D**). Additionally, in HEK293T cells, overexpression of WT FTO but not ΔNLS-FTO led to a significant decrease of m^6A in polyadenylated RNAs in the cell nucleus, while the change of nuclear cap-m^6A_m level in polyadenylated RNAs was not statistically significant. In the cytoplasm, m^6A in polyadenylated RNA showed a small change in percentage upon WT FTO expression, but cap-m^6A_m showed a larger decrease with overexpression of ΔNLS-FTO than WT FTO (**Figure 2.2E**). These results further indicate that the FTO-mediated demethylation of m^6A is prominent in the cell nucleus but also occurs in the cytoplasm, whereas cap-m^6A_m is mainly a target of FTO in the cytoplasm.

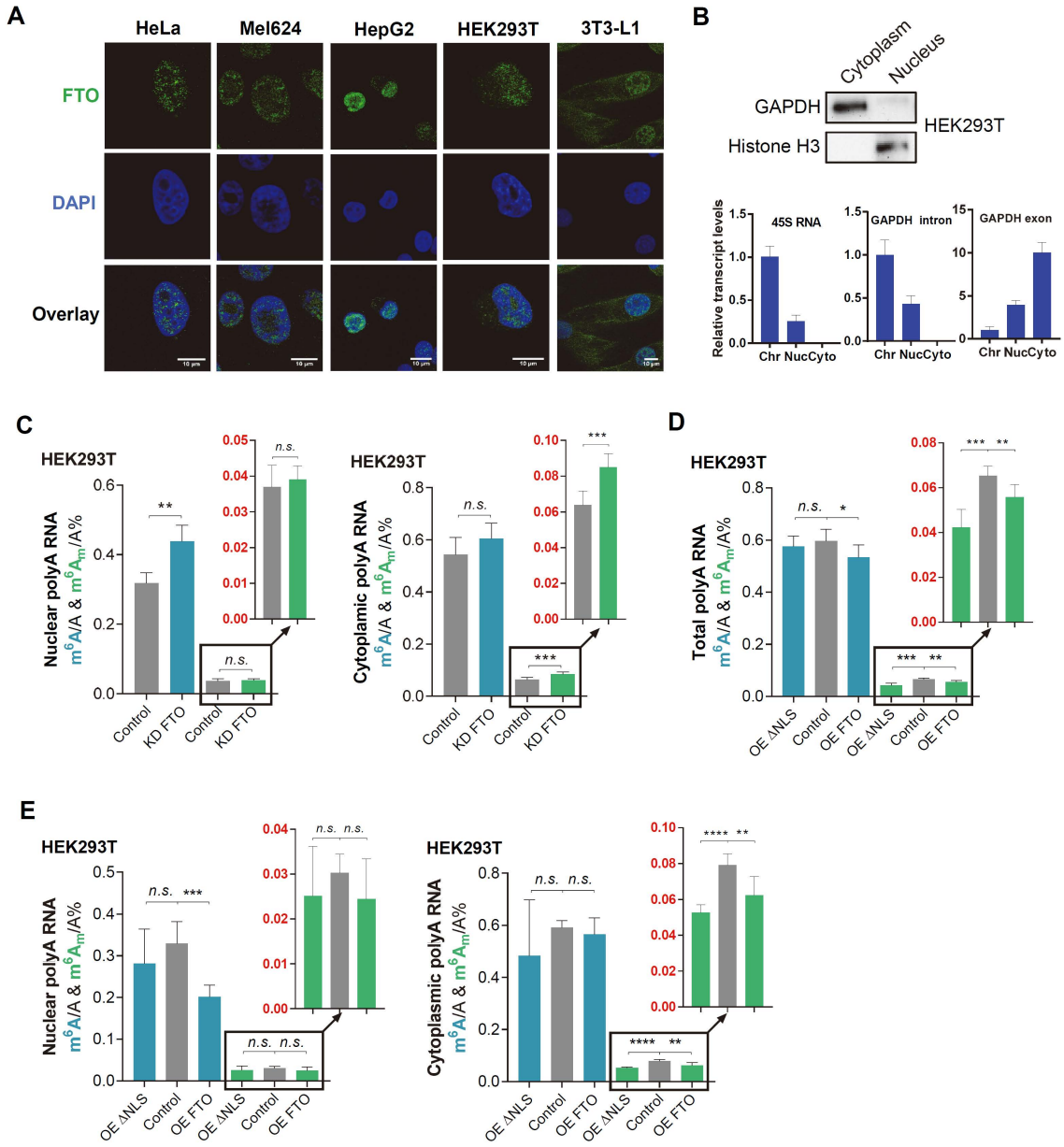

Figure 2.2 Spatial localization of FTO influences its demethylation of target substrates.
(**A**) Subcellular localization of FTO among the HeLa, Mel624, HepG2, HEK293T, and 3T3-L1 cell lines. The nucleus was stained with DAPI. Scale bars, 10 mm. Representative images were selected from three independent experiments. (**B**) Western blot and RT-qPCR validation of the cytoplasm and nucleus separation in HEK293T cells. (**C**) Quantification of m^6A/A ratios and cap-m^6A_m/A ratios in polyadenylated RNA from the nucleus and the cytoplasm of HEK293T cells by UHPLC-MS/MS upon FTO knockdown compared to control. (**D**) Quantification of m^6A/A ratio and cap-m^6A_m/A ratio on polyadenylated RNA from HEK293T cells by UHPLC-MS/MS upon overexpression of WT FTO or ΔNLS-FTO compared to control. (**E**) Quantification of m^6A/A ratios and cap-m^6A_m/A ratios in polyadenylated RNA from the cytoplasm and nucleus of HEK293T cells by UHPLC-MS/MS upon overexpression of WT FTO or ΔNLS-FTO compared to control. *p* values were determined using Student's *t*-test. $^{**}p < 0.01$, $^{***}p < 0.001$, $^{****}p < 0.0001$. *n.s.* means not significant. Error bars, mean ± s.d. for $n = 6$ experiments in (C) to (E).

2.2.1.3 Notable cytoplasmic m^{6}A demethylation by FTO in certain AML cell lines

Considering the m^{6}A level is at least 10-fold higher than that of cap-m^{6}A$_m$ in mRNA, even in cell cytoplasm, FTO can still mediate effective m^{6}A and cap m^{6}A$_m$ demethylation, in absolute terms. In certain acute myeloid leukaemia (AML) cell lines which our lab showed proliferation inhibition with FTO knockdown previously[60], we found extensive cytoplasmic expression of FTO (**Figure 2.3A**), suggesting the critical cytoplasmic m^{6}A demethylation roles of FTO in these cells. Accordingly, stable knockdown of FTO led to increased m^{6}A in both nucleus and cytoplasm, with dramatic increased cytoplasmic m^{6}A, whereas an increase of m^{6}A$_m$ only in the cytoplasmic but not nuclear fraction (**Figure 2.3B&C**). It is noteworthy that unlike the ratios of 1/10 to 1/15 between m^{6}A$_m$ and m^{6}A in HeLa, HEK293T, and 3T3-L1 cells, the m^{6}A$_m$ to m^{6}A ratios are among 1/20 to 1/30 in the NB4 and MONOMAC-6 cells (**Figure 2.3B**), as well as several other AML cells[59], showing the predominant m^{6}A demethylation by FTO.

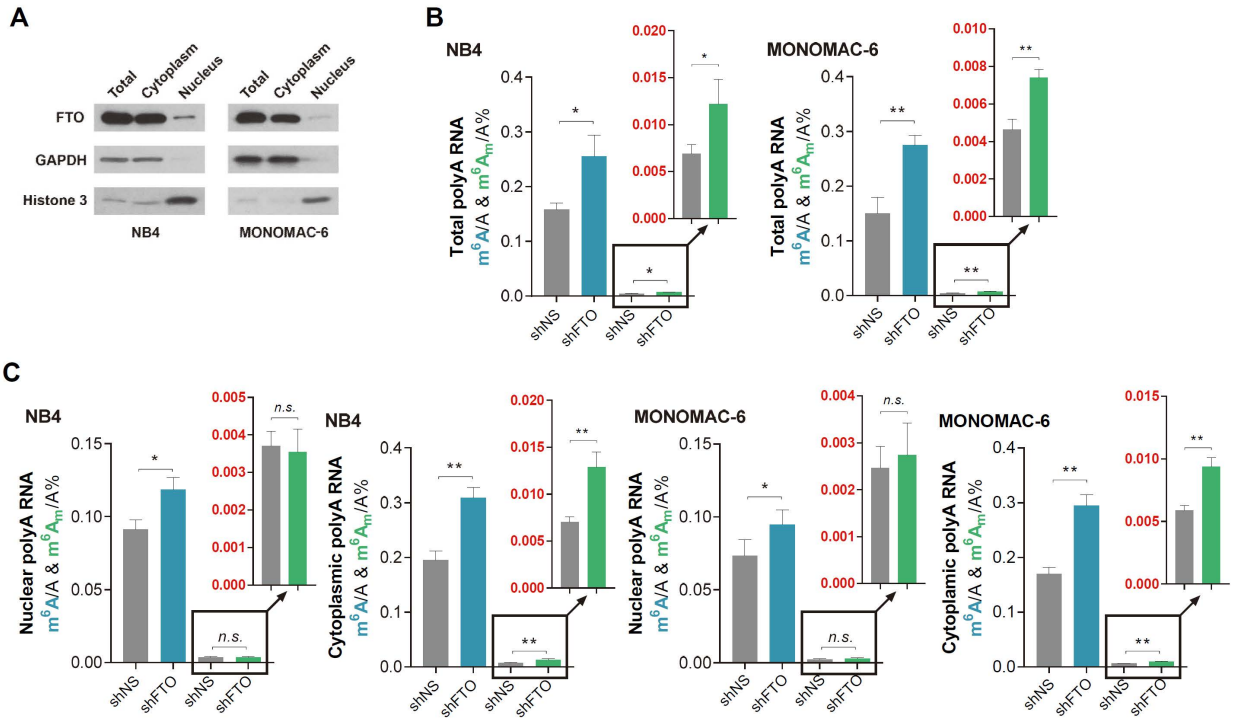

Figure 2.3 FTO-mediated m^{6}A and cap-m^{6}A$_m$ demethylation in certain AML cell lines

(**Figure 2.3, continued**) (**A**) Western blot showing the FTO expression in the total, cytoplasmic, and nuclear fraction of NB4 and MONOMAC-6 cells (**B**) Quantification of m^6A/A ratios and cap-m^6A_m/A ratios in total polyadenylated RNA from NB4 and MONOMAC-6 cells by UHPLC-MS/MS upon FTO knockdown compared to control. (**C**) Quantification of m^6A/A ratio and cap-m^6A_m/A ratio in polyadenylated RNA from nucleus and cytoplasm of NB4 and MONOMAC-6 cells by UHPLC-MS/MS upon FTO knockdown compared to control. *p* values were determined using Student's *t*-test. $*p < 0.05$, $**p < 0.01$. *n.s.* means not significant. Error bars, mean ± s.d. for $n = 4$ experiments in (B) and (C).

2.2.1.4 FTO-mediated m^6A demethylation influences transcript abundance

To understand the functional impact of m^6A *versus* cap-m^6A_m demethylation by FTO on mRNA, we analyzed transcript abundance changes of m^6A and cap-m^6A_m-containing transcripts upon FTO knockdown in HEK293T cells. The m^6A sites and the transcripts starting with cap-m^6A_m were adopted from previously published datasets[16,40]. Almost all of these annotated m^6A_m sites exist within 500 nt from the transcription start site (TSS) (**Figure 2.4A**).

To accurately dissect the individual effects of cap-m^6A_m and m^6A and to avoid cross-effects between these two modifications, we categorized all the transcripts into four groups. The first group of transcripts only contains cap-m^6A_m, the second group of transcripts only contains internal m^6A, the third group of transcripts contains both modifications, and the rest of transcripts were considered as the control group to compare against. Using this categorization scheme, we found that the overall abundance of transcripts only containing cap-m^6A_m did not appear to statistically change upon FTO knockdown in HEK293T cells, while the global transcript abundance of the other three groups showed statistically significant increases (**Figure 2.4B**).

Transient knockdown of FTO led to increased transcript abundance of the transcripts harboring only internal m^6A compared to the transcripts without m^6A or m^6A_m in HEK293T cells (**Figure 2.4C**); similar effects were also observed on these cells upon knockdown of ALKBH5, another m^6A demethylase (**Figure 2.4D**). However, knockdown of FTO or ALKBH5 appears to affect different subsets of transcripts (**Figure 2.4E**). This stabilization effect on m^6A methylated

transcripts was thought to be mediated by m^6A reader proteins IGF2BP1-3, which has been reported to recognize m^6A and stabilize target mRNAs[71], or through other yet to be discovered reading mechanisms.

The presence of m^6A_m adjacent to the 5' cap was previously reported to stabilize mRNA transcripts by preventing DCP2-mediated cap cleavage and microRNA-mediated mRNA degradation in HEK293T cells[40]. However, in comparison with the other three groups of transcripts, transcripts only containing cap-m^6A_m but not internal m^6A showed significantly smaller changes in transcript abundance upon FTO knockdown. FTO knockdown led to elevated cap-m^6A_m but this did not appear to associate with increased abundance of these transcripts, despite the proposed transcript stabilizing role of m^6A_m at the cap[40]. This effect is opposite of those observed for transcripts containing both m^6A_m and m^6A or transcripts only containing m^6A. Both of the latter two groups showed significantly larger increases in transcript abundance upon FTO knockdown compared to the control group (**Figure 2.4C**). Lastly, we grouped transcripts only containing m^6A *versus* non-m^6A (the others) without considering cap-m^6A_m (**Figure 2.4F**), and transcripts only containing cap-m^6A_m *versus* non-cap-m^6A_m (the others) without considering m^6A (**Figure 2.4G**). The transcripts containing m^6A showed increased abundance compared to the rest upon FTO knockdown (**Figure 2.4F**), while transcripts containing cap-m^6A_m showed reduced abundance compared to the rest upon FTO knockdown (**Figure 2.4G**).

These results suggest that though cap-m^6A_m could be associated with a higher global transcript abundance, the abundance of transcripts only bearing cap-m^6A_m dos not appear to respond to FTO knockdown. The change in abundance of these transcripts was significantly smaller than the transcripts containing neither m^6A_m nor m^6A upon FTO knockdown, whereas transcripts only containing m^6A or containing both m^6A and m^6A_m exhibited significantly larger

increases in their transcript abundance than transcripts containing neither or only cap-m^{6}A$_m$ upon FTO knockdown. We further cross-compared the list of transcripts containing only m^{6}A but not cap-m^{6}A$_m$ with the published FTO CLIP-seq results in the same cell line[50]. We clearly observed a statistically significant increased transcript abundance of the m^{6}A targets (bound by FTO), with no significant change for transcripts possessing m^{6}A but not bound by FTO (**Figure 2.4H**), further confirming that FTO mediates transcript abundance through internal m^{6}A demethylation of its mRNA targets.

In the previous analysis[40], transcripts containing dual modifications of both m^{6}A and cap-m^{6}A$_m$ and the transcripts only containing cap-m^{6}A$_m$ in HEK293T cells were mixed together. Thus, the reported transcript upregulation role of cap-m^{6}A$_m$ upon FTO knockdown likely can be attributed to internal m^{6}A from transcripts that contain both modifications. In addition, we mixed transcripts containing both m^{6}A and m^{6}A$_m$ with transcripts that only contain cap-m^{6}A$_m$ (all cap-m^{6}A$_m$) in HEK293T cells as previously described. Upon FTO knockdown, we only observed moderately larger transcript abundance changes of these all cap-m^{6}A$_m$ transcripts compared to transcripts starting with cap-A$_m$ upon FTO knockdown; however, we failed to observe such difference compared to transcripts that contain cap-C$_m$, U$_m$, or *N*$_m$s (the union set starting with all types of *N*$_m$) (**Figure 2.4I**). In fact, there is an even noticeably smaller transcript abundance change when comparing all cap-m^{6}A$_m$ transcripts with G$_m$-containing transcripts upon FTO knockdown (**Figure 2.4I**).

Finally, upon FTO knockdown, the transcripts only containing m^{6}A$_m$ still displayed notably smaller transcript abundance changes compared to cap *N*$_m$s-containing transcripts, while the transcripts only containing m^{6}A show the largest abundance increase (**Figure 2.4I**). We thus conclude that the transcript stabilizing effect previously observed for cap-m^{6}A$_m$ upon FTO

knockdown is most likely derived from the stabilizing role of internal m^{6}As that co-exist with cap-m^{6}A$_m$.

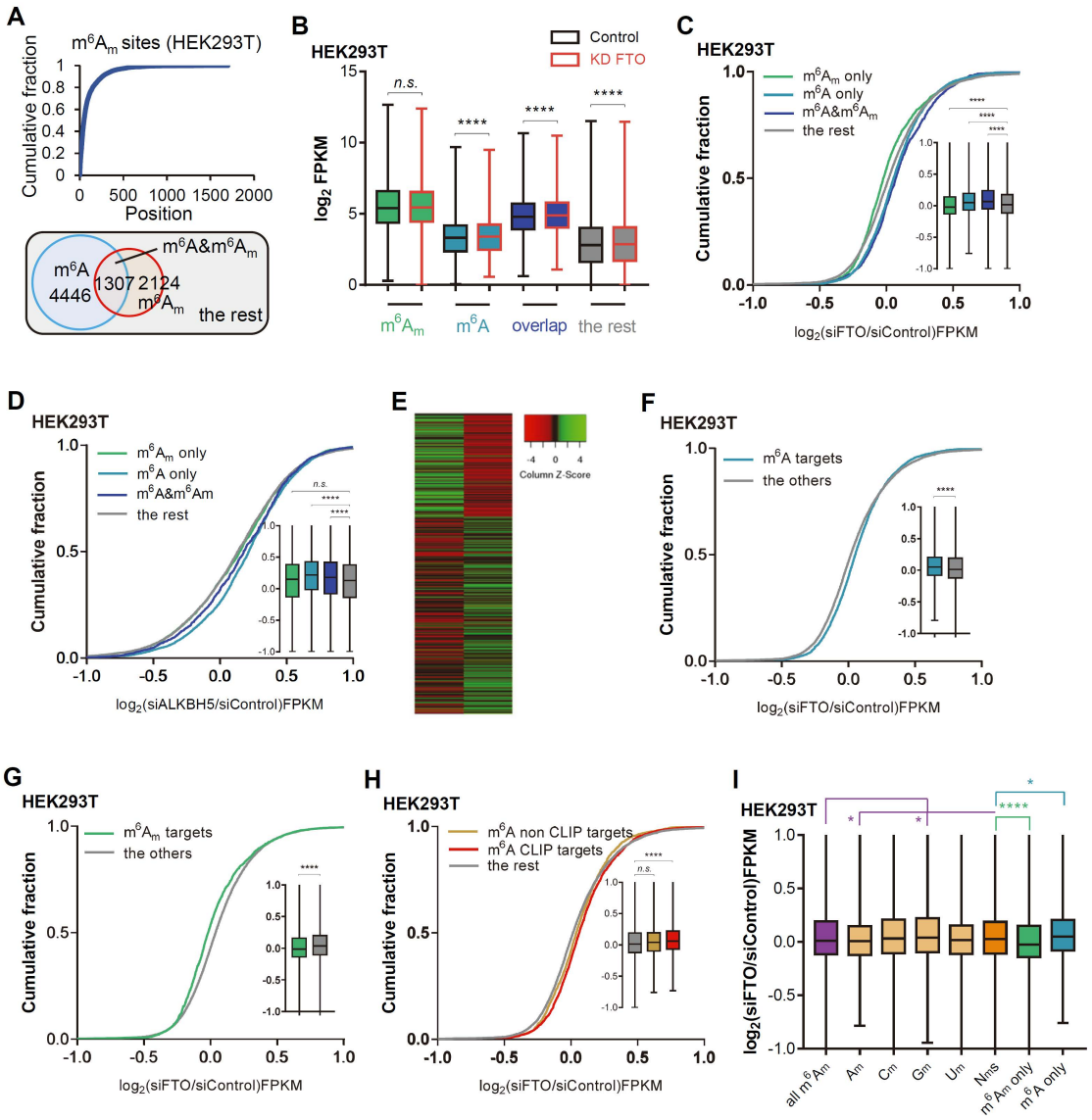

Figure 2.4 Gene expression regulation by FTO-mediated m^{6}A and cap-m^{6}A$_m$ demethylation. (**A**) Cumulative fraction of the cap-m^{6}A$_m$ sites along with mRNA starting with the transcription start site (top); a scheme for the transcripts grouping strategy (bottom). (**B**)-(**D**) mRNA transcripts are classified into four groups: transcripts only containing cap-m^{6}A$_m$, *n* = 2,016; only containing m^{6}A, *n* = 3,987; containing both m^{6}A and m^{6}A$_m$ (overlap), *n* = 1,307; and transcripts that contain neither m^{6}A nor m^{6}A$_m$ (labeled as the rest), *n* = 5,598. (B) The overall transcript abundance of each group in FTO knockdown and control samples shown by box plots. (C) The changes of transcript abundance of each group upon FTO knockdown were shown by cumulative curves. (D) The changes of transcript abundance of each group upon ALKBH5 knockdown were shown by cumulative curves. (**E**) Heatmap showing the differential transcript targets of FTO (left) and ALKBH5 (right). (**F**) mRNAs were classified into the transcripts containing only m^{6}A (*n* = 3,987)

(**Figure 2.4, continued**) and the rest (*n* = 8,921) as control. The changes of transcript abundance of each group upon FTO knockdown were shown by cumulative curves. (**G**) mRNAs were classified into the transcripts containing only cap-m^6A_m (*n* = 1,885) and the rest (*n* = 11,023) as control. The changes of transcript abundance of each group upon FTO knockdown were shown by cumulative curves. (**H**) mRNAs were classified into the FTO-bound m^6A methylated transcripts (*n* = 1,895), FTO-bound transcripts without m^6A (*n* = 2,092), and the rest (*n* = 8,896) as control. The changes of transcript abundance of each group upon FTO knockdown were shown by cumulative curves. (**I**) As previously reported (ref), mRNA expression levels are classified into groups, including mRNAs that start with m^6A_m (*n* = 3,323), A_m (*n* = 1,311), C_m (*n* = 2,655), G_m (*n* = 1,990), and N_ms (*n* = 7,688). The change of transcript abundance of each group upon FTO knockdown was shown by cumulative curves. For (B) to (D) and (F) to (I), data represent the average from two independent RNA-Seq datasets; each box shows the first quartile, median, and third quartile. *p* values were determined using the Wilcoxon test. **p* < 0.05, *****p* < 0.0001. *n.s.* means not significant. Error bars, mean ± s.d. for *n* indicated above.

2.2.2 Expanding the cellular substrate spectrum of FTO

To thoroughly survey the cellular RNA substrate bound to FTO, we performed the cross-linking immunoprecipitation followed by high-throughput sequencing (CLIP-Seq) using FLAG-tagged FTO in 3T3-L1 cells. Consistent with the eCLIP-seq and CLIP-seq results published at the same time[50,141], our data also showed that FTO was able to bind mRNA, tRNA, snRNA, snoRNA, and rRNA, among which mRNA was enriched as expected (**Figure 2.5A**). The purity of anti-FLAG-tagged pull-down and the ^{32}P labeled protein gel of CLIP were validated, indicating the formation of covalently linked FTO-nucleic acid complexes (**Figure 2.5B**).

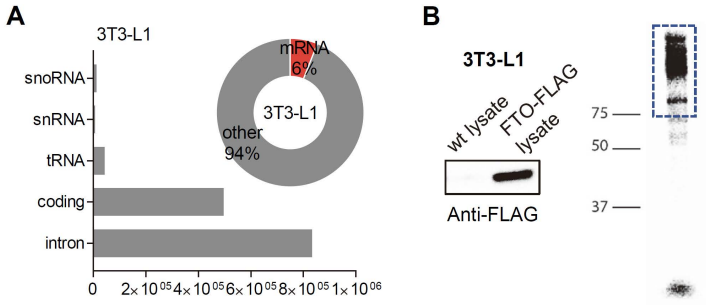

Figure 2.5 CLIP-Seq reveals the RNA binding targets of FTO in 3T3-L1 cells
(**A**) Bar graph summarizing the distribution of the reads of the FTO-bound RNA species in 3T3-L1 cells; donut graph showing the percentage of the FTO-bound mRNA in all FTO CLIP-seq RNA targets in 3T3-L1 cells. (**B**) Western blot showing the anti-FLAG pulldown purity (left); SDS-PAGE protein gel showing ^{32}P labeled FTO-nucleic acids complex (right).

We were particularly interested in non-mRNA CLIP-targeted RNA species and we examined the potential activity of FTO on those RNA species. Since rRNA occupied the majority of sequencing reads from the CLIP-Seq, we first assessed the effect of FTO knockdown or overexpression on the m^6A levels on mature rRNA in HeLa, HEK293T, and 3T3-L1 cell lines, respectively. No significant changes were observed for m^6A levels on mature rRNAs, including 28S rRNA and 18S rRNA (**Figure 2.6A-C**). We reasoned that rRNA can be typically over-represented from CLIP-Seq.

Reversible RNA methylation of snRNA was previously unprecedented. We carefully compared the m^6A levels of snRNA, including U1 RNA (a complex band of U1 RNA and 5.8S), U2 RNA, and U6 RNA, in wild-type (WT) and *Fto* homozygous KO ($Fto^{-/-}$) mouse Embryonic fibroblasts (MEF) cells (**Figure 2.6D**). We observed increased m^6A on the U6 RNA, but not other snRNAs, upon *Fto* depletion (**Figure 2.6E**), suggesting that U6 RNA m^6A could be reversibly modulated by FTO.

Besides m^6A, we also tested FTO-mediated demethylation towards m^6A_m in these U RNAs. After decapping, increased m^6A_m was observed in both U1/5.8s RNA and U2 RNA. The quantification results showed a reasonable level of m^6A_m in U2 RNA, with close to one m^6A_m *per* U2 RNA molecule (187 bp long) (**Figure 2.6F**). To determine if the m^6A_m is near the cap or internal, we measured the internal m^6A_m level without decapping; decapping is required to remove the cap structure and expose cap-m^6A_m before nuclease P1 and alkaline phosphatase digestion. Internal m^6A_m was also observed in both U2 and U1/5.8S RNA, with increased internal m^6A_m observed in U1/5.8s upon *Fto* depletion (**Figure 2.6G**). However, considering the average length of mammalian U1 snRNA and 5.8s rRNA (around 160 bp), the 0.1% ratio of internal m^6A_m/A indicates less than 0.05 m^6A_m *per* molecule of U1 snRNA. In U2 RNA, both the cap- and internal

m^6A_m modifications are more abundant, approaching 0.5 cap- and internal m^6A_m *per* molecule of U2 RNA, respectively. *Fto* KO led to a significant increase in the total m^6A_m level, most likely at the cap.

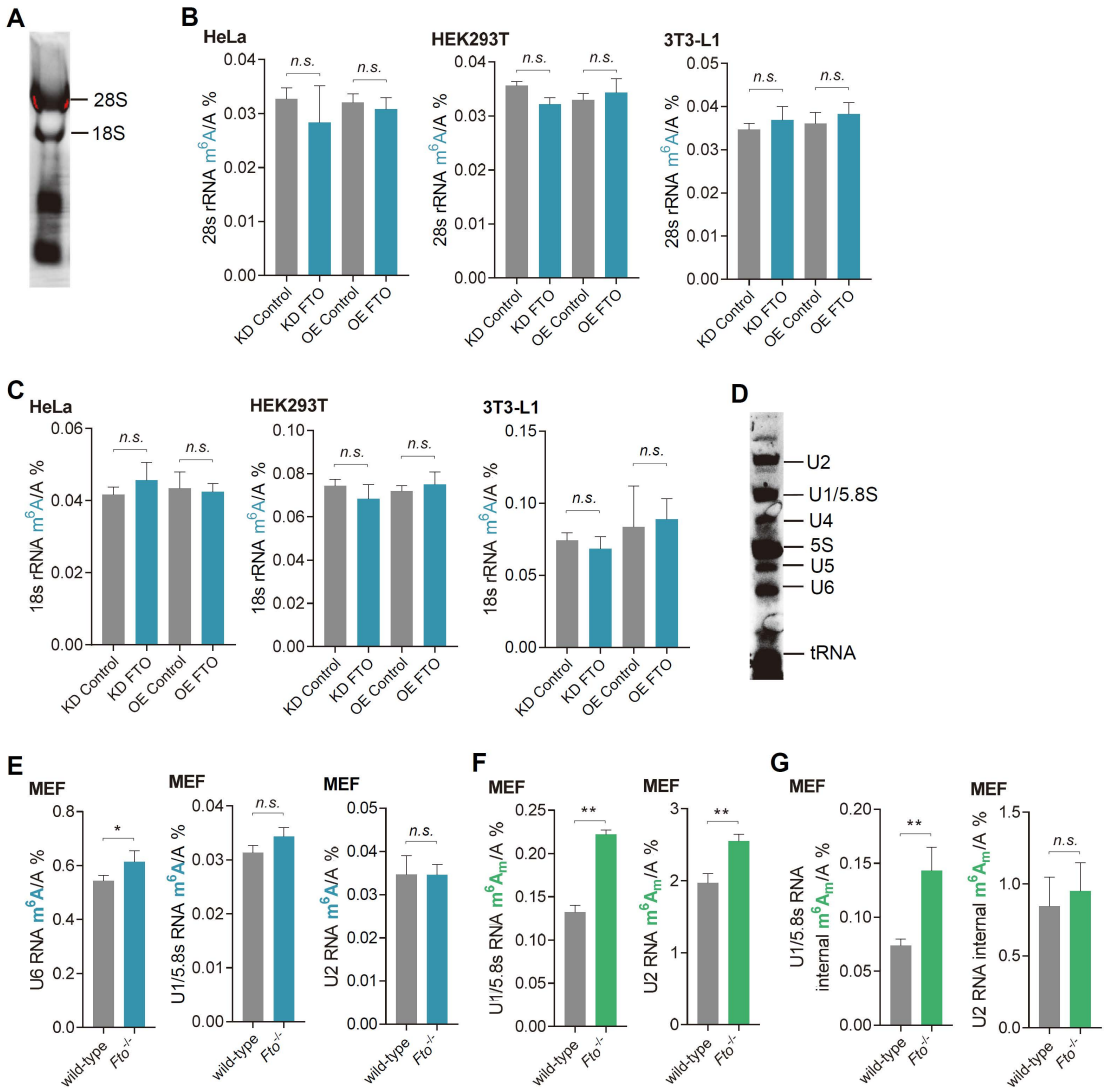

Figure 2.6 FTO mediates m^6A and cap-m^6A_m demethylation in snRNAs
(**A**) Separation of 28S rRNA and 18S rRNA from total RNA shown on a 2% agarose gel. (**B**) and (**C**) Quantification of the m^6A/A ratios by UHPLC-MS/MS upon FTO knockdown or overexpression in HeLa, HEK293T, and 3T3-L1 cells. (B) 28S rRNA. (C)18S rRNA. (**D**) Separation of individual snRNAs from the purified nuclear RNA < 200 nt shown on the 6% TEB-Urea gel. (**E**) Quantification of the m^6A/A ratios in U6 RNA, U1/5.8s RNA, and U2 RNA by UHPLC-MS/MS upon *Fto* KO in MEF cells. (**F**) Quantification of the internal and cap-m^6A_m/A ratios in U1/5.8s RNA and U2 RNA by UHPLC-MS/MS upon *Fto* KO in MEF cells. (**G**) Quantification of the internal m^6A_m/A ratios in U1/5.8s RNA and U2 RNA by UHPLC-MS/MS upon *Fto* KO in MEF cells. *p* values were determined using Student's *t*-test. *$p < 0.05$, **$p < 0.01$.

(**Figure 2.6, continued**) *n.s.* means not significant. Error bars, mean ± s.d. for $n = 3$ experiments in (B) and (C); for $n = 6$ experiments in (E) to (G).

2.2.3 FTO mediates tRNA m^1A demethylation to affect translation

2.2.3.1 tRNA m^1A is another substrate of FTO

In the CLIP-seq results, we observed that FTO associated with tRNA, and the distribution of CLIP reads in tRNA was significantly enriched compared to input. We first examined whether FTO exhibited biochemical demethylation activity towards tRNA by treating the purified total tRNA from HEK293T cells with mammalian FTO protein under standard demethylation conditions. The levels of abundant tRNA methylations, including m^1A, m^1G, m^7G, m^5C, m^2G, $m^2{}_2G$, A_m, and m^3C, were measured in the presence or absence of EDTA. Interestingly, in comparison with the control samples, incubation of purified tRNA with FTO led to a dramatic decrease of the m^1A level and a slight decrease of m^3C, but not levels of m^1G, m^7G, m^5C m^2G, $m^2{}_2G$, or A_m (**Figure 2.7A&B**), indicating that m^1A in tRNA is a biochemically viable substrate of FTO in addition to m^6A and m^6A_m in mRNA.

We then compared the demethylation activity of FTO towards tRNA m^1A and mRNA m^6A by incubating similar numbers of m^1A and m^6A (to achieve this, 100 ng purified mammalian polyadenylated RNA and 20 ng tRNA were pooled together based on the estimation that tRNA m^1A methylation percentage is around 2-4% while polyadenylated RNA m^6A methylation is around 0.4-0.8%) together with mammalian FTO in the presence or absence of EDTA. The demethylation activity of FTO towards tRNA m^1A was comparable to that of polyadenylated RNA m^6A (**Figure 2.7C**). Considering the high abundance of tRNA inside mammalian cells, the FTO-mediated demethylation towards tRNA m^1A could also be of functional importance.

m^1A58 is the most common m^1A site in tRNA, residing in the loop region of a TΨC stem-loop motif of tRNA[142,143], and can be actively reversed in HeLa and MEF cells[144]. We reasoned

that FTO may preferentially mediate m^1A demethylation in tRNAs with a selectivity towards a stem-loop structure, as previous studies suggested low activities of FTO towards m^1A in single-stranded nucleic acid substrates[131]. We synthesized two ssRNA probes, one with m^1A in a stem-loop sequence mimicking the TΨC loops in $tRNA^{His(GUG)}$ (contains m^1A58) and the other one with m^1A in an unstructured sequence (**Figure 2.7D**). Indeed, FTO exhibited low activity towards m^1A in the unstructured probe but a preference for the stem-loop probe (**Figure 2.7E**).

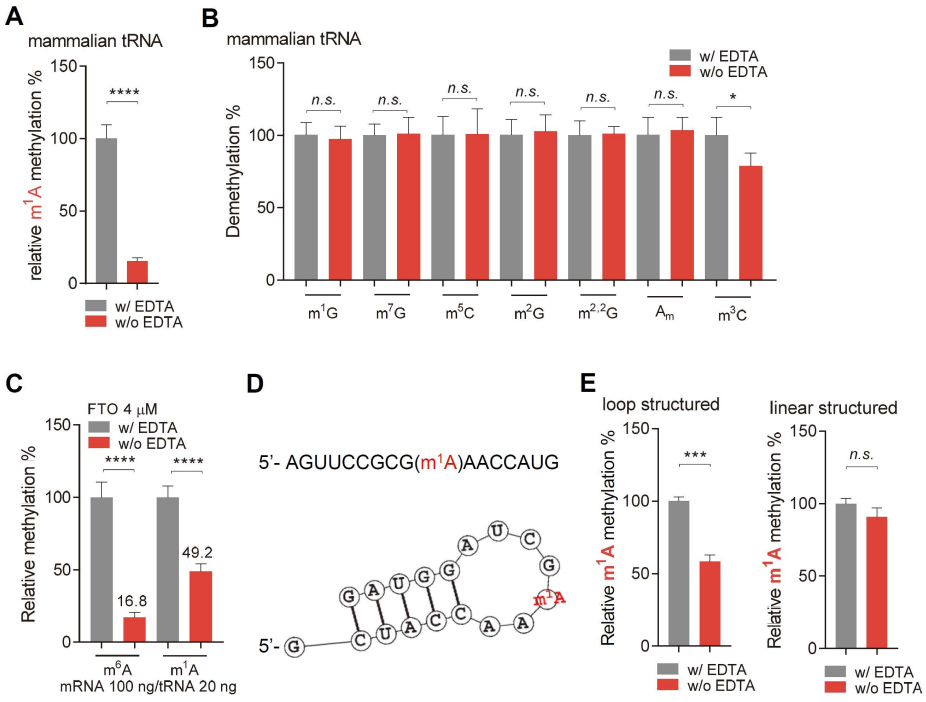

Figure 2.7 FTO demethylates tRNA m^1A *in vitro*

(**A**) *In vitro* demethylation of m^1A in tRNA isolated from HEK293T cells by human FTO. The demethylation efficiency was shown by the ratio of remained m^1A/G. (**B**) *In vitro* demethylation of m^1G, m^7G, m^5C m^2G, $m^2{}_2G$, or A_m in tRNA isolated from HEK293T cells by human FTO. The demethylation efficiency was shown by the ratios of remained modification/G. (**C**) *In vitro* demethylation of tRNA m^1A and mRNA m^6A isolated from HEK293T cells with the similar numbers of modifications by human FTO. (**D**) The sequence of the linear ssRNA probe containing m^1A (top); the sequence of the loop-structured ssRNA probe containing m^1A and the predicted structure by RNA fold server. (**E**) FTO exhibited m^1A demethylation activity preferentially in the loop structure revealed by *in vitro* demethylation assays with m^1A in a linear ssRNA probe and m^1A in a stem-loop structured probe. *p* values were determined using Student's *t*-test. $*p < 0.05$, $***p < 0.001$, $****p < 0.0001$. *n.s.* means not significant. Error bars, mean ± s.d. for $n = 3$ experiments in (A) to (C) and (E).

In HeLa, HEK293T, and 3T3-L1 cells, we found that FTO knockdown consistently led to the increase of the total m^1A level in tRNA, whereas the overexpression of ΔNLS-FTO led to the opposite effects with a consistent decrease of m^1A in tRNA (**Figure 2.8A&B**). Next, we separated the nuclear and cytoplasmic fractions of HEK293T cells with FTO knockdown *versus* the control. Both nuclear tRNA m^1A and cytoplasmic tRNA m^1A increased upon FTO knockdown, with cytoplasmic tRNA m^1A showing a notably larger increase (especially considering the ratio of abundance of tRNA in the cytoplasm *versus* nucleus) (**Figure 2.8C**). We also tested the tRNA m^1A level changes in two cell lines related to human leukemia. Stable knockdown of FTO led to significantly increased tRNA m^1A in both NB4 and MONOMAC-6 cells (**Figure 2.8D**).

Interestingly, the m^1A level in tRNA was more dramatically affected by the FTO-mediated demethylation compared to m^6A and cap-m^6A_m in mRNA in *Fto* KO MEF cells compared to WT control (**Figure 2.8E**), indicating the FTO-mediated m^6A and cap-m^6A_m demethylation in mRNA may be compensated during the culture of *Fto* KO cells but the effects of tRNA m^1A demethylation remained. Reminiscent of HEK293T cells, after cell fractionation (**Figure 2.8F**), we found that both nuclear tRNA m^1A and cytoplasmic tRNA m^1A showed noticeable increases upon *Fto* KO (**Figure 2.8G**). We further tested the changes of the tRNA m^1A levels as well as m^6A and cap-m^6A_m in mRNA in the brain tissue from five pairs of WT and $Fto^{-/-}$ mice (**Figure 2.8H**). Upon *Fto* depletion, while the m^6A and cap-m^6A_m in mRNA showed only slight increases, the tRNA m^1A level showed a significant increase (**Figure 2.8I**), indicating tRNA m^1A demethylation may play an important role in neuronal defects induced by dysregulation of FTO. It is also possible that the surviving *Fto* KO mice have adapted to the loss of *Fto* with compensated overall m^6A or cap-m^6A_m levels in mRNA. Many of the *Fto* KO mice still die early in our hands, suggesting the lack of demethylation in specific mRNA transcripts or other RNA species exhibits a critical effect.

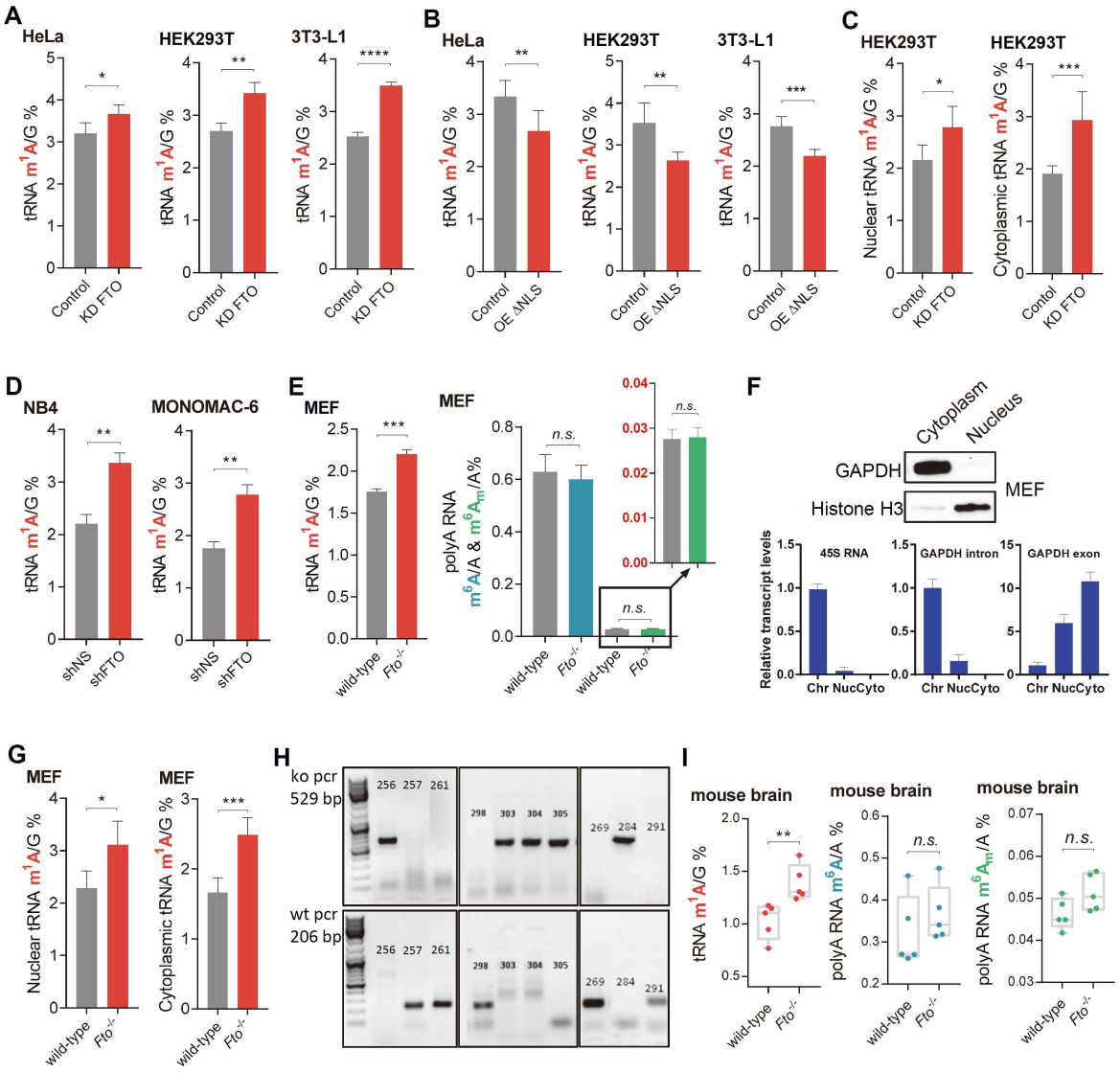

Figure 2.8 FTO demethylates tRNA m^{1}A in various cells and tissues

(**A**) Quantification of the m^{1}A/G ratios by UHPLC-MS/MS in total tRNA purified from HeLa, HEK293T, and 3T3-L1 cells, upon FTO knockdown. (**B**) Quantification of the m^{1}A/G ratios by UHPLC-MS/MS with ΔNLS-FTO overexpression in total tRNA purified from HeLa, HEK293T, and 3T3-L1 cells. (**C**) Quantification of the m^{1}A/G ratios by UHPLC-MS/MS in the nuclear and cytoplasmic tRNA purified from HEK293T cells upon FTO knockdown. (**D**) Quantification of the m^{1}A/G ratios by UHPLC-MS/MS in total tRNA purified from NB4 and MONOMAC-6 cells with stable knockdown of FTO. (**E**) Quantification of the tRNA m^{1}A/G ratios, m^{6}A/A ratios in polyadenylated RNAs, and cap-m^{6}A$_m$/A ratio in polyadenylated RNAs upon *Fto* KO in MEF cells by UHPLC-MS/MS. (**F**) Western blot and RT-qPCR validation of cytoplasm and nucleus separation of MEF cells. (**G**) Quantification of the m^{1}A/G ratios by UHPLC-MS/MS in nuclear and cytoplasmic tRNA purified from WT and *Fto* KO MEF cells. (**H**) PCR validation for *Fto*$^{-/-}$ and WT mice. (**I**) Quantification of the tRNA m^{1}A/G ratios, m^{6}A/A ratios by UHPLC-MS/MS in polyadenylated RNAs, and cap-m^{6}A$_m$/A ratios in polyadenylated RNAs in WT and *Fto* KO mouse brain tissues. *p* values were determined using Student's *t*-test. *$p < 0.05$, **$p < 0.01$, ***$p < 0.001$,

(**Figure 2.8, continued**) ****$p < 0.0001$. *n.s.* means not significant. Error bars, mean ± s.d. for $n = 4$ experiments in (A) to (E) and (G); for $n = 5$ experiments in (I).

We further validated the m^1A demethylation activity of FTO on target tRNAs selected from CLIP-Seq (**Figure 2.9A**). Biotin-labeled DNA probes complementary to tRNA species were used to specifically isolate the corresponding tRNA from 3T3-L1 cells and the m^1A level of specific tRNA targets was then measured using UHPLC-MS/MS. We found that the knockdown of FTO led to consistent increases of the m^1A levels in most top confident tRNAs targets bound to FTO, including $tRNA^{Glu(CUC)}$, $tRNA^{His(GUG)}$, $tRNA^{Gly(GCC)}$, $tRNA^{Gly(ACC)}$, $tRNA^{Asp(GUC)}$, $tRNA^{Lys(CUU)}$, $tRNA^{Gln(CUG)}$, and $tRNA^{Leu(CAA)}$ (**Figure 2.9B**). Therefore, the majority of tRNAs identified by CLIP-seq are substrates of FTO. Moreover, we also tested several tRNAs that were not FTO targets according to CLIP-seq, including $tRNA^{Ala(AGC)}$, $tRNA^{Asn(GUU)}$, $tRNA^{Gly(UCC)}$, and $tRNA^{Phe(GAA)}$, and found that FTO did not exhibit enzymatic activity to these non-targeted tRNAs (**Figure 2.9C**).

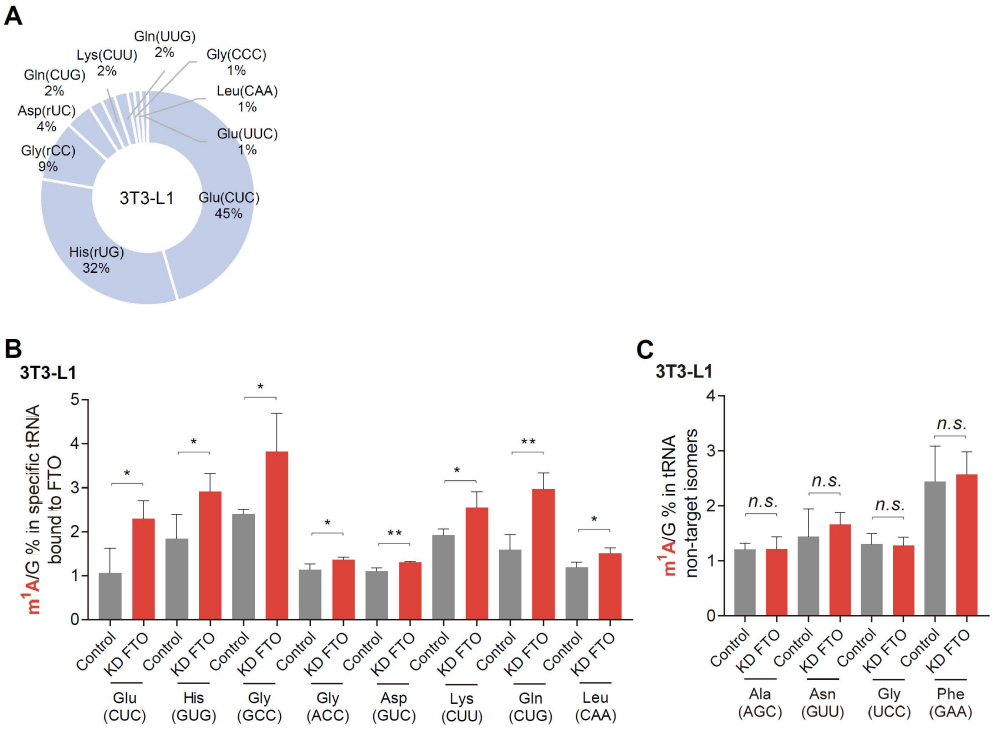

Figure 2.9 Individual tRNA targets of FTO inside cells.
(**A**) Top FTO-bound tRNAs identified by CLIP-seq with FLAG-tagged FTO in 3T3-L1 cells. (**B**) Quantification of the m^1A/G ratios in top tRNA targets bound to FTO by UHPLC-MS/MS upon

(**Figure 2.9, continued**) FTO knockdown in 3T3-L1 cells. (**C**) Quantification of the m^1A/G ratios in several non-CLIP tRNAs by UHPLC-MS/MS upon FTO knockdown. *p* values were determined using Student's *t*-test. *$p < 0.05$, **$p < 0.01$. *n.s.* means not significant. Error bars, mean ± s.d. for $n = 3$ experiments in (B) and (C).

It is surprising that FTO can demethylate both m^6A and cap-m^6A_m in mRNA as these two modifications share the identical chemical structure in the base moiety. The structure and context of tRNA m^1A are quite different from those of m^6A and cap-m^6A_m in mRNA. We asked why FTO could have distinct RNA species as demethylation substrates, especially the preference for the loop structure. We examined the protein structures of FTO and realized that the unique structural features may allow it to gain access to the modification sites in different RNA species. We noticed that the overall structure of FTO exhibited similarities with NSUN6, a tRNA m^5C methyltransferase[145]. The superimposition of FTO (raspberry) and NSUN6 (purple) with bound tRNA (orange) showed that the FTO activity site could gain access to tRNA m^1A58 (**Figure 2.10A**). However, another known mRNA m^6A demethylase, ALKBH5 (green), does not carry the similar structural fold as FTO does, which may explain the more constrained substrate specificity of ALKBH5 on mRNA m^6A (**Figure 2.10B**).

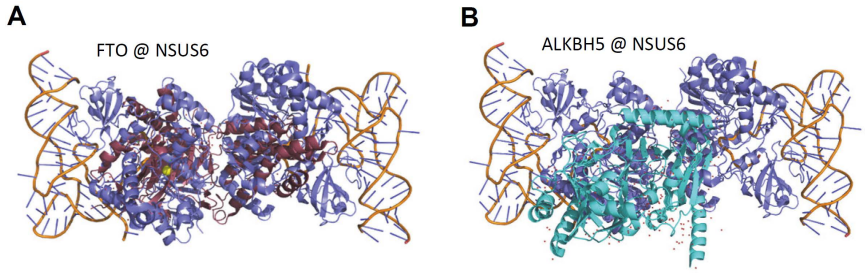

Figure 2.10 Superimposition of FTO and ALKBH5 with a tRNA methyltransferase
(**A**) FTO (raspberry) shows structural similarity with NSUN6 (purple). (**B**) The structure of ALKBH5 (green) is distinct from that of NSUN6 (purple).

2.2.3.2 FTO-mediated tRNA demethylation suppresses translation

A previous study from our lab revealed that the dynamic regulation of tRNA m^1A58 could impact translation initiation and elongation[144]. Therefore, we used an alkyne-modified glycine

analog, L-homopropargylglycine (HPG), to metabolically label newly synthesized proteins in WT and *Fto*$^{-/-}$ MEF cells. The HPG-labeled cells were then fluorescently labeled and analyzed by flow cytometry. We observed a notable increase in protein synthesis in the *Fto*$^{-/-}$ cells compared to the WT cells (**Figure 2.11A**).

To separate the effects of the FTO-mediated tRNA m^1A demethylation from the effects of the FTO-mediated adenosine demethylation in mRNA on translation, we performed an *in vitro* translation assay by using a rabbit reticulocyte-based luciferase reporter system. tRNAs extracted from *Fto*$^{-/-}$ and WT MEF cells were subjected to the *in vitro* luciferase mRNA translation assay using rabbit reticulocyte lysate, respectively. The activity of the translated luciferase protein was measured in the incubation mixture by a luminometer. We found the incubation of tRNAs extracted from *Fto*$^{-/-}$ MEF cells induced significantly higher luciferase signals than tRNAs extracted from the WT MEF cells, indicating that the FTO-mediated tRNA m^1A demethylation led to increased protein translation efficiency (**Figure 2.11B**).

We also designed reporter assays with six repeated codon sequences (6 × GAG(Glu) for the $tRNA^{Glu(CUC)}$, 6 × CAC(His) for the $tRNA^{His(GUG)}$, and 6 × GGA(Gly) for $tRNA^{Gly(UCC)}$) for FTO-bound targets $tRNA^{Glu(CUC)}$ and $tRNA^{His(GUG)}$, as well as a non-target $tRNA^{Gly(UCC)}$ added to the 5' of firefly luciferase (F-luc); a second *Renilla* luciferase (*R*-luc) encoded in the same plasmid was used to normalize the expression efficiency. A control reporter (F-luc plus *R*-luc) devoid of these 6× sequences was also transfected to normalize translation differences between *Fto*$^{-/-}$ and WT MEF cells introduced by any other factors such as translation initiation (*i.e.* variations of cellular levels of $tRNA^{iMet}$ and other tRNAs). We observed significantly elevated translation in the *Fto*$^{-/-}$ MEF cells compared to the WT MEF cells for both the reporters of FTO-bound targets $tRNA^{Glu(CUC)}$ and $tRNA^{His(GUG)}$, but not for the reporter of non-target $tRNA^{Gly(UCC)}$ (**Figure 2.11C**).

These results further indicate that the FTO-mediated tRNA m^1A demethylation negatively affects translation, which is consistent with the previous discovery that m^1A-methylated tRNAs are preferentially recognized and delivered to translation-active polysomes[144].

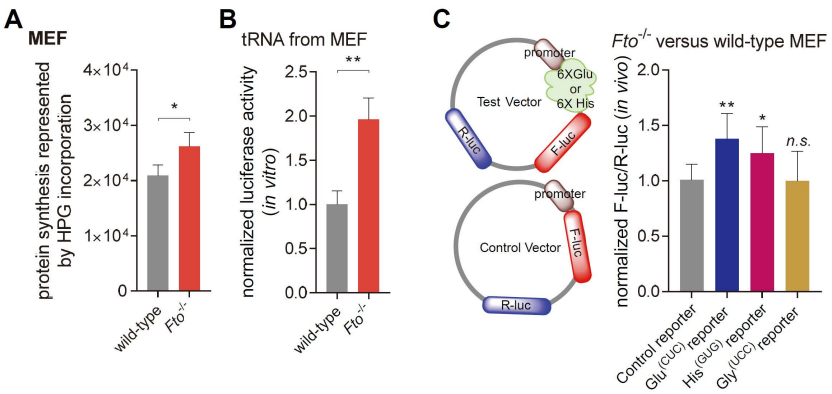

Figure 2.11 FTO-mediated tRNA m^1A demethylation suppresses translation
(**A**) Quantification of total protein synthesis in MEF cells with HPG incorporation by flow cytometry. (**B**) Quantification of in vitro translation efficiency by the supplementation of total tRNA purified from WT and *Fto*$^{-/-}$ MEF cells. (**C**) Schemes of designs for testing and control reporter assays; normalized protein synthesis level represented by reporter assays of two FTO-bound tRNA targets and one non-target tRNA compared to control. *p* values were determined using Student's *t*-test. *$p < 0.05$, **$p < 0.01$. *n.s.* means not significant. Error bars, mean ± s.d. for $n = 3$ experiments.

2.3 Conclusion and discussion

Here we report a systematic characterization of the cellular substrate spectrum of FTO (**Figure 2.12**). In our biochemical studies, we confirmed that FTO could effectively demethylate both internal m^6A and cap-m^6A_m from purified polyadenylated RNA (**Figure 2.1**). We were intrigued by how FTO demethylates m^6A and/or m^6A_m on target polyadenylated RNAs inside cells and the functional consequences of the demethylation. We found that FTO localization within the nucleus and cytoplasm can vary among cell types and FTO displayed distinct substrate repertoires inside the cell nucleus and cytoplasm (**Figure 2.2**). In certain leukemia cell lines, cytoplasmic FTO mediates extensive demethylation of internal m^6A in cytoplasmic polyadenylated RNA due to the predominant expression of FTO in the cytoplasm (**Figure 2.3**). This spatial regulation led to

different functional outcomes on target RNAs. We also found that in several cell lines, cytoplasmic FTO targeted both m^6A and cap-m^6A_m in polyadenylated RNAs while nuclear FTO preferentially reversed m^6A in nuclear polyadenylated RNA. Upon FTO knockdown, FTO-mediated mRNA m^6A demethylation rather than mRNA cap-m^6A_m demethylation associated with the gene expression regulation (**Figure 2.4**). Our analysis was later supported by two independent studies of the gene expression regulation by PCIF1, the methyltransferase of mRNA cap-m^6A_m[146,147].

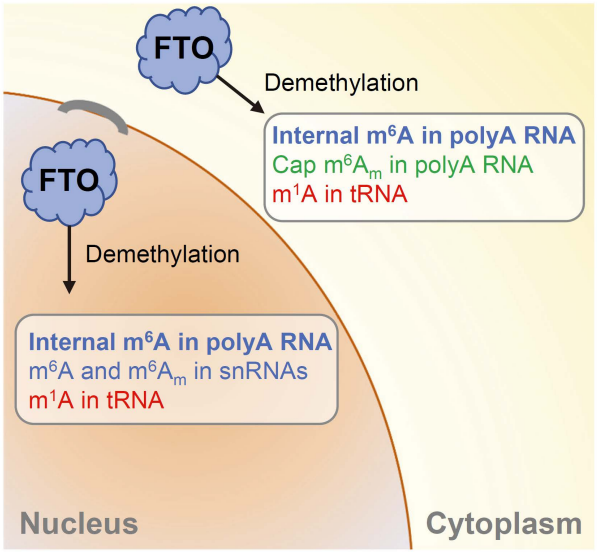

Figure 2.12 A model for FTO-mediated RNA demethylation inside cells
Nuclear m^6A is the main substrate of FTO in the cell nucleus. FTO also mediates moderate m^1A tRNA demethylation as well as m^6A (U6) and m^6A_m (U2 in particular but also U1) snRNA demethylation in the nucleus. FTO can also localize to the cytoplasm, mediating mRNA m^6A, cap-m^6A_m demethylation, and tRNA m^1A demethylation in the cytoplasm.

FTO CLIP-seq result revealed that FTO bound closely around known m^6A sites and in intronic regions, suggesting that FTO may mediate intronic m^6A demethylation in pre-mRNAs. In addition to FTO-mediated adenosine demethylation in mRNA, we identified additional nuclear RNA substrates, including m^6A in U6 RNA, internal and cap-m^6A_m in certain snRNAs (**Figure 2.5&2.6**). It has been reported that FTO deficiency promotes splicing[50,53] and snRNPs are involved in the splicing of mRNA[148]. Our study revealed a potential link between FTO-induced modification changes in snRNAs and mRNA splicing for the first time.

We also showed that FTO could mediate tRNA m^1A demethylation activity *in vitro*, in various cells, and in mouse brain tissue (**Figure 2.7-2.9**). The structural feature of FTO is distinct from that of ALKBH5, which may allow FTO to accomplish demethylation of different RNA substrates depending on the cellular context (**Figure 2.10**). A recent study also showed that FTO and ALKBH5 mediate m^6A demethylation through distinct mechanistic pathways[149], adding another layer to the context-dependent regulation and function of RNA demethylation. FTO-mediated tRNA m^1A demethylation affects translation of the targeted tRNAs (**Figure 2.11**), which is reminiscent of ALKBH1, another tRNA m^1A demethylase that regulates translation elongation. Note that FTO and ALKBH1 only share a few common tRNA targets, indicating the differential substrate preference of these two demethylases. The tRNA m^1A demethylation by FTO may also regulate the formation of tRNA fragments in certain biological context, which merits further studies. The mRNA cap-m^6A_m demethylation and tRNA m^1A demethylation by FTO could collectively suppress translation. However, it is noteworthy that cap-m^6A_m was also reported to have negligible effects on translation under basal conditions[150], and even suppresses translation based on *in vitro* translation assays and *in vivo* reporter assays[146].

Lastly, the substrates of FTO discussed in this chapter are all *in vitro* and cell-based substrates. Biochemically, mRNA cap-m^6A_m might be more susceptible to demethylation compared to mRNA internal m^6A as it is located at the 5' end of mRNA. However, extensive studies have shown that mRNA internal m^6A can definitely be actively and effectively demethylated by FTO, thereby modulating various biological processes affected by FTO dyregulation[42-62], especially in certain AML cells, where FTO can mediate up to ~40% mRNA internal m^6A demethylation[60]. Appropriate and sensitive detection methods and procedures are critical to investigate the FTO-mediate demethylation in future research.

2.4 Methods

2.4.1 Cell culture and tissues

WT and *Fto*$^{-/-}$ MEF cell lines were obtained from Prof. Arne Klungland[138]. Spontaneously immortalized clonal MEF cell lines were established from individual E13.5-E15.5 days-old embryos obtained from heterozygous *Fto*$^{+/-}$ crossings. Limbs were removed and remaining tissue chopped into small pieces and homogenized into single-cell suspension using a pipette. MEFs are grown in DMEM with 10% serum, 2 mM glutamine and penicillin/streptomycin. Cells grown for 4–7 days were trypsinized and frozen in complete medium with 10% DMSO as stock. Cells are grown in complete medium for 2–4 days before using them for the following analysis. Human HeLa, HepG2, HEK293T, Mel624, and 3T3-L1 cell lines were purchased from ATCC. The aforementioned cells were maintained in DMEM (Gibco, #11965) with 10% fetal bovine serum (FBS, Gibco, 10438-026) and 1× Pen/Strep (Gibco, #15140) at 37 °C with 5% CO_2. FTO stable knockdown and the knockdown control AML cells were obtained from Prof. Jianjun Chen and cultured as previously reported[60].

Wild-type and *Fto*$^{-/-}$ mouse brains were obtained from Prof. Arne Klungland. Littermate animals were used as *Fto*$^{+/+}$ controls (wild-type). The mice were bred and housed in a 12-hour light/dark cycle at the Comparative Medicine, Oslo University Hospital, Rikshospitalet, Norway, with a diet of pellets and water ad libitum. Brains were carefully removed from decapitated mice and quickly frozen on dry ice and stored at –80 °C.

2.4.2 Plasmid construction, siRNA knockdown, and plasmid transfection

FLAG-tagged human FTO in the pcDNA 3.0 vector was obtained as previously reported[12]. FLAG-tagged mouse FTO in the pCMV6-Entry vector was purchased from OriGene (MR208064). FLAG-tagged human ΔNLS-FTO mutant in pCMV6-Entry was generated by the deletion of 17

amino acids from the *N*-terminal of FTO full-length cDNA. High-purity plasmids used for mammalian cell transfection were prepared using HiSpeed Plasmid Maxi Kit (QIAGEN).

AllStars negative control siRNA (Qiagen, 1027281) was used as control siRNA in knockdown experiments. siRNA directed against human FTO (used in HEK293T and HeLa cells) was ordered from Qiagen (SI04293625, Hs_FTO_7 FlexiTube siRNA). Silencer® Select against mouse FTO (used in 3T3-L1 cells) was ordered from ThermoFisher (assay ID 166879). Cells were resuspended 16 hours prior to the transfection and maintained at 50% confluency for siRNA transfection or 80% confluency for plasmid transfection. Transfection was achieved by using Lipofectamine RNAiMAX (Invitrogen) for siRNA and Lipofectamine 2000 (Invitrogen) for DNA plasmids, following the manufacturer's protocols, respectively. The cells were harvested after 48 hours post siRNA transfection or 24 hours post plasmid transfection for subsequent experiments.

2.4.3 Cytoplasm and nucleus separation

Cytoplasm and nucleus were separated using NE-PER® Nuclear and Cytoplasmic Extraction Reagents (Thermo Scientific, 78833) following the manufacturer's protocol. According to the published protocol[151], the separation efficiency was validated using RT-qPCR for total RNA purified from different cellular fractions as well as western blot.

2.4.4 Immunofluorescent imaging sample preparation

Immunofluorescent imaging was performed as reported previously[66]. In brief, the cells were cultured in an 8-well chamber (Lab-Tek) after treatment indicated in each experiment. The cells were washed once in phosphate buffered saline (PBS) and then fixed in 4% paraformaldehyde in PBST (PBS with 0.05% Tween-20) at room temperature for 15 min. The fixing solution was removed, and −20 °C chilled methanol was immediately added to each chamber. After incubated

for 10 min at room temperature, the cells were rinsed once with PBS and blocked with blocking solution (1% BSA with PBST) for 1 hour at room temperature. After that, the blocking solution was replaced with the primary antibody (ab126605 for FTO, 1:1000 dilution in the blocking solution, identical to the previous report[138] and incubated for 1 hour at room temperature. After being washed 4 times with PBST (300 µl, 5–10 min for each wash), the secondary antibody (1:300 dilution in PBST) was added to the mixture and incubated at room temperature for 1 hour. After washing 4 times with PBST (300 µl, 5–10 min for each wash), an anti-fade reagent (Slowfade, Invitrogen) was added to mount the slides.

2.4.5 RNA purification

Total RNA was purified with TRIzol® reagents (Thermofisher Scientific, #15596018) from cell lysate. Polyadenylated RNA was purified from total RNA with two rounds of polyA tail purification using Dynabeads® mRNA DIRECT™ kit (Thermofisher Scientific, #61006). The rRNAs wer further removed using RiboMinus™ Eukaryote kit (Thermofisher Scientific, A1083708). Small RNAs (< 200 nt) were separated from total RNA and then subjected to size selection using 15% TBE-urea gel (Thermofisher Scientific, EC6885BOX). tRNA was then sliced and recovered from the gel.

For small nuclear RNAs, the nuclei were first isolated using aforementioned NE-PER kit and the total nuclear RNA was purified using TRIzol® reagents. Small nuclear RNAs (< 200 nt) were separated from total nuclear RNA and then subjected to size selection using 6% TBE-urea gel (Thermofisher Scientific, EC6865BOX). Individual small nuclear RNA was then sliced based on molecular weight and recovered from the gel.

2.4.6 Biotinylated single-stranded DNA probes

As previously reported[144], DNA probes were designed to complement with the 3' gene sequences of $tRNA^{Glu(CUC)}$, $tRNA^{His(GUG)}$, $tRNA^{Gly(GCC)}$, $tRNA^{Gly(ACC)}$, $tRNA^{Asp(GUC)}$, $tRNA^{Lys(CUU)}$, $tRNA^{Gln(CUG)}$, and $tRNA^{Leu(CAA)}$, $tRNA^{Ala(rGC)}$, $tRNA^{Asn(GUU)}$, $tRNA^{Gly(UCC)}$, and $tRNA^{Phe(rAA)}$. The probes used for tRNA selection are listed below:

For $tRNA^{Glu(CUC)}$ selection:

5'biotin-TTCCCTGACCGGGAATCGAACCCGGGCCG

For $tRNA^{His(GUG)}$ selection:

5'-biotin-TGCCGTCACTCGGATTCGAACCGAGGTTGCTG

For $tRNA^{Gly(GCC)}$ selection:

5'biotin-TGCATTGGCCGGGAATCGAACCCGGGGCCTC

For $tRNA^{Asp(GUC)}$ selection:

5'biotin-CTCCCCGTCGGGGAATCGAACCCCGGTCTC

For $tRNA^{Lys(CUU)}$ selection:

5'biotin-CCAACGTGGGGCTCGAACCCACGACCCT

For $tRNA^{Gln(CUG)}$ selection:

5'biotin-AGGTCCCACCGAGATTTGAACTCGGATCGCTGG

For $tRNA^{Leu(CAA)}$ selection:

5'biotin- TGTCAGAAGTGGGATTCGAACCCACGCCT

For $tRNA^{Ala(AGC)}$ selection:

5'biotin-TGGAGGATGCGGGCATCGATCCCGCTACC

For $tRNA^{Asn(GUU)}$ selection:

5'biotin-CGTCCCTGGGTGGGCTCGATCCACCAACC

For $tRNA^{Gly(UCC)}$ selection:

5’biotin- TGCGTTGGCCGGGAATCGAACCCGGGTCAAC

For $tRNA^{Phe(GAA)}$ selection:

5’biotin-TGCCGAAACCCGGGATCGAACCAGGGAC

2.4.7 Individual tRNA isolation

As previously reported[144], Streptavidin-conjugated C1 magnetic Dynabeads (Invitrogen) were used for individual tRNA target isolation. 20 µl of RNase-free beads were washed once with buffer A (10 mM Tris-HCl, pH 7.5, 2 mM EDTA, 2 M NaCl), and finally resuspended in 20 µl of buffer A. Subsequently, 200 µM of biotinylated oligonucleotides in 20 µl of water were mixed with resuspended Dynabeads in buffer A and incubated at room temperature for 30 min. After the incubation, the oligonucleotide-coated Dynabeads were then washed four times with buffer B (5 mM Tris-HCl, pH 7.5, 1 mM EDTA, 1 M NaCl) and equilibrated in 6× SSC solution (1× SSC is 0.15 M NaCl plus 0.015 M sodium citrate, pH 7.0). Total tRNA in 6× SSC solutions and the oligonucleotide-coated Dynabeads and were heated for 10 min at 75°C separately. The tRNA and beads were mixed and incubated together at 75 °C for another 10 min. Thereafter, the suspension was gently rotated at room temperature for 3 hours before washed, in succession, three times with 3× SSC, twice with 1× SSC, and several times with 0.1× SSC until the absorbance of the wash solution at 260 nm closed to zero. tRNA retained on the beads was eluted three times using RNase-free water.

2.4.8 Quantitative analysis of RNA modification levels

For the quantification of the m^6A and cap m^6A_m in polyadenylated RNA, purified polyadenylated RNA (described in the RNA purification section above) was further treated with

RppH (NEB, M0356S) in NEB Thermopol buffer for 2 hours to remove the cap. 50 ng polyadenylated RNA after the removal of the cap, purified tRNA and purified snRNAs were digested by nuclease P1 (Sigma, N8630), respectively, in 20 μl of buffer containing 25 mM NaCl and 2.5 mM $ZnCl_2$ for 1 h at 42 °C. Subsequently, 1 unit of alkaline phosphatase (Sigma, P5931) and NH_4HCO_3 (100 mM) were added, and the sample was incubated for another 1 h at 37 °C. The samples were then filtered (0.22 μm, Millipore) and injected into a C18 reverse phase column coupled online to Agilent 6460 LC-MS/MS spectrometer in positive electrospray ionization mode. The nucleosides were quantified by using retention time and the nucleoside to base ion mass transitions (268-to-136 for A; 296-to-150 for m^6A_m, 282-to-150 for m^6A and m^1A (retention times of 2.5 and 0.9 min, respectively)). Quantification was performed by comparing with the standard curve obtained from pure nucleoside standards running with the same batch of samples. The m^6A and m^6A_m levels were calculated as the ratio of m^6A and m^6A_m to A, respectively. The tRNA m^1A level was calculated as the ratio of m^1A to G.

2.4.9 Biochemistry assay of FTO activity *in vitro*

Similar to a previous report[144], the demethylation activity assay was performed in standard 20 μl of reaction buffer containing KCl (100 mM), $MgCl_2$ (2 mM), SUPERNase In (0.2 U/μl, life technology), L-ascorbic acid (2 mM), α-ketoglutarate (300 μM), $(NH_4)_2Fe(SO_4)_2 \cdot 6H_2O$ (150 μM), and 50 mM of HEPES buffer (pH 6.5). For m^6A and m^6A_m in polyadenylated RNA, 200 ng polyadenylated RNA purified from HEK293T cells was incubated with 2 μM FTO purified in mammalian cells (High concentration) or 0.2 μM FTO (low concentration) in the above reaction buffer for 3 hours and then quenched by the addition of 5 mM of EDTA, respectively. For tRNA m^1A, 200 ng tRNA purified from HEK293T cell was incubated with 2 μM FTO purified in mammalian cells in the aforementioned reaction buffer for 3 hours and then quenched by adding

1 mM of EDTA. An excessive amount of EDTA was added to control samples. To incubate similar amounts of m^1A and m^6A with FTO, 100 ng purified mammalian polyadenylated RNA and 20 ng tRNA were pooled together and reacted under the aforementioned demethylation condition; tRNA m^1A/G ratio is around 2-4% while polyadenylated RNA m^6A/A ratio is around 0.4-0.8%. The RNAs were then isolated with 100 μl TRIzol® reagents (Thermofisher Scientific, #15596018) using the standard protocol and subjected to RNA digestion prior to LC-MS/MS analysis.

Biochemical demethylation assays of FTO towards m^1A in single-stranded RNA (ssRNA) were conducted in 20 μl of reaction mixture together with 2 μM FTO purified from the mammalian cells and 100 ng probes. The reaction was incubated at 37 °C for 1 h and quenched by the addition of 5 mM of EDTA. An Excessive amount of EDTA was added to control samples. The samples were then centrifuged at 16000 *g* for 30 min at 4 °C. The supernatant was collected for RNA digestion prior to LC-MS/MS analysis. The sequences of the probes were designed as following: m^1A-containing unstructured ssRNA oligo 5'-AGUUCCGCG(m^1A)AACCAUG; m^1A-containing stem-loop RNA oligo (TΨC loop in $tRNA^{His(GUG)}$): 5'-CCCGGUUCG(m^1A)UUCCCGG.

2.4.10 Luciferase reporter assay

The luciferase activity was measured by the luminometer (SYNERGY|HTX) following the manufacturing settings of the luciferase reporter assay. Similar to a previous report[144], *in vitro* translation reaction was performed using the Flexi® Rabbit Reticulocyte Lysate System (Promega, L4540). Total tRNA purified from wild-type MEF cell and *Fto*$^{-/-}$ MEF cell was incubated for 30 min at 30 °C with the reaction mixture following the manufacturing protocol.

For luciferase reporter inside cells, $tRNA^{His(GUG)}$ and $tRNA^{Gly(UCC)}$ reporter was obtained as previously reported[144]. Similarly, F-luc-6×Glu(CUC) reporter plasmid was obtained by inserting the sequence of GAGGAGGAGGAGGAGGAG before the F-luc coding region. To

normalize translation differences between *Fto*$^{-/-}$ and wild-type MEF cells introduced by any other factors including initiation (*i.e.* variations of cellular levels of tRNA^{iMet} and other tRNAs), a control reporter (F-luc plus *R*-luc) devoid of these 6× sequences was also transfected. The normalization factor from this control reporter was applied to signals obtained from the 6×GAG(Glu)-reporter, 6×CAC(His)-reporter, and 6×GAA(Gly)-reporter. General protocol: The wild-type and *Fto*$^{-/-}$ MEF cells were maintained in the 6-well plates at 80% confluency. 500 ng of reporter plasmids (pmirGlo empty vector as control or pmirGlo-specific tRNA anti-codon inserted vector) were transfected into wild-type and *Fto*$^{-/-}$ MEF cells following the aforementioned plasmid transfection protocol. After 6 hours, each well was trypsin-digested, extensively washed with PBS, and re-seeded into a 96-well plate. After 18 hours from re-seeding, the cells in the 96-well plate were assayed using Dual-Glo® Luciferase Assay System (Promega, E2920).

2.4.11 Measurement of protein synthesis rate

HPG (Life Technologies; 50 nM final concentration) was added to the culture medium and incubated for 1 h. Cells were then lifted from plates and washed twice with phosphate buffered saline (PBS) and then fixed in 0.5 ml of 1% paraformaldehyde (Affymetrix) in PBS for 15 min on ice followed by permeabilizing in 200 µl PBS supplemented with 3% FBS (Sigma) and 0.1% saponin (Sigma) for 5 min at room temperature. The azide-alkyne reaction was performed with the Click-iT Cell Reaction Buffer Kit (Life Technologies) and azide-modified Alexa Fluor 488 (Life Technologies) at 5 mM final concentration. After a 30-minute reaction, the cells were washed twice with 3% BSA. All cells were filtered through a 40-µm cell strainer to obtain single-cell suspensions. For flow cytometric analysis, all sorted fractions were double sorted to ensure high purity. Data were analyzed by FlowJo (Tree Star) software.

2.4.12 CLIP-Seq

Similar to a previous report[144], in brief, for each cell line, 5 plates of cells in 15 cm style dish were grown until 80% confluency (~10^7 cells). The medium was aspirated and the cells were washed with PBS once and irradiated once with 400 mJ/cm2 at 254 nm in Stratalinker on ice. After irradiation, cells were harvested with a scraper, transferred to a microtube, pelleted at 4000 rpm for 3 min at 4 °C, and then lysed in RIPA lysis buffer (Sigma, R2078) with cOmplete™, Mini, EDTA-free Protease Inhibitor Cocktail and SUPERNase In at 4 °C for 4 hours. Subsequently, the lysis mixture was centrifuged at 17,000 g at 4 °C for 30 min and the supernatant was carefully collected. Meanwhile, add 100 µl Anti-FLAG® M2 Magnetic Beads to a fresh microtube, wash beads twice with 1 ml lysis buffer. Change to a new tube, leave the beads in the last wash until IP experiment. 100 µl of Anti-FLAG® M2 Magnetic Beads was added into the supernatant and mixed gently at 4°C for 4 hours. The supernatant was then discarded and the beads were washed for 3 times with 1 ml of high salt buffer and another 8 times with 1 ml of wash buffer. The RNAs were then eluted by proteinase K digestion following the manufacturer's protocol. Subsequently, RNAs were recovered by phenol/chloroform extraction and then subjected to library preparation using NEBNext® Multiplex Small RNA Library Prep Set for Illumina® (NEB, E7300S).

CLIP samples were pooled and sequenced with Hiseq-2000. Raw reads from CLIP samples were first trimmed according to recommended settings[152]. Gene structure annotations were downloaded from UCSC mm10 RefSeq/Repeatmasker. For CLIP-seq, we used a modified version of PARalyzer[153] to allow for all mutations, rather than just T to C mutations. For tRNA, the reads in each tRNA gene were counted. Similar to the previous report[50], RNA-seq with rRNA depletion for 3T3-L1 was reanalyzed and used as the input for CLIP-seq[154]. The CLIP-seq in HEK293T cells was reanalyzed[50].

2.4.13 Classification of the m^6A and m^6A_m only genes

The m^6A_m list was obtained from supplementary table 1 in the previous study[40]. The m^6A list was obtained from table S6 in the previous report[16]. In the reported m^6A list, the peak site was annotated. The genes containing both m^6A and m^6A_m were first classified by the overlap of two lists followed by deducting the genes that have m^6A in 5'UTR (though there must be some over deduction in this step as definitely not all the 5'UTR m^6As are m^6A_m, but just to be robust). m^6A only genes were classified by deducting genes containing both m^6A and m^6A_m mentioned above from the genes in the 2012 list. Similarly, cap m^6A_m only genes were classified by deducting genes containing both m^6A and m^6A_m mentioned above from the genes in the 2017 list.

2.4.14 Data availability

Sequencing data have been deposited into the Gene Expression Omnibus (GEO) under the accession number GSE106395. The analysis in **Figure 2.4** utilized data from GSE63753 and GSE78040.

Chapter 3

Physiological Substrate of FTO during Mammalian Development

3.1 Introduction: *Fto* KO leads to severe developmental defects

FTO associates with a variety of human developmental diseases[43,126-129]. *Fto* KO mice display quite notable developmental defects such as postnatal growth retardation, with a good portion of them showing postnatal or embryonic lethality[44,123-125]. Despite these intriguing phenotypes, the underlying mechanisms and physiological substrates remain elusive.

As we demonstrated in the last chapter, in addition to internal mRNA m^6A, mRNA cap-m^6A_m (installed by PCIF1), snRNA m^6A_m (installed by METTL4), and tRNA m^1A have all been shown to subject to the FTO-mediated demethylation in cell lines. However, both *Pcif1* KO mice and *Mettl4*-deficient mice display very mild phenotypes not consistent with *Fto* KO mice[155]. given the nuclear localization tendency of FTO in most tissues (except for adipose tissues)[156], one can speculate that translational regulation through FTO-mediated tRNA m^1A demethylation might not be a major contributor. In addition, in primary mouse and human tissues, positive correlations between mRNA m^6A level and FTO expression was observed[157]; as an m^6A eraser, FTO would be predicted to negatively correlate with mRNA m^6A levels. This observation suggests that internal m^6A on mature mRNA may not be the physiological substrate of FTO in these primary tissues.

Therefore, the functionally relevant substrate(s) of FTO during mammalian development have not been elucidated. FTO has been shown to bind extensively across pre-mRNA[50]. When investigating the subcellular substrates of FTO with cell fractionation, we observed notably increased m^6A levels on a subset of unprecedented nuclear RNAs associated with chromatin upon *Fto* KO in MEF cells. Accordingly, our lab recently revealed that chromosome-associated

regulatory RNAs (carRNAs), including promoter-associated RNAs (paRNAs), enhancer RNAs (eRNAs), and repeat RNAs, can be m^{6}A methylated by METTL3, and that this methylation can regulate chromatin state and transcription to impact cell differentiation of mouse embryonic stem cells (mESCs)[158].

Considering the depletion of m^{6}A writer components *Mettl3* or *Mettl14* also led to quite dramatic early embryo lethal phenotype and development defects in mammals[114,116], we thus hypothesized that it is likely m^{6}A on some nuclear or chromatin-associated RNA targets are physiological substrates of FTO during early development and in primary mammalian tissues. Beyond the characterization of the cellular substrate of FTO, we sought to investigate its exact physiological substrate(s) as well as the related functional pathways in mammalian tissues and during early development.

3.2 Results

3.2.1 m^{6}A demethylation of carRNAs by FTO in mESCs

3.2.1.1 Generation and characterization of the WT and *Fto* KO mESCs

To investigate the potential role of FTO in mammalian tissues and during development, we derived wild-type (WT) and *Fto* KO mouse embryonic stem cells (mESCs) from D4 mouse blastocysts (**Figure 3.1A&B**). Depletion of FTO protein in mESCs was verified (**Figure 3.1C**).

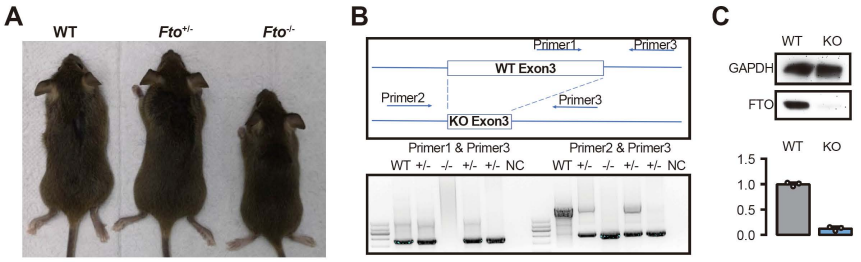

Figure 3.1 WT and *Fto* KO mESCs derived from D4 mouse blastocysts
(**A**) Image of WT, *Fto*$^{+/-}$, and *Fto*$^{-/-}$ mice. (**B**) Schematic diagram and an electrophoresis gel of PCR products showing the validation of WT and *Fto*$^{-/-}$ mESCs derived from WT and *Fto* KO mice (D4 mouse blastocysts). (**C**) Top: immunoblot assays showing the validation of *Fto* KO in mESCs.

(**Figure 3.1, continued**) Bottom: relative FTO protein levels from proteomics in WT and *Fto*$^{-/-}$ mESCs.

3.2.1.2 Quantification and profiling of m^{6}A in caRNA from mESCs

We first utilized UHPLC-MS/MS to quantify the changes of m^{6}A levels in cellular RNAs isolated from cytosolic, nuclear, and chromatin-associated fractions between WT and *Fto*$^{-/-}$ mESCs (**Figure 3.2A**). In line with the predominant nuclear localization of FTO in mESCs (**Figure 3.2B**), the m^{6}A level within total polyadenylated RNA showed only a small change upon *Fto* KO (**Figure 3.2C**), while the m^{6}A levels in the chromatin-associated RNA (caRNA) depleted of ribosomal RNA (rRNA) and in RNA isolated from soluble nuclear extracts (depletion of rRNA) were notably increased (**Figure 3.2D**). This observation suggested that FTO mediates m^{6}A demethylation of chromosome-associated RNA (caRNA, including ca-mRNA and carRNAs).

We next performed methylated RNA immunoprecipitation followed by high-throughput sequencing (MeRIP-seq) of caRNA after rRNA depletion with m^{6}A methylated spike-in controls in WT and *Fto*$^{-/-}$ mESCs. Therefore, the m^{6}A levels can be quantified with CPM values of m^{6}A-marked target transcripts mapped to the mouse genome divided by CPM values mapped to m^{6}A-modified spike-in control from caRNA MeRIP-seq. Reminiscence of the UHPLC-MS/MS results, the quantified overall m^{6}A level of caRNA consistently increased after depletion of *Fto* in three sequencing samples (**Figure 3.2E**). We then profiled the m^{6}A methylome on caRNA. Around 50,000 m^{6}A peaks were consistently identified from each sample and the known m^{6}A consensus motif GGAC was identified in both WT and *Fto*$^{-/-}$ mESCs (**Figure 3.2F**); m^{6}A peaks were highly reproducible (**Figure 3.2G**), displaying notable distributions in intron regions (**Figure 3.2H**). We also assessed the differentially expressed m^{6}A peaks and found many more hypermethylated peaks in samples from *Fto*$^{-/-}$ mESCs compared to those from WT (**Figure 3.2I**).

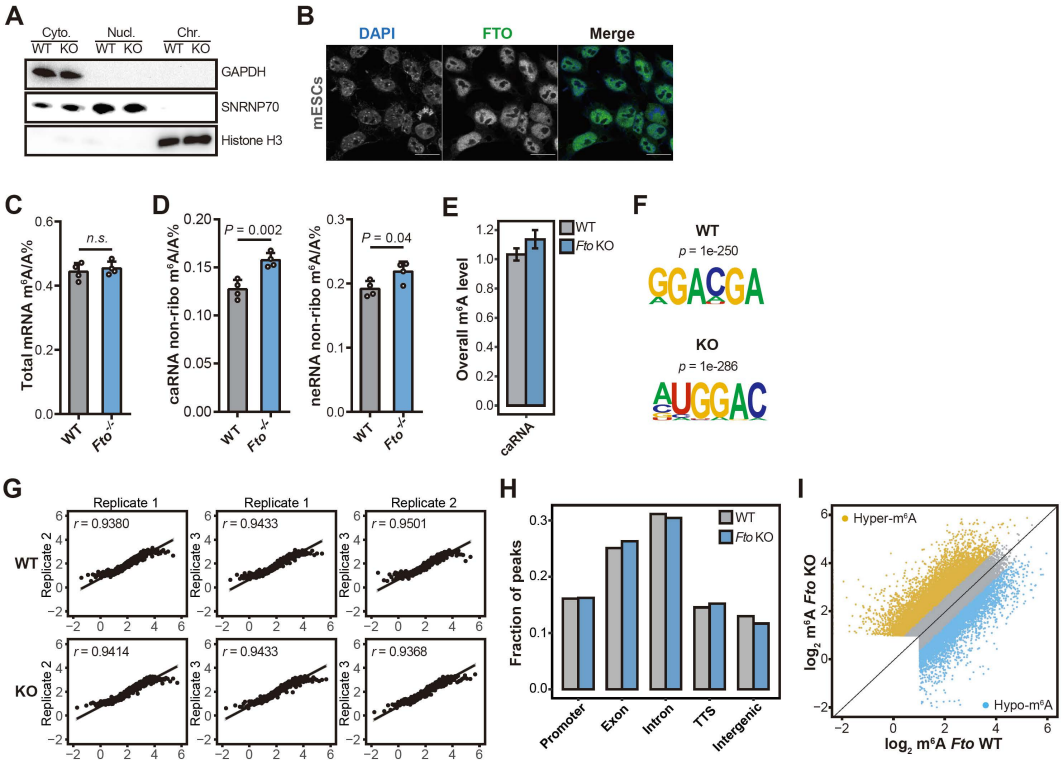

Figure 3.2 Differential caRNA m^{6}A methylation in WT and *Fto*$^{-/-}$ mESCs

(**A**) Immunoblot assays showing the cell fractionation efficiency of WT and *Fto*$^{-/-}$ mESCs. (**B**) Fluorescence images of DAPI (blue) and immunofluorescence of FTO (green) showing the predominant nuclear localization of the FTO protein in mESCs. Scale bars, 20 μm. (**C**) m^{6}A/A ratios of total polyadenylated RNA quantified by UHPLC-MS/MS in WT and *Fto*$^{-/-}$ mESCs. (**D**) m^{6}A/A ratios in non-ribosomal RNA from chromatin-associated fraction (caRNA) and soluble nuclear extract (neRNA) quantified by UHPLC-MS/MS in WT and *Fto*$^{-/-}$ mESCs. (**E**) Overall caRNA m^{6}A levels in *Fto*$^{-/-}$ mESCs normalized to WT mESCs. (**F**) Top consensus motifs identified from m^{6}A peaks from caRNA MeRIP-seq in WT and *Fto*$^{-/-}$ mESCs. (**G**) The correlations of m^{6}A levels between replicates from caRNA MeRIP-seq in WT and *Fto*$^{-/-}$ mESCs showing high reproducibility. *r* refers to Pearson's correlation coefficient. (**H**) Distribution of m^{6}A peaks in distinct genomic regions including promoter, exonic, intronic, TTS, and intergenic regions annotated by HOMER in WT and *Fto*$^{-/-}$ mESCs from caRNA MeRIP-seq. (**I**) A Scatter plot showing the m^{6}A level in WT and *Fto*$^{-/-}$ mESCs from caRNA MeRIP-seq m^{6}A peaks. Hypermethylated m^{6}A peaks (log_2FC of m^{6}A > 0.58): 9,814; hypomethylated m^{6}A peaks (log_2FC of m^{6}A < -0.58): 5,593. *p* values were determined using Student's *t*-test; *n.s.* means not significant. Error bars, mean ± s.d. for $n = 4$ experiments in (C) to (E).

3.2.1.3 FTO regulates the methylation and abundance of carRNAs and ca-mRNA

We further annotated chromatin-associated RNAs to the mRNA portion of caRNA (ca-mRNA), as well as carRNAs including paRNA, eRNA, and repeat RNAs[158]. The m^{6}A levels were elevated for all three groups of m^{6}A-marked carRNAs upon depletion of FTO (**Figure 3.3A**).

Accordingly, most m^{6}A-marked carRNAs displayed more hypermethylated m^{6}A peaks than hypomethylated peaks after *Fto* depletion, in particular repeat RNAs (**Figure 3.3B**). We also observed more pronounced hypermethylation of repeat RNAs in comparison with other groups of carRNAs (**Figure 3.3C**).

To understand how the FTO-mediated m^{6}A demethylation of carRNAs affects their abundance, we analyzed expression level changes of hypermethylated carRNAs after depletion of *Fto*. We found all three groups of carRNAs with m^{6}A hypermethylation exhibited reduced expression levels compared to non-hypermethylated carRNAs upon *Fto* KO (**Figure 3.3D**). Additionally, changes in expression levels of these carRNAs negatively correlated with m^{6}A changes upon *Fto* KO (**Figure 3.3E**), supporting a destabilization role of m^{6}A on these carRNAs. To focus on the direct effects of *Fto* KO, we further analyzed correlations between the abundance decrease of carRNAs and *Fto* KO-induced m^{6}A hypermethylation. We noticed that repeat RNAs displayed the strongest correlation in comparison with other carRNAs (**Figure 3.3F**), indicating repeat RNAs as the preferential substrates of FTO in mESCs (**Figure 3.3G**).

We also analyzed the mRNA portion of caRNA (ca-mRNA), most of which should be pre-mRNA but may also include partially processed mRNAs that were still associated with the chromatin in the purified caRNA; comparable numbers of differential m^{6}A peaks were identified in ca-mRNA and carRNAs. Notably, ca-mRNA also displayed increased m^{6}A level (**Figure 3.4A**) and contained more m^{6}A hypermethylated transcripts than hypomethylated ones upon *Fto* KO (**Figure 3.4B**), with the hypermethylated ca-mRNAs showing reduced levels on chromatin compared to the non-hypermethylated ca-mRNAs (**Figure 3.4C**). In line with the observation of the notable intronic distribution of m^{6}A peaks, demethylation of ca-mRNA occurs to both introns and exons (**Figure 3.4D&E**), which may affect pre-mRNA processing as previously

suggested[50,53]. Collectively, these observations suggested that FTO mediated m^{6}A demethylation of carRNAs and ca-mRNA in mESCs, resulting in their reduced abundance on chromatin.

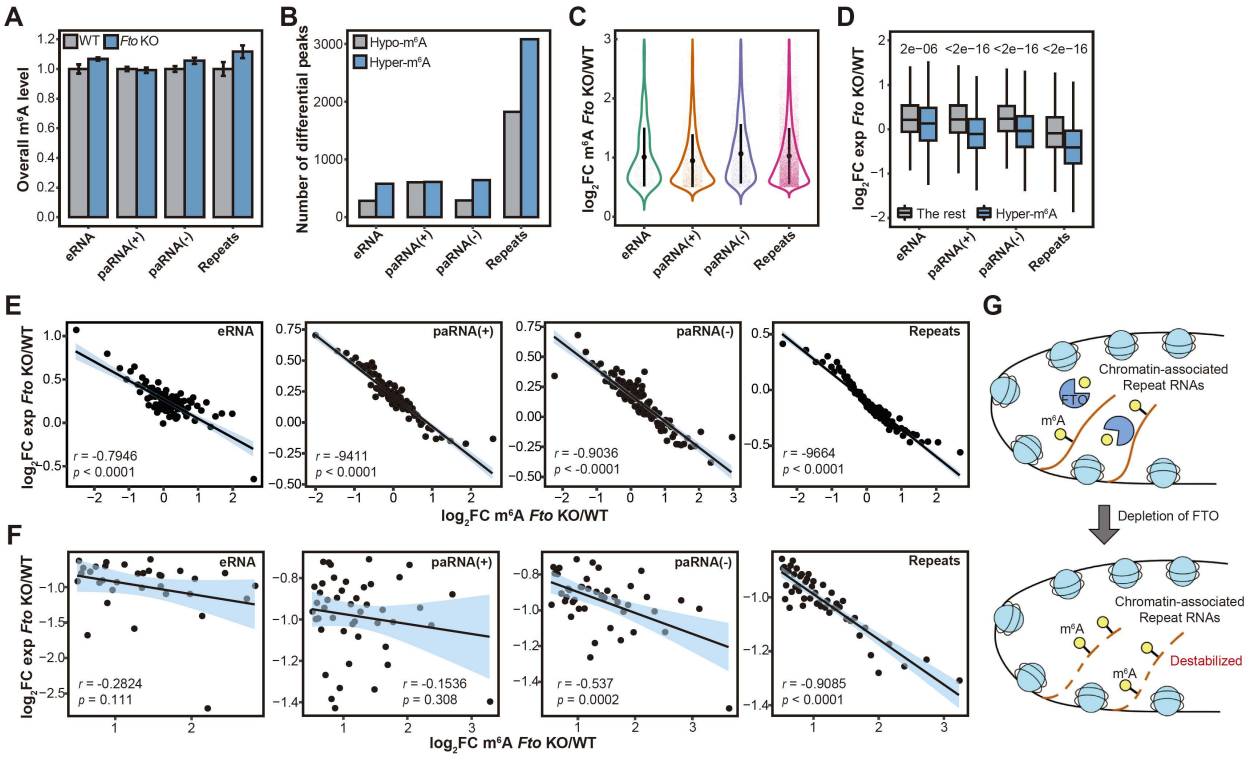

Figure 3.3 *Fto* KO causes elevated m^{6}A and reduced abundance of carRNAs
(**A**) Overall m^{6}A levels on m^{6}A-marked carRNAs in *Fto*$^{-/-}$ mESCs normalized to WT mESCs. (**B**) Number of *Fto* KO-induced differential m^{6}A peaks (log$_2$FC of m^{6}A > 0.58 or log$_2$FC of m^{6}A < -0.58) on carRNAs in *Fto*$^{-/-}$ mESCs compared to WT mESCs. paRNA(+) and paRNA(-) denote sense paRNA and antisense paRNA, respectively. (**C**) Violin plots showing the log$_2$ fold changes of hypermethylated m^{6}A peaks (log$_2$FC of m^{6}A > 0.58) on carRNAs in WT and *Fto*$^{-/-}$ mESCs. (**D**) Comparisons of log$_2$ fold changes of transcript abundance between hypermethylated carRNAs and the rest of m^{6}A-marked carRNAs upon *Fto* KO. *p* values were determined using a Wilcoxon signed-rank test. (**E**) and (**F**) carRNAs within each group were categorized into 50 bins based on their ranked fold changes of m^{6}A levels upon *Fto* KO. *r* refers to Pearson's correlation coefficient. *p* values represent Pearson's correlation coefficient determined using *t*-distribution. (E) Negative correlations of log$_2$ fold changes between transcript abundance of carRNAs and m^{6}A levels on carRNAs upon *Fto* KO. (F) Negative correlations of log$_2$ fold changes between decreased transcript abundance (log$_2$FC of transcript abundance < -0.58) of carRNAs and hypermethylation of m^{6}A (log$_2$FC of m^{6}A > 0.58) on carRNAs upon *Fto* KO. *r* refers to Pearson's correlation coefficient. *p* values represent Pearson's correlation coefficient determined using *t*-distribution. (**G**) A schematic model showing the elevated m^{6}A and destabilized transcripts of chromatin-associated repeat RNAs upon *Fto* depletion.

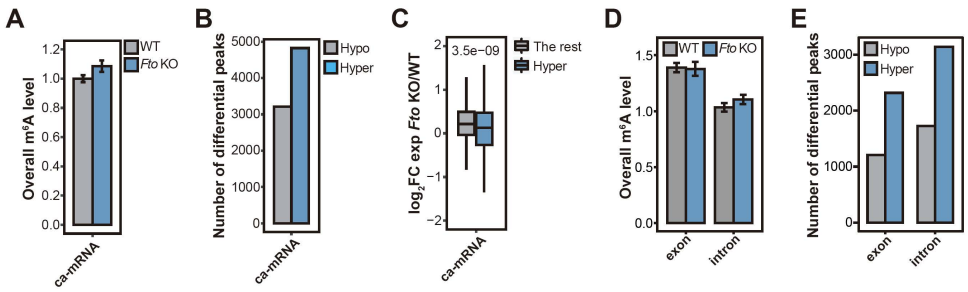

Figure 3.4 *Fto* KO causes elevated m^{6}A and reduced levels of ca-mRNAs
(**A**) Overall m^{6}A levels of m^{6}A-marked ca-mRNA in *Fto*$^{-/-}$ mESCs normalized to WT mESCs. (**B**) Numbers of *Fto* KO-induced differential peaks (log_2FC of m^{6}A > 0.58 or log_2FC of m^{6}A < -0.58) on ca-mRNA in WT and *Fto*$^{-/-}$ mESCs. (**C**) Log_2 fold changes of transcript abundance of hyper-methylated ca-mRNAs *versus* the rest of m^{6}A-marked ca-mRNAs upon *Fto* KO. *p* value was determined using a Wilcoxon signed-rank test. (**D**) Overall m^{6}A levels of introns and exons of m^{6}A-marked ca-mRNA in WT and *Fto*$^{-/-}$ mESCs. (**E**) Numbers of *Fto* KO-induced differential peaks (log_2FC of m^{6}A > 0.58 or log_2FC of m^{6}A < -0.58) in introns and exons of m^{6}A-marked ca-mRNA in WT and *Fto*$^{-/-}$ mESCs.

3.2.2 LINE1 RNA as a primary substrate of FTO in mESCs

3.2.2.1 FTO preferentially regulates the methylation and abundance of LINE1 RNA

Considering repeat RNAs were the most responsive among carRNAs upon *Fto* KO, we focused the rest of our study on repeat RNAs. For frequently modified repeat RNAs (possessing more than 1,000 m^{6}A peaks), we observed elevated m^{6}A levels (**Figure 3.5A**) and reduced abundance associated with m^{6}A hypermethylation (**Figure 3.5B**). Among repeat RNAs, we found that the long-interspersed element-1 (LINE1) family is the most responsive upon *Fto* KO, with m^{6}A-marked LINE1 RNA exhibiting the highest m^{6}A level (**Figure 3.5A**), the largest decrease in abundance associated with m^{6}A hypermethylation (**Figure 3.5B**), the highest number of hypermethylated peaks (**Figure 3.5C**) and the highest abundance on chromatin (**Figure 3.5D**) in WT mESCs. We thus analyzed the methylation profile along with LINE1 RNA and observed notably elevated m^{6}A density upon *Fto* KO (**Figure 3.5E**).

We observed a significantly reduced overall level of LINE1 RNA on chromatin upon *Fto* KO from caRNA-Seq (**Figure 3.5F**). We further validated the increased m^{6}A and decreased

abundance of LINE1 RNA in caRNA upon *Fto* KO by MeRIP-qPCR and RT-qPCR, respectively (**Figure 3.5G**). Additionally, we noticed that the reduction of LINE1 RNA abundance strongly correlated with *Fto* KO-induced m^{6}A hypermethylation (**Figure 3.5H**). We also analyzed how m^{6}A level and abundance of LINE1 RNA may affect the expression of nearby genes. With the depletion of *Fto*, the LINE1 RNA level and expression of the nearby gene tended to go down, accompanied by a generally increased m^{6}A level on the LINE RNA (**Figure 3.5I&J**).

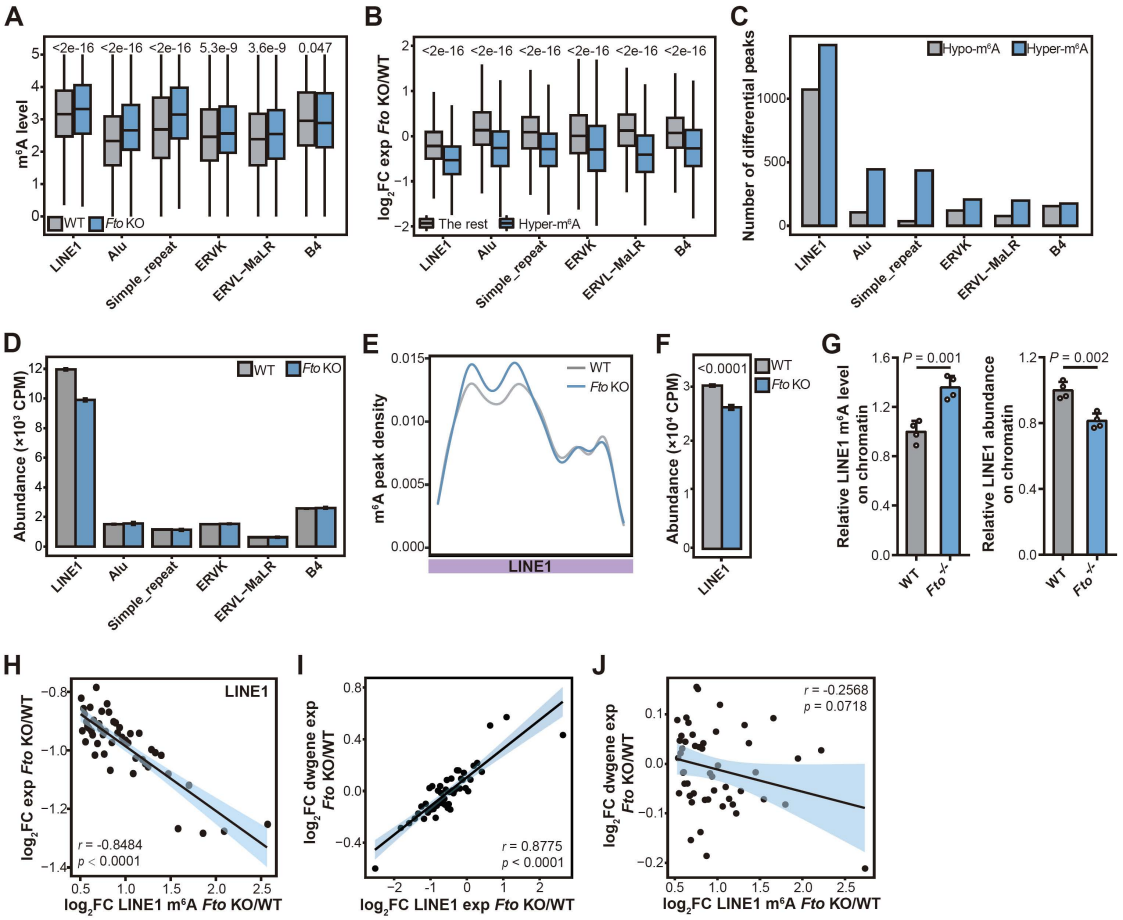

Figure 3.5 Overall profile of LINE1 RNA methylation and abundance upon *Fto* KO
(**A**) m^{6}A levels of repeat RNAs possessing more than 1,000 m^{6}A peaks based on analysis of caRNA MeRIP-seq data in WT and *Fto*$^{-/-}$ mESCs. (**B**) Log$_2$ fold changes of transcript abundance of hypermethylated repeat RNAs *versus* the rest of m^{6}A-marked repeat RNAs upon *Fto* KO. (**C**) Numbers of *Fto* KO-induced differential peaks (log$_2$FC of m^{6}A > 0.58 or log$_2$FC of m^{6}A < -0.58) in repeat RNAs in WT and *Fto*$^{-/-}$ mESCs. (**D**) Transcript abundance of m^{6}A-marked repeat RNAs quantified with CPM values from caRNA MeRIP-seq in WT and *Fto*$^{-/-}$ mESCs. (**E**) Metagene profiles of m^{6}A peak density along m^{6}A-marked LINE1 RNA in WT and *Fto*$^{-/-}$ mESCs. (**F**) The overall transcript abundance of LINE1 RNA quantified with CPM values from caRNA RNA-seq

(**Figure 3.5, continued**) analysis in WT and *Fto*$^{-/-}$ mESCs. (**G**) Relative m^{6}A fold enrichment (left) and relative expression levels (right) of LINE1 RNA on chromatin measured by MeRIP-qPCR and RT-qPCR, respectively, in WT and *Fto*$^{-/-}$ mESCs. (**H**) LINE1 RNA was categorized into 50 bins based on its ranked fold changes of m^{6}A levels upon *Fto* KO. A scatter plot showing a negative correlation of log$_2$ fold changes between decreased transcript abundance (log$_2$FC of transcript abundance < -0.58) of LINE1 RNA and hypermethylation of m^{6}A (log$_2$FC of m^{6}A > 0.58) on LINE1 RNA upon *Fto* KO. (**I**) LINE1 RNA was categorized into 50 bins based on its ranked fold changes of transcript abundance upon *Fto* KO. A scatter plot showing a positive correlation of log$_2$ fold changes of transcript abundance on chromatin between LINE1 RNA downstream genes and LINE1 RNA upon *Fto* KO. (**J**) LINE1 RNA was categorized into 50 bins based on its ranked fold changes of m^{6}A level upon *Fto* KO. A scatter plot showing a negative correlation of log$_2$ fold changes between transcript abundance on chromatin of LINE1 RNA downstream genes and hypermethylation of m^{6}A (log$_2$FC of m^{6}A > 0.58) on LINE1 RNA upon *Fto* KO. *p* values were determined using a Wilcoxon signed-rank test in (A) and (B). *p* values were determined using a two-tailed *t*-test in (G). *r* refers to Pearson's correlation coefficient; *p* value represents Pearson's correlation coefficient determined using *t*-distribution in (H) to (J).

With detailed analysis of LINE1 subfamilies, we found that LINE1 subfamilies with lower divergence tended to show higher m^{6}A levels (**Figure 3.6A**) and lower methylation fold changes after *Fto* depletion (**Figure 3.6B**). Moreover, we observed reduced abundance along with elevated m^{6}A level for almost all the top expressed LINE1 subfamilies on chromatin in *Fto*$^{-/-}$ mESCs compared to WT (**Figure 3.6C**). Therein, a young LINE1 subfamily L1Md_T displayed the highest abundance on chromatin and drastically repressed abundance (**Figure 3.6C**) associated with notably increased m^{6}A methylation near the 5' portion of the transcript (**Figure 3.6D**) upon *Fto* depletion.

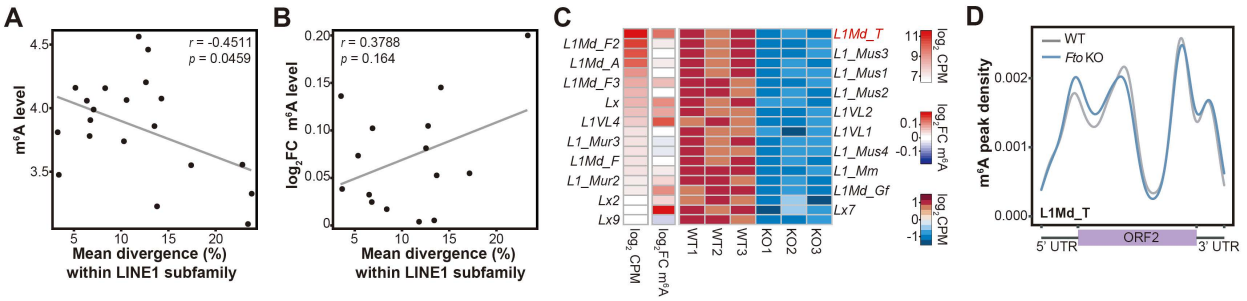

Figure 3.6 Methylation and abundance regulation of LINE1 subfamilies by FTO
(**A**) and (**B**) LINE1 subfamilies were ranked by average sequence divergence (< 25%) across different elements within each mouse LINE1 subfamily. (A) A scatter plot showing a negative correlation between the m^{6}A level of LINE1 subfamilies and their mean divergences in WT mESCs. (B) A scatter plot showing a positive correlation between the log$_2$ fold changes of m^{6}A

(**Figure 3.6, continued**) LINE1 subfamilies and their mean divergences upon *Fto* KO. (**C**) Heatmap showing the expression levels of LINE1 (log_2 CPM) of highly abundant LINE1 subfamilies on chromatin in WT mESCs, changes of m^6A level (log_2FC m^6A) and expression level (log_2FC CPM) of highly abundant LINE1 subfamilies on chromatin upon *Fto* KO. (**D**) Metagene profiles of m^6A peak density along m^6A-marked L1Md_T with three segments (5' UTR, ORF2, and 3' UTR) in WT and *Fto*$^{-/-}$ mESCs. *r* refers to Pearson's correlation coefficient. *p* values represent the Pearson's correlation coefficient determined using *t*-distribution in (A) and (B).

As LINE1 RNA was identified as a preferential substrate of FTO on chromatin, we performed fluorescence *in situ* hybridization (FISH) to image LINE1 RNA in mESCs, which showed that LINE1 RNA mainly localized to cell nucleus, in agreement with a previous study[159]. LINE1 RNA FISH and immunofluorescence of FTO revealed a notable colocalization of LINE1 RNA and FTO protein (**Figure 3.7A**). Moreover, the cross-linking immunoprecipitation followed by RT-qPCR (CLIP-RT-qPCR) experiments revealed a significant binding of LINE1 RNA by FTO using an anti-FTO antibody (**Figure 3.7B**), further confirming the direct interaction between FTO protein and LINE1 RNA.

LINE1 FISH showed that the fluorescence intensity derived from LINE1 RNA also decreased in the whole cell upon *Fto* KO (**Figure 3.7C**). We thus tested whether FTO has the same effect on total cellular LINE1 RNA in addition to the chromatin-associated LINE1 RNA as LINE1 RNA is known to be mainly nuclear localized. We indeed found that the LINE1 RNA m^6A methylation level and LINE1 RNA abundance in total RNA are affected by FTO similarly to those of chromatin-associated LINE1 RNA (**Figure 3.7D**). To investigate whether the observed changes of LINE1 RNA are dependent on the m^6A demethylation activity of FTO, we employed a known small molecule inhibitor of FTO[61] and found that the effects of *Fto* KO on total LINE1 RNA could be recapitulated by treating WT mESCs with the FTO inhibitor (**Figure 3.7E**).

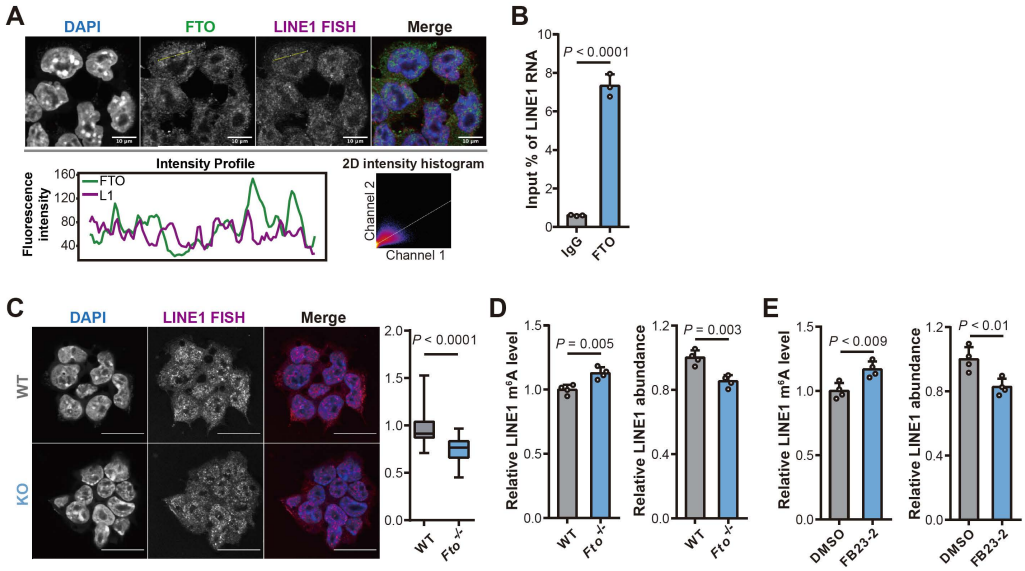

Figure 3.7 Effects of FTO on total cellular LINE1 RNA

(**A**) Fluorescence images, intensity profile, and 2D intensity histogram of LINE1 RNA FISH (magenta) and immunofluorescence of FTO (green) showing the colocalization of LINE1 RNA and FTO protein. Scale bars, 10 μm. (**B**) FTO CLIP-RT-qPCR of LINE1 in mESCs with IgG as the negative control. (**C**) Left: reduced LINE1 RNA level measured by LINE1 RNA FISH (magenta) caused by *Fto* KO. The nucleus was stained with DAPI (blue). Scale bars, 20 μm. Right: boxplots showing relative intensities quantified by using ImageJ. (**D**) Relative m^{6}A enrichment and expression levels of total LINE1 RNA measured by MeRIP-qPCR and RT-qPCR, respectively, in total RNA from WT and *Fto*$^{-/-}$ mESCs. (**E**) Relative m^{6}A enrichment and expression levels of total LINE1 RNA in total RNA measured by MeRIP-qPCR and RT-qPCR, respectively, in mESCs with or without FTO inhibitor treatment for 72 hours. *p* values were determined using a two-tailed *t*-test in (B) to (E). Representative images were selected from three independent experiments in (A) and (C).

3.2.2.2 Correlations between FTO and METTL3 or YTHDC1

As a previous study uncovered carRNA m^{6}A methylation by METTL3 and decay of some of the methylated carRNAs by YTHDC1 in mESCs[158], we reasoned that the function of FTO as a naturally existing demethylase that reverses m^{6}A on carRNAs should be associated with METTL3 and YTHDC1. We thus analyzed correlations of m^{6}A level changes and abundance changes of carRNAs between *Fto* KO and either *Mettl3* KO or *Ythdc1* CKO in mESCs with a focus on LINE1 RNA.

We first assessed m^{6}A changes induced by depletion of *Fto*, *Mettl3*, or *Ythdc1* in carRNAs. For all three groups of carRNAs and LINE1 RNA, we observed distinct negative correlations of m^{6}A level fold changes between *Fto* KO-induced hypermethylation and *Mettl3* KO-induced hypomethylation (**Figure 3.8A**), consistent with the notion that FTO mediates demethylation of a portion of m^{6}A installed by METTL3. In line with the proposed decay-promoting role of YTHDC1 on m^{6}A-marked carRNAs, the *Fto* KO-induced hypermethylation displayed clear positive correlations with the *Ythdc1* CKO-induced hypermethylation (**Figure 3.8A**). Notably, fold changes of m^{6}A level for repeat RNAs, especially LINE1 RNA, exhibited the strongest correlations among carRNAs. Interestingly, we observed positive correlations for m^{6}A fold change between these hypomethylated m^{6}A peaks upon *Fto* KO and upon *Mettl3* KO (**Figure 3.8C**), which suggests that loss or decreased levels of these m^{6}A sites upon *Fto* KO might be owing to the impeded m^{6}A deposition by METTL3.

We next assessed expression changes upon deletion of *Fto*, *Mettl3*, or *Ythdc1*, respectively. Specifically, we categorized transcripts of carRNAs into four groups: hypermethylated transcripts with upregulated abundance (hyper-up), hypermethylated transcripts with downregulated abundance (hyper-down), hypomethylated transcripts with upregulated abundance (hypo-up), and hypomethylated transcripts with downregulated abundance (hypo-down). As expected, we observed distinct negative correlations between expression level fold changes of repeat RNAs, especially LINE1 RNA, in *Fto* KO-induced hyper-down transcripts and in *Mettl3* KO-induced hypo-up transcripts, showing direct opposite effects of FTO *versus* METTL3 as m^{6}A demethylase and methyltransferase on repeat RNAs, respectively (**Figure 3.9A**). Accordingly, we also observed distinct negative correlations between *Fto* KO-induced hyper-down transcripts and *Ythdc1* CKO-induced upregulated transcripts for repeat RNAs, especially LINE1 RNA (**Figure 3.9B**),

consistent with an association between two proteins: lower FTO activity led to more m^{6}A methylation on repeat RNAs, more decay through YTHDC1 and reduced repeat RNA levels.

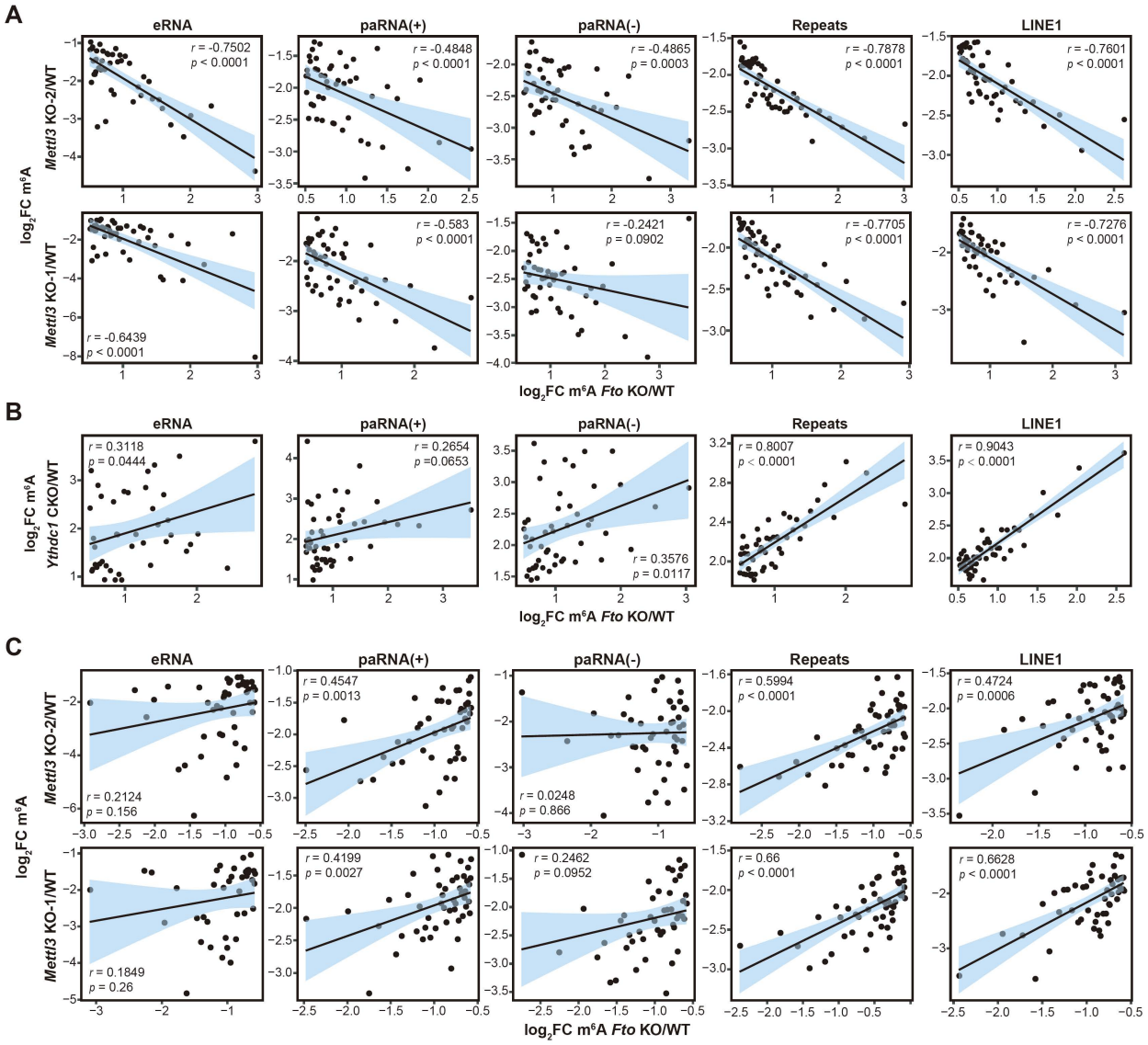

Figure 3.8 Correlations of carRNA m^{6}A level changes between *Fto* KO and *Mettl3* KO or *Ythdc1* cKO

(**A**) to (**C**) carRNAs within each group and LINE1 RNA were categorized into 50 bins based on their ranked fold changes of m^{6}A levels upon *Fto* KO. (A) Negative correlations of log$_2$ fold changes between hypermethylation of m^{6}A (log$_2$FC of m^{6}A > 0.58) on both carRNAs and LINE1 RNA upon *Fto* KO, and between hypomethylation of m^{6}A (log$_2$FC of m^{6}A < −0.58) on both carRNAs and LINE1 RNA upon *Mettl3* KO. (B) Positive correlations of log$_2$ fold changes of m^{6}A hypermethylation (log$_2$FC of m^{6}A > 0.58) on both carRNAs and LINE1 RNA between *Fto* KO over WT as well as *Ythdc1* cKO over control. (C) Correlations of log$_2$ fold changes of hypomethylation of m^{6}A (log$_2$FC of m^{6}A < -0.58) on both carRNAs and LINE1 RNA between *Fto* KO over WT as well as *Mettl3* KO over WT. *r* refers to Pearson's correlation coefficient. *p* values represent Pearson's correlation coefficient determined using *t*-distribution.

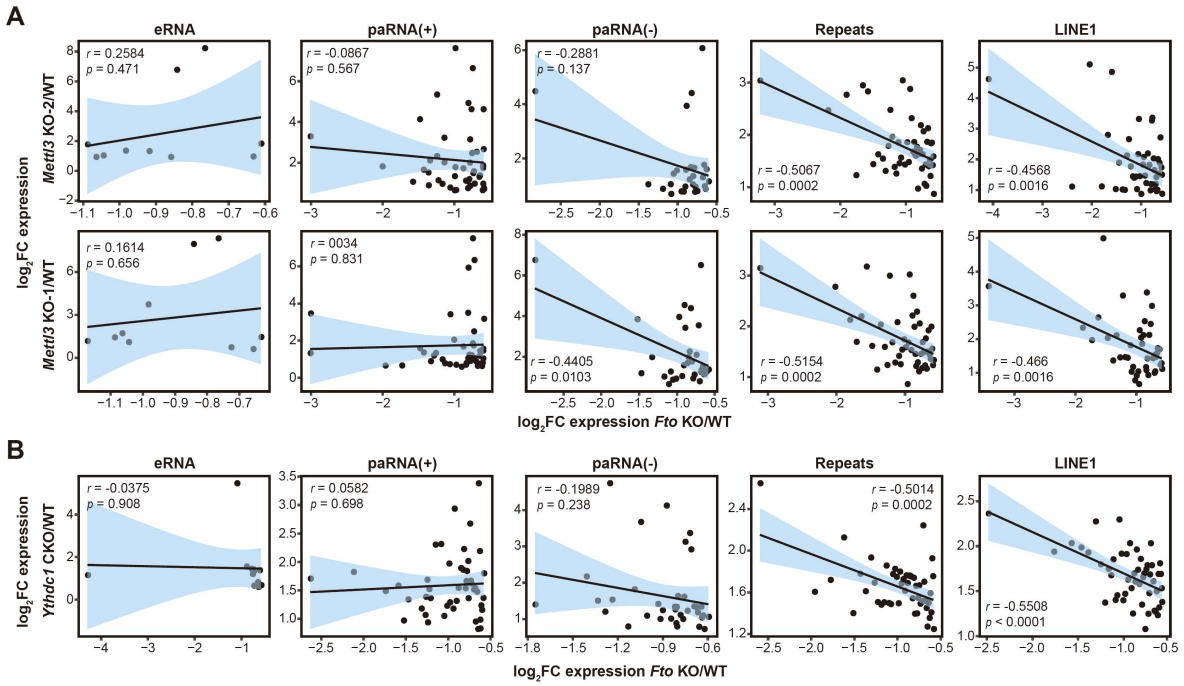

Figure 3.9 Correlations of carRNA transcript level changes between *Fto* KO and *Mettl3* KO or *Ythdc1* cKO

(**A**) and (**B**) each group of carRNAs including LINE1 RNA were categorized into 50 bins based on their ranked fold changes of transcript abundance upon *Fto* KO. (A) Correlations of log_2 fold changes of transcript abundance for carRNAs and LINE1 RNA between hyper-down transcripts (log_2FC of m^6A > 0.58, log_2FC of transcript abundance < -0.58) upon *Fto* KO and hypo-up transcripts (log_2FC of m^6A < -0.58, log_2FC of transcript abundance > 0.58) upon *Mettl3* KO. (B) Correlations of log_2 fold changes of transcript abundance of carRNAs and LINE1 RNA between hyper-down transcripts (log_2FC of m^6A > 0.58, log_2FC of transcript abundance < -0.58) upon *Fto* KO and upregulated transcripts (log_2FC of transcript abundance > 0.58) upon *Ythdc1* cKO. *r* refers to Pearson's correlation coefficient. *p* values represent Pearson's correlation coefficient determined using *t*-distribution.

3.2.2.3 FTO mediated-m^6A demethylation of LINE1 RNA is functionally important

Previous studies have shown critical roles of LINE1 RNA during early development[159,160]. Thus, we measured the capacity of WT and *Fto*$^{-/-}$ mESCs to form embryoid bodies (mEBs). We found that *Fto* KO led to induced differentiation, as shown by increased cell proliferation upon induction of differentiation (**Figure 3.10A-C**) with aberrant expression of differentiation markers (**Figure 3.10D).** As expected from our results above, we observed a 20% decrease in LINE1 RNA abundance in total RNA upon *Fto* KO on day 0. Notably, by day 6 of differentiation, LINE1 RNA

levels were reduced by 80% in *Fto* KO mESCs compared to WT (**Figure 3.10E)**. In addition, we noticed that *Fto* KO led to impaired mESC proliferation (**Figure 3.10F-H)**. Knockdown of LINE1 RNA with antisense oligos (ASOs) in WT mESCs (**Figure 3.10I)** could partially recapitulate the induced differentiation (**Figure 3.10A)** and the proliferation deficiency (**Figure 3.10F)** caused by *Fto* KO. Only targeted delivery of dCas13b-*wt*FTO but not dCas13b-*mut*FTO to LINE1 RNA in *Fto*$^{-/-}$ mESCs (**Figure 3.10J&K)** could partially reverse the induced differentiation (**Figure 3.10C&D)** and defected proliferation (**Figure 3.10G&H)**. These findings suggest that LINE1 RNA impacts mESC differentiation and proliferation in an m^{6}A-dependent manner.

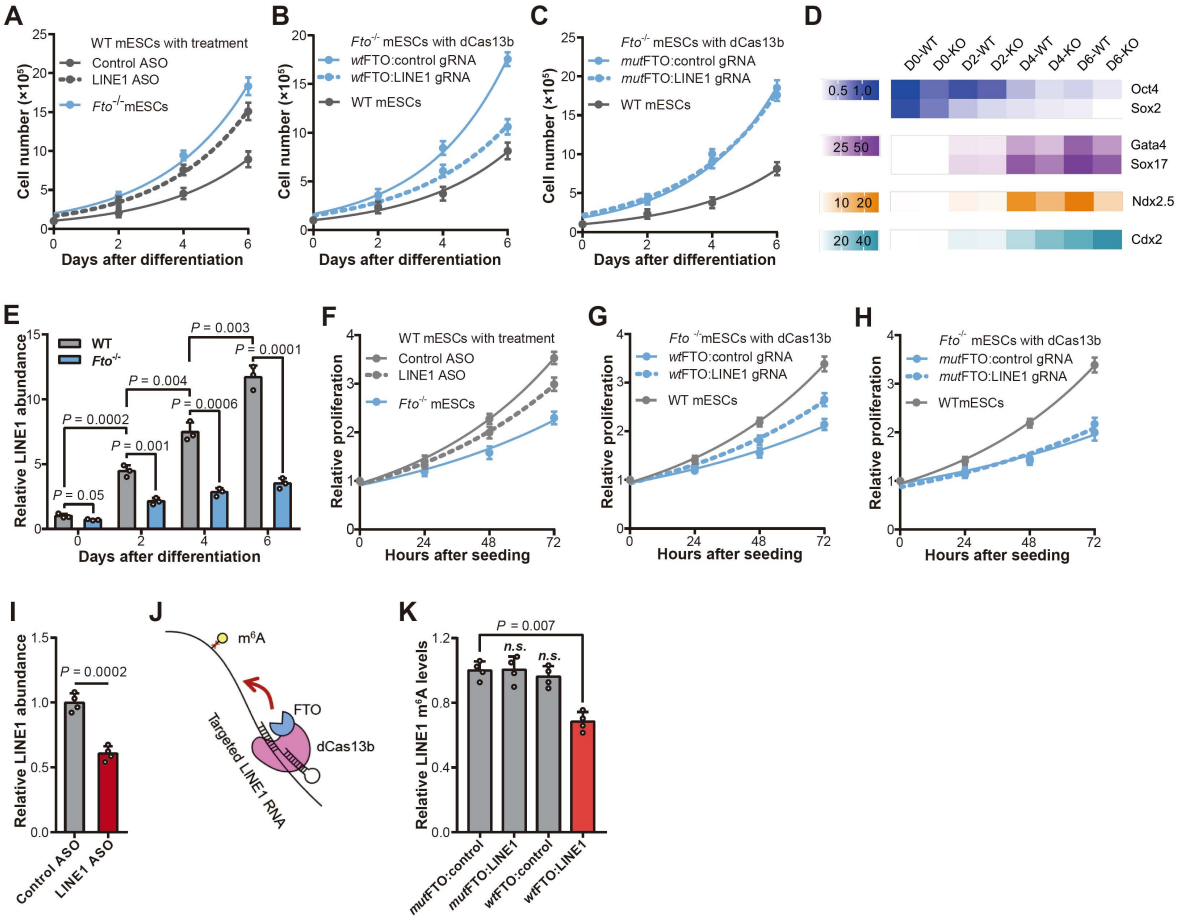

Figure 3.10 LINE1 RNA is a functionally relevant substrate of FTO in mESCs
(**A**) to (**C**) mEB formation capacity was represented by cell proliferation upon induction of differentiation. (A) Differentiation of *Fto*$^{-/-}$ mESCs (blue solid line) were compared to that of WT mESCs with the treatment of control ASO (grey solid line) or LINE1 ASO (grey dotted line). (B) Differentiation of *Fto*$^{-/-}$ mESCs rescued with dCas13b-*wt*FTO with gRNA targeting m^{6}A-marked

(**Figure 3.10, continued**) LINE1 (LINE1 gRNA, blue dotted line) or control gRNA (blue solid line) were compared to the differentiation of WT mESCs (grey solid line). (C) Differentiation of *Fto*$^{-/-}$ mESCs rescued with dCas13b-*mut*FTO with gRNA targeting m^{6}A-marked LINE1 (LINE1 gRNA, blue dotted line) or control gRNA (blue solid line) were compared to the differentiation of WT mESCs (grey solid line). Only targeted delivery of WT FTO to LINE1 RNA in *Fto*$^{-/-}$ mESCs could partially rescue the induced differentiation. (**D**) Heatmap showing the expression levels of differentiation marks measured by RT-qPCR during differentiation in WT and *Fto*$^{-/-}$ mESCs. (**E**) Relative expression levels of LINE1 RNA in total RNA measured by RT-qPCR in WT and *Fto*$^{-/-}$ mESCs during differentiation. (**F**) Proliferation of *Fto*$^{-/-}$ mESCs (blue solid line) compared to WT mESCs with the treatment of control ASO (grey solid line) or LINE1 ASO (grey dotted line). (**G)** and (**H**) dCas13b-FTO (wild-type or inactive mutant) constructs with gRNA targeting m^{6}A-marked LINE1 (LINE1 gRNA) or control gRNA were applied to modulate the m^{6}A methylation level of LINE1. Only targeted delivery of WT FTO to LINE1 RNA in *Fto*$^{-/-}$ mESCs could partially rescue the defected proliferation. (G) Proliferation of *Fto*$^{-/-}$ mESCs rescued with dCas13b-*wt*FTO and control gRNA (blue solid line) or LINE1 gRNA (blue dotted line) compared to that of WT mESCs (grey solid line). (H) Proliferation of *Fto*$^{-/-}$ mESCs rescued with dCas13b-*mut*FTO and control gRNA (blue solid line) or LINE1 gRNA (blue dotted line) compared to that of WT mESCs (grey solid line). (**I**) Relative expression level of LINE1 RNA in total RNA quantified by RT-qPCR in Mel624 cells with LINE1 ASO knockdown compared to control. (**J**) A schematic model showing the CRISPR dCas13b-FTO facilitated site-specific demethylation system. (**K**) Relative m^{6}A enrichment of LINE1 RNA in total RNA measured by MeRIP-qPCR in *Fto*$^{-/-}$ mESCs rescued with dCas13b-*wt*FTO or dCas13b-*mut*FTO, respectively. Only targeted delivery of WT FTO to LINE1 RNA in *Fto*$^{-/-}$ mESCs led to significantly decreased m^{6}A on LINE1 RNA. *p* values were determined using a two-tailed *t*-test in (E), (I), and (K).

3.2.3 Chromatin and transcriptional regulation by FTO in mESCs

3.2.3.1 Alteration of FTO affects chromatin state and transcription

Given that m^{6}A methylation on carRNAs regulates chromatin state and transcription[158], we sought to evaluate potential functions of FTO in regulating chromatin accessibility and transcription. We performed a deoxyribonuclease (DNase) I–treated terminal deoxynucleotidyl transferase-mediated deoxyuridine triphosphate nick-end labeling (TUNEL) assay, and found more closed chromatin in *Fto*$^{-/-}$ mESCs compared to WT (**Figure 3.11A)**. Accordingly, we observed reduced nascent RNA synthesis upon *Fto* KO using 5-ethynyl uridine (EU) labeling (**Figure 3.11B)**. Moreover, when we treated mESCs with an FTO inhibitor[61], the closed chromatin and reduced transcription upon *Fto* KO were recapitulated (**Figure 3.11C&D)**, indicating that the observed effects were mediated through the m^{6}A demethylation activity of FTO.

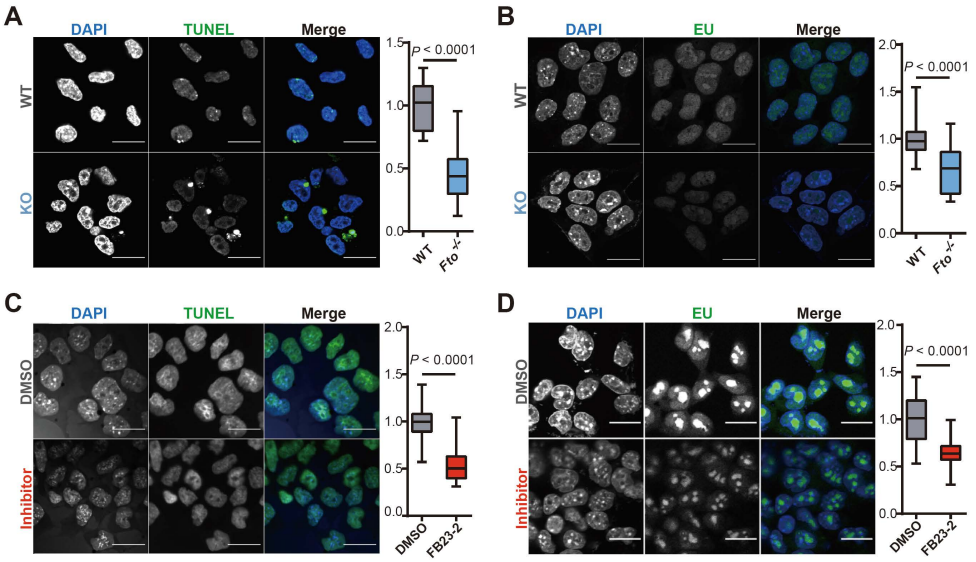

Figure 3.11 Closed chromatin and reduced transcription upon depletion or inhibition of FTO (**A**) Left: more globally closed chromatin measured by using the DNase I – TUNEL assay followed by fluorescence imaging was observed upon *Fto* KO. Scale bars, 20 μm. Right: boxplots showing relative intensities quantified by using ImageJ. (**B**) Left: reduced total nascent RNA synthesis measured by using EU labeling followed by fluorescence imaging was observed upon *Fto* KO. Scale bars, 20 μm. Right: boxplots showing relative intensities quantified by using ImageJ. (**C**) and (**D**) WT mESCs were treated with FTO inhibitor or DMSO as the control for 72 hours. (C) Left: more globally closed chromatin measured by using the DNase I–TUNEL assay followed by fluorescence imaging was observed for FTO inhibitor treatment compared to controls. Scale bars, 20 μm. Right: boxplots showing relative intensities quantified by using ImageJ. (D) Left: reduced total nascent RNA synthesis measured by using EU labeling followed by fluorescence imaging was observed for FTO inhibitor treatment compared to controls. Scale bars, 20 μm. Right: boxplots showing relative intensities quantified by using ImageJ. Representative images were selected from three independent experiments; *p* values were determined using a two-tailed *t*-test.

3.2.3.2 Features of chromatin state changes caused by *Fto* KO

To examine the chromatin accessibility across the genomes of WT and *Fto*$^{-/-}$ mESCs, we performed the Assay for Transposase-Accessible Chromatin using sequencing (ATAC-seq)[161,162]. Reminiscence of the DNase I–TUNEL assay, we observed reduced overall ATAC-seq signal intensity upon *Fto* KO (**Figure 3.12A)**. We obtained more differentially decreased peaks by merging the peaks into united peak sets (**Figure 3.12B)**. To gain detailed insight into changes caused by *Fto* KO, we assessed quantitative decreases of ATAC-seq signal intensity, defined as gained-closed regions, through 1 kb sliding windows[163]. 4,683 gained-closed regions were

identified in *Fto*$^{-/-}$ mESCs compared to WT. We annotated genomic distribution of gained-closed regions and observed notable accessibility decreases in intronic and intergenic regions (**Figure 3.12C)**. Additionally, gene ontology (GO) analysis of gained-closed regions revealed an enrichment of molecular functions related to transcription regulation and biological processes related to development (**Figure 3.12D)**.

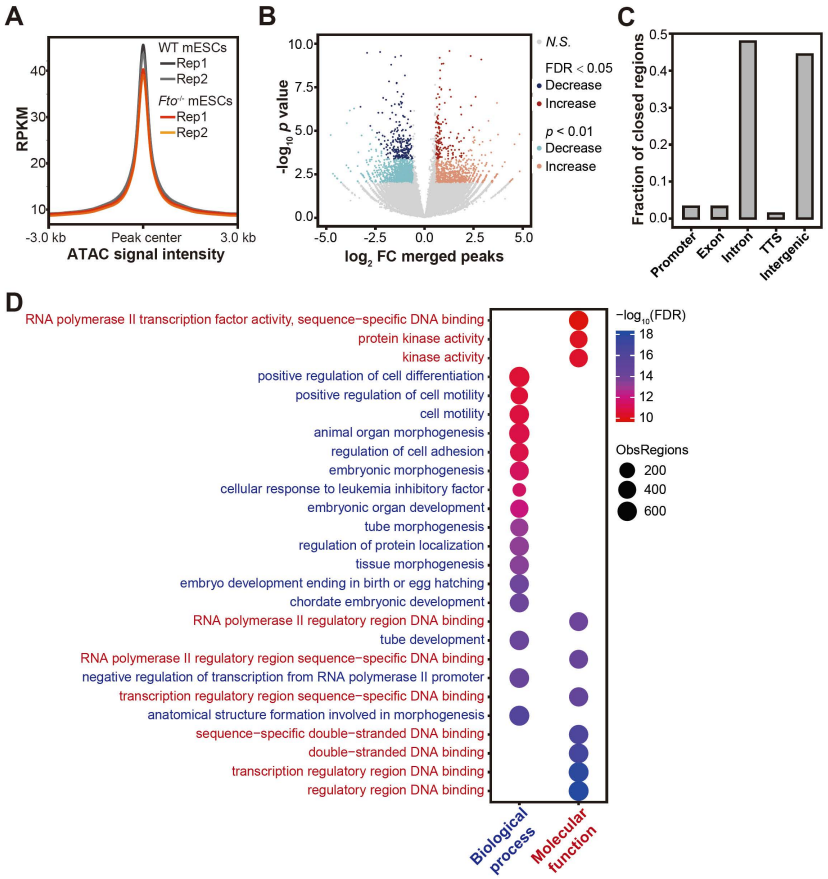

Figure 3.12 Overall profile of chromatin accessibility upon *Fto* KO
(**A**) Density plots showing the overall ATAC-seq signal quantified with FPKM in WT and *Fto*$^{-/-}$ mESCs. (**B**) A volcano plot showing the comparison of differential peaks from ATAC-seq results upon *Fto* KO. Significant increased peaks are shown in red ($p < 0.01$: 889; FDR < 0.05: 164) and significant decreased peaks are shown in blue ($p < 0.01$: 1397; FDR < 0.05: 251). (**C**) The genomic distribution (promoter, exonic, intronic, TTS, and intergenic regions annotated by HOMER) of gained-closed regions defined by 1 kb sliding windows from ATAC-seq results upon *Fto* KO. (**D**) GO analysis of top enriched biological processes (labeled in blue) and molecular functions (labeled in red) of gained-closed regions.

We next compared the gained-closed regions caused by FTO depletion with profiles of histone modifications[164] and Pol II binding[165] from published ChIP-seq datasets in mESCs. Gained-closed regions upon *Fto* KO were enriched with H3K4Me1, H3K4Me3, H3K27Ac, and Pol II binding sites in WT mESCs, indicating that the activity of FTO correlates with transcription activation in WT mESCs. Additionally, these gained-closed regions induced by *Fto* KO further overlapped with regions showing increased binding by histones marked with H3K4me3 and H3K27Ac upon *Mettl3* KO[158] (**Figure 3.13)**, which suggests that the FTO-affected regions associate with METTL3 in mESCs.

Considering EP300 and YY1 can be recruited by carRNAs to promote active transcription[158], we compared *Fto* KO-induced chromatin accessibility changes with genomic locations of EP300 and YY1 in WT and *Mettl3*$^{-/-}$ mESCs[158]. We found that the gained-closed regions upon *Fto* KO were enriched with EP300 and YY1 binding in WT mESCs, suggesting that these regions are more open before FTO depletion. In addition, the elevated DNA binding of EP300 and YY1 in *Mettl3*$^{-/-}$ mESCs showed increased enrichments with the gained-closed regions caused by *Fto* KO (**Figure 3.13)**. These findings were consistent with a transcriptional activation role of FTO in WT mESCs, involving the binding of EP300 and YY1 in regions with carRNA m^{6}A demethylation by FTO to facilitate opening of the local chromatin. Perhaps not surprisingly, we also observed a slight enrichment of gained-closed regions induced by *Fto* KO in the METTL3 ChIP-seq profile (**Figure 3.13)**, suggesting that the reduced chromatin accessibility caused by FTO depletion may impede the binding of METTL3 to certain genomic regions and subsequently reduce the nearby RNA m^{6}A methylation.

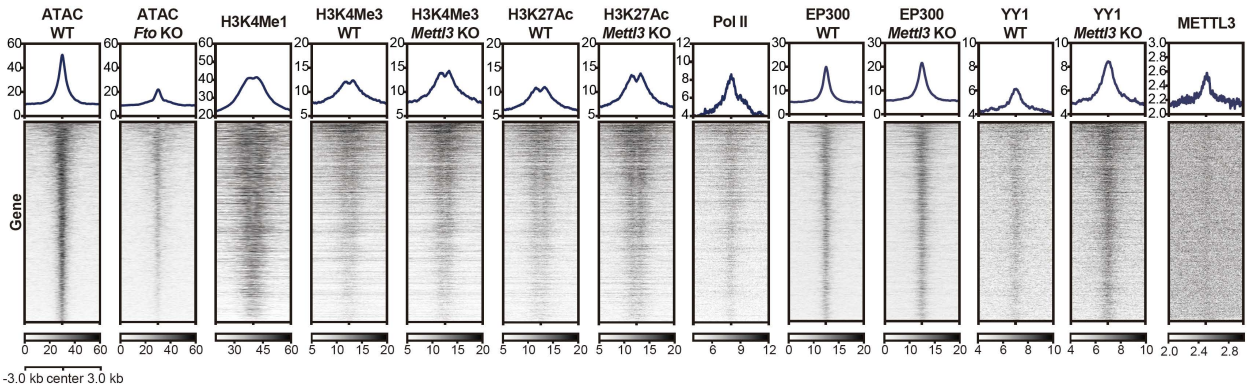

Figure 3.13 Genomic features of gain-closed regions upon *Fto* KO
Gained-closed regions and ChIP-seq datasets were plotted in heatmap views. The left two panels represent the gained-closed regions from ATAC-seq in *Fto*$^{-/-}$ mESCs compared to WT mESCs. The right eleven panels represent the enriched DNA-binding sites of H3K4Me1 in WT mESCs, H3K4Me3 in both WT and *Mettl3*$^{-/-}$ mESCs, H3K27Ac in both WT and *Mettl3*$^{-/-}$ mESCs, Pol II in WT mESCs, EP300 in both WT and *Mettl3*$^{-/-}$ mESCs, YY1 in both WT and *Mettl3*$^{-/-}$ mESCs, and METTL3 in WT mESCs from corresponding ChIP-seq results, respectively. Binding sites of H3K4Me3, H3K27Ac, EP300, and YY1 in *Mettl3*$^{-/-}$ mESCs showed increased overlap with *Fto* KO-induced gained-closed regions compared to their binding sites in WT mESCs.

3.2.3.3 FTO regulates chromatin states through LINE1 RNA m^{6}A demethylation

In line with the cross-comparison of ATAC-seq and ChIP-Seq of histone modifications, slight reductions in protein levels of the active histone marks H3K4Me3 and H3K427Ac were observed, accompanied by a slight elevation of the repressive histone mark H3K27Me3 upon *Fto* KO (**Figure 3.14A)**. Given histone modifications could be modulated through m^{6}A methylation of mRNAs encoding histone modifiers[166], we evaluated the m^{6}A level and expression level of mRNAs encoding histone modifiers that may affect the aforementioned histone modifications. We did not find notably increased m^{6}A peaks, and only observed minimal or opposite changes in their expression levels. We also looked into protein level changes as m^{6}A on mRNA could impact translation[65]. Again, minimal changes or opposite changes were observed, suggesting that effects of FTO on chromatin state in mESCs were less likely due to the m^{6}A demethylation of mRNAs encoding histone modifiers.

Therefore, we further investigated the role of FTO-mediated m^{6}A demethylation on LINE1 RNA in chromatin regulation. Indeed, knockdown of LINE1 RNA in mESCs recapitulated the more closed chromatin observed for FTO depletion (**Figure 3.14B)**. To establish a causal relationship, we performed targeted LINE1 RNA demethylation with the delivery of dCas13b-*wt*FTO and inactive dCas13b-*mut*FTO into *Fto*$^{-/-}$ mESCs. We found that only the delivery of dCas13b-*wt*FTO (**Figure 3.14C)** but not inactive dCas13b-*mut*FTO (**Figure 3.14D)** to LINE1 RNA partially rescued the more closed chromatin state in *Fto*$^{-/-}$ mESCs.

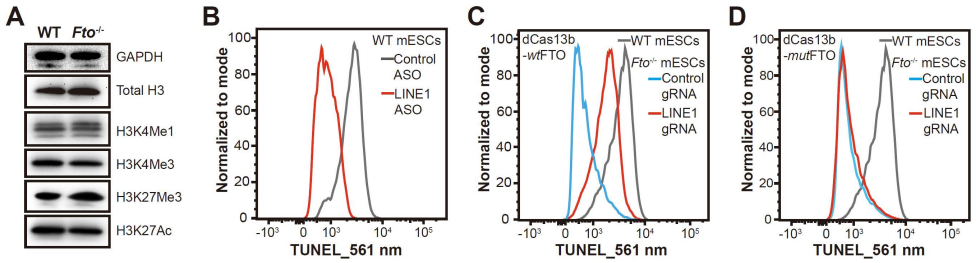

Figure 3.14 LINE1 RNA plays a key role in FTO-mediated chromatin state regulation
(**A**) Immunoblot assays showing histone modification levels in WT and *Fto*$^{-/-}$ mESCs. (**B**) LINE1 RNA knockdown with LINE1 ASO (red) led to more closed chromatin measured by using Dnase I – TUNEL assay followed by flow cytometry in mESCs compared to control ASO (grey) in WT mESCs. (**C**) TUNEL signal for *Fto*$^{-/-}$ mESCs rescued with dCas13b-*wt*FTO using gRNA targeting LINE1 and control gRNA (blue) were compared to that of WT mESCs (grey). (**D**) TUNEL signal of *Fto*$^{-/-}$ mESCs rescued with dCas13b-*mut*FTO and control gRNA (blue) or LINE1 gRNA (red) were compared to WT mESCs (grey). Only targeted delivery of WT FTO to LINE1 RNA in *Fto*$^{-/-}$ mESCs could partially rescue the more closed chromatin.

Our working model so far predicts that changes of m^{6}A level on LINE1 RNA proceed and induce chromatin state changes. To validate, we treated WT mESCs with FTO inhibitor and monitored the kinetics of LINE1 RNA m^{6}A levels and chromatin accessibility. Inhibition of FTO first led to increased LINE1 RNA m^{6}A methylation (within 6 hours), causing its subsequent decay and reduced level in mESCs (after 12 hours), which eventually resulted in more closed chromatin (**Figure 3.15)**. The time-course inhibition data supports that the closed chromatin may limit access of m^{6}A methyltransferases, which could explain a portion of hypomethylated m^{6}A peaks observed as secondary effects after FTO depletion.

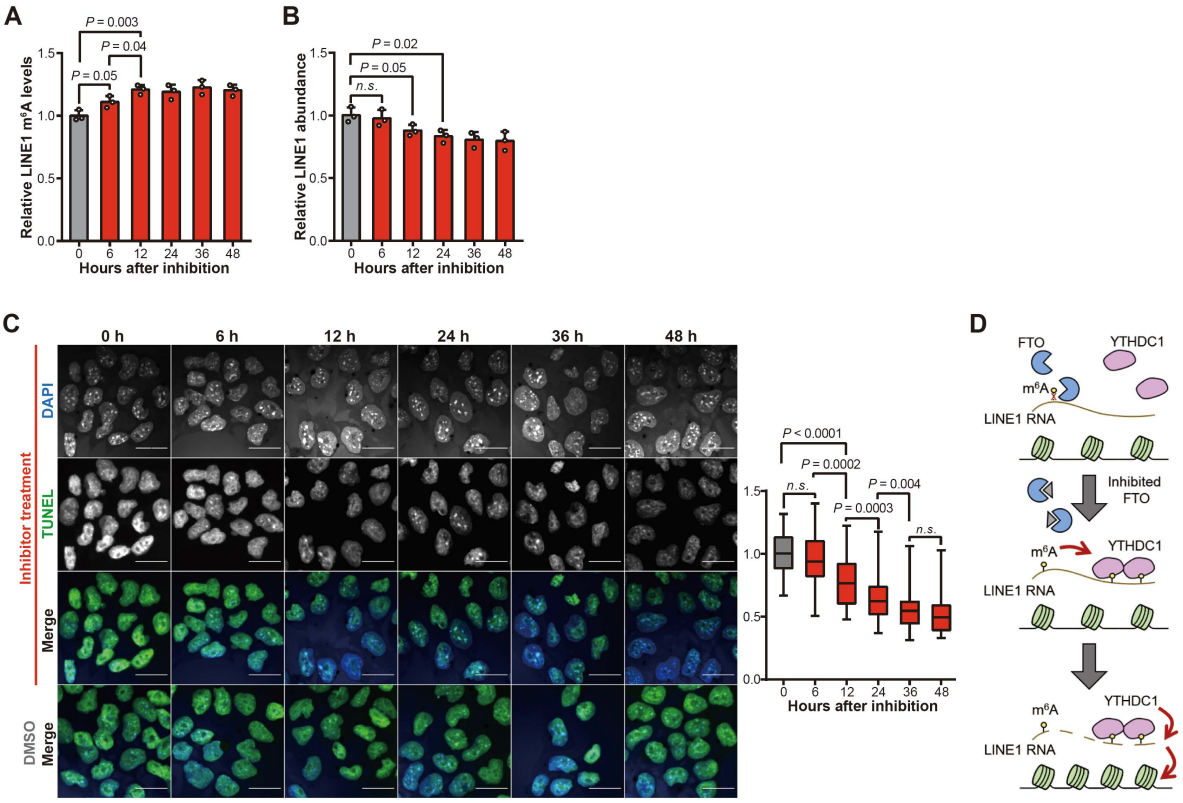

Figure 3.15 Time-course inhibition of FTO shows the dynamic of LINE1 RNA and chromatin states

(**A**) The relative m^{6}A levels of LINE1 RNA measured by MeRIP-qPCR during a time course of 48-hour treatment with an FTO inhibitor in WT mESCs. (**B**) The relative expression levels of LINE1 RNA measured by RT-qPCR during a time course of 48-hour treatment with an FTO inhibitor in WT mESCs. (**C**) Left: gradually closed chromatin measured by using the DNase I – TUNEL assay followed by fluorescence imaging during a time course of 48-hour treatment with an FTO inhibitor in mESCs. Scale bars, 20 μm. Right: boxplots showing relative intensities quantified by using ImageJ. Representative images were selected from three independent experiments. (**D**) A schematic model showing a plausible mechanism by which FTO inhibition led to closed chromatin. *p* values were determined using a two-tailed *t*-test. *n.s.* means not significant in (A) to (C).

3.2.4 LINE1 RNA m^{6}A is a physiological substrate of FTO in mammals

3.2.4.1 FTO correlates with LINE1 RNA m^{6}A and abundance across mammalian tissues

A recent study probed m^{6}A methylomes across mouse and human tissues, revealing potential correlations between the overall mRNA m^{6}A level and the expression levels of m^{6}A writers or erasers[157]. To our surprise, mRNA m^{6}A showed a positive correlation with FTO expression across mouse and human tissues, suggesting that mature mRNA m^{6}A might not be the

primary substrate of FTO in mammalian tissues. Given its nuclear localization tendency in most tissues, we speculated that FTO might also exhibit substrate preference to repeat RNAs, especially LINE1 RNA in most mammalian tissues.

Indeed, we reanalyzed the published m^{6}A methylomes[157] and found m^{6}A level of repeat RNAs negatively correlated with FTO expression level across mouse tissues (**Figure 3.16A)**. Analogous to mESCs, LINE1 RNA was relatively abundant and possessed a high average m^{6}A level among repeat RNAs in mouse tissue (**Figure 3.16B)**. We thus performed MeRIP-RT-qPCR in total RNA isolated from mouse tissues and confirmed that high m^{6}A level correlates with low LINE1 RNA abundance (**Figure 3.16C)**. We further found that the expression level of FTO negatively correlated with the m^{6}A level of LINE1 RNA, while positively correlated with LINE1 RNA abundance across mouse tissues, in agreement with a LINE1-RNA-demethylation role of FTO (**Figure 3.16D)**. Similar patterns of the negative correlation between LINE1 RNA m^{6}A and FTO expression, the positive correlation between LINE1 RNA abundance and FTO expression, and the negative correlation between LINE1 RNA m^{6}A and LINE1 RNA abundance were also observed across human tissues (**Figure 3.16E&F)**. These analyses and our experimental validation reveal that high FTO expression tends to correlate with low LINE1 RNA m^{6}A methylation and high LINE1 RNA abundance across mouse and human tissues.

In comparison with the other m^{6}A demethylase ALKBH5, negative correlations were observed between mRNA m^{6}A level and expression level of ALKBH5 across both mouse and human tissues[157], consistent with an mRNA m^{6}A demethylation role of ALKBH5. However, a clear negative correlation was not observed between the m^{6}A level of repeat RNAs and ALKBH5 expression across mouse tissues based on our analysis (**Figure 3.17A)**, though we cannot completely rule out that ALKBH5 could mediate m^{6}A demethylation of certain subfamilies in

repeat RNAs. Our MeRIP-RT-qPCR results validated that the expression level of ALKBH5 displays no clear correlation with m^{6}A level or abundance of LINE1 RNA across mouse tissues (**Figure 3.17B)**. Likewise, we did not observe any notable correlations between the expression of ALKBH5 and the m^{6}A level or abundance of LINE1 RNA across human tissues (**Figure 3.17C)**. These findings suggest that LINE1 RNA m^{6}A is a primary substrate of FTO but not ALKBH5 across mouse and human tissues.

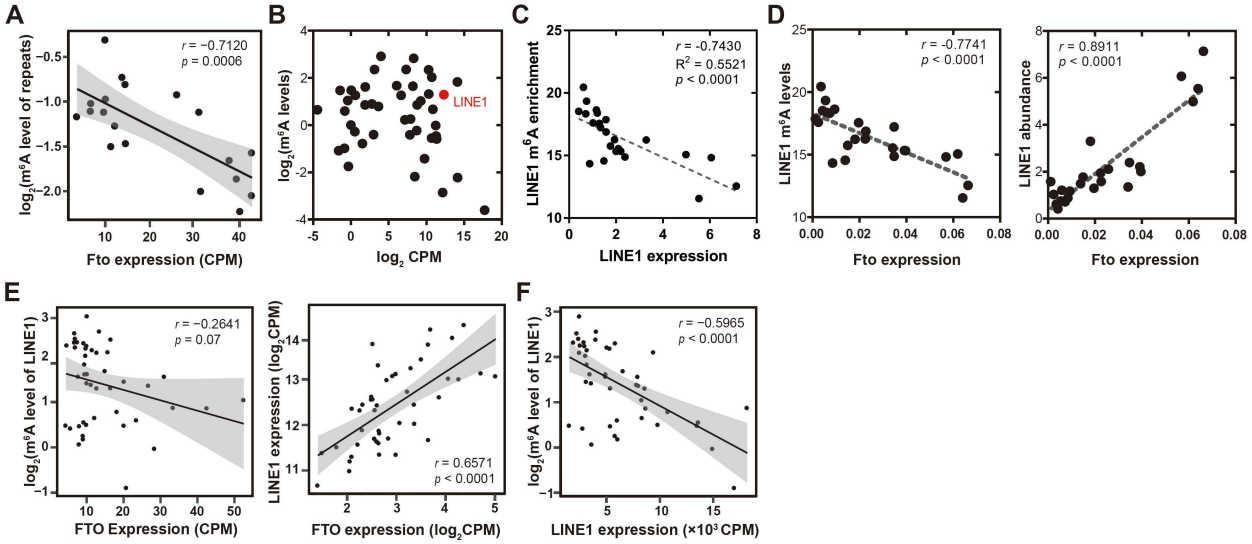

Figure 3.16 Correlation of *FTO* expression with LINE1 RNA m^{6}A and abundance across mouse and human tissues

(**A**) and (**B**) Analyses from m^{6}A MeRIP-seq datasets across mouse tissues. (A) A scatter plot showing a negative correlation between the calculated overall m^{6}A level of repeat RNAs and the expression level of FTO. (B) A scatter plot showing the average expression level (Log_2 CPM) and calculated average m^{6}A level of RNA species among Repeat RNAs. (**C**) and (**D**) Across mouse tissues, m^{6}A fold enrichment of LINE1 RNA was measured by MeRIP-qPCR; LINE1 RNA abundance and the expression level of FTO were measured by RT-qPCR. (C) A scatter plot showing a negative correlation between m^{6}A fold enrichment and the expression level of LINE1 RNA. (D) Left: a scatter plot showing a negative correlation between m^{6}A fold enrichment of LINE1 RNA and the expression level of FTO. Right: a scatter plot showing a positive correlation between the relative expression levels of LINE1 RNA and FTO. (**E**) and (**F**) Analyses from m^{6}A MeRIP-seq datasets across human tissues. (E) Left: A scatter plot showing the negative correlation between m^{6}A fold enrichment of LINE1 RNA and the expression level of FTO. Right: A scatter plot showing a positive correlation between the expression levels of LINE1 RNA and FTO. (F) A scatter plot showing a negative correlation between m^{6}A fold enrichment of LINE1 RNA and the expression level of FTO. *r* refers to Pearson's correlation coefficient; *p* values represent Pearson's correlation coefficient using *t*-distribution.

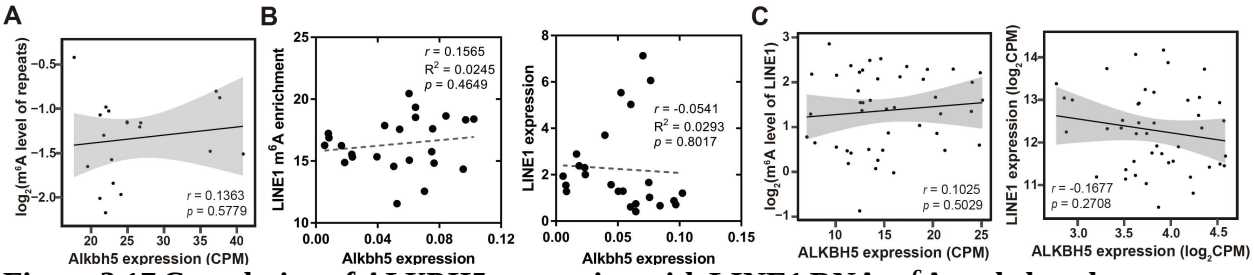

Figure 3.17 Correlation of *ALKBH5* expression with LINE1 RNA m^{6}A and abundance across mouse and human tissues

(**A**) A scatter plot showing a negligible correlation between the calculated overall m^{6}A level of repeat RNAs and the expression level of ALKBH5 across mouse tissues analyzed from the MeRIP-seq dataset. (**B**) Across mouse tissues, m^{6}A fold enrichment of LINE1 RNA was measured by MeRIP-qPCR; LINE1 RNA abundance and the expression level of ALKBH5 were measured by RT-qPCR. Left: a scatter plot showing a negligible correlation between m^{6}A fold enrichment of LINE1 RNA and the expression level of ALKBH5. Right: a scatter plot showing a negligible correlation between the relative expression levels of LINE1 RNA and. (**C**) Analyses from m^{6}A MeRIP-seq datasets across mouse tissues. Left: a scatter plot showing a negligible correlation between m^{6}A fold enrichment of LINE1 RNA and the expression level of ALKBH5 across human tissues analyzed from MeRIP-seq datasets. Right: a scatter plot showing a negligible correlation between the expression levels of LINE1 RNA and ALKBH5 across human tissues analyzed from RNA-seq datasets. *r* refers to Pearson's correlation coefficient; *p* values represent the Pearson's correlation coefficient using *t*-distribution.

3.2.4.2 FTO mediates LINE1 RNA m^{6}A demethylation in mouse cerebellum

In line with a previous report[130], we found the highest FTO mRNA expression in the cerebellum (**Figure 3.18A)**. Therefore, we decided to study the mouse cerebellum as an example to establish LINE1 m^{6}A demethylation by FTO and the subsequent effect on LINE1 RNA level in tissues. We measured m^{6}A level and expression level of LINE1 RNA in total RNA isolated from the cerebellum of pairs of WT, *Fto*$^{+/-}$, and *Fto*$^{-/-}$ mice, respectively. We indeed observed an increased m^{6}A level and decreased abundance of LINE1 RNA with FTO depletion (**Figure 3.18B)**.

Furthermore, we derived mouse neural stem cells (mNSCs) from WT and *Fto* KO mice and performed similar measurements. We again observed an increased m^{6}A level and decreased abundance of LINE1 RNA from mNSCs upon *Fto* KO (**Figure 3.18C)**. Accordingly, we observed that *Fto* KO in mNSCs led to a globally more closed chromatin state and reduced nascent RNA synthesis (**Figure 3.18D&E)**, indicating the FTO-mediated m^{6}A demethylation of LINE1 RNA

may play broad regulatory roles in mouse tissues and developmental cells. Reminiscent of mESCs, the LINE1 RNA level in mNSCs was notably reduced upon *Fto* KO after differentiation (**Figure 3.18F)**. Moreover, compared to undifferentiated mNSCs, the FTO protein level and LINE1 RNA abundance were both significantly elevated in differentiated mNSCs (**Figure 3.18G)**.

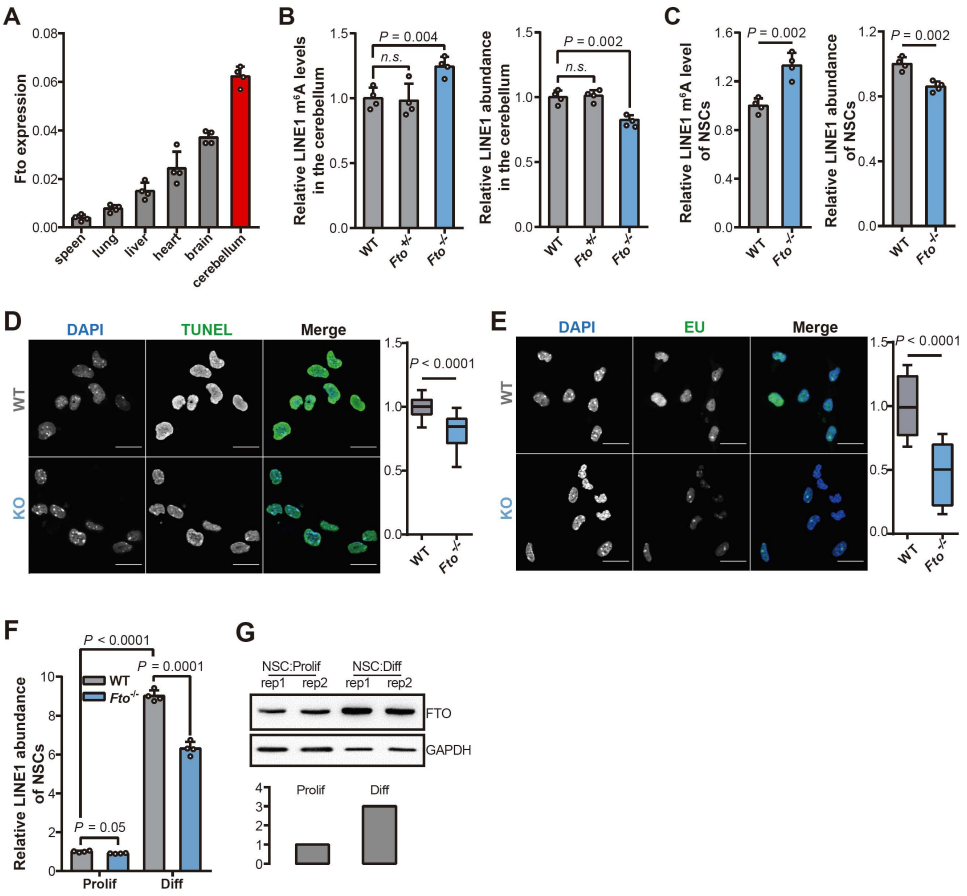

Figure 3.18 FTO mediates LINE1 RNA demethylation in mouse cerebellum and mNSCs
(**A**) Expression levels of FTO across mouse tissues measured by RT-qPCR. (**B**) Left: relative m^6A fold enrichment of LINE1 RNA in the total RNA isolated from the cerebellum of WT, *Fto*$^{+/-}$, and *Fto*$^{-/-}$ mice measured by using MeRIP-qPCR. Right: relative expression levels of LINE1 RNA in the total RNA isolated from the cerebellum of WT, *Fto*$^{+/-}$, and *Fto*$^{-/-}$ mice measured by using RT-qPCR. (**C**) Left: relative m^6A fold enrichment of LINE1 RNA in *Fto*$^{-/-}$ mNSCs normalized to WT mNSCs quantified by MeRIP-qPCR. Right: the relative expression level of LINE1 RNA in *Fto*$^{-/-}$ mNSCs normalized to WT mNSCs quantified by RT-qPCR. (**D**) Left: chromatin openness measured by DNase I – TUNEL assay followed by fluorescent imaging in *Fto*$^{-/-}$ mNSCs compared to WT. Scale bars, 20 μm. Right: boxplots showing relative intensities quantified by using ImageJ. (**E**) Left: total nascent RNA synthesis measured by EU labeling followed by fluorescent imaging in *Fto*$^{-/-}$ mNSCs compared to WT. Scale bars, 20 μm. Right: boxplot showing relative intensities quantified by using ImageJ. (**F**) and (**G**) Both FTO protein expression and LINE1 RNA abundance increase in differentiated NSCs compared to undifferentiated NSCs. (F) The relative expression

(**Figure 3.18, continued**) level of LINE1 RNA in total RNA measured by RT-qPCR in WT and *Fto*$^{-/-}$ mNSCs before and after differentiation. (G) Top: Immunoblot assays showing FTO expression in WT mNSCs before and after differentiation; bottom: relative FTO protein levels normalized to GAPDH quantified by using ImageJ. *p* values were determined using a two-tailed *t*-test in (B) to (F). Representative images were selected from three independent experiments in (D) and (E).

3.2.4.3 FTO affects oocyte development through LINE1 RNA

Lastly, given the importance of both FTO[44,123-125] and LINE1 RNA[159,160] during mouse early development, we assessed whether the FTO-mediated LINE1 m^{6}A demethylation contributed to the regulation of early development using mouse oocyte as an example. Our analysis of mouse oocyte development[167] revealed downregulation of both LINE RNA abundance and FTO expression from the PGC stage to the MII stage (**Figure 3.19A)**. We indeed observed that *Fto* KO mice display oocyte defects with significantly smaller ovaries and reduced follicles (**Figure 3.19B)**. The numbers of GV oocytes collected from 4-week-old *Fto*$^{-/-}$ mice were significantly decreased compared to WT control mice (**Figure 3.19C)**. We also observed significantly reduced SN oocytes upon *Fto* KO (**Figure 3.19D)**, indicating that loss of *Fto* leads to the impeded ability to maturation and fertilization of oocytes. Similar to what we observed in mESCs, mNSCs, and mouse cerebellum, in GV oocytes, *Fto* KO led to more than 50% reduction of LINE1 RNA abundance (**Figure 3.19E)** and dramatically closed chromatin (**Figure 3.19F)**, revealing a general role of FTO-mediated LINE1 RNA m^{6}A demethylation in mammals.

We asked whether mRNA cap-m^{6}A$_m$ and snRNA m^{6}A$_m$ are involved in the FTO-mediated defects during early mammalian development. The mRNA cap-m^{6}A$_m$ demethylation mediated by FTO is mostly a cytoplasmic event[63]. and the knockout of the corresponding mRNA cap-m^{6}A$_m$ methyltransferase does not affect viability and fertility in mice[168], excluding its involvement in mammalian early development. In cell nucleus, FTO was recently reported to demethylate m^{6}A$_m$ on snRNA[86]. METTL4 was identified as the snRNA m^{6}A$_m$ methyltransferase[169]. To examine

whether snRNA m^6A_m contributes to mESC differentiation and proliferation regulation, we measured mEB formation capacity and proliferation of WT and *Mettl4*$^{-/-}$ mESCs. A reduced mEB formation capacity and an induced proliferation, opposite to effects of FTO depletion, would be expected for METTL4 depletion if snRNA m^6A_m contributes to the differentiation regulation in mESCs. On the contrary, we observed induced mESC differentiation and reduced proliferation (**Figure 3.20A&B)** upon *Mettl4* KO, indicating that snRNA m^6A_m is not associated with the FTO-mediated differentiation and proliferation regulation in mESCs. Lastly, *Mettl4* KO was reported not to affect mouse viability[155]. Our studies also confirmed no noticeable effect of *Mettl4* KO on oocyte development in mice (**Figure 3.20C-E)**. These studies in mESCs and mouse oocytes exclude snRNA m^6A_m as a substrate of FTO that functionally affects mouse early development.

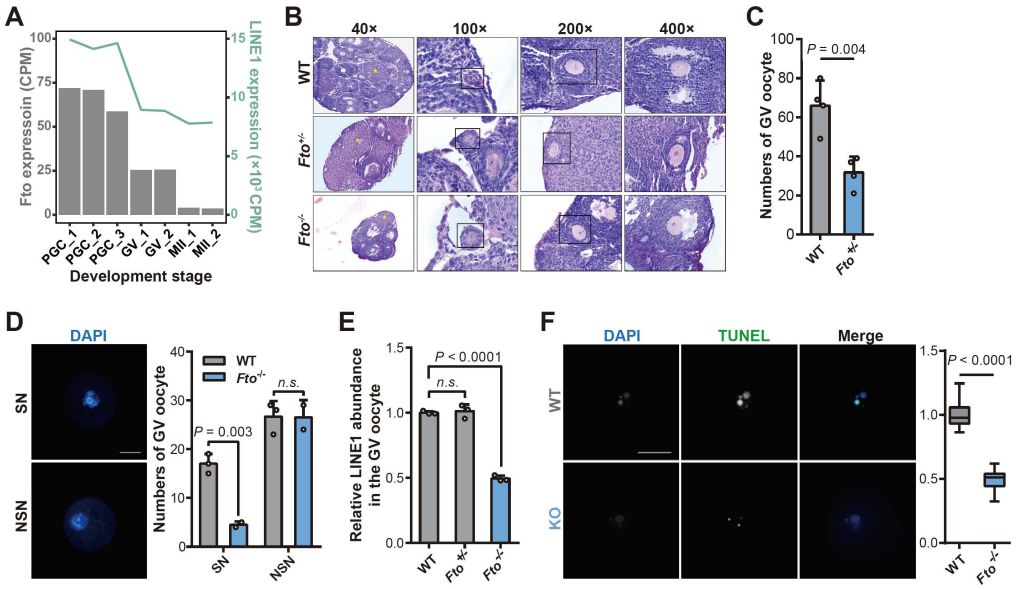

Figure 3.19 FTO-mediated LINE1 RNA demethylation during oocyte development
(**A**) FTO (line) and LINE1 RNA (bar) abundance quantified with CPM values from RNA-seq datasets during oocyte development showing decreases of both FTO (line) and LINE1 RNA (bar) abundances during oocyte development. (**B**) HE staining of the ovaries from 7-week-old WT, *Fto*$^{+/-}$ and *Fto*$^{-/-}$ mice. Those from *Fto*$^{-/-}$ mice display oocyte defects with a smaller ovary and reduced follicles. (**C**) Numbers of GV oocytes collected from four 4-week-old *Fto*$^{-/-}$ mice and WT control. (**D**) Left: Fluorescence imaging showing the SN and NSN GV oocytes. Scale bars, 50 μm; right: numbers of SN and NSN GV oocytes collected from two 4-week-old *Fto*$^{-/-}$ mice and three WT control. (**E**) Relative expression levels of LINE1 RNA in the total RNA isolated from the GV oocytes of WT, *Fto*$^{+/-}$, and *Fto*$^{-/-}$ mice measured by RT-qPCR. (**F**) Left: more globally closed

(**Figure 3.19, continued**) chromatin based on the DNase I – TUNEL assay followed by fluorescence imaging was observed for oocytes of *Fto*$^{-/-}$ mice compared to WT. Scale bars, 20 μm; right: boxplot showing relative intensities quantified by using ImageJ. *p* values were determined using a two-tailed *t*-test in (C) to (F); *n.s.* means not significant. Representative images were selected from three independent experiments in (D) and (F).

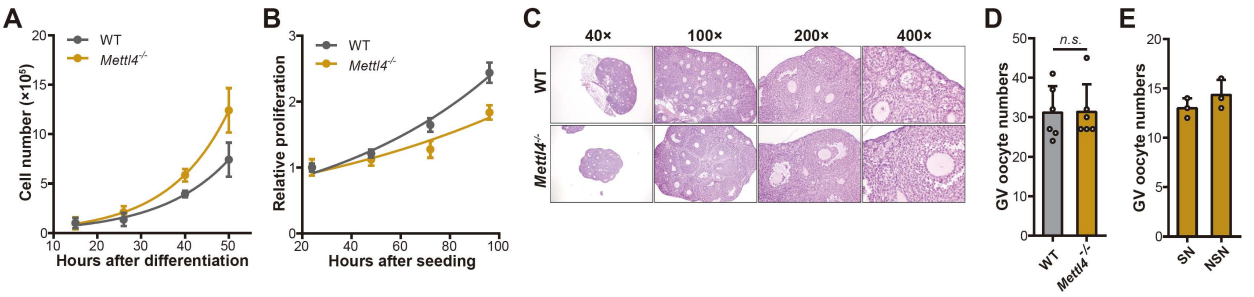

Figure 3.20 snRNA m^{6}A$_m$ is not a functionally relevant substrate of FTO in mESCs and oocyte development

(**A**) mEB formation capacity represented by cell proliferation upon induction of differentiation for *Mettl4*$^{-/-}$ mESCs compared to WT mESCs. (**B**) Proliferation of *Mettl4*$^{-/-}$ mESCs compared to WT mESCs. (**C**) HE staining of the ovaries from 3-week-old WT and *Mettl4*$^{-/-}$ mice. No obvious defects can be observed upon *Mettl4* KO. (**D**) Comparable numbers of GV oocytes were collected from six 9-week-old *Mettl4*$^{-/-}$ mice and WT control. (**E**) Comparable numbers of SN and NSN GV oocytes were collected from three 9-week-old *Mettl4*$^{-/-}$ mice. The SN/NSN ratio is similar to normal WT mice at this age. *p* values were determined using a two-tailed *t*-test in (D) and (E); *n.s.* means not significant.

3.3 Conclusion and discussion

In summary, this study addresses the question of the presence and functional relevance of RNA m^{6}A demethylation in mammals. We discovered that FTO mediates m^{6}A demethylation of carRNAs and positively impacts their abundance in mESCs (**Figure 3.2&3.3)**. Among carRNAs, we revealed that repeat RNAs, especially LINE1 RNA, were the primary substrates of FTO in mESCs (**Figure 3.5&3.6)**. We validated the binding and m^{6}A demethylation of LINE1 RNA by FTO, and observed decreased total LINE1 RNA level upon depletion or inhibition of FTO (**Figure 3.7)**. Our analysis revealed the correlations of m^{6}A level and transcript abundance changes of carRNAs between *Fto* KO and either *Mettl3* KO or *Ythdc1* CKO mESCs (**Figure 3.8&3.9)**. Functionally, we demonstrated that *Fto* KO led to induced differentiation and defected

proliferation for mESCs, which can be recapitulated by knockdown of LINE1 RNA using ASOs in WT mESCs and partially rescued by targeted demethylation of m^6A on LINE1 RNA using dCas13b-*wt*FTO (**Figure 3.10)**, directly supporting the functional relevance of FTO-mediated LINE1 RNA m^6A demethylation in mESCs.

We further showed that *Fto* depletion in mESCs led to reduced chromatin accessibility and suppressed transcription, revealed the genomic features of *Fto* KO-induced gained-closed regions, and established a causal relationship between the FTO-mediated LINE1 RNA m^6A demethylation and chromatin state regulation (**Figure 3.11**-**3.15)**. Moreover, our analysis further showed that the m^6A level of LINE1 RNA negatively correlated with FTO expression, and accordingly the LINE1 RNA abundance positively correlated with FTO expression across mouse and human tissues (**Figure 3.16)**. In contrast, ALKBH5, another RNA m^6A demethylase, did not show any correlations with the m^6A level or transcript level of LINE1 RNA (**Figure 3.17)**, suggesting the demethylation specificity of FTO towards LINE1 RNA m^6A. These results may also offer an explanation of a slight positive correlation observed between mRNA m^6A and FTO expression across both mouse and human tissues[157]. Higher FTO expression will lead to higher LINE1 RNA level and potentially more open chromatin. The more open chromatin could enable better access of METTL3 to its mRNA substrates and thus more mRNA m^6A methylation in certain tissues. This hypothesis could be tested with kinetic studies of time-course FTO inhibition or controllable FTO expression in the future.

Our investigations of mouse cerebellum and mNSCs from WT and *Fto* KO mice confirmed increased LINE1 RNA m^6A and reduced LINE1 RNA level in *Fto* KO samples compared with WT controls. In mNSCs we further showed chromatin state changes induced by *Fto* depletion and the role of FTO-mediated LINE1 RNA m^6A demethylation during mNSC differentiation (**Figure**

3.18). Lastly, we demonstrated the FTO-mediated LINE1 RNA m^6A demethylation in the mouse oocyte and reveals a critical role of this process during oocyte development as an *in vivo* model (**Figure 3.19)**, in which we excluded demethylation of snRNA m^6A_m as a key contributing factor (**Figure 3.20)**. Together, our results suggest broad roles of LINE1 RNA demethylation in mammalian tissues and during development. The important roles of LINE1 RNA and other repeat RNAs during development and in specific mammalian tissues have been increasingly noticed in recent years. Its demethylation by FTO presents a new pathway and a new layer of regulation that may broadly affect diverse biological processes.

3.4 Methods

3.4.1 Cell culture and tissues

shNC and shFTO Mel624 cell lines were obtained from Dr. Yu-Ying He as previously reported[55]. WT mESCs (mouse embryonic stem cells), *Fto*$^{-/-}$ mESCs, WT mNSCs (mouse neural stem cells), and *Fto*$^{-/-}$ mNSCs cell lines were obtained from the laboratory of Dr. Yawei Gao. Mel624 cells were maintained in DMEM (Gibco) with 10% fetal bovine serum (FBS, Gibco), 0.5 ug/mL puromycin (Gibco) and 1× Pen/Strep (Gibco) at 37 °C with 5% CO_2. mESCs were maintained in DMEM (Invitrogen) supplemented with 15% FBS (GeminiBio), 1% nucleosides (100×) (Millipore), 1 mM L-glutamine (Gibco), 1% nonessential amino acid (Gibco), 0.1 mM 2-mercaptoethanol (Sigma), 1,000 U/ml LIF (Millipore), 3 μM CHIR99021 (Stemcell) and 1 μM PD0325901 (Stemcell) in 37 °C and 5% CO_2. mNSCs were derived from neonatal mice, digested by Accutase (Sigma) and cultured in NSC expansion medium [DMEM/F12 supplemented with 1% N2 (Invitrogen) and 2% B27 (Invitrogen), 20 ng/mL basic fibroblast growth factor (bFGF; R&D Systems) and 10 ng/mL epidermal growth factor (EGF; Peprotech)]. Wild-type and *Fto*$^{-/-}$ mouse tissues were obtained from the laboratory of Dr. Yawei Gao.

3.4.2 Cell fractionation

Fractionation of mESCs or Mel624 cells was performed following the published protocol[170] with the optimized concentration of NP40 (Sigma) for each cell line. In brief, 5×10^6 to 10^7 cells were harvested and washed with 1 mL cold PBS/1 mM EDTA buffer, then centrifuged at 4 °C with 500 g to collect the cell pellet. 200 μL ice-cold lysis buffer (10 mM Tris-HCl, pH = 7.5, 0.05% NP40, 150 mM NaCl) were added to the cell pellet and incubated on ice for 5 min, then gently pipetted up the cell lysate over 2.5 volumes of chilled sucrose cushion (24% RNase-free sucrose in lysis buffer) and centrifuged at 4 °C with 15,000 g for 10 min. All the supernatant was collected as the cytoplasmic fraction and the nuclei pellet was washed once by gently adding 200 μL ice-cold PBS/1mM EDTA to the nuclei pellet without dislodging the pellet. The nuclei pellet was resuspended in 200 μL prechilled glycerol buffer (20 mM Tris-HCl, pH = 7.9, 75 mM NaCl, 0.5 mM EDTA, 0.85 mM DTT, 0.125 mM PMSF, 50% glycerol) with gentle flicking of the tube. Then equal volume of cold nuclei lysis buffer (10 mM HEPES, pH = 7.6, 1 mM DTT, 7.5 mM $MgCl_2$, 0.2 mM EDTA, 0.3 M NaCl, 1 M UREA, 1% NP-40) was added, followed by vigorous vortexing for 5 seconds twice. The nuclei pellet mixtures were incubated for 2 min on ice, then centrifuged at 4 °C with 15,000 g for 2 min. The supernatant was collected as the soluble nuclear fraction (nucleoplasm). The pellet was gently rinsed with cold PBS/1 mM EDTA without dislodging and then collected as the chromosome-associated fraction.

3.4.3 RNA purification

Total RNA was purified with TRIzol reagents (Thermo Scientific) and the rRNA was removed using RiboMinus Eukaryote kit (Thermo Scientific). Total RNA samples used for RT-qPCR were isolated by using the RNeasy kit (Qiagen) with an additional on-column DNase digestion step. Polyadenylated RNA was purified from total RNA with two rounds of polyA tail

purification using Dynabeads® mRNA DIRECT™ kit (Thermo Scientific). RNA concentration was measured by NanoDrop 8000 Spectrophotometer (Thermo Scientific).

3.4.4 Quantitative analysis of m^{6}A levels *via* UHPLC-MS/MS

50 ng non-ribosomal RNA from cell fractionation or polyadenylated RNA was digested by nuclease P1 (Sigma), respectively, in 20 μl of buffer containing 25 mM NaCl and 2.5 mM $ZnCl_2$ for 1 h at 42 °C. Subsequently, 1 unit of FastAP (Thermo Scientific) in 10× FastAP buffer was added, and the sample was incubated for 4 h at 37 °C. The samples were then filtered (0.22 μm, Millipore) and injected into a C18 reverse-phase column coupled online to Agilent 6460 LC-MS/MS spectrometer in positive electrospray ionization mode. The nucleosides were quantified by using retention time and the nucleoside to base ion mass transitions (268 to 136 for A; 282 to 150 for m^{6}A. Quantification was performed by comparing with the standard curve obtained from pure nucleoside standards running with the same batch of samples. The m^{6}A level was calculated as the ratio of m^{6}A to A.

3.4.5 Chromosome-associated RNA (caRNA) m^{6}A-Seq

1 μL 1:1000 diluted m^{6}A spike-in from EpiMark *N*^{6}-Methyladenosine Enrichment Kit (NEB) was added to 1 μg non-ribosomal total RNA isolated from chromatin-associated fraction. RNA was adjusted to 10 ng/μl in 100 μl and fragmented using a BioRuptor ultrasonicator (Diagenode) with 30 s on/off for 30 cycles. 5% of the fragmented RNA was saved as input. m^{6}A-IP was performed using EpiMark *N*^{6}-Methyladenosine Enrichment Kit (NEB) following the manufacturer's protocols. Library preparation was performed by using SMARTer Stranded Total RNA-Seq Kit v2 - Pico Input Mammalian (TaKaRa) following the manufacturer's protocols.

Sequencing was carried out at the University of Chicago Genomics Facility on an Illumina NovaSeq machine in pair-end mode with 100 base pair (bp) per read.

3.4.6 DNase I-TUNEL assay

mESCs, mNSCs, or Mel624 cells were resuspended and transferred to Nunc Lab-Tek II Chamber Slide (8-well, Thermo Scientific) 16 h prior to treatment. The DNase I-TUNEL assay was performed by using DeadEnd Fluorometric TUNEL System (Promega) following the manufacturer's protocols. Cells were treated with 1 u/mL of DNase I (Thermo Scientific) for 5 min at 37 °C before rTdT labeling. Cell nucleus was stained with DAPI (Sigma). ProLong Diamond Antifade Mountant (Invitrogen) was added before fluorescence imaging capture. Images were captured with Olympus FV1000 confocal or Leica SP8 Laser Scanning confocal, and the intensity of nuclear TUNEL signal was quantified using Fiji (ImageJ) software. Flow cytometry was performed on a BD Fortessa (BD), and data were analyzed using Flowjo (Treestar).

3.4.7 Nascent RNA labeling assay

mESCs, mNSCs, or Mel624 cells were resuspended and transferred to Nunc Lab-Tek II Chamber Slide (8-well, Thermo Scientific) 16 h prior to treatment. The nascent RNA synthesis assay was performed by using Click-It RNA Imaging Kits (Invitrogen) following the manufacturer's protocols. Cell nucleus was stained with DAPI (Sigma). ProLong Diamond Antifade Mountant (Invitrogen) was added before fluorescence imaging capture. Images were captured with Olympus FV1000 confocal and the intensity of EU signal was quantified using ImageJ (Fiji) software.

3.4.8 ATAC-Seq

ATAC-seq for mESCs cells was performed following the published protocols[161,162]. In brief, 5 × 10^6 cells were harvested and washed once with PBS buffer. The cell pellet was resuspended in 50 μL of cold lysis buffer and centrifuged at 4 °C with 500 g. Then the transposition reaction and purification were conducted. The transposed DNA fragments were amplified through PCR. Library preparation was performed by using Nextera DNA Flex Library Prep Kit following the manufacturer's protocols. Sequencing was carried out at the University of Chicago Genomics Facility on an Illumina HiSeq 2000 machine in single-end read mode with 50 bp reads per read.

3.4.9 mRNA m^{6}A-Seq

1 ug polyadenylated RNA was adjusted to 10 ng/μl in 100 μl and fragmented using a BioRuptor ultrasonicator (Diagenode) with 30 s on/off for 30 cycles. 5% of the fragmented RNA was saved as input. m^{6}A-IP was performed using EpiMark *N*^{6}-Methyladenosine Enrichment Kit (NEB) following the manufacturer's protocols. Library preparation was performed by using TruSeq Stranded mRNA Library Prep Kit (Illumina) following the manufacturer's protocols. Sequencing was carried out at the University of Chicago Genomics Facility on an Illumina HiSeq 2000 machine in single-end read mode with 50 bp reads per read.

3.4.10 ChIP-seq for histone modification

Mel624 cells were cross-linked by adding 1% formaldehyde directly to the media for 10 min at RT. Cross-linking was stopped by adding glycine to a final concentration of 0.125 M and incubating for 5 min at RT. The media was removed and the cells were washed twice with ice-cold PBS. Chromatin immunoprecipitation was performed using the iDeal ChIP-seq kit for Histone (Diagenode) following the manufacturer's protocols. Library preparation was performed by using

NEBNext® Ultra™ II DNA Library Prep Kit for Illumina (NEB) following the manufacturer's protocols. Sequencing was carried out at the University of Chicago Genomics Facility on an Illumina HiSeq 4000 machine in pair-read mode with 50 bp per read.

3.4.11 LINE1 FISH

LINE1 RNA FISH was performed according to the manufacturer's standard protocol (Biosearch Technologies). Cells were cultured on 10 mm #1.5 cover glass. Fixation was performed in 4% paraformaldehyede (PFA) for 10 min, followed by permeabilization for 20 min in 0.5% Triton dissolved in PBS. Samples were washed by Stellaris® RNA FISH Wash Buffer A with 10% Formamide, and blocked by 1 μg/ul yeast tRNA (Thermo Scientific) at 37 °C for 2 h. Probes targeting LINE1 RNA were diluted in Stellaris® RNA FISH Hybridization Buffer with 10% Formamide at 1:100 dilution to a final concentration of 12.5 nM. Hybridization was performed in a humid environment at 37 °C for 16 h. Samples were washed by RNA FISH Wash Buffer A and stained with DAPI. FISH co-staining with FTO immunofluorescence was performed following the manufacturer's standard protocol (Biosearch Technologies). After the hybridization of FISH probes, samples were equilibrated by PBS and blocked by blocking buffer (2% BSA, 0.05% Triton, 0.2 U/ul SUPERase•In™ RNase Inhibitor in PBS) for 1 h. FTO antibody (Abcam) at 1:100 dilution in blocking buffer were incubated for 1 h at room temperature. Samples were washed by blocking buffer and stained by Alexa 488 conjugated 2nd antibody (Invitrogen) for 1 h. Then samples were stained by DAPI and fixed again by 4% PFA for 10 min.

3.4.12 LINE1 antisense oligo (ASO) knockdown

Published morpholino ASO targeting mouse LINE1 was used for LINE1 knockdown, with its reverse complement (RC) as control[159]. Morpholino ASO targeting ORF2 of human LINE1 was

designed with software available at GENE Tools LLC. Morpholino ASO was ligated with FITC for the detection of nucleofection. Nucleofection of mESCs and Mel624 cells was performed on Amaxa™ 4D-Nucleofector (Lonza) by using P3 Primary Cell 4D-Nucleofector™ X Kit (Lonza) and SF Cell Line 4D-Nucleofector X Kit (Lonza), respectively, following the manufacturer's standard protocol. 5×10^6 cells were used for nucleofection with 5 nmol of ASO in a 100 ul system.

3.4.13 dCas13b plasmid transfection

Cells were resuspended 16 h prior to the transfection and maintained at around 80% confluency for plasmid transfection. Transfection was achieved by using Lipofectamine 3000 Transfection Reagent (Invitrogen) for dCas13b plasmids following the manufacturer's protocols and the published protocol[171].

3.4.14 EB differentiation

mESCs were trypsinized and a total of 10^5 cells per well were cultured in ultra-low cluster plates (Costar) in DMEM (Gibco) supplemented with 15% FBS (Gibco), 1mM L-glutamine (Gibco), 0.1 mM mercaptoethanol (Sigma), 1% nonessential amino acid (Gibco). EBs were collected and counted every 48 h after seeded until six days. Total RNA of EBs was extracted and analyzed for LINE1 RNA and the marker genes using RT-qPCR.

3.4.15 Cell proliferation assay

5000 cells were seeded per well in a 96-well plate. The cell proliferation was measured by assaying cells at various time points using the CellTiter 96® Aqueous One Solution Cell Proliferation Assay (Promega) following the manufacturer's protocols.

3.4.16 RT-qPCR

Total RNA or purified non-ribosomal RNA was reverse transcribed by using Maxima™ H Minus cDNA Synthesis Master Mix (Thermo Scientific). RT-qPCR was performed by using FastStart Essential DNA Green Master (Roche). m^6A and non-m^6A spike-in from EpiMark N^6-Methyladenosine Enrichment Kit were used as the control for m^6A level analysis in MeRIP-RT-qPCR. Actb was used as the control for expression level analysis in RT-qPCR. Relative changes in expression were calculated using the ΔΔCt method.

3.4.17 Western blot

Protein samples were prepared from respective cells by lysis in RIPA buffer (Invitrogen) containing 1 × protease inhibitor cocktail (Roche). Protein concentration was measured by NanoDrop 8000 Spectrophotometer (Thermo Scientific). Lysates were boiled at 95 °C with 4 × loading buffer (Biorad) for 5 min. Denatured protein was loaded into 4-12% NuPAGE Bis-Tris gel and transferred to PVDF membranes (Life Technologies). Membranes were blocked in PBST with 5% milk for 30 min at RT, incubated in a diluted primary antibody solution at 4 °C overnight, washed and incubated in a dilution of secondary antibody conjugated to HRP for 1 h at RT. Protein bands were detected using SuperSignal West Dura Extended Duration Substrate kit (Thermo) on FluroChem R (Proteinsimple).

3.4.18 GV oocyte collection, DAPI staining, and RNA extraction

Germinal vesicle oocytes were obtained from female mice's ovaries 48 h after intraperitoneal injection of pregnant mare serum gonadotropin (PMSG). Adherent cumulus cells were removed by mouth pipette. Briefly, the collected oocytes were fixed with 4% paraformaldehyde for 1 h, and then permeabilized for 15 min with 0.5% Triton X-100 in 0.5%

PBS-BSA. After three times of washing, all samples were stained with DAPI (1 ug/ml) for 20 min. For RNA extraction, GV oocytes without cumulus cells were transferred to 500 ul Trizol Reagent and then mixed well with 100 ul chloroform added. The mixture was transferred Qiagen MaXtract High-Density tubes (129046). After centrifuge, the upper and aqueous phase was removed. RNA was precipitated by adding equal volume isopropanol and washing by 75% ethanol.

3.4.19 *In vivo* DNase I-TUNEL assay for GV oocytes

GV oocytes were washed twice with PBS. *In vivo* permeabilization was performed with 0.5% Triton X-100 in extraction buffer (50 mM NaCl, 3 mM $MgCl_2$, 0.5% Triton X-100 and 300 mM sucrose in 25 mM HEPES, pH 7.4) for 5 min on ice. GV oocytes were washed twice in extraction buffer without Triton X-100 and then moved into 1 U/ml DNase I in the same buffer for 5 min at 37 °C. 2 % PFA was used for 10 min at room temperature. DNase I assay was performed as described above. GV oocytes were manipulated using a mouse pipette and were reacted in a 96-well U-type plate and finally transferred to PBS drops covered by paraffin oil on a glass-bottom cell culture dish (NEST) for imaging with a ZEISS LSM 880 microscope.

3.4.20 caRNA m^{6}A-Seq data analysis

Raw reads were trimmed by Trimmomatics[152] to remove low-quality bases and adapters, then aligned to the mouse genome (mm10), together with spike-in genomes including unmodified control RNA and m^{6}A methylated control RNA (NEB) using HISAT (version 2.1.0)[172] with '--rna-strandness RF -k 5' parameters. Annotation file, version M20 in gtf format for mouse, were downloaded from GENCODE database (https://www.gencodegenes.org/). Mapped reads were separated by strands with SAMtools (version 1.9)[173] and m^{6}A peaks on each strand were called using MACS2[174] with the parameter '--nomodel' separately. Significant peaks with $q < 0.01$

identified by MACS2 were considered. Then, featureCounts[175] was used to calculate the number of reads on each peak. For each pair of samples, peaks with at least 5 reads in the input sample and also more reads in m^{6}A IP sample than Input were kept. Peaks identified in at least two biological replicates were merged using mergePeaks in Homer software and used in the following analysis.

3.4.21 Quantification of m^{6}A levels of carRNAs and ca-mRNAs

Chromatin-associated regulatory RNAs (carRNAs), including enhancer RNA (eRNA), promoter-associated RNA (paRNA), and repeat RNAs, were defined in the previous work[158]. Counts of reads were calculated by featureCounts[175] and then normalized to per million total aligned reads to calculate counts per million (CPM). carRNAs with at least 10 reads in more than two Input samples were kept for further analysis. The m^{6}A ratio of m^{6}A modified spike-in ($r_{spike-in}$) was calculated by (CPM_{IP} + 0.01)/(CPM_{Input} + 0.01). For each sample, the m^{6}A normalized factor (nf) was defined as $r_{spike-in}$ divided by the average value of $r_{spike-in}$ from WT samples. The whole m^{6}A level of each sample was represented by nf. For each carRNA and peak, the m^{6}A level was calculated as (CPM_{IP} + 0.01)/(CPM_{Input} + 0.01) * nf. The m^{6}A level of ca-mRNAs was also calculated from caRNA m^{6}A-Seq data.

3.4.22 Differential m^{6}A regions

The m^{6}A-labeled region (carRNA, ca-mRNA) was defined as the region with the mean m^{6}A level bigger than 2 in WT or *Fto* KO samples. Within these m^{6}A-labeled regions, the m^{6}A-hyper (log_2 fold change > 0.58) and m^{6}A-hypo regions (log_2 fold change < -0.58) were identified. The Pearson correlation coefficiency of m^{6}A level on m^{6}A labeled peaks was used to assess the reproducibility between the biological replicates.

3.4.23 *Mettl3* KO and *Ythdc1* CKO caRNA m^{6}A-Seq data analysis

Mettl3 KO and *Ythdc1* CKO chromatin-associated RNA m^{6}A-seq data was downloaded from NCBI's Gene Expression Omnibus (GEO) with GSE number GSE133600. Data analysis was conducted as described above.

3.4.24 Tissue specific total RNA m^{6}A-Seq data analysis

Tissue-specific total RNA m^{6}A-seq data were downloaded from Genome Sequence Archive (GSA) with CRA001315 for human tissues and cell lines and CRA001962 for mouse tissues. Data analysis was conducted as described above. Specifically, the m^{6}A value of LINE1 RNA was calculated as total CPM_{IP}/total CPM_{Input} of LINE1 family and the m^{6}A value of repeat RNAs was calculated as total CPM_{IP}/total CPM_{Input} of total repeats.

3.4.25 ATAC-Seq data analysis

Single-end sequencing reads were first trimmed by Trim_Galore to remove potential adaptor sequences and low-quality nucleotides. Clean reads were then aligned to reference genomes (mm9 and hg19 for mouse and human, respectively) by Bowtie2[176], with only uniquely mapped reads retained for downstream analysis. Reads aligned to mitochondria genome were removed, together with PCR duplicated reads. ATAC-seq peaks were identified by MACS2[174]. To identify differentially opened ATAC-seq peaks, all peaks were merged into a united peak set by Homer. Reads were counted on peaks by FeatureCounts[175], and DESeq2[177] was employed to perform statistical analysis. To identify differentially genomic regions, diffReps[178] was used with the default window size of 1 kb and step size of 100 bp. Functional enrichment analysis of differentially opened regions was performed by GREAT.

3.4.26 ChIP-Seq data analysis

Paired-end sequencing reads were first trimmed by Trim_Galore to remove potential adaptor sequences and low-quality nucleotides. Clean reads were then aligned to hg19 reference genomes by Bowtie2[176], with only uniquely mapped reads retained for downstream analysis. Normalization was performed by the deepTools package.

3.4.27 mRNA m^{6}A-Seq data analysis

Single-end sequencing reads were first trimmed by Trim_Galore to remove potential adaptor sequences and low-quality nucleotides. Clean reads were then aligned to reference genomes (mm9 for and hg19 for mouse and human, respectively) by Hisat[172], with only uniquely mapped reads retained for downstream analysis. ExomePeak package was used to identify m^{6}A peaks and differentially methylated m^{6}A peaks. Gene expression analysis was performed by Cuffnorm on all input samples with the default geometric library normalization method.

3.4.28 Antibodies

The antibodies used in this study are listed below: Rabbit monoclonal anti-FTO antibody (Abcam, ab126605); Mouse monoclonal anti-FTO antibody (Abcam, ab92821); Rabbit Polyclonal anti-H3K27Ac antibody (Abcam, ab4729); Rabbit polyclonal anti-H3K4Me1 antibody (Abcam, ab8895); Rabbit polyclonal anti-H3K4Me3 antibody (Abcam, ab8580); Mouse polyclonal anti-H3K27Me3 antibody (Abcam, ab8898); Rabbit monoclonal anti-Histone H3 antibody (Cell Signaling, 4499); Rabbit monoclonal anti-GAPDH antibody (Cell Signaling, 5174); Mouse monoclonal anti-U1 snRNP 70 antibody (Santa Cruz, sc-390988).

3.4.29 Data availability

Sequencing data have been deposited into the Gene Expression Omnibus (GEO) under the accession number GSE151704 and GSE151780. The analysis in **Figure 3.8&3.9** utilized data from GSE133600. The analysis in **Figure 3.13** utilized data from GSE140561, GSE28247, and ENCODE ChIP-Seq database. The analysis in **Figure 3.16&3.17** utilized data from CRA001315 and CRA001962. The analysis in **Figure 3.19** utilized data from GSE75738.

Chapter 4

Context-dependent Roles of FTO in Human Cancers

4.1 Introduction: FTO associates with human cancers

Extensive functional characterizations of FTO have been done in human cancer cells recently, in which FTO can localize to both cell cytoplasm and nucleus. In line with our conclusion in section **2.2.1.4**, FTO has been shown to mediate internal m^6A demethylation of key transcripts that contribute to cancer progression[56-62]. As we showed in section **2.2.1.3**, up to 40% of total m^6A in polyadenylated RNA can be reversed by FTO in certain leukemia cells, in which FTO can be extensively expressed in the cytoplasm to demethylate cytoplasmic m^6A in polyadenylated RNA, linking the oncogenic role of FTO to its cytoplasmic m^6A demethylation activity[60,63]. As the first identified m^6A demethylase, FTO has been an attractive target for inhibitor development against m^6A pathways in disease treatment[179]. Small molecule inhibitors have been developed to target the demethylation activity of FTO to potentially treat AML[61,62]. FTO overexpression in leukemia cells has been shown to lead to increased tolerance of tyrosine kinase inhibitor (TKI) therapy[48]. These results shed light on overcoming the therapy resistance by modulating the FTO-mediated mRNA m^6A demethylation pathways.

In collaboration with Professor Yu-Ying He from the Department of Medicine, we identified the function and underlying mechanism of FTO in promoting melanoma tumorigenesis and resistance to immunotherapy. We also investigated the role of FTO in arsenic-induced skin tumorigenesis and the pathways involved in FTO degradation. In this chapter, I present two collaborative projects to demonstrate the biological significance of FTO-mediated m^6A demethylation in melanoma and arsenic tumorigenicity. Functionally, these two studies could

potentially help the development of new mechanism-based prevention and therapy by targeting FTO; in mechanistic perspective, we provided novel examples revealing a differential mechanism involved in FTO-mediated chromatin regulation in cancer cells compared to stem cells, and the autophagy-mediated expression regulation of FTO in response to the stress, adding a new layer to the context-dependent regulation of RNA demethylation.

4.2 Results

4.2.1 FTO regulates melanoma tumorigenicity and its response to immunotherapy

4.2.1.1 FTO is a pro-tumorigenic factor in melanoma

Melanoma is one of the deadliest and therapy-resistant cancers[180]. To determine the role of FTO in human melanoma, we analyzed FTO protein levels in the melanocytes of normal human skin and malignant melanoma samples. We found that FTO expression was low in epidermal melanocytes in normal skin but significantly increased across diagnoses of melanoma (**Figure 4.1A&B**). We then examined the FTO protein levels in normal human epidermal melanocytes (NHEM) and a panel of melanoma cell lines. Except for WM35 (BRAF mutation, Human) cells, we observed upregulation of FTO in six of the tested cell lines, particularly in Mel624 (BRAF mutation, Human) and B16F10 (BRAF wild-type, Mouse) cells, two aggressive model melanoma cell lines, as well as WM115 (BRAF mutation, Human), WM793 (BRAF mutation, Human), WM3670 (BRAF and NRAS mutation, Human), and CHL-1 (BRAF and NRAS wild-type, Human) (**Figure 4.1C**). These results suggest that FTO plays a pro-tumorigenic role in melanoma development.

To determine the biological function of FTO in melanoma cells, we performed both gain- and loss-of-function studies in melanoma cells. Knockdown of FTO in FTO-high Mel624 cells led to decreased cell growth/proliferation, migration, invasion, and cell viability, while overexpression

of FTO in WM35 (with a low FTO protein level similar to NHEM) displayed markedly opposite patterns (**Figure 4.1D-H**). To elucidate the role of FTO in melanoma pathogenesis *in vivo*, we performed xenograft and syngeneic melanoma tumorigenesis assays. FTO knockdown markedly reduced tumor growth and tumor volume of Mel624 cells, whereas forced overexpression of FTO in WM35 induced tumor growth (**Figure 4.1I&J**). These findings suggest that FTO is critical to malignant traits of melanoma cells *in vitro*, and plays an oncogenic role in melanoma tumor growth *in vivo*.

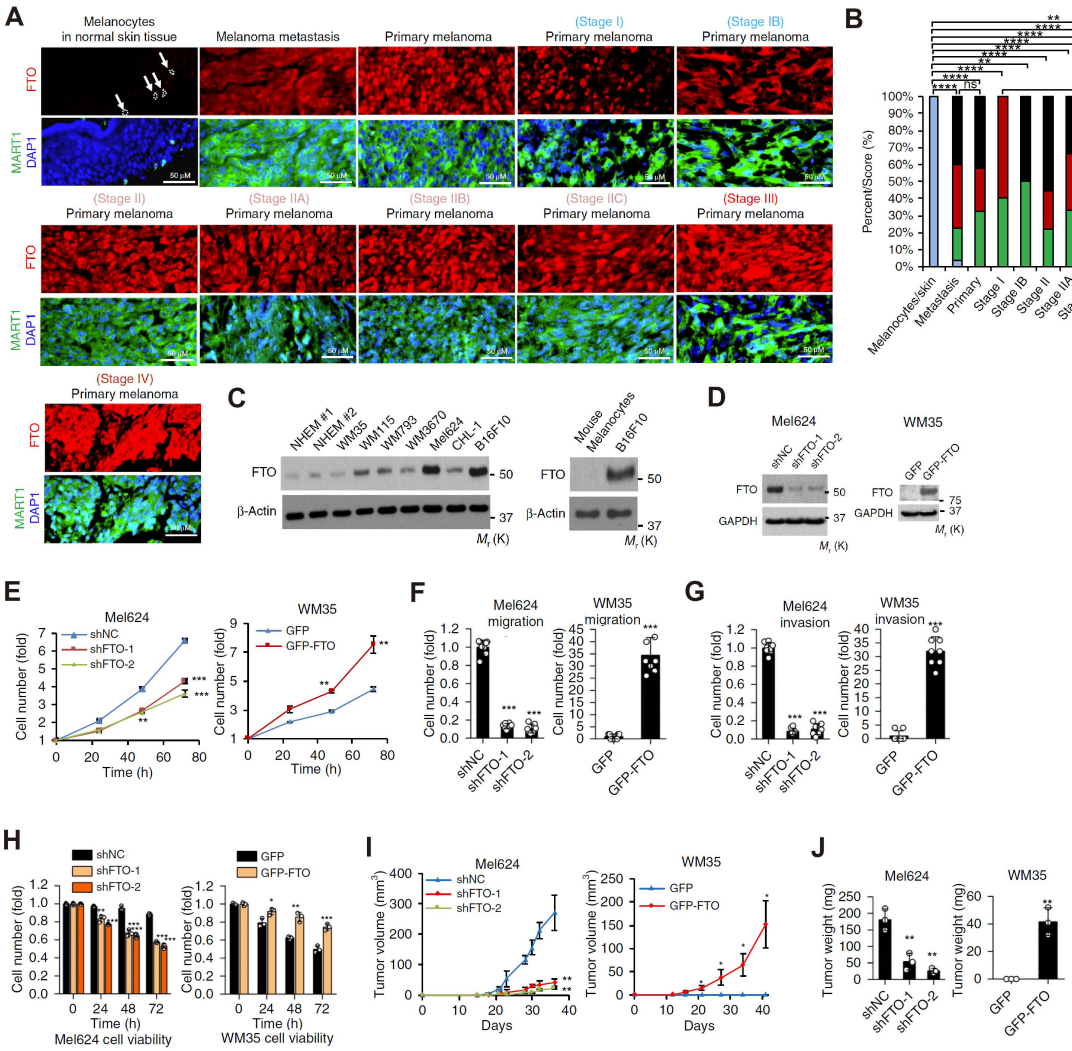

Figure 4.1 FTO is upregulated in melanoma and associated with melanoma tumorigenicity (**A**) Immunofluorescence staining of FTO (red) and MART1 (green, used to specifically identify melanocytes in normal skin and melanoma cells) in normal human skin and melanoma tissues. Nuclei are counterstained with DAPI in blue. Scale bar, 50 μm. The arrows indicate representative

(**Figure 4.1, continued**) melanocytes in the normal human epidermis. $n = 16$, epidermal melanocytes in normal skin; $n = 64$, metastasis; $n = 36$, primary melanoma; and $n = 65$, melanoma at stages I–IV. (**B**) Percentage of tumors (in stacked column format) for each score of FTO. 0 (Negative), 1 (Weak), 2 (Medium), and 3 (Strong); *p* values were determined using Mann–Whitney *U*-test. $*p < 0.05$, $**p < 0.01$, $***p < 0.001$, $****p < 0.0001$. *n.s.* means not significant. (**C**) Immunoblot analysis of the protein levels of FTO and β-actin as a loading control in normal melanocytes and melanoma cells. (**D**) Immunoblot showing the validation of FTO knockdown in Mel624 cells and FTO overexpression in WM35 cells. (**E**) to (**J**) Experiments in Mel624 cells with shNC (negative control knockdown) and shFTO (FTO knockdown), or in WM35 cells with GFP (control vector overexpression) and GFP-FTO (FTO overexpression). (E) Cell proliferation assay. (F) Cell migration assay. (G) Cell invasion assay. (H) Cell viability assay of cells in suspension. (I) Average tumor volume (mm^3) at different days after subcutaneous injection in the immune-compromised nude mice ($n = 3$). (J) Final tumor weight ($n = 3$). *p* values were determined using Student's *t*-test; $*p < 0.05$, $**p < 0.01$, $***p < 0.001$. Error bars, mean ± s.d. for $n \geq 3$ experiments in (F) to (J) unless indicated otherwise.

4.2.1.2 FTO regulates melanoma tumorgenicity through mRNA m^6A demethylation

To examine the role of FTO in m^6A regulation, we investigated the effect of FTO knockdown on m^6A levels in mRNA and found that FTO knockdown led to increased m^6A levels in purified mRNA from both Mel624 and B16F10 cells (**Figure 4.2A**).

We utilized both candidate and unbiased screening approaches to determine the potential mRNA targets of FTO in its melanoma-promoting function (**Figure 4.2B**). Starting with a candidate approach, we focused on the genes that are known to be associated with melanoma growth and in particular response to immunotherapy, including known melanoma-promoting genes PD-1 (PDCD1), PD-L1 (CD274), and CD47 (**Figure 4.2C**). FTO knockdown significantly decreased PD-1 expression, but had minimal effect on PD-L1 or CD47. Next, we employed microarray analysis to compare the gene expression in Mel624 cells with or without FTO knockdown and identified 106 genes that were significantly altered by FTO knockdown.

To probe whether the differential expressed genes were subjected to FTO-mediated m^6A demethylation, we performed MeRIP-Seq and analyzed the m^6A profile in control and FTO knockdown Mel624 cells. The GGACU motif was identified to be highly enriched within m^6A

sites in Mel624 cells (**Figure 4.2D**). FTO knockdown led to elevated m^6A distribution in both 5' UTR and 3' UTR with negligible effect on the coding region sequence (CDS) region (**Figure 4.2E**), which is consistent with the altered peak distribution (**Figure 4.2F**). FTO knockdown cells also showed an increased number of m^6A methylated genes (**Figure 4.2G**). Through MeRIP-seq, we identified more than 1,000 potential transcriptome-wide m^6A-modified gene targets for FTO, including the melanoma-promoting genes CXCR4 and SOX10. However, PD-1 was undetectable in either microarray or RNA-seq analysis (**Figure 4.2H**), possibly due to the relatively low mRNA expression level.

Next, we validated a set of downregulated genes, including PD-1, CXCR4, SOX10, ANGPTL2, CTSV, FCMR, NOP16, and RAB40, as well as one upregulated gene p21 (CDKN1A), identified from the sequencing results upon FTO knockdown (**Figure 4.2I**). Consistently, m^6A MeRIP-RT-qPCR experiments validated the increased m^6A levels in the transcripts of PD-1, CXCR4, SOX10, CTSV, and NOP16 revealed by data analysis (**Figure 4.2J**), suggesting these genes as potential targets of FTO. Notably, we observed a reduced m^6A level in the transcript p21, which was opposite to the demethylation activity of FTO, indicating other mechanisms is involved.

Among the identified target genes, PD-1 has been shown to be expressed in some melanoma cells and act as an intrinsic pro-tumorigenic factor to promote melanoma tumor growth[181]. Since PD-1 has been successfully targeted in immune cells for cancer immunotherapy, understanding the regulation of PD-1 may have a broader impact on cancer biology and immunotherapy response in melanoma. In addition, transcripts of CXCR4 and SOX10, two targets revealed by MeRIP-Seq, are critical melanoma-promoting genes as well[182-184]. Therefore, we decided to focus our study on investigating the regulatory mechanism of PD-1, CXCR4, and SOX10 mRNA expression by FTO.

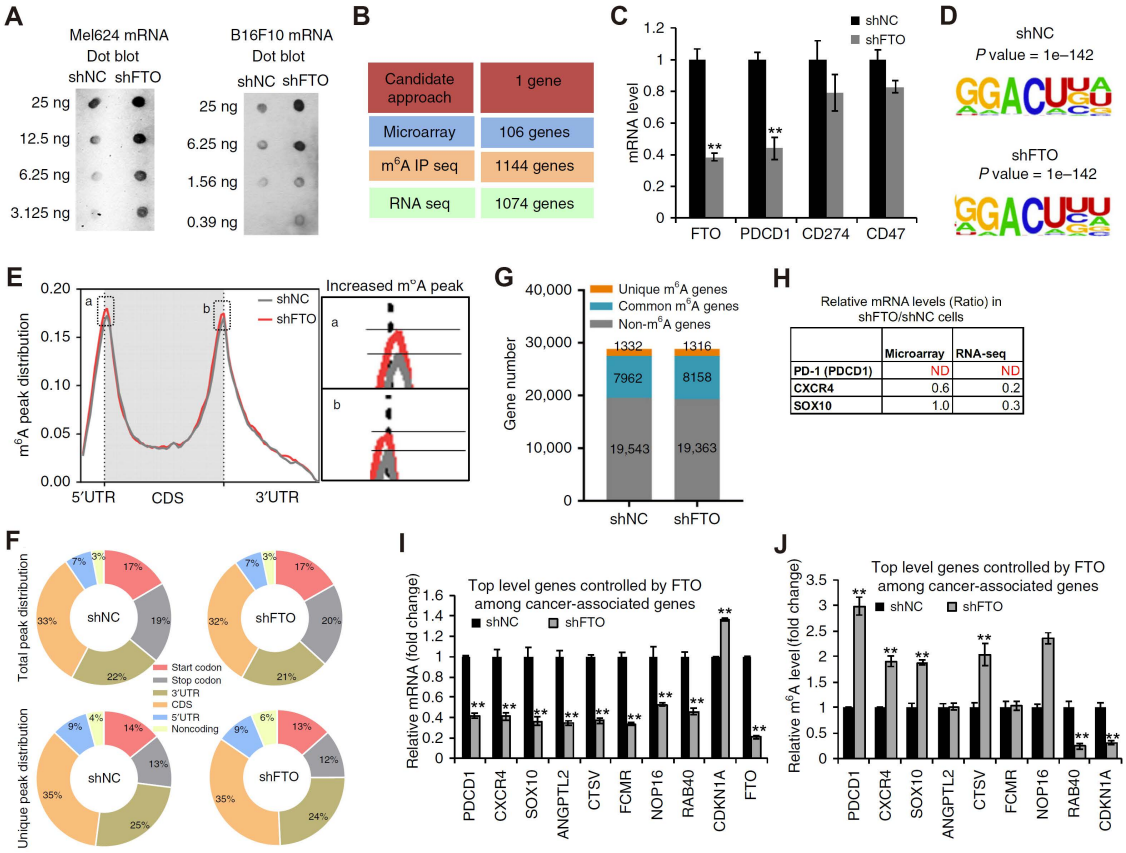

Figure 4.2 Identify potential targets of FTO from MeRIP-Seq

(**A**) m^{6}A dot blot assays using polyadenylated RNA of Mel624 and B16F10 cells with or without FTO knockdown. (**B**) Schematic summary for analysis of FTO target genes and the number of genes identified in each category. (**C**) Relative mRNA expression levels of FTO, PD-1, PD-L1, and CD47 in Mel624 cells with or without FTO knockdown. (**D**) Top consensus m^{6}A motif identified by HOMER with m^{6}A peaks in Mel624 cells with or without FTO knockdown. (**E**) Distribution of m^{6}A peaks across the length of mRNA. Region of 5' UTR was binned into 10 segments, CDS was binned into 50 segments, and 3' UTR was binned into 40 segments. The percentage of m^{6}A peaks that fall within each bin was determined. (**F**) The proportion of common m^{6}A peak distribution in the indicated regions across the entire set of mRNA transcripts (top) and the appearance of new m^{6}A peaks (unique peaks in shFTO), or loss of existing m^{6}A peaks (unique peaks in shNC) after FTO knockdown (bottom). (**G**) Number of m^{6}A-modified genes identified in m^{6}A-seq in shNC and shFTO Mel624 cells. (**H**) Ratio of gene expression in shFTO *vs* shNC Mel624 cells using microarray or RNA-seq analysis. ND, not detected. (**I**) RT-qPCR analysis showing mRNA levels of target genes in Mel624 cells with or without FTO knockdown. (**J**) Gene-specific m^{6}A MeRIP-RT-qPCR analysis of gene-specific m^{6}A enrichment in Mel624 cells with shNC or shFTO. *p* values were determined using Student's *t*-test; $*p < 0.05$, $**p < 0.01$. Error bars, mean ± s.d. for $n \geq 3$ experiments in (C), (I) and (J).

We noticed that FTO knockdown led to reduced, whereas FTO overexpression led to elevated protein levels of PD-1, CXCR4, and SOX10 (**Figure 4.3A**). Note that the overexpression

of demethylase-inactive mutants displayed negligible effects on mRNA and protein levels of these targets (**Figure 4.3B**), or melanoma cell proliferation (**Figure 4.3C**), indicating that FTO promotes the expression of melanoma-intrinsic PD-1, CXCR4, and SOX10 in an m^6A-dependent manner.

Next, we performed a series of rescue experiments to investigate whether these melanoma-promoting genes are responsible for FTO-mediated melanoma tumorgenicity. Overexpression of PD-1 in FTO knockdown cells could rescue the decreased cell proliferation and migration (**Figure 4.3D**). Accordingly, overexpression of CXCR4 (**Figure 4.3E**) and SOX10 (**Figure 4.3F**) in FTO knockdown cells also led to similar patterns. These results validate that PD-1, CXCR4, and SOX10 are critical downstream targets of FTO and responsible for its function in melanoma. Indeed, all melanoma cell lines showed increased protein levels and mRNA levels of PD-1 compared to normal melanocytes (**Figure 4.3G**).

To further determine whether the regulation of these melanoma-promoting genes by FTO is m^6A-dependent, we assessed the role of m^6A by knocking down the m^6A methyltransferase complex METTL3 and METTL14. Double knockdown of METTL3 and METTL14 in FTO knockdown cells can rescue the protein levels (**Figure 4.3H**) and mRNA levels (**Figure 4.3I**) of PD-1, CXCR4, and SOX10, respectively, to a level similar to that in the control cells.

The function of m^6A in regulating gene expression is executed mostly through the readers. Considering the upregulation of these target genes is associated with hypermethylation, we focused our study on YTHDF2, which can promote the degradation of m^6A methylated transcripts[66]. We found that YTHDF2 knockdown significantly increased the mRNA levels of all three genes while knockdown of YTHDF1 or YTHDF3 showed minimal effects (**Figure 4.4A**). Moreover, FTO knockdown led to decreased mRNA stability of PD-1, CXCR4, and SOX10, which can be rescued by YTHDF2 knockdown (**Figure 4.4B&C**). Accordingly, knockdown of YTHDF2 increased,

while overexpression of YTHDF2 decreased, cell proliferation and migration of melanoma cells *in vitro* (**Figure 4.4D**) as well as tumor growth *in vivo* (**Figure 4.4E&F**). These findings reveal that YTHDF2-mediated degradation of m^{6}A methylated RNA controls the expression of the FTO targeted genes in melanoma cells.

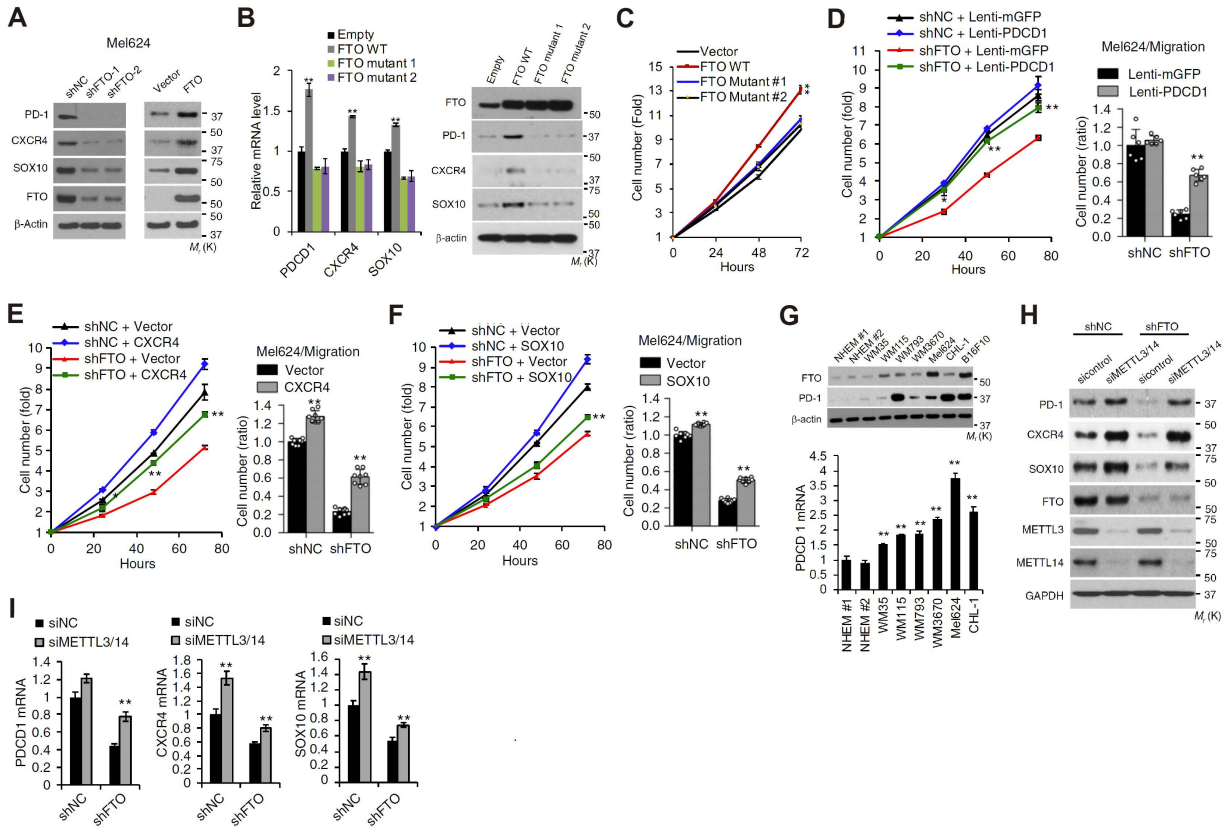

Figure 4.3 PD-1, CXCR4, and SOX10 are functionally relevant targets of FTO
(**A**) Immunoblot showing protein expression of PD-1, CXCR4, SOX10, and FTO, in Mel624 cells with stable knockdown (left) or overexpression of FTO (right) compared to the corresponding controls. (**B**) RT-qPCR (left) and immunoblot (right) showing RNA and protein expression of WT FTO, inactive mutant 1 (H231A/D233A), and inactive mutant 2 (R316Q/R322Q), as well as PDCD1, CXCR4, and SOX10, respectively, in Mel624 cells. (**C**) Cell proliferation assay upon overexpression of WT FTO or inactive mutants compared to control. (**D**) to (**F**) Cell proliferation assay (left) and cell migration assay (right) in control and FTO stable knockdown Mel624 cells. (D) with overexpression of PD-1 or control vector. (E) with overexpression of CXCR4 or control vector. (F) with overexpression of SOX10 or control vector. (**G**) Protein (top) and mRNA (bottom) expression levels of PD-1 in normal melanocytes and melanoma cells. (**H**) and (**I**) In control and FTO stable knockdown Mel624 cells with siRNA double knockdown of METTL3/14 or siRNA control. (H) Immunoblot analysis showing protein expression of PD-1, CXCR4, SOX10, FTO, METTL3, METTL14, and GAPDH. (I) RT-qPCR analysis showing mRNA levels of PD-1, CXCR4, and SOX10. *p* values were determined using Student's *t*-test; **p* < 0.05, ***p* < 0.01. Error bars, mean ± s.d. for $n \geq 3$ experiments in (B) to (I).

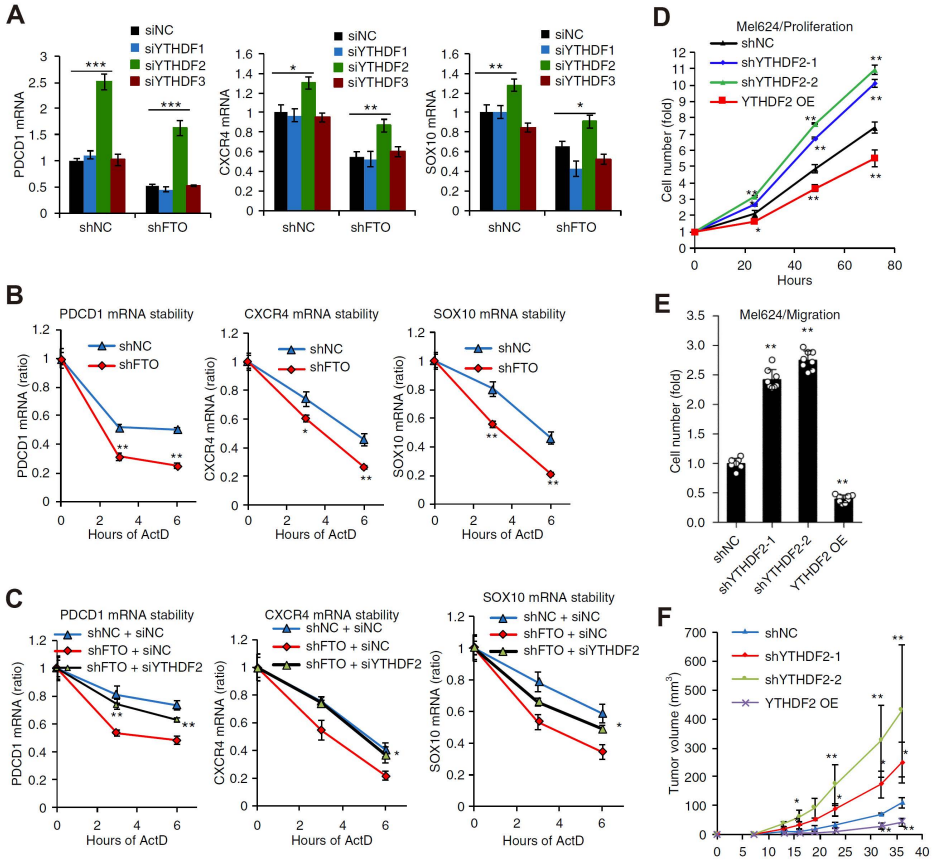

Figure 4.4 FTO regulates the expression of target genes through YTHDF2-mediated decay (**A**) RT-qPCR showing mRNA levels of PD-1, CXCR4, and SOX10 in control and FTO stable knockdown Mel624 cells with siRNA knockdown of YTHDF1-3 or siRNA control. (**B**) RT-qPCR after ActD treatment showing mRNA stability of PD-1, CXCR4, and SOX10 in control and FTO stable knockdown Mel624 cells. (**C**) RT-qPCR showing mRNA levels of PD-1, CXCR4, and SOX10 in control and FTO stable knockdown Mel624 cells with siRNA knockdown of YTHDF2 or control. (**D**) and (**E**) In control, YTHDF2 siRNA knockdown, and YTHDF2 overexpression Mel624 cells. (D) Cell proliferation assay. (E) Cell migration assay. (**F**) Tumor growth of Mel624 cells with or without knockdown, or overexpression of YTHDF2 after subcutaneous injection in nude mice ($n = 3$). p values were determined using Student's t-test; $*p < 0.05$, $**p < 0.01$, $***p < 0.001$. Error bars, mean ± s.d. for $n \geq 3$ experiments.

4.2.1.3 FTO is induced by metabolic stress and affects melanoma immunotherapy

We were intrigued by how FTO is upregulated in melanoma cells. We found that the metabolic stress conditions, especially starvation, led to both increased mRNA levels (**Figure 4.5A**) and protein levels (**Figure 4.5B**) of FTO and PD-1, which is associated with the elevated m^6A level in total RNA in Mel624 cells (**Figure 4.5C**). Since these conditions are also known to

induce autophagy (**Figure 4.5B**), we reasoned that FTO upregulation by metabolic stress was mediated through the autophagy pathway. Indeed, knockdown of the autophagy essential genes ATG5 or ATG7 can rescue the starvation-induced FTO and PD-1 mRNA expression, as well as NF-κB activity (**Figure 4.5D**). Moreover, we found that knockdown of the NF-κB subunit p65 (RELA) can markedly reduce the metabolic stress-induced FTO and PD-1 expression (**Figure 4.5E**). These results reveal that FTO and PD-1 are induced by metabolic stress through the autophagy and NF-κB pathways.

Lastly, we investigated whether FTO knockdown affects immunotherapy response of melanoma cells[185]. C57BL/6 mice bearing B10F10 melanomas were treated with anti-PD-1 antibody or isotype control IgG. Anti-PD-1 antibody had no effect on tumor growth of control B16F10 cells but significantly inhibited tumor growth of FTO knockdown tumors (**Figure 4.5F**). However, we failed to observe a similar outcome of FTO knockdown on severely combined immunodeficient (NOD/SCID) interleukin-2 receptor (IL-2R) gamma chain null NSG mice (**Figure 4.5F**). These findings indicate that FTO knockdown diminishes the resistance to PD-1 blockade in melanoma immunotherapy, and the effect of FTO knockdown on anti-PD-1 blockade is dependent on the immune system. Furthermore, we found that interferon-gamma (IFNγ) led to downregulated FTO protein level in a dose-dependent manner associated with increased m^6A levels in total RNA, but did not affect the protein levels of other m^6A effectors (**Figure 4.5G&H**). We also noticed that FTO knockdown sensitized melanoma cells to IFNγ-induced cell death, whereas overexpression of wild-type FTO but not inactive mutants led to suppressed IFNγ-induced melanoma cell death (**Figure 4.5I**). Moreover, we found that overexpression of PD-1, CXCR4, or SOX10 can inhibit IFNγ-induced cell death in FTO knockdown Mel624 cells (**Figure 4.5J**). Consistently, blocking IFNγ increased tumor growth of both control and B16F10 melanoma cells

with FTO knockdown in C57BL/6 mice (**Figure 4.5K**). These data reveal that FTO inhibition enables a response to anti-PD-1 blockade in melanoma *in vivo*, and to IFNγ-induced killing in melanoma cells *in vitro* through regulating melanoma cell-intrinsic PD-1, CXCR4, and SOX10.

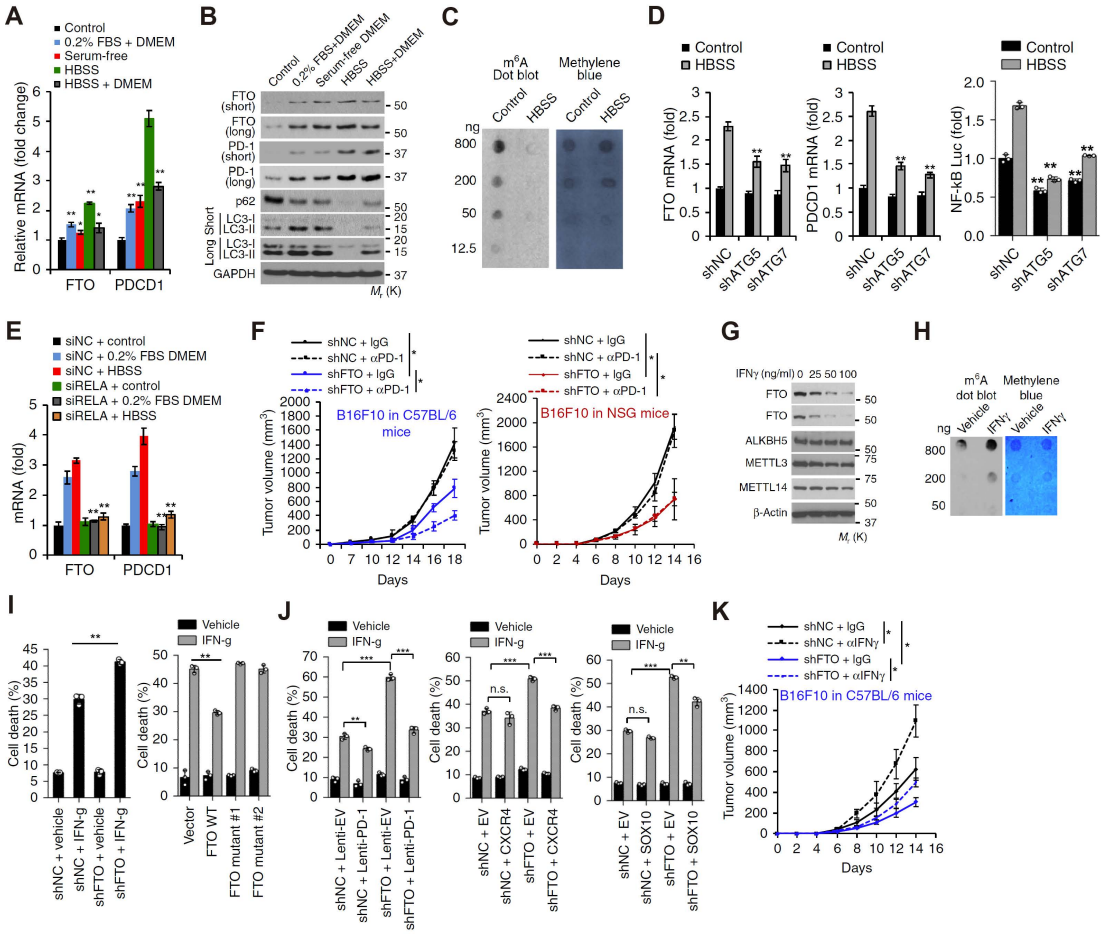

Figure 4.5 Metabolic stress-induced FTO regulates melanoma response to anti-PD-1 and IFNγ

(**A**) RT-qPCR showing mRNA levels of FTO and PD-1 in Mel624 cells cultured in control medium (10% FBS DMEM), 0.2% FBS DMEM, serum-free DMEM, Hanks' balanced salt solution containing calcium and magnesium (HBSS), or a combination of DMEM and HBSS. (**B**) Immunoblot analysis of FTO, PD-1, p62, and LC3-I/II (short and long exposure) in Mel624 cells cultured as in (A). (**C**) m^6A dot blot assays using total RNA in Mel624 cultured with control medium or HBSS. (**D**) RT-qPCR analysis showing mRNA levels of FTO, PD-1, and NF-κB in Mel624 cells cultured in control medium and HBSS with or without knockdown of ATG5 or ATG7. (**E**) qPCR analysis of FTO and PD-1 mRNA levels in Mel624 cells with or without knockdown of RELA and with or without metabolic stress. (**F**) Tumor growth kinetics of control and FTO knockdown B16F10 cells in C57BL/6 (left) or (right) NSG mice treated with anti-PD-1 or control IgG. (**G**) Immunoblot analysis of FTO, ALKBH5, METTL3, METTL14, and GAPDH in Mel624 cells with IFNγ treatment (100 ng/ml) or vehicle for 24 h. (**H**) m^6A dot blot assays using

(**Figure 4.5, continued**) total RNA of Mel624 cells treated as (G). (**I**) Apoptosis assay in Mel624 cells without IFNγ treatment (50 ng/ml) for 48 h. Left: with or without FTO knockdown; Right: overexpression of vector, WT FTO, or inactive mutants. (**J**) Treated with IFNγ (50 ng/ml) or vehicle for 48 h, apoptosis assay in control and FTO knockdown Mel624 cells overexpressing vector or PD-1, CXCR4, and SOX10. (**K**) Tumor growth of control and FTO knockdown B16F10 cells in C57BL/6 mice treated with the anti-IFNγ antibody or control IgG. *p* values were determined using Student's *t*-test; $*p < 0.05$, $**p < 0.01$. *n.s.* means not significant. Error bars, mean ± s.d. for $n \geq 3$ experiments unless indicated otherwise in (A), (D) to (F), and (I) to (K).

4.2.2 Context-dependent chromatin regulation by FTO in melanoma cells

4.2.2.1 FTO does not correlate with LINE1 RNA abundance across cancer cells

In chapter **3**, our results established FTO as a LINE1 RNA m^6A demethylase in mESCs, mNSCs, mouse cerebellum, and mouse oocytes, and suggested that FTO also mediated LINE1 RNA demethylation in many mouse and human tissues. Using mESCs as an example, we showed that the FTO-mediated LINE1 RNA m^6A demethylation can notably impact chromatin state and transcription, which may play broad regulatory roles in mammalian tissues as well as during development. In contrast to the positive correlations between FTO expression and mRNA m^6A across mouse and human tissues, FTO expression displayed an evidently negative correlation with mRNA m^6A across human cell lines (most of them are cancer cell lines)[157].

We reasoned that FTO may play different roles depending on cellular context. Indeed, we analyzed the published m^6A methylome datasets of selected human cell lines and observed a different pattern related to LINE1 RNA level and FTO expression. Despite that the m^6A level of LINE1 RNA negatively correlated with FTO expression across these cells (**Figure 4.6A**), the abundance of LINE1 RNA was not associated with FTO expression (**Figure 4.6B**). Furthermore, the m^6A levels of LINE1 RNA showed a negligible correlation with the expression levels of LINE1 RNA in these cancer cells (**Figure 4.6C**). These data suggest that although FTO may still act as an m^6A demethylase of LINE RNA, the m^6A demethylation may not noticeably affect LINE1 RNA abundance in these human cell lines.

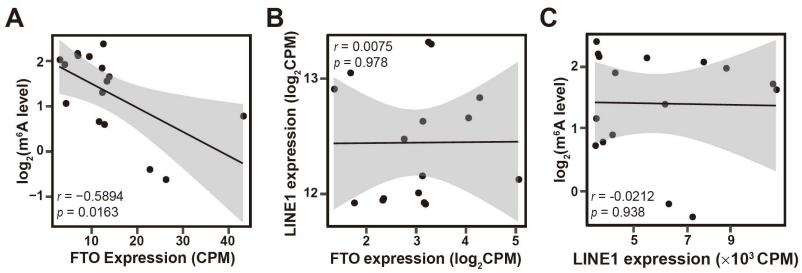

Figure 4.6 Correlations between FTO expression and LINE1 RNA across cancer cells
(**A**) to (**C**) The m^{6}A MeRIP-seq datasets from human cell lines (most are cancer cell lines), including HEK293T cells, GOS cells, HT29 cells, Jurkat cells, K562 cells, U2OS cells, U251 cells, and WPMY cells were analyzed. (A) A scatter plot showing a negative correlation between the m^{6}A level of LINE1 RNA and FTO expression. (B) A scatter plot showing a negligible correlation between the expression levels of LINE1 RNA and FTO. (C) A scatter plot showing a negligible correlation between the m^{6}A level and LINE1 RNA abundance.

4.2.2.2 Complexity in FTO-mediated regulation of melanoma tumorigenicity

As shown in the section **4.2.1**, in Mel624 cells, knockdown of FTO increased m^{6}A methylation in the critical pro-tumorigenic melanoma cell-intrinsic genes including PD-1, CXCR4, and SOX10, leading to increased RNA decay through the m^{6}A reader YTHDF2, thereby reducing the melanoma tumorigenicity and the resistance to anti-PD-1 blockade. However, we also observed the upregulation of several important tumor suppressors associated with minimal mRNA m^{6}A changes or even decreased mRNA m^{6}A upon FTO knockdown[186], including IL24, PTEN, and p21, suggesting the complexity in FTO-mediated regulation of melanoma tumorigenicity. Thus, we focused on the melanoma system to study the context-dependent role of FTO in chromatin regulation.

We first compared the m^{6}A changes of caRNA (rRNA depleted) and polyadenylated RNAs by UHPLC-MS/MS upon FTO knockdown in Mel624 cells. We observed increased m^{6}A levels in both caRNA and mRNA upon FTO depletion (**Figure 4.7A**). More m^{6}A increase was observed in mRNA because the absolute m^{6}A level (shown as m^{6}A/A ratio) in mRNA is ~4-fold higher than that in caRNA with rRNA depletion. We next measured the chromatin openness and nascent RNA synthesis in Mel624 cells. To our surprise, knockdown of FTO in Mel624 cells led to more open

chromatin and increased nascent RNA synthesis (**Figure 4.7B&C**), which were opposite to those observed in the stem cells.

To gain more details in the chromatin accessibility changes, we performed ATAC-seq in control and FTO-knockdown Mel624 cells. We observed markedly increased overall signal intensity (**Figure 4.7D**) and identified many more differentially increased ATAC-seq peaks (**Figure 4.7E**) upon FTO knockdown. Notably, gained-open regions defined by sliding windows are enriched with H3K27Ac binding sites in Mel624 cells, showing an increased H3K27Ac enrichment in these regions upon FTO knockdown (**Figure 4.7F**). This finding prompted us to examine histone modification changes upon FTO knockdown. Consistent with the increased H3K27Ac ChIP signals, upon FTO knockdown, Mel624 cells showed a clearly elevated level of the active histone mark H3K27Ac, but reduced repressive mark H3K27Me3 (**Figure 4.7G**).

To explore the role of LINE1 RNA in Mel624 cells, we measured LINE1 RNA abundance in total RNA and observed a negligible change upon FTO knockdown (**Figure 4.7H**), which again was distinct from that observed in the stem cells. Moreover, knockdown of LINE1 RNA in Mel624 cells led to only minimal changes of chromatin accessibility (**Figure 4.7I&J**), indicating minimal roles of LINE1 RNA in chromatin regulation in MEL624 cells.

Therefore, we sought to investigate whether FTO affects chromatin accessibility mainly through m^6A demethylation of the mRNAs encoding histone modifiers in this cancer cell line[166]. We analyzed the expression levels and m^6A levels of mRNA encoding histone modifiers for H3K27ac and H3K27Me3 in Mel624 cells. Upon FTO knockdown, we observed decreased expression of the transcript encoding the histone methyltransferase EZH2, while the expression of transcripts encoding histone acetyltransferase EP300 and histone demethylase KDM6B was increased (**Figure 4.7K**). We then evaluated the m^6A level changes of these mRNAs and found

that FTO knockdown led to increased m^{6}A levels for all three cases (**Figure 4.7L**). These data suggest that higher m^{6}A stabilizes EZH2 mRNA but destabilizes EP300 and KDM6B transcripts. We reason that the destabilization role of m^{6}A in EZH2 transcript is mediated through the decay pathway *via* YTHDF2[66], whereas the stabilization effect of m^{6}A on EP300 and KDM6B transcripts is likely endorsed by IGF2BPs[71]. Indeed, we confirmed the roles of the m^{6}A readers on these transcripts with mRNA half-life experiments measured by RT-qPCR (**Figure 4.7M**).

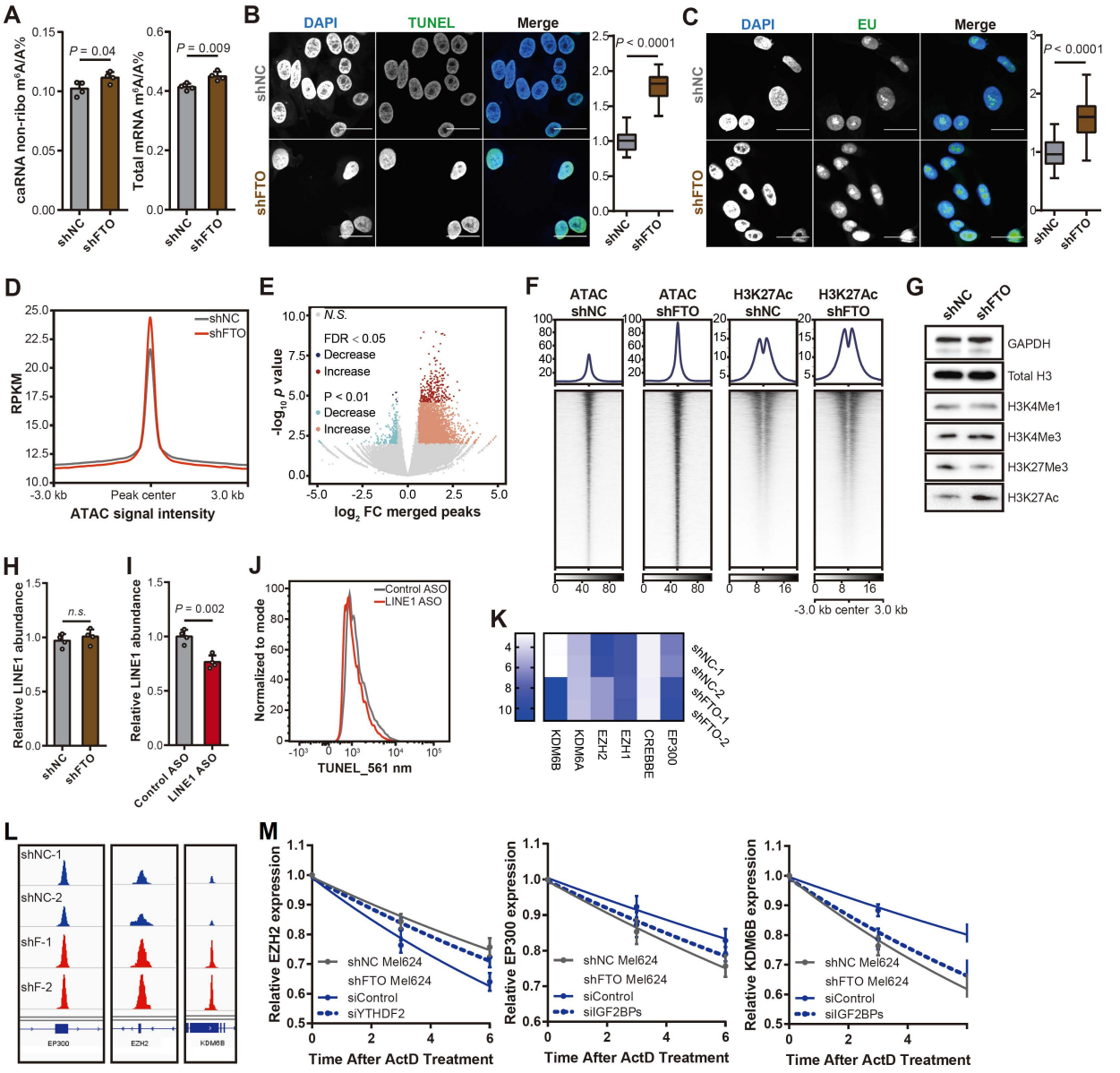

Figure 4.7 FTO mediates chromatin states through m^{6}A demethylation of mRNA encoding histone modifiers in melanoma cells

(**Figure 4.7, continued**) (**A**) m^6A/A ratios measured by UHPLC-MS/MS on caRNA after depletion of rRNA (left) and on total polyA-tailed RNA (right) in Mel624 cells with FTO knockdown compared to control. (**B**) Left: more open chromatin measured with the DNase I–TUNEL assay followed by fluorescence imaging was observed for Mel624 cells with FTO knockdown compared to control. Scale bars, 30 μm. Right: boxplots showing relative intensities quantified by using ImageJ. (**C**) Left: elevated total nascent RNA synthesis measured by using EU labeling followed by fluorescence imaging for Mel624 cells with FTO knockdown compared to control. Scale bars, 30 μm. Right: boxplot showing relative intensities quantified by using ImageJ. (**D**) Density plots showing the overall ATAC-seq signals quantified with FPKM in Mel624 cells with FTO knockdown compared to control. (**E**) A volcano plot showing a comparison of differential peaks from ATAC-seq in *Fto*$^{-/-}$ mESCs compared to WT. Significantly increased peaks are shown in red ($p < 0.01$: 8097; FDR < 0.05: 261) and significantly decreased peaks are shown in blue ($p < 0.01$: 278; FDR < 0.05: 5). (**F**) Gained-open regions upon FTO knockdown from ATAC-seq results were enriched with histone H3K27Ac mark based on ChIP-seq results. Gained-open regions and ChIP-seq results were plotted in heatmap views. The left two panels represent the gained-open regions from ATAC-seq results upon FTO knockdown in Mel624 cells. A higher H3K27Ac level was observed for these regions when comparing FTO knockdown to control. Gained-opened regions were defined by 1 kb sliding windows along the genome. (**G**) Immunoblot assays showing dysregulated levels of H3K27Ac and H3K27Me3 in Mel624 cells with FTO knockdown compared to control. (**H**) Relative expression level of LINE1 RNA in total RNA quantified by RT-qPCR in Mel624 cells with FTO knockdown compared to control. (**I**) The relative expression level of LINE1 RNA in total RNA quantified by RT-qPCR in Mel624 cells with LINE1 ASO knockdown compared to control. (**J**) Chromatin openness measured by using the DNase I – TUNEL assay followed by flow cytometry in Mel624 cells treated with LINE1 ASO compared to control. (**E**) A heatmap showing dysregulated expression levels of EP300, KDM6B, and EZH2 quantified with FPKM values from RNA-seq in Mel624 cells with FTO knockdown compared to control. (**F**) IGV profiles showing m^6A peaks on *EP300*, *KDM6B*, and *EZH2* transcripts in Mel624 cells with FTO knockdown compared to control. *r* refers to Pearson's correlation coefficient. (**G**) Half-life time RT-qPCR experiments of EZH2, EP300, and KDM6B. *p* values were determined using a two-tailed *t*-test; *n.s.* means not significant in (A) to (C), (I) and (H). Representative images were selected from three independent experiments in (B) and (C).

4.2.3 Autophagy of FTO is impaired by arsenic to promote tumorigenesis

4.2.3.1 Arsenic-induced FTO upregulation associates with tumorigenicity

In section **4.2.1.3**, we showed that FTO can be induced by metabolic stress through the autophagy and NF-κB pathways, presenting another example of context-dependent regulation of FTO and m^6A under stress conditions. Intriguingly, as we investigated the potential role of mRNA m^6A in arsenic-induced tumorigenicity, we found that chronic (up to 28 weeks) low-level arsenic (100 nM) exposure of HaCaT cells (As cells) led to substantially upregulated FTO (but only

moderate or no effect on other m^6A effectors) associated with decreased RNA m^6A level (**Figure 4.8A&B**). Treatment with a low level of arsenic for 72 h of HaCaT cells also led to induced FTO protein and decreased m^6A (**Figure 4.8C**). Similar FTO upregulation caused by arsenic treatment was detected in NHEK cells as well (**Figure 4.8D**).

We derived the tumorigenic cells (As-T, Arsenic-Tumorigenic cells) from tumors formed by As cells (control cells did not develop tumor) in mice (**Figure 4.8E**) and observed upregulated FTO protein levels in all four As-T cells (**Figure 4.8F**). In addition, both As and As-T cells exhibited decreased RNA m^6A levels (**Figure 4.8G**), along with increased proliferation and survival (**Figure 4.8H**). We next assessed the levels of RNA m^6A and FTO protein in arsenic-induced premalignant human skin lesions and arsenical keratoses, in comparison with normal human skin. FTO was upregulated and negatively correlated with m^6A level in arsenical keratoses (**Figure 4.8I-L**), suggesting FTO as a pro-tumorigenic factor in arsenic-induced skin lesions.

To further examine the functional significance of FTO upregulation in arsenic-induced tumorigenicity, we constructed FTO KO HaCaT cells (**Figure 4.8M**) using CRISPR. FTO depletion led to decreased cell proliferation, anchorage-independent growth, clonogenic growth, 3D cell growth, and survival in suspension of HaCaT cells (**Figure 4.8N**). FTO depletion also drastically inhibited the tumor growth of As-T cells in mice (**Figure 4.8O**). We employed the arsenic-UVB skin co-carcinogenesis mouse model (that is to treat mice with arsenic, UVB irradiation, or both) and found that epidermis-specific FTO depletion (K14Cre; $Fto^{flox/flox}$) can inhibit skin tumorigenesis induced by arsenic (**Figure 4.8P**). Taken together, these findings reveal that FTO is required for arsenic-induced cell proliferation, survival, malignant transformation, and tumorigenesis.

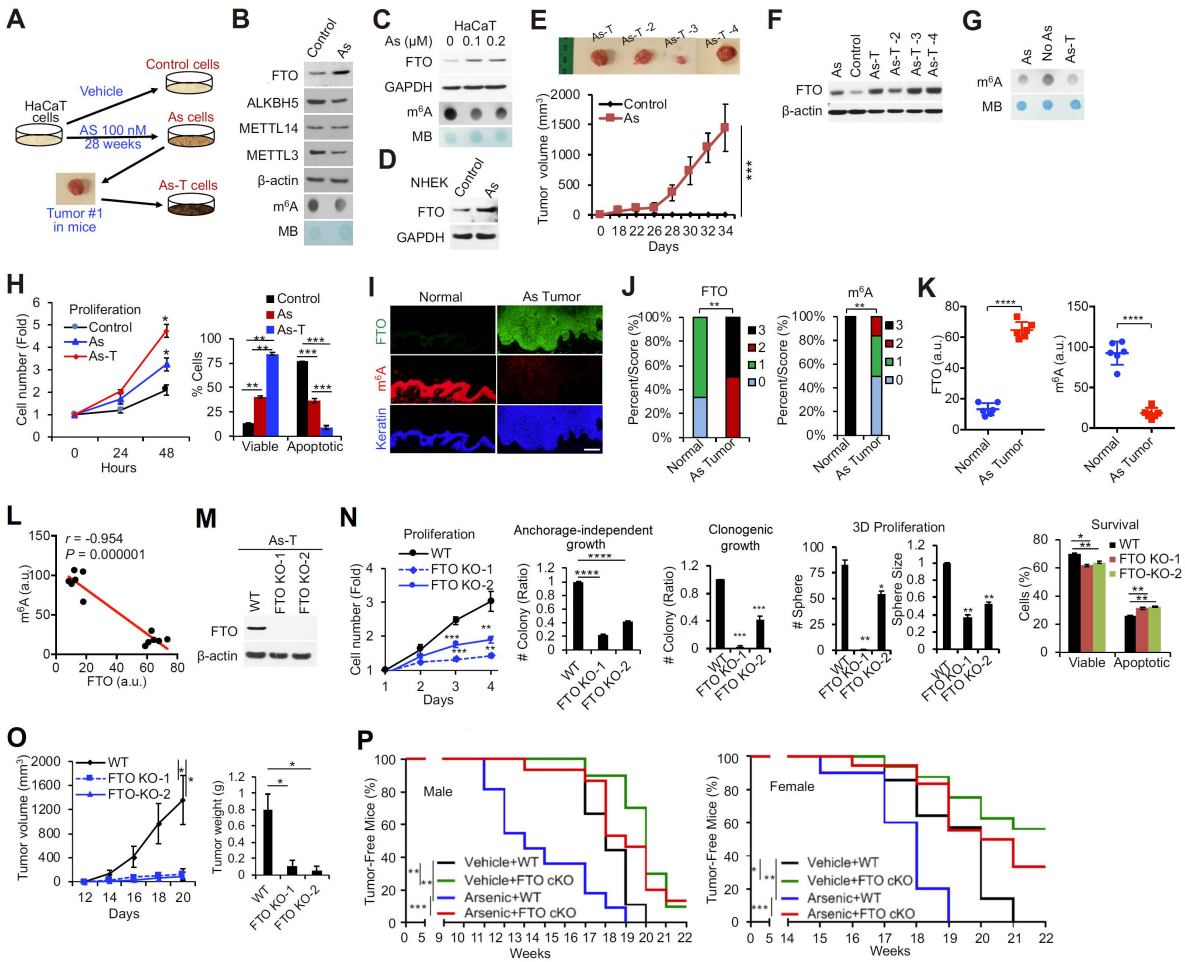

Figure 4.8 FTO is upregulated by arsenic and required for arsenic-induced tumorigenicity
(**A**) Schematic summary of arsenic experiment design. (**B**) Immunoblot analysis showing protein levels of m^{6}A effectors, and dot blot analysis showing RNA m^{6}A levels in control and As cells. (**C**) Immunoblot analysis of FTO protein expression and m^{6}A dot blot assay in HaCaT cells treated with arsenic at different doses for 72 h. (**D**) Immunoblot analysis of FTO protein expression in NHEK cells upon arsenic treatment. (**E**) Final tumor images (top) and tumor volume (bottom) following subcutaneous injection of control and As cells in nude mice. (**F**) Immunoblot analysis showing FTO protein levels in control, As, and As-T cells. (**G**) m^{6}A dot blot assays in control, As, and As-T cells. (**H**) Cell proliferation assay (left) and cell viability assay (right, cells in suspension for 72 h using flow cytometric analysis with Annexin V/propidium iodide staining) in control, As, and As-T cells. (**I**) Immunofluorescence staining of FTO protein (green), RNA m^{6}A (red), and keratin (blue) in normal human skin (n = 6) and arsenic lesions (n = 6). Scale bar, 100 μm. (**J**) Percentage of samples (in stacked column format) for each score of FTO protein (left) and RNA m^{6}A (right). (**K**) Quantification of levels of FTO protein (left) and RNA m^{6}A (right) using ImageJ. (**L**) The negative correlation of m^{6}A levels with FTO levels shown by Spearman test. (**M**) Immunoblot analysis validating *Fto* KO using two independent sgRNAs in As-T cells. (**N**) Cellular phenotypes upon *Fto* KO in As-T cells in the order of cell proliferation assay, soft agar assay, clonogenic assay, sphere-forming assay of 3D proliferation, and apoptosis assay. (**O**) Tumor volume (left) and final weight (right) upon *Fto* KO in NSG mice. (**P**) Kaplan-Meier curves of tumorigenesis in UVB-irradiated mice with wild-type FTO (WT; FTO$^{flox/flox}$) or skin-specific FTO

(**Figure 4.8, continued**) conditional KO (*Fto* cKO; K14Cre; $Fto^{flox/flox}$) with or without arsenic exposure. Vehicle + WT (Male: $n = 9$, Female: $n = 14$); Vehicle + *Fto* cKO (Male: $n = 10$, Female $n = 16$); Arsenic + WT (Male:$n = 11$, Female $n = 10$); Arsenic + *Fto* cKO (Male: $n = 15$, Female $n= 18$). p values were determined using Student's t-test in (E), (H), (K), (N), and (O); using Mann–Whitney U-test in (J); using log-rank test (I). $*p < 0.05$, $**p < 0.01$, $***p < 0.001$, $****p < 0.0001$. Error bars, mean ± s.d. for $n \geq 3$ experiments unless indicated otherwise.

4.2.3.2 NEDDL4 as a critical target of FTO in arsenic tumorigenesis

To identify the potential m^6A demethylation targets of FTO upon arsenic exposure, we performed m^6A MeRIP-Seq in control and As-T cells. In line with FTO upregulation by arsenic, our analysis showed that the number of hypomethylated m^6A peaks was 6-fold more than that of hypermethylated peaks in As-T cells compared to control cells (**Figure 4.9A**), with the typical m^6A consensus motif GGACU identified in both control and As-T cells (**Figure 4.9B**). Accordingly, As-T cells showed evident loss of m^6A peaks at both 5' UTR and 3' UTR in the transcriptome (**Figure 4.9C**), as well as altered m^6A peak distribution (**Figure 4.9D**).

We established the following criteria to narrow down the range of target genes of FTO upon arsenic tumorigenic: (i) hypomethylation with differential expression in our MeRIP-Seq data; (ii) potential role in cancer progression; (iii) altered expression in both human and mouse SCC datasets[187] (**Figure 4.9E**). Among the 40 candidate genes, we selected to initially focus on neural precursor cell-expressed developmentally down-regulated 4 like (NEDD4L), a ubiquitin ligase controlling TGF-b[188], PI3K/AKT[189], and WNT[190] signaling pathways, which suggests a tumor-suppressive role for NEDD4L.

Our data analysis revealed a significantly hypomethylated peak of the NEDD4L transcript in As-T cells (**Figure 4.9F**), which can be further confirmed by m^6A MeRIP-qPCR (**Figure 4.9G**). In line with the downregulation of NEDD4L revealed by the sequencing data, our low-throughput validations showed decreased mRNA and protein levels (**Figure 4.9H**) as well as the mRNA stability of NEDD4L in As-T cells compared to control cells (**Figure 4.9I**), suggesting that arsenic

regulates NEDD4L RNA degradation. Moreover, FTO depletion in As-T cells could reverse the reduced m^{6}A methylation (**Figure 4.9J**), decreased mRNA and protein levels (**Figure 4.9K**), as well as the reduced RNA stability of NEDD4L (**Figure 4.9L**) caused by arsenic, confirming NEDD4L is a target of FTO upon arsenic tumorigenic. Overexpression of WT FTO but not inactive mutants in *Fto* KO As-T cells led to decreased mRNA and protein levels of NEDD4L (**Figure 4.9M)**, which suggests that FTO regulates the expression of NEDD4L through an m^{6}A-dependent manner.

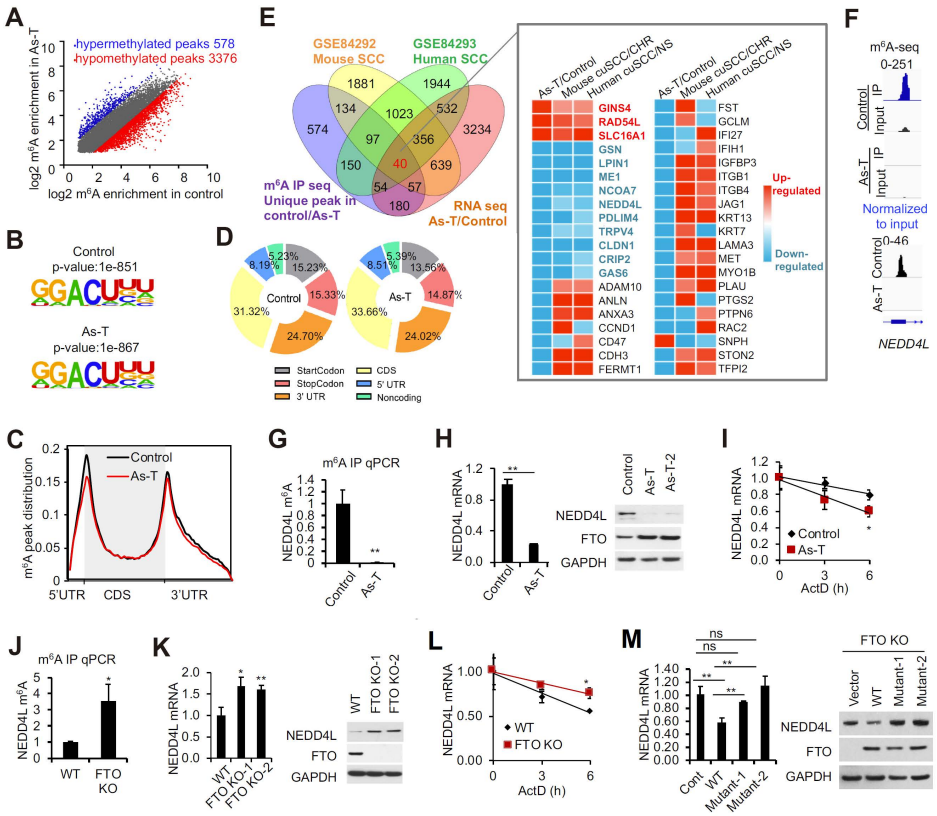

Figure 4.9 NEDDL4 is a potential target of FTO upregulation by arsenic
(**A**) Scatter plots showing hypomethylated and hypermethylated genes in As-T cells compared to control cells. (**B**) Top consensus m^{6}A motif identified by HOMER with m^{6}A peaks in control and As-T cells. (**C**) Metagene profile of the m^{6}A distribution across the transcriptome in control and As-T cells. (**D**) The proportion of m^{6}A peak distribution in the indicated regions across the entire set of mRNA transcripts in control and As-T cells. (**E**) Venn diagram (left) showing the overlap between genes with differential expression or m^{6}A peaks in four datasets: m^{6}A seq (unique m^{6}A peaks in control/As-T), RNA seq (As-T/control), RNA seq (Mouse cuSCC/non-tumor skin (CHR)), and RNA seq (human cuSCC/normal skin (NS)). Heatmap (right) showing normalized expression value for the candidate genes. (**F**) Visualization of the most significantly changed m^{6}A

(**Figure 4.9, continued**) peak on the NEDD4L transcript in control and As-T cells. (**G**) MeRIP-RT-qPCR analysis of m^6A levels of NEDD4L in control and As-T cells. (**H**) RT-qPCR analysis showing mRNA level (left) and immunoblot analysis showing protein level of NEDD4L in control and As-T cells. (**I**) RT-qPCR analysis of NEDD4L mRNA stability in control and As-T cells. (**J**) to (**L**) In As-T cells with or without *FTO* KO. (J) MeRIP-RT-qPCR analysis showing m^6A levels of NEDD4L. (K) RT-qPCR analysis showing mRNA level (left) and immunoblot analysis showing protein level of NEDD4L. (L) RT-qPCR analysis of NEDD4L mRNA stability. (**M**) RT-qPCR analysis of mRNA level (left) and immunoblot analysis of protein level of NEDD4L in *FTO* KO As-T cells with overexpression of WT FTO or inactive mutants. *p* values were determined using Student's *t*-test. $*p < 0.05$, $**p < 0.01$. Error bars, mean ± s.d. for $n \geq 3$ experiments in (G) to (M).

Next, we investigated whether NEDD4L was responsible for FTO-mediated function in arsenic tumorigenicity. Indeed, NEDD4L knockdown (**Figure 4.10A**) could reverse the effect of FTO depletion on cell proliferation, anchorage-independent growth, and cell survival in suspension (**Figure 4.10B**). Consistently, NEDD4L knockdown also prevented the effect of FTO depletion on tumor growth *in vivo* (**Figure 4.10C**). These results revealed NEDD4L as a functionally relevant downstream target of FTO responsible for its function in arsenic-induced malignant transformation.

Moreover, knockdown of the mRNA m^6A methyltransferase co-factor METTL14 diminished the effect of FTO depletion on NEDDL4 mRNA stability (**Figure 4.10D**), mRNA and protein level (**Figure 4.10E**), as well as tumor growth (**Figure 4.10F**). In contrast, knockdown of PCIF1, the mRNA cap-m^6A_m methyltransferase[146,147,150], displayed negligible effects on the FTO-mediated mRNA and protein regulations of NEDD4L (**Figure 4.10G**), excluding the role of cap-m^6A_m demethylation in stabilizing NEDD4L mRNA. Considering hypermethylated m^6A in NEDD4L transcripts upon FTO depletion led to increased mRNA stability, we reckon that the plausible m^6A reader involved in this regulation could be IGF2BP1-3, a group of m^6A readers that stabilize m^6A-modified transcripts[71]. We found that individual knockdown of IGF2BP1-3 could rescue the increased mRNA level of NEDDL4 upon *FTO* KO (**Figure 4.10H**). Furthermore, triple knockdown of all three IGF2BPs diminished the effect of FTO depletion on NEDD4L mRNA

stability (**Figure 4.10I**), and mRNA and protein level (**Figure 4.10J**). Together, these findings strongly indicate FTO regulates NEDD4L mRNA stability through mRNA m^{6}A demethylation in association with m^{6}A reader IGF2BPs.

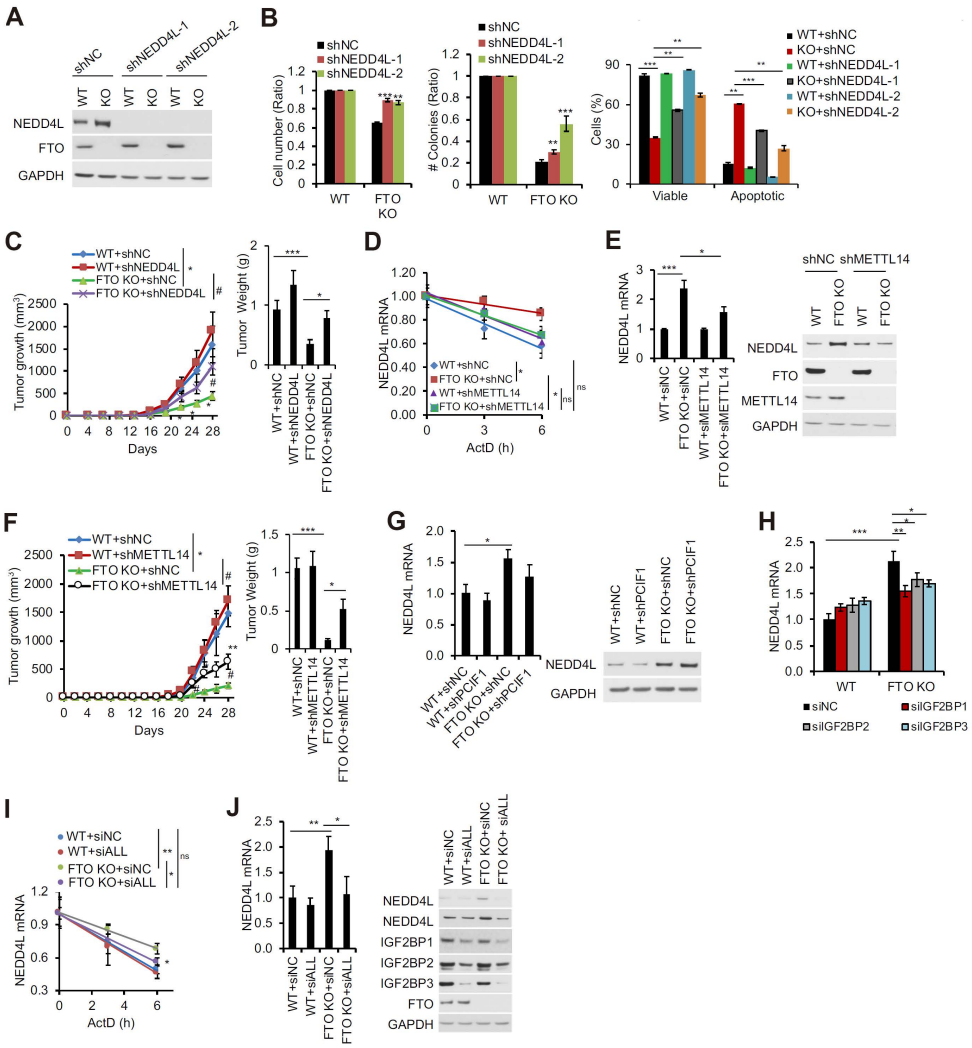

Figure 4.10 FTO regulates NEDD4L stability with IGF2BPs through m^{6}A demethylation
(**A**) to (**J**) In As-T cells with or without *FTO* depletion. (A) Immunoblot analysis validating NEDDL4L knockdown. (B) Cellular phenotypes with or without NEDD4L knockdown in the order of cell proliferation assay, soft agar assay, and apoptosis assay. (C) Tumor volume (left) and weight (right) with or without NEDD4L knockdown following the subcutaneous injection into NSG mice. (D) RT-qPCR analysis showing NEDD4L mRNA stability with or without METTL14 knockdown. (E) RT-qPCR analysis showing mRNA level (left) and immunoblot analysis showing protein level of NEDD4L with or without METTL14 knockdown. (F) Tumor volume (left) and weight (right) with or without METTL14 knockdown following the subcutaneous injection into NSG mice. (G) RT-qPCR analysis showing mRNA level (left) and immunoblot analysis showing protein level of NEDD4L with or without PCIF1 knockdown. (H) RT-qPCR analysis of mRNA level of NEDD4L with or without individual knockdown of IGF2BP1-3. (I) RT-qPCR analysis

(**Figure 4.10, continued**) showing NEDD4L mRNA stability with or without triple knockdown of all IGF2BPs. (J) RT-qPCR analysis showing mRNA level (left) and immunoblot analysis showing protein level of NEDD4L with or without triple knockdown of all IGF2BPs. *p* values were determined using Student's *t*-test. $*p < 0.05$, $**p < 0.01$. Error bars, mean ± s.d. for $n \geq 3$ experiments.

4.2.3.3 Arsenic stabilizes FTO protein by inhibiting autophagic degradation

We sought to investigate the underlying mechanism by which FTO was upregulated by arsenic. We found that FTO mRNA levels remained unchanged in As and As-T cells compared to control cells (**Figure 4.11A**), indicating that arsenic did not alter FTO mRNA abundance. We next assessed the effect of arsenic on FTO protein stability by treating the cells with cycloheximide (CHX) over a time course. As compared with control cells, we observed increased FTO protein stability in As-T cells (**Figure 4.11B**), indicating that arsenic led to reduced FTO protein degradation.

Therefore, we examined the role of protein degradation through either the proteasome[191] or the autophagic-lysosomal[192] pathways, two critical protein degradation pathways. Inhibition of proteasome by MG132 led to FTO protein accumulation to a similar degree in control and As-T cells (**Figure 4.11C**). In contrast, inhibition of lysosome by bafilomycin A1 (BfnA1) led to significantly increased FTO protein accumulation in control cells compared to As-T cells (**Figure 4.11D**). In addition, we observed reduced autophagy in As-T cells, as indicated by decreased accumulation of LC3-II, the surrogate marker for autophagosome accumulation, upon lysosome inhibition (**Figure 4.11D**). These data suggest that arsenic stabilizes FTO protein by impairing the autophagy degradation pathway. Consistently, we observed increased interaction between FTO and LC3 with BfnA1 treatment by using the proximity ligation assay (PLA), revealing the interaction between FTO and autophagosomes (**Figure 4.11E**). Consistently, our gene set

enrichment analysis (GSEA) obtained downregulation of both “Lysosome” and “Phagosome” pathway-related genes in mouse cuSCCs compared to non-tumor skin (**Figure 4.11F**).

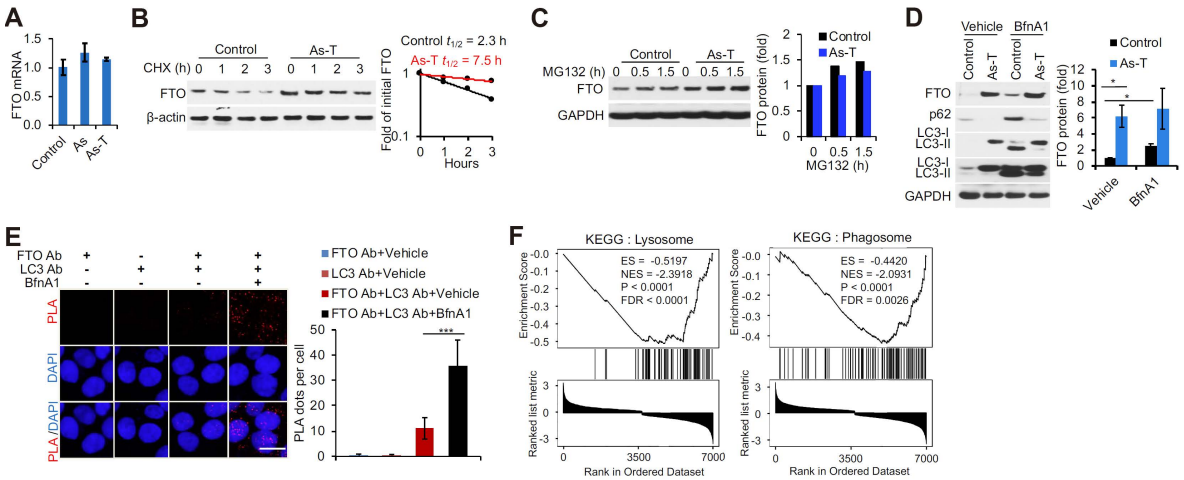

Figure 4.11 Arsenic impairs autophagic degradation to stabilize FTO protein
(**A**) RT-qPCR analysis of FTO mRNA levels in control, As, and As-T cells. (**B**) Left: immunoblot analysis of FTO protein levels in control and As-T cells treated with cycloheximide (CHX, 100 μg/ml) over a time course; right: $t_{1/2}$ (half-life) calculated from quantification of the immunoblot results. (**C**) Left: immunoblot analysis of FTO protein levels in control and As-T cells with or without MG132 treatment; right: quantification of the immunoblot results. (**D**) Left: immunoblot analysis showing protein levels of FTO, p62, LC3-I/II in control and As-T cells with or without BfnA1 (50 nM, 6 h); right: quantification of the immunoblot results. (**E**) Left: PLA assays showing the interaction between FTO and LC3 in HaCaT cells treated with vehicle or BfnA1 (50 nM, 6 h); right: quantification of the number of PLA red dots per cell. Scale bar: 20 μm. (**F**) Gene set enrichment analysis (GSEA) of “Lysosome” (KEGG) and “Phagosome” (KEGG) pathway-related genes in mouse cuSCC *versus* non-tumor skin. ES: enrichment score. NES, normalized enrichment scores. *p* values were determined using Student’s *t*-test. **p* < 0.05, ****p* < 0.001. Error bars, mean ± s.d. for $n \geq 3$ experiments in (A) to (E).

To determine the mechanism by which arsenic compromised the autophagic degradation of FTO, we mined our RNA-seq data for the effect of arsenic on autophagy-related genes and observed decreased expression of OPTN, LAPM1, p62, and ATG5 in As-T cells compared to control cells, which can be validated by RT-qPCR (**Figure 4.12A**). Among them, p62 is one factor that targets specific cargoes for autophagy[193]. Accordingly, the p62 protein level was downregulated by arsenic (**Figure 4.12B**). Next, we assessed whether p62 regulated FTO protein stability. Indeed, p62 knockdown led to increased, whereas p62 overexpression led to reduced

FTO protein level (**Figure 4.12C**), which also held for the protein stability of FTO (**Figure 4.D&E**). Accordingly, overexpression of p62 led to increased NEDD4L mRNA levels in As-T cells but not in As-T cells with FTO depletion, indicating that p62 regulated NEDD4L expression through FTO (**Figure 4.12F**). In addition, PLA supported the co-localization of p62 and FTO in HaCaT cells (**Figure 4.12G**).

We asked how arsenic led to reduced p62 expression. Our KEGG network analysis revealed that "Autophagy-animal", "Phagosome", "Lysosome", "NF-κB signaling pathway", and "TNF signaling pathway" were significantly enriched by downregulated genes in As-T cells compared to control cells from RNA-Seq (**Figure 4.12H**). Consistently, GSEA showed that genes associated with TNF-signaling pathway were downregulated in As-T cells compared to control cells (**Figure 4.12I**). Previous studies have shown that NF-κB-induced cytokine TNFα elevates p62 expression[194]. We thus hypothesized that arsenic led to reduced p62 expression through downregulating signaling of cytokines such as TNFα. Indeed, we found that TNFα treatment led to increased mRNA and protein levels of p62 associated with decreased FTO protein level (**Figure 4.12J**). These findings demonstrate that arsenic stabilizes FTO protein through downregulating TNFα-pathway-mediated p62 expression. Lastly, we assessed whether p62 regulates FTO stability through autophagy. We noticed p62 overexpression led to increased autophagy (**Figure 4.12K**). PLA analysis also showed that p62 overexpression led to enhanced co-localization of FTO with LC3 (**Figure 4.12L**).

Considering that in preadipocytes, FTO knockdown decreases the expression of autophagy genes, including ATG5 and ATG7, and inhibits autophagy[195], we asked whether FTO also regulates autophagy in response to arsenic damage. In contrast, we found that FTO depletion in As-T cells led to increased autophagy, as shown by p62 accumulation and formation of LC3-II

upon BfnA1 treatment (**Figure 4.12M**). Accordingly, FTO depletion led to decreased p62 mRNA levels, consistent with the decreased p62 protein levels in FTO-depleted cells under homeostatic conditions (**Figure 4.12M**). In addition, under serum starvation conditions that can induce autophagy[196], we found that FTO depletion led to increased phosphorylation of AMPK, decreased phosphorylation of the mTOR substrate p70S6K, increased protein levels of ATG5, ATG7, and LC3-II (**Figure 4.12N**). Together, our results demonstrate that p62 mediates autophagic degradation of FTO; and FTO, in turn, suppresses autophagy.

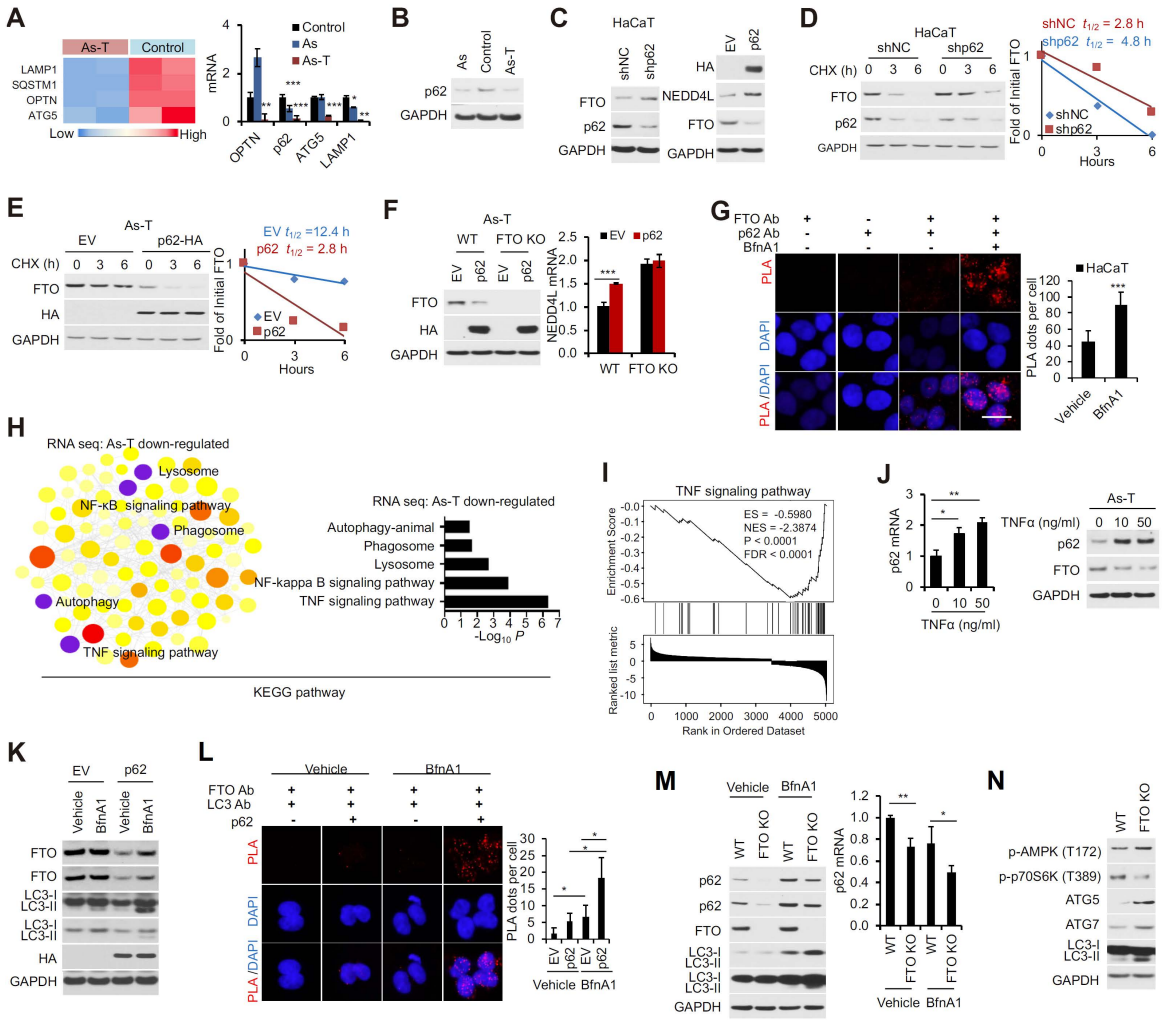

Figure 4.12 FTO is degraded by p62-mediated autophagy and in turn suppresses autophagy (**A**) Left: Heatmap showing altered expression of the genes in autophagy/lysosome pathways between As-T and control cells; right: RT-qPCR analysis showing mRNA levels of OPTN, p62, ATG5, and LAMP1 in control, As, and As-T cells. (**B**) Immunoblot analysis of p62 protein levels in control, As, and As-T cells. (**C**) Left: immunoblot analysis of FTO protein levels in HaCaT cells

(**Figure 4.12, continued**) with or without p62 knockdown; right: immunoblot analysis of FTO and NEDDL4 protein levels in HaCaT cells overexpressing vector (EV) or p62 (HA tag). (**D**) Left: immunoblot analysis of FTO protein levels in HaCaT cells with or without p62 knockdown treated with cycloheximide (CHX, 100 μg/ml) over a time course; right: $t_{1/2}$ (half-life) calculated from the quantification of the immunoblot results. (**E**) Left: immunoblot analysis of FTO protein levels in HaCaT cells overexpressing vector or p62 treated with cycloheximide (CHX, 100 μg/ml) over a time course; right: $t_{1/2}$ (half-life) calculated from quantification of the immunoblot results. (**F**) In As-T cells with or without FTO depletion in combination with overexpressing vector or p62: immunoblot analysis of FTO and p62 (left); RT-qPCR analysis of NEDD4L mRNA levels (right). (**G**) Left: PLA assays showing the interaction FTO and p62 in HaCaT cells treated with vehicle or BfnA1; right: quantification of the number of PLA red dots per cell. Scale bar: 20 μm. (**H**) Left: KEGG network enriched by top downregulated genes in As-T compared to control cells from RNA-Seq; right: selected pathways in KEGG network. Each node represents an enriched KEGG term. (**I**) GSEA analysis of 'TNF signaling pathway'-related genes As-T cells *versus* control cells. (**J**) In As-T cells with or without TNFα treatment: RT-qPCR analysis of p62 mRNA levels (left); immunoblot analysis of FTO and p62 (right). (**K**) Immunoblot analysis showing protein levels of FTO, LC3-I/II, and p62 in As-T cells treated with vehicle or BfnA1 (50 nM, 6 h) combined with overexpressing vector or p62. (**L**) Left: PLA assays showing the interaction FTO and LC3 in cells as (K); right: quantification of the number of PLA red dots per cell. Scale bar: 20 μm. (**M**) In As-T cells with or without FTO depletion in combination with treatment of vehicle or BfnA1 (50 nM, 6 h): immunoblot analysis showing protein levels of FTO, LC3-I/II, and p62 (left); RT-qPCR analysis of p62 mRNA levels (right). (**N**) Immunoblot analysis showing protein levels of autophagy regulators in As-T cells with or without FTO depletion in combination with treatment of low serum (0.5% FBS) overnight. *p* values were determined using Student's *t*-test. $*p < 0.05$, $**p < 0.01$. Error bars, mean ± s.d. for $n \geq 3$ experiments.

4.3 Conclusion and discussion

Collaborative efforts from Professor Yu-Ying He's group and our group pictured the complex regulatory mechanism by which FTO and m^{6}A controled the melanoma and arsenic tumorgenicity (**Figure 4.13**).

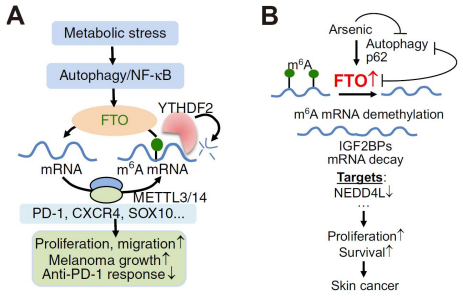

Figure 4.13 Proposed models for the regulatory and functional roles of FTO in melanoma pathogenesis and arsenic-induced tumorigenesis

(**Figure 4.13, continued**) (**A**) Schematic summary of autophagy and NF-κB-involved pathways in modulating metabolic stress-induced FTO expression as well as FTO-mediated mRNA m^6A demethylation associated withYTHDF2-mediated mRNA decay of key transcripts that control the melanoma tumorigenicity and response to anti-PD-1 blockade. (**B**) Schematic summary of a positive feedback loop between FTO and autophagy dysregulation, leading to self-sustained maintenance of FTO upregulation and m^6A hypomethylation in arsenic-induced malignant transformation and tumorigenesis, thereby regulating arsenic tumorigenicity in turn at least partially through FTO-mediated mRNA m^6A demethylation in NEDD4L mRNA associated with reader protein IGF2BPs.

In the melanoma study, we demonstrated that FTO inhibition led to suppressed melanoma tumorigenicity (**Figure 4.1**) and the expression of melanoma cell-intrinsic genes PD-1, CXCR4, and SOX10 (**Figure 4.2&4.3**), at least partially through mRNA m^6A demethylation by FTO followed by YTHDF2-mediated decay of m^6A methylated mRNA (**Figure 4.4**). We showed that FTO inhibition enabled an anti-melanoma response to anti-PD-1 therapy in mice (**Figure 4.5**). Our findings may provide new opportunities for developing improved melanoma therapies by inhibiting the FTO pathway combined with anti-PD-1 therapy.

In the arsenic study, we demonstrated that arsenic promoted FTO protein stability by impairing selective autophagy and thus induced malignant transformation and tumorigenesis (**Figure 4.8, 4.11&4.12**). FTO decreased internal m^6A modification and stability of its functional downstream target NEDD4L mRNA (**Figure 4.9&10**). Our results provide an epitranscriptomic molecular axis as the post-transcriptional mechanism in arsenic-induced tumorigenesis, and thus may help the development of new mechanism-based prevention and therapy by targeting FTO and m^6A RNA methylation to reduce the skin cancer burden in arsenic-exposed individuals worldwide.

Using melanoma cells as an example, our study revealed that the FTO-mediated chromatin regulation largely depended on cellular context. Our data analysis showed that LINE1 RNA abundance did not appear to be associated with FTO expression in human cancer cells. In fact, LINE1 RNA m^6A demethylation did not appear to affect LINE1 RNA level in these cancer cells

(**Figure 4.6**). Internal mRNA m^6A sites have been assigned as functionally relevant substrates of FTO in previous studies of many cancer cell lines[56,58-62]. In mESCs and relevant cells or tissues, FTO served as a demethylase of LINE1 RNA and potentially other carRNAs to exert a chromatin regulation function. However, in at least one melanoma cell line, Mel624, we showed that the chromatin state regulation can be mediated through m^6A demethylation by FTO on mRNAs that encode histone modifiers, which may lead to upregulation of some critical tumor suppressors by promoting their transcription (**Figure 4.7**).

Besides the context-dependent chromatin regulation, we also revealed that (i) FTO targets tended to be either IGF2BP or YTHDF2 targets (**Figure 4.4, 4.7&4.10**); (ii) FTO can be upregulated by metabolic stress and starvation through autophagy and NF-κB-associated pathways in melanoma cells (**Figure 4.5**); (iii) dysregulation of FTO and autophagy formed a positive feedback loop, leading to self-sustained FTO upregulation and malignant traits in arsenic-induced tumorigenic cells (**Figure 4.12**). Note that knockdown of the autophagy essential genes ATG5 or ATG7 reduced starvation-induced FTO mRNA level in melanoma cells (**Figure 4.5**), while FTO protein was subjected to p62-meidated autophagic degradation in arsenic-induced tumorigenic cells (**Figure 4.11&12**). Inhibition of autophagy by FTO in arsenic-induced tumorigenic cells (**Figure 4.12**) was consistent with a previous report that FTO activated the mTORC1 pathway and thus inhibited autophagy in MEF cells[197]. However, our findings was opposite to those reported in preadipocytes, in which FTO knockdown decreased the expression of ATG5 and ATG7 and reduced autophagy[195]. These discrepancies, again, could be due to the cell-type specific or context-dependent role of FTO in autophagy, which warrants future investigation.

As we discussed in chapter **2** and chapter **3**, in contrast to FTO, mRNA m^6A has been known as the sole substrate of ALKBH5. However, ALKBH5-mediated m^6A demethylation also

depends on the context of PTMs and in response to stress conditions. In collaboration with Professor Zhijian Qian from the University of Florida, we found that reactive oxygen species (ROS)-induced stress could activate ERK/JNK signaling to promote ALKBH5 phosphorylation and SUMOylation, leading to inactivation of ALKBH5 demethylase activity and thus global mRNA m^6A hypermethylation, which consequently led to the synchronized expression of thousands of genes including key DNA repair genes to protect cells from DNA damage and ROS-induced cell death. In lung cancer cells, mutant K-RAS can hijack this ERK/JNK/ALKBH5-mediated m^6A methylation upregulation axis to induce chemoresistance by enhancing DNA damage repair pathways (manuscript under review).

In addition to human cancers, emerging data have suggested the profound impacts of FTO-mediated mRNA m^6A demethylation on human heart diseases. Mice with a cardiomyocyte restricted *Fto* cKO have been shown to display faster progression of heart failure with reduced hypertrophy[198]. FTO has also been reported to regulate cardiac function during homeostasis, remodeling, and regeneration[43]. In collaboration with Professor Federica Accornero from the Ohio State College of Medicine, we profiled the mRNA m^6A in human heart failure samples compared to healthy samples to show the remodeling and potential impact of mRNA m^6A in cardiac pathophysiology (**Figure 4.14A&B**). We found an increase in mRNA m^6A content in human heart failure samples associated with significantly decreased expression of FTO (**Figure 4.14C&D**). Further, we compared all m^6A sites regulated in human hearts with the ones occurring in isolated rat hypertrophic cardiomyocytes to define cardiomyocyte-specific m^6A events conserved across species. Our results identified 38 shared transcripts targeted by m^6A during stress conditions (**Figure 4.14E**), and 11 events that were unique to unstressed cardiomyocytes (**Figure 4.14F**), indicating the simultaneously coexisted conservativity and heterogeneity of m^6A profile and

function, depending on the specific biological contexts. Given our new findings and understanding of the FTO's role in mammals, it would be intriguing to profile the m^{6}A on repeat RNAs especially LINE1 RNA as well as the chromatin accessibility in heart failure samples compared to non-failure samples in the future.

Taken together, our studies emphasize context-dependent RNA demethylation regulation. Careful analysis of the function and functional relevance of FTO in specific cell context or under specific stress conditions will be critical in future studies of RNA demethylation.

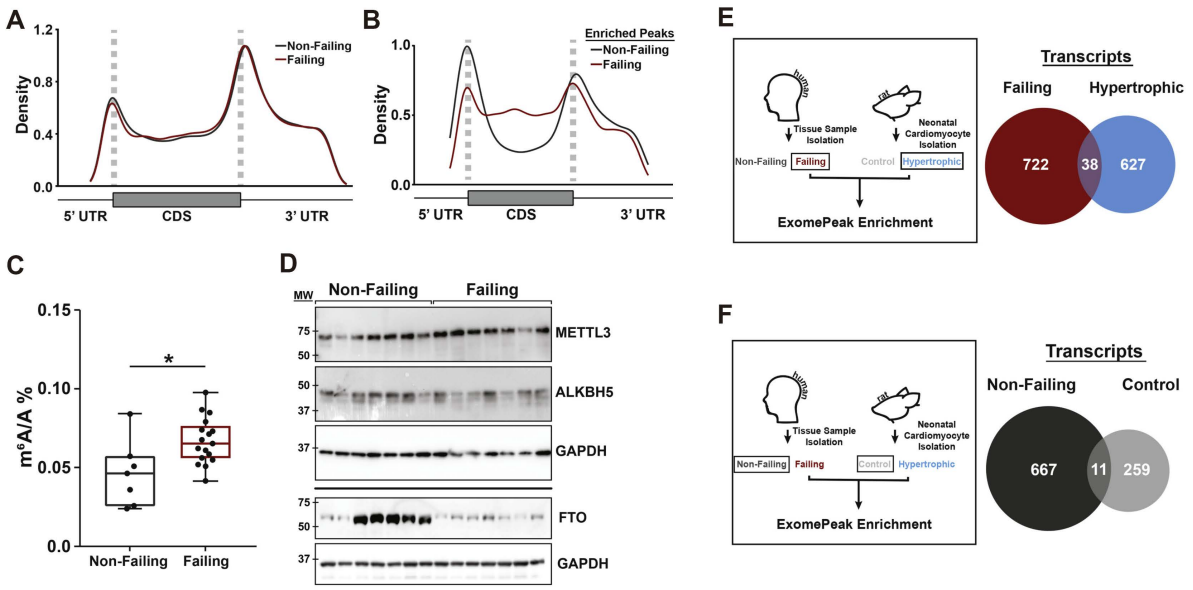

Figure 4.14 Remodeling of the m^{6}A landscape in the heart failures
(**A**) Metagene profiles of total peak distribution in non-failing (gray) and failing (red) hearts were plotted *via* density across mRNA regions. (**B**) Metagene profiles showing the distribution of peaks enriched in non-failing (gray) and failing (red) hearts were plotted *via* density across mRNA regions. Failing samples have more enriched peaks in total, with enrichment in frequency in CDS, stop codon, 3' UTR, and intronic regions. (**C**) Quantification of m^{6}A/A ratios on polyadenylated RNA from non-failing (n = 7) and failing (n = 17) human heart samples (**D**) Immunoblot on non-failing and failing heart protein lysates measuring expression of METTL3, ALKBH5 and FTO. (**E**) Left: general schematic for m^{6}A peak comparison between human failing and neonatal rat cardiomyocyte hypertrophic samples; right: Venn diagram of transcripts containing enriched m^{6}A peaks in failing (red) and rat hypertrophic cardiomyocytes (blue) (FC > 1.5 by exomePeak). Comparison found 38 transcripts to be co-enriched. (**F**) Left: general schematic for m^{6}A peak comparison between human non-failing and neonatal rat control cardiomyocytes samples; right: Venn diagram of transcripts containing enriched m^{6}A peaks in non-failing (dark gray) and rat cardiomyocytes control (light gray) (FC > 1.5 by exomePeak). Comparison found 11 transcripts

(**Figure 4.14, continued**) to be co-enriched. *p* value was determined using Student's *t*-test. *$p < 0.05$. Error bars, mean ± s.d. for $n \geq 7$ experiments.

4.4 Methods

4.4.1 Human skin tumor samples

Section **4.2.1**:

All human specimens were studied after approval by the University of Chicago Institutional Review Board. The human melanoma array was obtained from US Biomax.

Section **4.2.3**:

All human specimens were studied after approval by the University of Chicago Institutional Review Board. Normal human skin samples were obtained from the archives in the tissue bank of the Section of Dermatology (Department of Medicine, University of Chicago). The arsenical keratoses were obtained from the clinical follow-up for arsenic-exposed cohorts that evaluate the health effects of exposure, including skin cancer, in Bangladesh.

4.4.2 Cell culture

Section **4.2.1&4.2.2**:

WM35, WM115, WM793, and WM3670 were kindly provided by Dr. Meenhard Herlyn (Wistar Institute, Philadelphia, PA). Mel624, CHL-1, SK-mel30, and B16F10 cells were purchased from ATCC or provided by the Comprehensive Cancer Center Core Facilities at the University of Chicago. Melanoma cells were maintained in DMEM (Dulbecco's modified Eagle's medium) medium (Invitrogen) supplemented with fetal bovine serum (FBS, 10% HyClone), penicillin (100 U/ml), and streptomycin (100 μg/ml, Invitrogen, Carlsbad, CA). NHEM cells (Normal Human Epidermal Melanocytes) were purchased from Lonza and cultured in 95% air and 5%

CO_2 at 37 °C in NHEM defined medium obtained from Lonza according to the manufacturer's instructions.

Section **4.2.3**:

HaCaT (human keratinocyte) and HEK-293T cells were maintained in Dulbecco's modified Eagle's medium (Invitrogen, Carlsbad, CA) supplemented with 10% fetal bovine serum (Gibco), 100U/ml penicillin, and 100ug/ml streptomycin (Invitrogen, Carlsbad, CA). Normal Human Epidermal Keratinocyte (NHEK) cells were purchased from Lonza and maintained in KGM Gold keratinocyte growth basal medium (Lonza, #00192151) and KGM Gold keratinocyte growth medium supplements and growth factors (Lonza, #00192152).

4.4.3 Lentiviral generation and infection

Lentivirus was produced by co-transfection into HEK-293T cells with lentiviral vectors in combination with the pCMVdelta8.2 packaging vector and pVSV-G envelope vector using GenJet Plus DNA In Vitro Transfection Reagent (Signagen). Virus-containing supernatants were collected 24–48 h after transfection and used to infect recipients. Target cells were infected in the presence of Polybrene (8 μg/ml) (Sigma-Aldrich) and selected with puromycin (Santa Cruz Biotechnology, 1 μg/ml) for 6 days.

Section **4.2.1**:

Lentiviral particles of shNC (Negative control) and shFTO for humans and mice were purchased from Santa Cruz Biotechnology. pLKO.1 plasmids of shNC, shFTO, shATG5, shATG7, and shYTHDF2 (human) were obtained from Sigma. pLenti plasmids of overexpression control (mGFP) and overexpression of PDCD1(mGFP-PDCD1), CXCR4, and SOX10 for humans were obtained from Origene (Origene, Rockville, MD).

Section **4.2.3**:

Lentiviral vectors expressing shRNA targeting negative control (shNC), METTL14 (shM14), FTO (shFTO), NEDD4L (shNEDD4L), PCIF1 (shPCIF1), and p62 (shp62) for humans were purchased from Sigma. pcDNA4-HA-p62 was provided by Qing Zhong (University of California) (Addgene plasmid #28027)[199]. WT and FTO mutant 1 (H231A/D233A) and mutant 2 (R316Q/R322Q) were generated as described previously[12]. Cells with FTO deletion using the CRISPR method were prepared as adapted from the method described previously[200]. The guide RNA sequences are FTO KO-1: GAAGCGCACCCCGACTGCCG; FTO KO-2: ACGGTCCCCTGGCCAGTGAA.

4.4.4 Luciferase reporter assays

Using GenJet Plus DNA In Vitro Transfection Reagent (Signagen), cells were transfected with pGL3 NF-κB-Luc (1 μg) and pRL-TK (0.025 μg), as a control for transfection efficiency (Promega), according to the manufacturer's instructions. Luciferase reporter assays (Promega) were carried out according to the manufacturer's instructions.

4.4.5 siRNA transfection

Using GenMute siRNA Transfection Reagent (Signagen), cells were transfected with siRNA (Dharmacon), targeting negative control (NC), METTL3, METTL14, YTHDF1, YTHDF2, and YTHDF3 (for section **4.2.1**), and an individual gene or the combination of IGF2BP1, IGF2BP2, IGF2BP3 (for section **4.2.3**) according to the manufacturer's instructions.

Section **4.2.2**:

Transfection was achieved by using Lipofectamine RNAiMAX (Invitrogen) following the manufacturer's protocols for siRNA control and targeting genes ordered from ThermoFisher.

4.4.6 Quantitative real-time PCR (RT-qPCR)

RT-qPCR assays were carried out using a CFX Connect real-time system (Bio-Rad, Hercules, CA) with Bio-Rad iQ SYBR Green Supermix (Bio-Rad). The threshold cycle number (CQ) was analyzed in triplicate for each sample.

Section **4.2.1**:

The CQ values for ANGPTL2, RAB40B, CTSV, RBBP9, NOP16, FCMR, PDCD1, CD274, CD47, CDKN1A, METTL3, METTL14, FTO, ALKBH5, YTHDF1, YTHDF2, YTHDF3, ATG5, ATG7, GAPDH, β-actin, and HPRT1 were normalized against HPRT1, GAPDH, or β-actin.

Section **4.2.3**:

The CQ values for FTO, NEDD4L, ATG5, OPTN, p62, LAMP1, IGF2BP1, IGF2BP2, and IGF2BP3 were normalized against GAPDH.

Please refer to section **3.4.16** for RT-qPCR in section **4.2.2**.

4.4.7 Flow cytometric analysis of apoptosis

Apoptosis was analyzed using the annexin V-FITC apoptosis detection kit (eBioscience), following the manufacturer's instructions. Cells were then by a BD FACS Calibur flow cytometer (BD Biosciences). For cell viability assay in cells in suspension, poly-hydroxyethyl methacrylate (poly-HEMA) plates were used to culture cells in suspension. A solution of poly-HEMA (Sigma–Aldrich, St. Louis, MO) mixed in ethanol was poured onto polystyrene bacteriological dishes. After the poly-HEMA had dried, the same procedure was repeated once followed by extensive washing with phosphate buffered saline (PBS).

4.4.8 Migration and invasion assay

For migration and invasion analysis, cell (5×10^4) suspension (150 µl of serum-free medium) were seeded onto 8-mm Pore Transwell Inserts (Corning) coated with Matrigel for invasion assay, or without Matrigel for migration assay. Lower chambers were filled with complete medium (900 µl). Cells on the Transwell Inserts were then fixed with paraformaldehyde/PBS (4%) for 30 min. Next, fixed cells were stained with hematoxylin solution (Sigma-Aldrich) for 1 h. Then microphotograms of the cells migrated onto the lower side of the filter were imaged using a microscope. From the microphotograms, cells that migrated or invaded onto the lower side of the filter were manually counted. Cell numbers were quantified from ten randomly selected fields with the same area (500 µm × 500 µm) per Transwell insert.

4.4.9 Soft agar colony formation and 3D on-top culture in Matrigel

For soft agar assay, in 35-mm Petri dishes, 3000 cells were resuspended in 0.3% Agarose-low gelling temperature (Sigma-Aldrich) in DMEM with FBS (10%) and layered over 1 ml 0.5% agar in DMEM with 10% FBS. Colonies with more than eight cells were counted. For 3D on-top culture, 4-well glass chamber slides (BD Biosciences) were coated with 120 ml of growth factor reduced Matrigel per well; 5000 cells were seeded per well in DMEM with fetal bovine serum (10%) and Matrigel (10%).

4.4.10 Cell proliferation assay

Cell proliferation was assessed using the Cell Counting Kit-8 (CCK-8) (Sigma-Aldrich, St. Louis, MO) following the manufacturer's protocol.

4.4.11 Histological analysis

H&E staining was performed by the Immunohistochemistry core facility at the University of Chicago.

4.4.12 Sphere formation assay

The sphere formation assay was performed as described previously[201]. The cell culture was first harvested in 10% FBS medium and passed through a 40 μm nylon mesh (Fisher, 22363547). Then cells were harvested in 10% FBS medium and passed through a 40 μm nylon mesh (Fisher, 22363547). Then cells were gently resuspended in the sphere medium (1-2 ml). Cells were next plated in 6-well ultra-low attachment plates (Corning, 3471) at a density of 1,000 cells per well in culture medium DMEM/F12 (1:1) (Invitrogen) with 2% B27 serum-free supplement (17504-044, Invitrogen, Frederick, MD), 20 ng/ml EGF (E9644, Sigma, St. Louis), 0.4% bovine serum albumin (B4287, Sigma), 4 μg/ml insulin (Sigma, St. Louis, MO, #19278), and antibiotics, and cultured for 7-14 days at 37 °C with 5% CO2. The number and size of tumor spheres per well were quantified.

4.4.13 Immunofluorescence and immunohistochemistry

For immunofluorescence analysis, cells were first fixed with paraformaldehyde/PBS (4%) for 30 min, followed by permeabilized in Triton X-100/PBS (0.5%) for 20 min. Next cells were washed with PBS, blocked with PBS supplemented with 2% normal goat serum (Invitrogen) for 30 min, and stained for actin filaments with rhodamine-labeled phalloidin (Invitrogen, Carlsbad, CA). Then cells were washed three times with Triton X-100/TBS (0.1%) for 10 min and fixed in Prolong Gold Antifade with DAPI (Invitrogen), followed by observation under a fluorescence microscope (Olympus IX71).

For Human Melanoma Tissue Microarray staining, melanoma tissue array slides were obtained from US Biomax (Rockville, MD). After removing the blocking solution (3% albumin from chicken egg white (Sigma-Aldrich) in PBS), tissue array slides were incubated at 4 °C with primary rabbit anti-FTO, goat anti-PD-1, or mouse anti-MART1 for 18 h. After removing the primary antibodies, slides were washed with PBS solution with 0.025% TritonX-100. Tissue array slides were then incubated at room temperature with Alexa Fluor 594-conjugated secondary rabbit IgG (Jackson ImmunoResearch), Alexa Fluor 488-conjugated secondary mouse IgG (Jackson ImmunoResearch), and Alexa Fluor 405-conjugated secondary goat IgG (Jackson ImmunoResearch), then washed with TritonX-100 (0.025% in PBS), and mounted with Prolong Gold Antifade with DAPI (Invitrogen) for cell nucleus counterstaining in FTO/MART1 staining, or with Fluoromount Mounting Medium (Sigma-Aldrich) in FTO/PD-1/MART1 staining. Two investigators independently scored the immunofluorescence intensity and staining blindly, as 3 (strong), 2 (medium), 1 (weak), and 0 (negative). ImageJ (NIH) was also used for analyzing melanoma cells and tissue arrays. Areas of the same size were selected. The intensity of a selected area was measured followed by background subtraction to calculate mean pixel density. Stained samples were analyzed using a fluorescence microscope (Olympus IX71).

Section **4.2.1**:

Antibodies used are as follows: anti-FTO (Abcam, ab126605, 1:100); anti-MART1 (NOVUS, NBP 2–15197, 1:100); Rhodamin-phalloidin (Life technologies, R415, 1:100); anti-PD-1 (R&D Systems, Cat# AF1086 Minneapolis, 1:100).

Section **4.2.3**:

Antibodies used are as follows: anti-LC3B (Abcam, ab192890, 1:200), anti-FTO (Abcam, ab92821, 1:200), and anti-p62 (Sigma-Aldrich, P0067, 1:400).

4.4.14 *In situ* proximity ligation assay (PLA)

The PLA assay was performed according to the manufacturer's instructions (Sigma). Briefly, cells were first fixed with 4% paraformaldehyde/PBS and then permeabilized in 0.5%(v/v) Triton X-100. After blocking with 5% normal goat serum (Invitrogen, Carlsbad, California), cells were incubated overnight with the following primary antibodies at 4 °C in 1XPBS/1%BSA: anti-p62 (Rabbit) (Sigma-Aldrich, P0067, 1:400); anti-LC3B (rabbit) (Abcam, ab192890,1:200), and anti-FTO (mouse) (Abcam, ab92821, 1:200). In-situ PLA detection was performed using a Duolink Detection Kit (Sigma-Aldrich) with a pair of nucleotide-labeled secondary antibodies. After ligation and amplification of PLA probes, signals were examined by a fluorescence microscope (Olympus IX71).

4.4.15 Immunoblotting

Cell lysates were obtained using RIPA buffer (Pierce) containing inhibitors for proteases and phosphatases. Protein abundance was then analyzed by SDS-PAGE, and transferred onto nitrocellulose membranes followed by immunoblotting.

Section **4.2.1**:

Antibodies used are as follows: Anti-ALKBH5 (Millipore Co., ABE 1013, 1:2000); anti-Beta-actin (Santa Cruz, SC-47778, 1:5000); anti-CXCR4 (Santa Cruz, SC-53534, 1:200); anti-CXCR4 (Novusbio, NBP1-77067SS, 1:5000); FTO (Santa Cruz, SC-271713, 1:200); GAPDH (Santa Cruz, SC-47724, 1:5000); GFP (Cell Signaling Technology, 2555S, 1:1000); LC3B (Cell Signaling Technology, 3868S, 1:1000); METTL14 (Millipore Co., ABE 1338, 1:1000); METTL3 (Proteintech, 15073-I-AP, 1:1000); p62 (Progen Biotechnik GmbH, GP62-C, 1:10,000); p70s6K (Cell Signaling Technology, 2708S, 1:2000); PD-1 (Proteintech, 66220-I-Ig, 1:5000); p-p70s6K (Cell Signaling Technology, 9234S, 1:1000); and SOX10 (Santa Cruz, SC-365692, 1:2000).

Section **4.2.3**:

Antibodies used were as follows: anti-FTO (Santa Cruz, SC-271713, 1:500); anti-p62 (Progen Biotechnik GmbH, GP62-C, 1:10,000); anti-METTL14 (Millipore Co., ABE 1338, 1:1000); anti-ATG5 (12994, Cell Signaling Technology, 1:1000); anti-ATG7 (8558, Cell Signaling Technology, 1:1000); anti-GAPDH (Santa Cruz, sc-47724, 1:5000); anti-b-actin (Santa Cruz, SC-47778, 1:5000); anti-ALKBH5 (Millipore Co., ABE 1013, 1:2000); anti-HA (Santa Cruz, sc-7392, 1:5000); anti-IGF2BP1 (Cell Signaling Technology, 8482, 1:1000); anti-IGF2BP2 (Cell Signaling Technology,14672, 1:1000); anti-IGF2BP3 (Cell Signaling Technology, 57145, 1:1000); anti-NEDD4L (Cell Signaling Technology, 4013, 1:1000); anti-LC3 (Abcam, ab192890, 1:1000); p-AMPK T172 (Cell Signaling Technology, 2535S, 1:1000, 1:000), p-ULK1 S555 (Cell Signaling Technology, 5869S, 1:1000); and p-p70S6K T389 (Cell Signaling Technology, 9234S, 1:1000).

Please refer to section **3.4.17** for immunoblotting in section **4.2.2**.

4.4.16 Mouse tumorigenesis and treatment

All of the animal procedures used were approved by the institutional animal care and use committee at the University of Chicago. Nude mice were purchased from Harlan Sprague-Dawley. C57BL/6 mice were obtained from Envigo. NSG (severely combined immunodeficient (NOD/SCID) interleukin-2 receptor (IL-2R) gamma chain null) mice were obtained from Jackson Laboratory. For xenograft experiments, one million cells were injected subcutaneously into the right flanks of 6-week-old female nude or C57BL/6 mice. Tumor growth was monitored and measured weekly by a caliper, and tumor volume was calculated using the formula, Tumor volume (mm^3) = $d^2 \times D/2$, where d and D are the shortest and the longest diameters, respectively. For treatment with anti-PD-1 antibody (BioXCell, clone RMP1-14) or isotype control IgG antibody (BioXCell, clone 2A3), B16F10 melanoma cells (5×10^5) were inoculated subcutaneously into

C57BL/6 or NSG mice. When the tumors reached a volume of 80–100 mm^3, mice were treated with anti-PD-1 or isotype control antibody (200 μg/mouse) by i.p. injection, every other day for three times. For IFNγ blockade treatment, C57BL/6 mice were treated with anti-IFNγ antibody (BioXcell, Clone XMG1.2) or isotype control IgG (BioXcell, Clone HRPN) (250 μg/mouse) every other day after tumor cell inoculation.

4.4.17 Analysis of tumor infiltrating lymphocytes (TILs)

Tumor tissue from B16F10 tumor-bearing mice (Day 14 after tumor cell inoculation) was dissociated by digestion with 2.5 mg/ml collagenase type IV (Worthington Biochemical, LS004188) and 100 μg/ml DNAse (Sigma-Aldrich, DN25) in RPMI 1640 with 5% FBS for 45 min at 37 °C. After digestion, tumor tissue was passed through 70-μm filters and mononuclear cells were collected on the interface fraction between 40 and 80% per cell. Live cells (Zombie NIR negative) were gated using Zombie-violet (Catalog: 423105) staining. Next cells were gated using FSC-A and FSC-H to exclude doublets. Lymphocytes were gated on SSC-A and FSC-A. $CD4^+$ and $CD8^+$ TILs were gated on $CD45^+CD3^+$ cells.

The following mAbs recognizing the indicated antigens were used: FITC-anti-CD3 (Clone: 17A2, Catalog: 100204, 1:100), BV605-anti-CD4 (Clone: GK1.5, Catalog: 100451, 1:200), PE-Cy7-anti-CD8 (Clone: 53–6.7, Catalog: 100722, 1:200), PerCP-Cy5.5-anti-CD45 (Clone: 30-F11, Catalog: 103129, 1:400), Zombie-violet (Catalog: 423105), and APC-anti-IFNG (Clone: XMG1.2, Catalog: 505810, 1:100) (BioLegend). For assessment of IFNγ, cells were stimulated with 50 ng/ml phorbol 12-myristate 13-acetate (Sigma-Aldrich, P8139) and 1 μg/ml ionomycin (Fisher Scientific, BP25271) in the presence of Brefeldin A (BioLegend, 420601) for 4 h. After incubation, cells were then fixed. After surface staining, cells were permeabilized using the BioLegend Kit (Catalog: 421002) and. Data were analyzed using FlowJo (version 10.5.3; FlowJo LLC).

4.4.18 Mice and UVB/Arsenic treatment

All animal procedures have been approved by the University of Chicago Institutional Animal Care and Use Committee. Mice with wild type (WT; $FTO^{flox/lox}$, kindly provided by Dr. Pumin Zhang) and conditional skin-specific FTO deletion (*Fto* cKO, K14Cre;$FTO^{flox/lox}$) in the SKH-1 background were generated used for UVB irradiation and arsenic treatment experiments. Mice will be exposed to arsenic continuously in drinking water and then repeated UVB irradiation as described previously. Mice will be treated with arsenite (106277; EMD Millipore) in drinking water at 1.25 mg/L starting at 21 days of age, as described previously 12; Next, at 42 days of age, mice will be irradiated Start with UVB 80 mJ/cm^2 and increase UV dose by 10% every week until it reaches 100 mJ/cm^2.

4.4.19 m^6A dot blot assay

Total RNA was extracted using an RNeasy plus Mini Kit (QIAGEN, Hilden, Germany), following the manufacturer's protocol. For mRNA isolation, total RNA was extracted using an RNeasy mini kit with DNase I on-column digestion, followed by polyadenylated RNA extraction using a Dynabeads mRNA Purification Kit (Life Technology, Carlsbad, CA). Then mRNA was concentrated with an RNA Clean & Concentrator-5 kit (Zymo Research, Irvine, CA). Briefly, RNA samples were loaded onto Amersham Hybond-N + membrane (GE Healthcare, Chicago, IL) and crosslinked to the membrane with UV radiation. Then the membrane was blocked with 5% nonfat dry milk (in 1X PBST) for 1–2 h, incubated with a specific anti-m^6A antibody (Synaptic Systems, 202003, 1:2000) overnight at 4 °C followed by HRP-conjugated anti-rabbit IgG (Cell Signaling Technology) for 1 h at room temperature, and then developed with Thermo ECL SuperSignal Western Blotting Detection Reagent (Thermo Fisher Scientific, Waltham, MA).

4.4.20 mRNA stability assay

A transcriptional inhibitor, actinomycin D (2 μM), inhibits mRNA transcription. Each sample was harvested at 0, 3, and 6 h after treatment with actinomycin D. Total RNA was isolated with an RNeasy plus mini kit (QIAGEN). The HPRT1 housekeeping gene was used as a loading control. HPRT1 mRNA does not contain m^6A modifications, is not bound by YTHDF2, and is rarely affected by actinomycin D treatment[66].

4.4.21 mRNA m^6A MeRIP-Seq

100–150 μg total RNA was extracted from cells using TRIzol following the manufacturer's protocol. mRNA was purified using a Dynabeads mRNA DIRECT Kit following the manufacturer's protocols. One microgram mRNA was sonicated to ~200 nt, 5% of fragmented mRNA was saved as input, and m^6A containing mRNA fragments were enriched with an EpiMark N6-Methyladenosine Enrichment Kit following the manufacturer's protocols. Finally, together with the input, IP RNA was extracted using RNA Clean and Concentrator kit (Zymo Research), followed by library preparation using the TruSeq stranded mRNA sample preparation kit (Illumina).

4.4.22 mRNA m^6A MeRIP-Seq data analysis

General pre-processing of reads: sequencing were performed using Illumina Hiseq4000 with single end 80 bp read length. The adapters were removed by using cutadapt for m^6A-seq, reads were aligned to the reference genome (hg38) in Tophat v2.0.14 using the parameter -g 1–library-type = fr-firststrand. RefSeq Gene structure annotations were obtained from the UCSC Table Browser. If a gene had multiple isoforms, the longest isoform was used. In order to eliminate the interference caused by introns in peak calling, aligned reads were extended to 150 bp (average

fragment size) and converted from genome-based coordinates to isoform-based coordinates. The method used for peak calling was adopted from published work with modifications[15]. For calling m^6A peaks, a gene's longest isoform was scanned using a sliding window (100 bp) with a step of 10 bp. To minimize bias from potential inaccuracy in gene structure annotation and/or the longest isoform, windows with read counts of less than 1/20 of the top window in both m^6A-IP and the input were excluded. The read counts in each window for each gene were normalized by the median count of all windows for the gene. The differential windows between IP and input samples were identified using a Fisher exact test. If the FDR < 0.01 and $\log_2$(Enrichment Score) ≥ 1, the window was considered as positive. Overlapping positive windows were merged. To obtain the enrichment score of each peak (or window), the following four numbers were calculated: (1) read counts of the IP samples in the current peak/window, (2) median read counts of the IP sample in all 100 bp windows on the current mRNA, (3) read counts of the input sample in the current peak/window, and (4) median read counts of the input sample in all 100 bp windows on the current mRNA. For each window, the enrichment score was calculated as $(a \times d)/(b \times c)$.

4.4.23 Gene-specific m^6A MeRIP-RT-qPCR

MeRIP-RT-qPCR was performed to assess the relative abundance of the selected mRNA in m^6A MeRIP-Seq dataset. Briefly, total RNA was isolated with RNeasy mini kit. With 500 ng RNA kept as an input sample, the remaining RNA was used for m^6A-immunoprecipitation. 100 μg of RNA was diluted into 500 μl IP buffer (150 mM NaCl, 0.1% NP-40, 10 mM Tris, pH 7.4, 100 U RNase inhibitor) and incubated with m^6A antibody (Synaptic Systems). The mixture was rotated at 4 °C for 2 h, then Dynabeads® Protein A (Thermo Fisher Scientific, Waltham, MA) coated with BSA was added into the solution and rotated for an additional 2 h at 4 °C. After washing by IP buffer with RNase inhibitors four times, the m^6A IP portion was eluted with elution

buffer (5 mM Tris-HCL pH 7.5, 1 mM EDTA pH 8.0, 0.05% SDS, and 4.2 µl Proteinase K (20 mg/ml)18. The final eluted mRNA was concentrated with an RNA Clean & Concentrator-5 kit (Zymo Research, Irvine, CA). The same amount of the concentrated IP RNA or input RNA from each sample was used for the cDNA library. The mRNA expression was determined by the number of amplification cycles (Cq). The relative m^6A levels in genes were calculated by the m^6A levels (m^6A IP) normalized using the expression of each gene (Input).

4.4.24 Microarray analysis

RNA was extracted from Mel624 cells with or without FTO knockdown with the RNeasy Mini Kit (Qiagen, Hilden, Germany), according to the manufacturer's instructions. Total RNA concentration and purity were determined with NanoDrop (Thermo Scientific, Waltham, Mass), and total RNA integrity was confirmed with the Agilent Bioanalyzer (Agilent Technologies, Santa Clara, Calif). The RNA samples were processed with the HumanHT-12 v4.0 Gene Expression BeadChip microarray (Illumina) at the Functional Genomics Core Facility of the University of Chicago.

4.4.25 Differentially expressed genes (DEG) analysis

The DEG was performed by NetworkAnalyst (http://www.networkanalyst.ca), an R programming languages-based tool for comprehensive gene expression profiling 20. The edgeR method was selected with adjusted $P < 0.05$ to identify the DEGs between mouse and human non-tumor skin (CHR) and cuSCC.

4.4.26 GO, KEGG, GSEA, Venn diagram, and heatmap analysis

Gene ontology (GO) enrichment and Kyoto Encyclopedia of Genes and Genomes (KEGG) pathway enrichment analyses were performed using Metascape and NetworkAnalyst. $P < 0.05$ was

considered to indicate a significantly enriched DEG. (ref). Gene Set Enrichment Analysis (GSEA) and the heatmap of relatively significant genes were performed using NetworkAnalyst and WebGestalt (ref). Venn diagram was generated with the following statistical cutoff: p value < 0.05 in combination with $\log_2$(fold change) > 0.5 or < -0.5 for human cuSCC/CHR and mouse cuSCC/NS, or $\log_2$(TPM) > 0.5 or < -0.5 for As-T cells/Control cells.

4.4.27 ATAC-Seq and data analysis of ATAC-Seq and ChIP-Seq

Please refer to section **3.4.8** for library preparation of ATAC-Seq; section **3.4.25** for ATAC-Seq data analysis; and section **3.4.26** for ChIP-Seq data analysis.

4.4.28 DNase I-TUNEL assay and nascent RNA labeling assay

Please refer to section **3.4.6** for DNase I-TUNEL assay; and section **3.4.7** for Nascent RNA labeling assay.

4.4.29 Statistical analyses

Statistical analyses were carried out using Prism 6 and 7 (GraphPad). Data were obtained from at least three independent experiments and for statistical significance were analyzed using Student's *t*-test or Mann–Whitney *U*-test. $P < 0.05$ was considered statistically significant.

4.4.30 Data availability

Section **4.2.1**:

Sequencing data and microarray data have been deposited into the Gene Expression Omnibus (GEO) under the accession number GSE112902 and GSE128961, respectively.

Section **4.2.2**

Sequencing data have been deposited into the Gene Expression Omnibus (GEO) under the accession number GSE151780. The analysis in **Figure 4.7** utilized data from the ENCODE ChIP-Seq database.

Section **4.2.3**:

Sequencing data have been deposited into the Gene Expression Omnibus (GEO) under the accession number GSE145923. The analysis in **Figure 4.7** utilized data from GSE84292 and GSE84293.

Chapter 5

Summary and Perspectives

5.1 Context-dependent function and regulation of RNA m^{6}A and FTO

The mechanistic and functional studies of RNA m^{6}A in assorted biological contexts have underscored multifaceted and tunable features of its functions. Why does context matter in m^{6}A epitranscriptomics? An m^{6}A effector may exhibit different expression levels, PTMs, cellular localization, and phase separation, depending on cell types and/or in response to environmental stimuli. Meanwhile, the intrinsic heterogeneity of RNA molecules further complicates the local contexts of m^{6}A and challenges interpretation of experimental data: (i) diversity in RNA species, including mRNA, tRNA, rRNA, and other abundant non-coding/regulatory RNAs; (ii) a wide range of cellular abundances for RNA species including individual mRNA sequences—1 to 50 copies for most protein-coding genes[202]; (iii) complex RNA secondary structures (stem, loop, and bulge, *etc*); (iv) varying compaction and thus accessibility of individual RNA sequences depending on cellular localization and translation state[203]; as well as other variable factors. Moreover, *cis*-elements in RNAs and *trans*-elements including different RNA binding proteins (RBPs) may regulate the interactions between m^{6}A effectors and RNA substrates. Together, the occurrence and biological outcome of RNA m^{6}A can be highly context-dependent, providing a unique potential to tune gene expression in different biological processes.

5.1.1 FTO-mediated RNA demethylation is context-dependent

In 2011, the discovery of FTO as the first RNA demethylase launched the concept that RNA modifications can be dynamic and actively reversed, thereby reigniting the investigations of m^{6}A biology. FTO was later reported to be able to remove m^{6}A$_m$, a modification that has an

identical chemical structure in the base moiety to m^6A and is found on the second base adjacent to the 5' cap (cap-m^6A_m), in a portion of mRNAs[133-135]. Part of my doctoral work comprehensively characterized the substrate spectrum of FTO by carefully validating FTO binding targets from CLIP-Seq results, revealing that FTO possesses effective demethylation activity towards m^1A in specific tRNAs, m^6A_m in some snRNAs, as well as internal m^6A and cap-m^6A_m in mRNA[63].

FTO was originally found in cell nucleus but could shuttle to the cytoplasm in certain cell lines[63,138,139]. The spatial regulation of FTO may modulate its accessibility towards cellular substrate(s), leading to distinct substrate preference in the nucleus *versus* the cytoplasm. FTO mediates tRNA m^1A, mRNA internal m^6A, and cap-m^6A_m demethylation in the cytoplasm, but mostly mRNA m^6A demethylation in cell nucleus, perhaps because the mRNA cap moiety is bound by cap-binding proteins in the nucleus and not accessible for demethylation[137]. Additionally, the level of cap-m^6A_m is below one-tenth of that of internal m^6A in mRNA in multiple cell lines and tissues[47,59,63,146,204]. In terms of the absolute amount, FTO predominantly mediates demethylation of internal m^6A *versus* cap-m^6A_m inside cells despite cap-m^6A_m being a preferred substrate *in vitro*. Functionally, the effect of FTO on regulating transcript abundance assigned to cap-m^6A_m demethylation[40] was carefully dissected by us and proven to be associated with mRNA internal m^6A demethylation[63]. This confusion was further resolved as the deposition of cap-m^6A_m by its methyltransferase PCIF1 does not alter gene expression or transcript stability[146,147]. The role of cap-m^6A_m in translation was also controversial[40,150], which could also be context-dependent and remains to be clarified.

In melanoma and arsenic-tumorigenic cells, FTO-targeted m^6A can be either recognized by IGF2BPs or YTHDF2. Locations of internal m^6A sites on an mRNA add complexity to the context-dependent function of m^6A, as exemplified by *MYC*, which is enriched with m^6A and plays

a central role in oncogenic process[205] (**Figure 5.1**). In collaboration with Professor Jianjun Chen from City of Hope, we found that FTO mainly targeted the m^{6}A at 5' UTR and middle exons, while ALKBH5 demethylated m^{6}A at coding region instability determinant (CRD) near 3'UTR. Tethering reporter assays further revealed that YTHDF2 exhibited stronger binding to 5'UTR and CDS, while IGF2BPs preferred binding to CRD. Thus, stability of *MYC* can be positively regulated by IGF2BPs, but negatively regulated by YTHDF2. To investigate the crosstalk among m^{6}A effectors and the function of m^{6}A in the specific regions of mRNA at the whole-genome level, we also performed PAR-CLIP-Seq of multiple m^{6}A effectors (including YTHDF1-2, IGF2BP1-3, METTL3/14, ALKBH5, and FTO) and m^{6}A MeRIP-Seq with stable overexpression or knockdown of m^{6}A writers and erasers (manuscript in preparation).

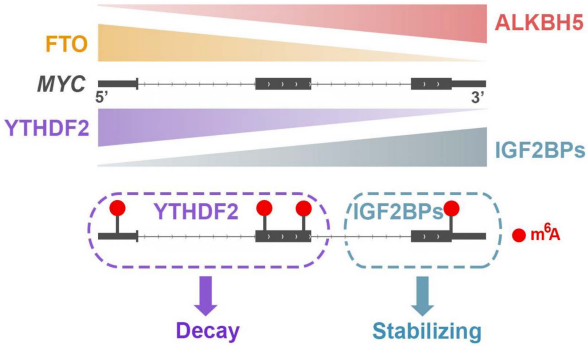

Figure 5.1 A schematic model showing gene region specific m^{6}A regulation on mRNA
FTO and ALKBH5 demethylate m^{6}A at different regions on *MYC*. YTHDF2 and IGF2BPs recognize these m^{6}A sites with different preferences to regulate the stability of *MYC*.

In addition to the translocation in cell lines, FTO was also found *in vivo* in the cytoplasm, specifically in the adipose tissue[156], consistent with our observation that one-third of FTO can be distributed in the cytoplasm of 3T3-L1 cells. These findings indicate that the involvement of FTO in metabolic processes could be associated with tRNA m^{1}A or cap-m^{6}A$_m$ demethylation. However, in most mammalian tissues and stem cells, FTO is predominantly nuclear-localized. FTO has been shown to play vital roles during mammalian development; the *Fto*$^{-/-}$ mice display intriguing phenotypes, including a notable proportion of embryo and postnatal lethality as well as postnatal

growth retardation. Therefore, my major work focused on the nuclear regulatory roles of FTO to identify the physiologically relevant substrate(s) of FTO contributing to these intriguing phenotypes, and to address the important question of the presence and functional relevance of RNA m^6A demethylation in mammals.

We found FTO demethylates m^6A within repeat RNAs, especially LINE1 RNA, thereby affecting their abundance to regulate chromatin state in mESCs, mNSCs, and certain mouse tissues. In mESCs and mNSCs, this FTO-mediated m^6A demethylation of LINE1 RNA regulates chromatin state and plays important roles in differentiation and proliferation. Analysis of the m^6A methylome across human and mouse tissues suggests LINE1 RNA m^6A as a general substrate of FTO in most tissues, indicating LINE1 RNA m^6A demethylation as a prevalent process in mammals. Depletion of FTO leads to notable ovary and oocyte defects with dramatic reduction of LINE1 RNA level in GV oocytes, revealing the physiological significance of this process. Of note, FTO-mediated chromatin regulation depends on the biological context. Though LINE1 RNA m^6A is a general substrate of FTO and responsible for the effects of FTO on chromatin state in the aforementioned stem cells and mammalian tissues, this is not necessarily the case in certain cancer cells in which m^6A demethylation of mRNAs encoding histone modifiers may dominate chromatin regulation. The context-dependent m^6A methylation and demethylation regulation is crucial in assessing physiologically relevant functions of methylation effectors.

5.1.2 FTO is regulated by biological context

Careful analysis of the functionally relevant substrate of FTO in a specific cell context will be critical in future studies of RNA demethylation. How does cell context regulate FTO in turn? What is the molecular basis for differential expression and cellular localization of FTO protein? FTO protein has been shown to bear multiple PTMs, including ubiquitination, phosphorylation,

and SUMOylation. The translocation and expression of FTO can be regulated by ubiquitination at Lys-216[206]. Casein kinase II (CKII)-mediated phosphorylation of FTO at Thr-150 was also shown to regulate the nucleocytoplasmic shuttling of FTO[207]. In hepatocellular carcinoma (HCC), SIRT1 actives RANBP2, a critical component of small ubiquitin-related modifiers (SUMOs) E3 ligase, to mediate FTO SUMOylation at Lys-216 and therefore promotes FTO degradation[57].

The expression of FTO has also been reported to be associated with autophagy signaling and stress response. In melanoma cells, starvation-induced FTO mRNA is associated with the function of certain autophagy essential genes[55]. On the other hand, arsenic compromises autophagic degradation of FTO. It is noteworthy that though a positive feedback loop is formed between the upregulated FTO and suppressed autophagy in arsenic tumorigenic cells (in revision), FTO knockdown impairs autophagy in preadipocytes[195], presenting another example of the context-dependent role of FTO. Moreover, FTO can be induced in response to stress like UV damage[49] and heat shock[54] to fine-tune the RNA m^6A at specific sites.

In addition to expression regulation, inhibition of FTO by an endogenous oncometabolite 2-hydroxyglutarate (2-HG) suppresses leukemia progression[59]. This effect is again context-dependent, as FTO high AML cells are more sensitive to 2-HG inhibition[59]. Our collaborative study with Professor Haojie Huang from Mayo Clinic in prostate cancer cells also identified a lncRNA that can bind to FTO to modulate the global mRNA m^6A demethylation and consequently control the prostate cancer progression (manuscript in preparation).

It is also likely that FTO can be recruited to different cellular substrates by its interacting partners. The additional *C*-terminal domain of FTO, which is absent in the other AlkB family proteins[208,209], may endow FTO with the ability to associate with protein partners or protein-RNA interactions. These structural features may allow FTO to accomplish demethylation of different

RNA substrates *via* interacting with diverse partner proteins depending on the cellular context. Indeed, among all the identified protein partners of FTO, SFPQ is known to facilitate the demethylation site preference along the mRNA[210]. Note that SFPQ helps maintain chromosome integrity and is spotted in the list of LINE1 RNA binding proteins[211-213]. One can speculate that SFPQ could play an important role in guiding FTO to its LINE1 RNA targets.

Collectively, FTO protein is subjected to the regulation of specific cellular and molecular contexts, including PTMs, external stimuli, and certain cell signaling pathways. It is important to take into consideration these context complexities to refine and advance our understanding of the regulations of FTO and m^{6}A demethylation (**Figure 5.2**).

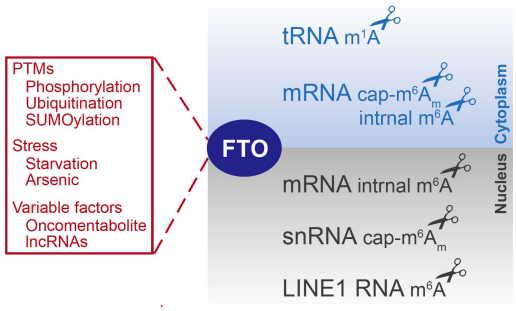

Figure 5.2 A schematic model showing the context-dependent regulation and function of FTO
The expression (degradation), cellular localization, and demethylase activity can be regulated by PTMs, stress, and cell signaling, potentially providing explanations for the multifunctionality and the specificity of FTO-mediated demethylation dependent on the biological context.

5.2 Chromatin and transcriptional regulation by RNA m^{6}A

The mechanistic and functional studies during the past decade mainly focused on how m^{6}A plays regulatory roles at the post-transcriptional level. Emerging evidence has suggested the co-transcriptional mechanism of m^{6}A deposition. Dynamics of RNA polymerase II (RNAP II) can impact the deposition of m^{6}A on mRNAs as slow or paused RNAP II enhances m^{6}A installation through a better association with MTC[214]. The crosstalk between MCT and transcription factors or

histone modifications can mediate the specificity of m^{6}A deposition. Transcription factors SMAD family member2/3 (SMAD2/3) promotes the binding of the MTC to nascent mRNA to facilitate the transcript selectivity[215]. Guided by transcription factor CCAAT Enhancer Binding Protein Zeta (CEBPZ), METTL3 associates with chromatin and localizes at the transcriptional start sites of active genes to methylate coding regions[104]. The gene body-enriched histone mark H3K36Me3 directly binds to METTL14, which endows m^{6}A deposition favoring CDS and 3' UTR[216].

There have been emerging studies in recent years which also revealed a feedback regulation in addition to the traditional central dogma (**Figure 5.3**). RNA m^{6}A could affect transcription and chromatin structure. The mechanism can be (i) mRNA m^{6}A impacts the metabolism of the mRNAs that encode histone modifiers, transcriptional factors, or key proteins in transcription regulation; (ii) m^{6}A regulates the cellular fate of pre-mRNA and some critical ncRNAs, especially carRNAs.

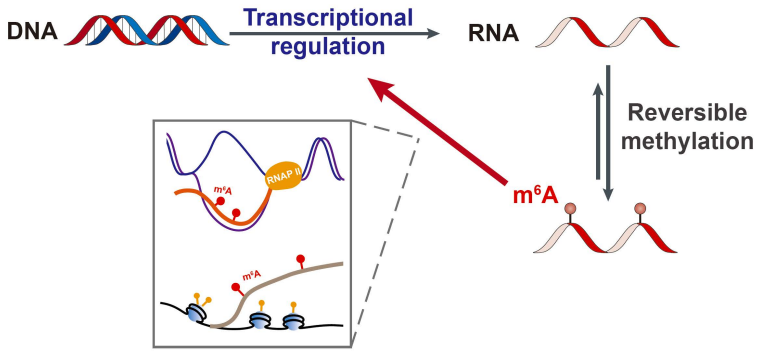

Figure 5.3 A schematic model showing the direct transcriptional regulation by RNA m^{6}A
Chromatin state and transcription can be directly regulated by m^{6}A on pre-mRNA and carRNAs.

5.2.1 Transcriptional regulation by mRNA m^{6}A

mRNA m^{6}A could further modulate gene expression through transcriptional regulation by histone modifications. As shown in section **4.2.2**, FTO mediates chromatin and transcriptional regulation in melanoma cells through this mechanism. In mNSCs, CBP and p300, transcripts encoding acetyltransferases for the active transcription mark H3K27Ac, are m^{6}A methylated. These transcripts are stabilized upon loss of m^{6}A and lead to increased H3K27Ac[166]. During

bacterial infection, KDM6B is m^{6}A-modified and undergoes YTHDF2-mediated degradation. Loss of YTHDF2 stabilizes *KDM6B* transcript to induce H3K27Me3 demethylation, thereby enhancing the downstream transcription[217]. In AML cells, promoter-bound METTL3 deposits m^{6}A in the coding region of transcripts encoding transcription factors SP1 and SP2 to promote their translation. METTL3 depletion leads to significantly reduced protein expression of SP1 and SP2, indicating an activating role of mRNA m^{6}A in SP1- and SP2-dependent transcription[104]. In certain cancer cells, IGF2BP1 can increase the mRNA level of transcription factor SRF by stabilizing its 3'UTR m^{6}A, thereby promoting SRF-dependent transcriptional activity[108].

Additionally, mRNA m^{6}A has been shown to play important roles in circadian rhythm maintenance[218] and cell cycle control[121]. Considering circadian rhythm could involve a negative feedback loop on gene expression through transcription repression[219], and cell cycle control is closely connected to histone mRNA metabolism, DNA replication, and transcription[220,221], one can speculate that m^{6}A on mRNAs that encode clock proteins and cell cycle markers could also indirectly regulate transcription and result in prolonged effects.

5.2.2 Transcriptional regulation by m^{6}A on pre-mRNA

It is not surprising that mRNAs encoding key proteins in transcriptional regulation are m^{6}A methylated, therefore m^{6}A could affect transcription through tuning the levels of these mRNAs and thus proteins. Moreover, the m^{6}A methylation on pre-mRNA can be reversible and can play important roles in transcription and pre-mRNA processing as well as nuclear decay of certain regulatory RNAs to affect the transcriptional outcome.

m^{6}A is found on the RNA moiety in the formation of RNA:DNA hybrids to regulate the stability of R-loops, thereby affecting transcription initiation, elongation, and termination. In human pluripotent stem cells (hPSCs), YTHDF2 can be recruited to these m^{6}A sites where it

subsequently facilitates the degradation of RNA:DNA hybrids. METTL3 depletion leads to the accumulation of R-loops, implying a critical role for m^6A processing in safeguarding genomic stability[222]. However, in Hela cells, instead of accelerating the removal of R-loops, m^6A promotes R-loop formation to assist transcription termination, and therefore METTL3 aids transcription termination[223]. A study of DNA double-strand break (DSB) repair provided evidence that RNA m^6A leads to the accumulation of RNA:DNA hybrids. In U2OS cells, methylated RNA by METTL3 is enriched at DSBs, which can be recognized and protected by YTHDC1[224].

The connection between RNA m^6A and the transcriptional process was supported by genetic analyses of m^6A quantitative trait loci (QTLs)[225]. m^6A has been reported to regulate the occupancy and promoter-proximal pausing of RNAP II. m^6A sites in pre-mRNA interact with hnRNPG to modulate RNAP II occupancy, thereby affecting alternative splicing likely through RNAP II pausing[72]. In *Drosophila*, MTC interacts with chromatin and binds to promoters to aid the release of RNAP II from the paused state. Knockdown of METTL3 or METTL14 hinders transcriptional elongation, revealing positive feedback of m^6A on the transcription machinery[226]. The model of the co-transcriptional interplay between m^6A and histone modifications reveals the transcriptional induction role of RNA m^6A. m^6A co-transcriptionally directs KDM3B by YTHDC1 to target chromatin to demethylate H3K9Me2. The existence of m^6A promotes the demethylation of H3K9me2 and consequently promotes the overall transcriptional activity in gene bodies[227].

5.2.3 Chromatin and transcriptional regulation by m^6A on carRNAs

Our lab revealed critical nuclear regulation events mediated through reversible carRNA m^6A methylation[158]. In mESCs, METTL3 or YTHDC1 depletion increases global chromatin accessibility and activates nascent transcription. A portion of m^6A on carRNAs is installed by METTL3 and negatively correlates with carRNA abundance. YTHDC1 recognizes and recruits

the nuclear exosome targeting (NEXT) complex to some of these m^{6}A sites, ultimately facilitating the degradation of at least a subset of methylated carRNAs. Upon METTL3 depletion, m^{6}A-methylated carRNAs display reduced m^{6}A levels and increased abundance. Meanwhile, the downstream genes of these methylated carRNAs exhibit elevated transcription rates. Moreover, loss of m^{6}A on carRNAs leads to enrichment of active histone markers and open chromatin at carRNA loci[158]. Note that in mESCs and endometrial cancer cells, this chromatin regulation through carRNA degradation mediated by METTL3-m^{6}A-YTHDC1 axis dominates; however, in other cancer cells, YTHDC1 may carry out other nuclear functions. Cell context is important when dissecting the exact regulatory pathways. As discussed in chapter **3**, FTO demethylates m^{6}A within repeat RNAs, especially LINE1 RNA, which affects their abundance and consequently regulates chromatin state in multiple stem cells and mammalian tissues. This process appears to provide a decent explanation for FTO-associated developmental defects.

Reversible m^{6}A on these key regulatory RNAs serves as a switch that can globally tune chromatin state and directly modulate transcription of hundreds to thousands of genes, adding another layer of chemical modifications on bio-macromolecules to chromatin regulation in addition to DNA and histone modifications, which may have broad implications in the development and normal function of mammalian tissues and human diseases. Two latest studies further extended the chromatin state regulation by showing that RNA m^{6}A methylation of ERVs is critical to their transcript stability[228] and the establishment of local heterochromatin[229].

5.3 Future directions

5.3.1 Advance the m^{6}A sequencing method

The initial transcriptome-wide mappings of m^{6}A sites relying on the anti-m^{6}A antibody to enrich m^{6}A-containing RNA fragments with a length of 100~200 nt (MeRIP-Seq), together with

the following improved versions, including PA-m^{6}A-Seq[17], miCLIP-Seq[18], and m^{6}A-LAIC-seq[230], have become useful tools in the field and have enabled many studies of m^{6}A and its biological functions. However, the antibody-based strategy suffers from several major limitations, such as low resolution, a lack of stoichiometric information, a requirement of a large amount of input materials, and a limited ability to compare m^{6}A methylation across conditions[231]. More recently, a series of antibody-free methods have been developed. MAZTER-seq[19] and m^{6}A-REF-seq[20] utilize the MazF RNase to selectively cleave RNA at unmethylated ACA motifs but not methylated m^{6}ACA motifs[232], allowing quantitative detection of m^{6}A at m^{6}ACA motifs with single-nucleotide resolution after subtraction. Unfortunately, these methods only capture ~16% of m^{6}A sites in this specific motif in the mammalian system. No need for subtraction, DART-seq method fuses an m^{6}A-binding YTH domain to an RNA editing enzyme to induce mutations at sites adjacent to m^{6}A residues[21]. This method maps global m^{6}A using limited input material and potentially enables compartmentalized m^{6}A detection through an additional fusion of localization elements. However, it still lacks quantitative information regarding the m^{6}A site and stoichiometry.

A quantitative technique requiring low-input RNAs that profiles whole-transcriptome m^{6}A sites with stoichiometric information is demanded. Such a 'perfect' method may empower the evaluation of contributions of specific m^{6}A sites to biological significances and enable the analysis of potential global dynamic changes during cell-state transition, cell signaling or stress responses.

5.3.2 Interplay between different RNA modifications and/or other epigenetic marks

As introduced in section **1.2**, more than 170 post-transcriptional modifications existing on multiple RNA species have been identified to date; the list of RNA modifications is still growing. Some RNA modifications existing on different RNA species are reported to be deposited by the same writer, including m^{1}A on tRNA/mRNA (by TRMT6/61A, TRMT61B, or TRMT10C)[233,234],

ac^{4}C on tRNA/rRNA/mRNA (by *N*-acetyltransferase 10, NAT10)[235], m^{5}C on tRNA/mRNA (by NSUN2 or NSUN6)[145,236,237], and m^{3}C on tRNA/mRNA (by METTL8)[238]. Meanwhile, some RNA modifications can be subjected to oxidative demethylation mediated by the same eraser (oxidizer), such as m^{1}A on tRNA/mRNA (by ALKBH3)[239,240], m^{5}C on tRNA/mRNA (by TET2 or TRDMT1)[241-243], not to mention the complex substrate spectrum of FTO[63]. How do these effectors balance the multifunctionality and the specificity? How does the biological context regulate the role of these effectors? Efforts have been made to study the context-dependent function and regulation of FTO. As discussed in section **5.1.2**, future research will hopefully answer the question of how FTO is regulated to approach its preferential substrates dependent on the biological context. Of note, *N*^{6}-hydroxymethyladenosine (hm^{6}A) is a stable intermediate of FTO-mediated m^{6}A demethylation[132,149]. It would be intriguing to study the function of this intermediate modification, especially with the recently designed m^{6}A-SEAL method[244].

Besides the intermediate, modification interdependence has been reported in tRNAs, in which one modification is a prerequisite for another. For instance, methylation of cytosine to m^{3}C is a pre-requisite for the subsequent cytosine-to-uridine (C-to-U) deamination[245]. Enzymes for each of these two steps are required to exert the function. Adenosine-to-inosine (A-to-I) editing is one of the most abundant RNA editing events. Does this functionally interdependent activity also exist on mRNA and other RNA species? Moreover, different modifications can exist on the same transcript (i.e., internal m^{6}A and cap-m^{6}A$_m$). The combinational effect of these modifications may be distinct to the individual function of each modification. The interaction of different RNA modification effectors also needs to be considered. A recent study demonstrated that FTO can interact with tRNA methyltransferase 10A (TRMT10A) and cooperatively tune mRNA translation of target transcripts by generating the codon usage bias through the crosstalk of mRNA m^{6}A and

tRNA m^1G9[246]. This model may provide a new angle to study the interplay of RNA modifications, especially in the translation process where mRNA, tRNA, and mRNA coordinates with each other.

In section **5.2**, we discussed the complex regulatory network of epigenetic pathways with m^6A as a central player inside. Similar to RNA modifications on different RNA species, studies have revealed that modification effectors can functionalize across RNA and DNA, including TET2 (m^5C on tRNA/mRNA; DNA 5mC and oxidative derivatives)[241,242,247,248], ALKBH1 (tRNA m^1A and DNA 6mA)[144,249], and METTL4 (snRNA m^6A_m and DNA 6mA)[155,169,250]. Again, it would be interest to investigate the underlying mechanism of their multifunctionality and specificity. m^6A[222-224], m^5C[224] and m^3C[251] have been found on the RNA moiety of the RNA:DNA hybrids to regulate its stability, thereby potentially affecting the transcription process. Do DNA modifications also exist on the RNA:DNA hybrids? If so, how do they crosstalk with RNA modifications and regulate RNA:DNA hybrids? In addition to the targeted editing of specific RNA methylation sites, simultaneous profiling and integrative analysis (even at single-cell level) of epigenome and epitranscriptome would add a new dimension to the growing canvas of gene regulation and further decipher the multi-layer regulatory information that controls a plethora of biological functions.

5.3.3 Site-specific editing of RNA modifications

Despite the progress in understanding the biological roles of mRNA m^6A, the field lacked tools to dissect the causal relationship between specific m^6A sites on the modified RNAs and functional consequences for a long time. Recently, the targeted methylation editing systems have been established taking advantage of CRISPR-based technology. The engineered m^6A writer by fusing methyltransferase domains from METTL3 and METTL14 to catalytically inactive Cas9 (dCas9) can be directed to the desired region on the transcript of interest by sgRNA to achieve single-site methylation, whereas site-specific removal m^6A can be achieved by fusing the full-

length ALKBH5 or FTO to dCas9[252]. Similar targeted m^{6}A deposition systems can be also constructed by fusing binding-impaired methyltransferase truncations to dCas13b[253]. This dCas13b system can further direct site-specific m^{6}A installation in distinct cellular compartments by adding a certain signal sequence to it[253]. These m^{6}A enzyme-dCas systems can serve as versatile toolboxes to explore the regional effects of m^{6}A methylation. Incorporation of writers and erasers of other RNA modifications in these systems may enable the study of the crosstalk and interdependence discussed in section **5.3.2**.

In addition to the bacteria-based systems, a CRISPR–Cas-inspired RNA targeting system (CIRTS) has also been developed as a platform for engineering and delivering diverse programmable RNA effectors to target transcripts[254]. CIRTS is composed of a single-stranded RNA-binding protein, an RNA hairpin-binding protein, an effector protein, and a guide RNA. Components of CIRTS are built entirely from the human genome, and the protein part is much smaller than that of natural CRISPR–Cas systems. Engineered m^{6}A 'reader' proteins have been successfully constructed and delivered *via* CIRTS to modulate the translation or stability of target transcripts. Site-specific installation or removal of m^{6}A by an engineered 'writer' or 'eraser' with CIRTS could offer a humanized system to manipulate the human RNA epi-transcriptome.

5.3.4 m^{6}A-mediated chromatin regulation: towards epigenetic inheritance

Studies of critical roles of m^{6}A on carRNAs offer numerous opportunities for both basic studies of gene regulation and their potential involvement in human diseases. There are still many questions that remain to be answered. We have not identified all of the nuclear m^{6}A effectors. How do these effectors interact with transcription factors, chromatin remodelers, histone modifiers, and DNA methylation systems? What are the pathways in which these effectors and nuclear RNA m^{6}A integrate into the transcriptional regulation network? How does cellular signaling regulate carRNA

methylation and its overall impacts on transcription? Could tuning of carRNA methylation synergize with existing therapies that target epigenetic pathways? There are clearly other reader proteins involved to modulate the stability of m^6A methylated carRNAs besides YTHDC1. While promoting the decay of some carRNAs, YTHDC1 also plays a role in other nuclear processes dependent on RNA m^6A methylation. Its post-translational modification status could be a key factor in its biological function and this can be very much cell context-dependent. YTHDC1 is prone to granule formation and is known to form the YTH nuclear body[255]. YTHDC1 in and outside of the granule may perform very different functions.

It is interesting that repeat RNAs are quite heavily methylated. One can speculate that the initial methylation is a way to control the activation of retrotransposon RNAs, leading to their decay during evolution. Additional regulatory roles might have evolved later on. It is not known how reversible methylation on repeat RNAs affects development and normal tissue function in general. We have shown that different cellular contexts would lead to opposite outcomes and we currently do not know what determines the dominant effects and effectors. Of note, RNA-dependent chromatin targeting of TET2 has also been reported to regulate ERVL and ERVL-associated gene expression by transcriptional repression through RNA hm^5C[256]. Do other RNA modifications also exist on repeat RNAs and play regulatory roles?

Lastly, we have shown that *Fto* KO led to oocyte defect likely through impaired LINE1 RNA m^6A demethylation. How does this process affect the maternal-to-zygotic transition? Chromatin states, histone modifications and certain RNA species have been implicated in transgenerational epigenetic inheritance[257,258]. Could some of the RNA modification information be inherited either through maternal effector proteins or inheritable chromatin state or histone modification set up by nuclear RNA methylation? These are all intriguing questions in the future.

LIST OF REFERENCES

1 Berger, S. L., Kouzarides, T., Shiekhattar, R. & Shilatifard, A. An operational definition of epigenetics. *Genes Dev* **23**, 781-783 (2009).

2 Luo, C., Hajkova, P. & Ecker, J. R. Dynamic DNA methylation: In the right place at the right time. *Science* **361**, 1336-1340 (2018).

3 Schubeler, D. Function and information content of DNA methylation. *Nature* **517**, 321-326 (2015).

4 Jones, P. A. Functions of DNA methylation: islands, start sites, gene bodies and beyond. *Nat Rev Genet* **13**, 484-492 (2012).

5 Lawrence, M., Daujat, S. & Schneider, R. Lateral Thinking: How Histone Modifications Regulate Gene Expression. *Trends Genet* **32**, 42-56 (2016).

6 Bannister, A. J. & Kouzarides, T. Regulation of chromatin by histone modifications. *Cell Res* **21**, 381-395 (2011).

7 Cohn, W. E. & Volkin, E. Nucleoside-5′-Phosphates from Ribonucleic Acid. *Nature* **167**, 483-484 (1951).

8 Boccaletto, P. *et al.* MODOMICS: a database of RNA modification pathways. 2017 update. *Nucleic Acids Res* **46**, D303-D307 (2018).

9 Pan, T. Modifications and functional genomics of human transfer RNA. *Cell Res* **28**, 395-404 (2018).

10 Sloan, K. E. *et al.* Tuning the ribosome: The influence of rRNA modification on eukaryotic ribosome biogenesis and function. *RNA Biol* **14**, 1138-1152 (2017).

11 He, C. Grand challenge commentary: RNA epigenetics? *Nat Chem Biol* **6**, 863-865 (2010).

12 Jia, G. *et al.* N6-methyladenosine in nuclear RNA is a major substrate of the obesity-associated FTO. *Nat Chem Biol* **7**, 885-887 (2011).

13 Perry, R. P. & Kelley, D. E. Existence of methylated messenger RNA in mouse L cells. *Cell* **1**, 37-42 (1974).

14 Desrosiers, R., Friderici, K. & Rottman, F. Identification of methylated nucleosides in messenger RNA from Novikoff hepatoma cells. *Proc Natl Acad Sci U S A* **71**, 3971-3975 (1974).

15 Dominissini, D. *et al.* Topology of the human and mouse m6A RNA methylomes revealed by m6A-seq. *Nature* **485**, 201-206 (2012).

16 Meyer, K. D. *et al.* Comprehensive analysis of mRNA methylation reveals enrichment in 3' UTRs and near stop codons. *Cell* **149**, 1635-1646 (2012).

17 Chen, K. *et al.* High-resolution N(6)-methyladenosine (m(6)A) map using photo-crosslinking-assisted m(6)A sequencing. *Angew Chem Int Ed Engl* **54**, 1587-1590 (2015).

18 Linder, B. *et al.* Single-nucleotide-resolution mapping of m6A and m6Am throughout the transcriptome. *Nat Methods* **12**, 767-772 (2015).

19 Garcia-Campos, M. A. *et al.* Deciphering the "m(6)A Code" via Antibody-Independent Quantitative Profiling. *Cell* **178**, 731-747 e716 (2019).

20 Zhang, Z. *et al.* Single-base mapping of m(6)A by an antibody-independent method. *Sci Adv* **5**, eaax0250 (2019).

21 Meyer, K. D. DART-seq: an antibody-free method for global m(6)A detection. *Nat Methods* **16**, 1275-1280 (2019).

22 Shi, H., Wei, J. & He, C. Where, When, and How: Context-Dependent Functions of RNA Methylation Writers, Readers, and Erasers. *Mol Cell* **74**, 640-650 (2019).

23 Bokar, J. A., Shambaugh, M. E., Polayes, D., Matera, A. G. & Rottman, F. M. Purification and cDNA cloning of the AdoMet-binding subunit of the human mRNA (N6-adenosine)-methyltransferase. *RNA* **3**, 1233-1247 (1997).

24 Wang, P., Doxtader, K. A. & Nam, Y. Structural Basis for Cooperative Function of Mettl3 and Mettl14 Methyltransferases. *Mol Cell* **63**, 306-317 (2016).

25 Wang, X. *et al.* Structural basis of N(6)-adenosine methylation by the METTL3-METTL14 complex. *Nature* **534**, 575-578 (2016).

26 Sledz, P. & Jinek, M. Structural insights into the molecular mechanism of the m(6)A writer complex. *Elife* **5**, e18434 (2016).

27 Liu, J. *et al.* A METTL3-METTL14 complex mediates mammalian nuclear RNA N6-adenosine methylation. *Nat Chem Biol* **10**, 93-95 (2014).

28 Ping, X. L. *et al.* Mammalian WTAP is a regulatory subunit of the RNA N6-methyladenosine methyltransferase. *Cell Res* **24**, 177-189 (2014).

29 Yue, Y. *et al.* VIRMA mediates preferential m(6)A mRNA methylation in 3'UTR and near stop codon and associates with alternative polyadenylation. *Cell Discov* **4**, 10 (2018).

30 Wen, J. *et al.* Zc3h13 Regulates Nuclear RNA m(6)A Methylation and Mouse Embryonic Stem Cell Self-Renewal. *Mol Cell* **69**, 1028-1038 e1026 (2018).

31 Patil, D. P. *et al.* m(6)A RNA methylation promotes XIST-mediated transcriptional repression. *Nature* **537**, 369-373 (2016).

32 Mendel, M. *et al.* Methylation of Structured RNA by the m(6)A Writer METTL16 Is Essential for Mouse Embryonic Development. *Mol Cell* **71**, 986-1000 e1011 (2018).

33 Doxtader, K. A. *et al.* Structural Basis for Regulation of METTL16, an S-Adenosylmethionine Homeostasis Factor. *Mol Cell* **71**, 1001-1011 e1004 (2018).

34 Pendleton, K. E. *et al.* The U6 snRNA m(6)A Methyltransferase METTL16 Regulates SAM Synthetase Intron Retention. *Cell* **169**, 824-835 e814 (2017).

35 Shima, H. *et al.* S-Adenosylmethionine Synthesis Is Regulated by Selective N(6)-Adenosine Methylation and mRNA Degradation Involving METTL16 and YTHDC1. *Cell Rep* **21**, 3354-3363 (2017).

36 Warda, A. S. *et al.* Human METTL16 is a N(6)-methyladenosine (m(6)A) methyltransferase that targets pre-mRNAs and various non-coding RNAs. *EMBO Rep* **18**, 2004-2014 (2017).

37 van Tran, N. *et al.* The human 18S rRNA m6A methyltransferase METTL5 is stabilized by TRMT112. *Nucleic Acids Res* **47**, 7719-7733 (2019).

38 Ma, H. *et al.* N(6)-Methyladenosine methyltransferase ZCCHC4 mediates ribosomal RNA methylation. *Nat Chem Biol* **15**, 88-94 (2019).

39 Zheng, G. *et al.* ALKBH5 is a mammalian RNA demethylase that impacts RNA metabolism and mouse fertility. *Mol Cell* **49**, 18-29 (2013).

40 Mauer, J. *et al.* Reversible methylation of m(6)Am in the 5' cap controls mRNA stability. *Nature* **541**, 371-375 (2017).

41 Mauer, J. & Jaffrey, S. R. FTO, m(6)Am, and the hypothesis of reversible epitranscriptomic mRNA modifications. *FEBS Lett* **592**, 2012-2022 (2018).

42 Hess, M. E. *et al.* The fat mass and obesity associated gene (Fto) regulates activity of the dopaminergic midbrain circuitry. *Nat Neurosci* **16**, 1042-1048 (2013).

43 Mathiyalagan, P. *et al.* FTO-Dependent N(6)-Methyladenosine Regulates Cardiac Function During Remodeling and Repair. *Circulation* **139**, 518-532 (2019).

44 Zhang, Q. *et al.* The RNA demethylase FTO is required for maintenance of bone mass and functions to protect osteoblasts from genotoxic damage. *Proc Natl Acad Sci U S A* **116**, 17980-17989 (2019).

45 Zhou, J. *et al.* N(6)-Methyladenosine Guides mRNA Alternative Translation during Integrated Stress Response. *Mol Cell* **69**, 636-647 e637 (2018).

46 Yu, J. *et al.* Dynamic m6A modification regulates local translation of mRNA in axons. *Nucleic Acids Res* **46**, 1412-1423 (2018).

47 Engel, M. *et al.* The Role of m(6)A/m-RNA Methylation in Stress Response Regulation. *Neuron* **99**, 389-403 e389 (2018).

48 Yan, F. *et al.* A dynamic N(6)-methyladenosine methylome regulates intrinsic and acquired resistance to tyrosine kinase inhibitors. *Cell Res* **28**, 1062-1076 (2018).

49 Xiang, Y. *et al.* RNA m(6)A methylation regulates the ultraviolet-induced DNA damage response. *Nature* **543**, 573-576 (2017).

50 Bartosovic, M. *et al.* N6-methyladenosine demethylase FTO targets pre-mRNAs and regulates alternative splicing and 3'-end processing. *Nucleic Acids Res* **45**, 11356-11370 (2017).

51 Li, L. *et al.* Fat mass and obesity-associated (FTO) protein regulates adult neurogenesis. *Hum Mol Genet* **26**, 2398-2411 (2017).

52 Yang, Y. *et al.* Extensive translation of circular RNAs driven by N(6)-methyladenosine. *Cell Res* **27**, 626-641 (2017).

53 Zhao, X. *et al.* FTO-dependent demethylation of N6-methyladenosine regulates mRNA splicing and is required for adipogenesis. *Cell Res* **24**, 1403-1419 (2014).

54 Zhou, J. *et al.* Dynamic m6A mRNA methylation directs translational control of heat shock response. *Nature* **526**, 591-594 (2015).

55 Yang, S. *et al.* m(6)A mRNA demethylase FTO regulates melanoma tumorigenicity and response to anti-PD-1 blockade. *Nat Commun* **10**, 2782 (2019).

56 Cui, Q. *et al.* m(6)A RNA Methylation Regulates the Self-Renewal and Tumorigenesis of Glioblastoma Stem Cells. *Cell Rep* **18**, 2622-2634 (2017).

57 Liu, X. *et al.* SIRT1 Regulates N(6)-Methyladenosine RNA Modification in Hepatocarcinogenesis by Inducing RANBP2-Dependent FTO SUMOylation. *Hepatology* DOI: 10.1002/hep.31222 (2020).

58 Niu, Y. *et al.* RNA N6-methyladenosine demethylase FTO promotes breast tumor progression through inhibiting BNIP3. *Mol Cancer* **18**, 46 (2019).

59 Su, R. *et al.* R-2HG Exhibits Anti-tumor Activity by Targeting FTO/m(6)A/MYC/CEBPA Signaling. *Cell* **172**, 90-105 e123 (2018).

60 Li, Z. *et al.* FTO Plays an Oncogenic Role in Acute Myeloid Leukemia as a N(6)-Methyladenosine RNA Demethylase. *Cancer Cell* **31**, 127-141 (2017).

61 Huang, Y. *et al.* Small-Molecule Targeting of Oncogenic FTO Demethylase in Acute Myeloid Leukemia. *Cancer Cell* **35**, 677-691 e610 (2019).

62 Su, R. *et al.* Targeting FTO Suppresses Cancer Stem Cell Maintenance and Immune Evasion. *Cancer Cell* **38**, 79-96 e11 (2020).

63 Wei, J. *et al.* Differential m(6)A, m(6)Am, and m(1)A Demethylation Mediated by FTO in the Cell Nucleus and Cytoplasm. *Mol Cell* **71**, 973-985 e975 (2018).

64 Shi, H. *et al.* YTHDF3 facilitates translation and decay of N(6)-methyladenosine-modified RNA. *Cell Res* **27**, 315-328 (2017).

65 Wang, X. *et al.* N(6)-methyladenosine Modulates Messenger RNA Translation Efficiency. *Cell* **161**, 1388-1399 (2015).

66 Wang, X. *et al.* N6-methyladenosine-dependent regulation of messenger RNA stability. *Nature* **505**, 117-120 (2014).

67 Hsu, P. J. *et al.* Ythdc2 is an N(6)-methyladenosine binding protein that regulates mammalian spermatogenesis. *Cell Res* **27**, 1115-1127 (2017).

68 Wojtas, M. N. *et al.* Regulation of m(6)A Transcripts by the 3'->5' RNA Helicase YTHDC2 Is Essential for a Successful Meiotic Program in the Mammalian Germline. *Mol Cell* **68**, 374-387 e312 (2017).

69 Roundtree, I. A. *et al.* YTHDC1 mediates nuclear export of N(6)-methyladenosine methylated mRNAs. *Elife* **6**, e31311 (2017).

70 Xiao, W. *et al.* Nuclear m(6)A Reader YTHDC1 Regulates mRNA Splicing. *Mol Cell* **61**, 507-519 (2016).

71 Huang, H. *et al.* Recognition of RNA N(6)-methyladenosine by IGF2BP proteins enhances mRNA stability and translation. *Nat Cell Biol* **20**, 285-295 (2018).

72 Zhou, K. I. *et al.* Regulation of Co-transcriptional Pre-mRNA Splicing by m(6)A through the Low-Complexity Protein hnRNPG. *Mol Cell* **76**, 70-81 e79 (2019).

73 Wu, B. *et al.* Molecular basis for the specific and multivariant recognitions of RNA substrates by human hnRNP A2/B1. *Nat Commun* **9**, 420 (2018).

74 Liu, N. *et al.* N6-methyladenosine alters RNA structure to regulate binding of a low-complexity protein. *Nucleic Acids Res* **45**, 6051-6063 (2017).

75 Liu, N. *et al.* N(6)-methyladenosine-dependent RNA structural switches regulate RNA-protein interactions. *Nature* **518**, 560-564 (2015).

76 Alarcon, C. R. *et al.* HNRNPA2B1 Is a Mediator of m(6)A-Dependent Nuclear RNA Processing Events. *Cell* **162**, 1299-1308 (2015).

77 Edens, B. M. *et al.* FMRP Modulates Neural Differentiation through m(6)A-Dependent mRNA Nuclear Export. *Cell Rep* **28**, 845-854 e845 (2019).

78 Zhang, F. *et al.* Fragile X mental retardation protein modulates the stability of its m6A-marked messenger RNA targets. *Hum Mol Genet* **27**, 3936-3950 (2018).

79 Hsu, P. J. *et al.* The RNA-binding protein FMRP facilitates the nuclear export of N(6)-methyladenosine-containing mRNAs. *J Biol Chem* **294**, 19889-19895 (2019).

80 Wu, R. *et al.* A novel m(6)A reader Prrc2a controls oligodendroglial specification and myelination. *Cell Res* **29**, 23-41 (2019).

81 Edupuganti, R. R. *et al.* N(6)-methyladenosine (m(6)A) recruits and repels proteins to regulate mRNA homeostasis. *Nat Struct Mol Biol* **24**, 870-878 (2017).

82 Louloupi, A., Ntini, E., Conrad, T. & Orom, U. A. V. Transient N6-Methyladenosine Transcriptome Sequencing Reveals a Regulatory Role of m6A in Splicing Efficiency. *Cell Rep* **23**, 3429-3437 (2018).

83 Geula, S. *et al.* Stem cells. m6A mRNA methylation facilitates resolution of naive pluripotency toward differentiation. *Science* **347**, 1002-1006 (2015).

84 Wei, G. *et al.* Acute depletion of METTL3 identifies a role for N6-methyladenosine in alternative intron/exon inclusion in the nascent transcriptome. *bioRxiv*, 2020.2009.2010.291179 (2020).

85 Tang, C. *et al.* ALKBH5-dependent m6A demethylation controls splicing and stability of long 3'-UTR mRNAs in male germ cells. *Proc Natl Acad Sci U S A* **115**, E325-E333 (2018).

86 Mauer, J. *et al.* FTO controls reversible m(6)Am RNA methylation during snRNA biogenesis. *Nat Chem Biol* **15**, 340-347 (2019).

87 Lesbirel, S. *et al.* The m(6)A-methylase complex recruits TREX and regulates mRNA export. *Sci Rep* **8**, 13827 (2018).

88 Du, H. *et al.* YTHDF2 destabilizes m6A-containing RNA through direct recruitment of the CCR4–NOT deadenylase complex. *Nat Commun* **7**, 12626 (2016).

89 Park, O. H. *et al.* Endoribonucleolytic Cleavage of m(6)A-Containing RNAs by RNase P/MRP Complex. *Mol Cell* **74**, 494-507 e498 (2019).

90 Kretschmer, J. *et al.* The m(6)A reader protein YTHDC2 interacts with the small ribosomal subunit and the 5'-3' exoribonuclease XRN1. *RNA* **24**, 1339-1350 (2018).

91 Ke, S. *et al.* m(6)A mRNA modifications are deposited in nascent pre-mRNA and are not required for splicing but do specify cytoplasmic turnover. *Genes Dev* **31**, 990-1006 (2017).

92 Shi, H. *et al.* m(6)A facilitates hippocampus-dependent learning and memory through YTHDF1. *Nature* **563**, 249-253 (2018).

93 Choe, J. *et al.* mRNA circularization by METTL3-eIF3h enhances translation and promotes oncogenesis. *Nature* **561**, 556-560 (2018).

94 Meyer, K. D. *et al.* 5' UTR m(6)A Promotes Cap-Independent Translation. *Cell* **163**, 999-1010 (2015).

95 Coots, R. A. *et al.* m(6)A Facilitates eIF4F-Independent mRNA Translation. *Mol Cell* **68**, 504-514 e507 (2017).

96 Mao, Y. *et al.* m(6)A in mRNA coding regions promotes translation via the RNA helicase-containing YTHDC2. *Nat Commun* **10**, 5332 (2019).

97 Choi, J. *et al.* N6-methyladenosine in mRNA disrupts tRNA selection and translation-elongation dynamics. *Nat Struct Mol Biol* **23**, 110 (2016).

98 Fu, Y. & Zhuang, X. m(6)A-binding YTHDF proteins promote stress granule formation. *Nat Chem Biol* **16**, 955-963 (2020).

99 Ries, R. J. *et al.* m(6)A enhances the phase separation potential of mRNA. *Nature* **571**, 424-428 (2019).

100 Yang, P. *et al.* G3BP1 Is a Tunable Switch that Triggers Phase Separation to Assemble Stress Granules. *Cell* **181**, 325-345 e328 (2020).

101 Guillen-Boixet, J. *et al.* RNA-Induced Conformational Switching and Clustering of G3BP Drive Stress Granule Assembly by Condensation. *Cell* **181**, 346-361 e317 (2020).

102 Barbieri, I. & Kouzarides, T. Role of RNA modifications in cancer. *Nat Rev Cancer* **20**, 303-322 (2020).

103 Huang, H., Weng, H. & Chen, J. m(6)A Modification in Coding and Non-coding RNAs: Roles and Therapeutic Implications in Cancer. *Cancer Cell* **37**, 270-288 (2020).

104 Barbieri, I. *et al.* Promoter-bound METTL3 maintains myeloid leukaemia by m(6)A-dependent translation control. *Nature* **552**, 126-131 (2017).

105 Shen, C. *et al.* RNA Demethylase ALKBH5 Selectively Promotes Tumorigenesis and Cancer Stem Cell Self-Renewal in Acute Myeloid Leukemia. *Cell Stem Cell* **27**, 64-80 e69 (2020).

106 Wang, J. *et al.* Leukemogenic Chromatin Alterations Promote AML Leukemia Stem Cells via a KDM4C-ALKBH5-AXL Signaling Axis. *Cell Stem Cell* **27**, 81-97 e88 (2020).

107 Chen, M. *et al.* RNA N6-methyladenosine methyltransferase-like 3 promotes liver cancer progression through YTHDF2-dependent posttranscriptional silencing of SOCS2. *Hepatology* **67**, 2254-2270 (2018).

108 Muller, S. *et al.* IGF2BP1 promotes SRF-dependent transcription in cancer in a m6A- and miRNA-dependent manner. *Nucleic Acids Res* **47**, 375-390 (2019).

109 Lin, X. *et al.* RNA m(6)A methylation regulates the epithelial mesenchymal transition of cancer cells and translation of Snail. *Nat Commun* **10**, 2065 (2019).

110 Ma, J. Z. *et al.* METTL14 suppresses the metastatic potential of hepatocellular carcinoma by modulating N(6)-methyladenosine-dependent primary MicroRNA processing. *Hepatology* **65**, 529-543 (2017).

111 Zhang, S. *et al.* m(6)A Demethylase ALKBH5 Maintains Tumorigenicity of Glioblastoma Stem-like Cells by Sustaining FOXM1 Expression and Cell Proliferation Program. *Cancer Cell* **31**, 591-606 e596 (2017).

112 Zhang, C. *et al.* Hypoxia induces the breast cancer stem cell phenotype by HIF-dependent and ALKBH5-mediated m(6)A-demethylation of NANOG mRNA. *Proc Natl Acad Sci U S A* **113**, E2047-2056 (2016).

113 Liu, J. *et al.* m(6)A mRNA methylation regulates AKT activity to promote the proliferation and tumorigenicity of endometrial cancer. *Nat Cell Biol* **20**, 1074-1083 (2018).

114 Frye, M., Harada, B. T., Behm, M. & He, C. RNA modifications modulate gene expression during development. *Science* **361**, 1346-1349 (2018).

115 Aguilo, F. *et al.* Coordination of m(6)A mRNA Methylation and Gene Transcription by ZFP217 Regulates Pluripotency and Reprogramming. *Cell Stem Cell* **17**, 689-704 (2015).

116 Batista, P. J. *et al.* m(6)A RNA modification controls cell fate transition in mammalian embryonic stem cells. *Cell Stem Cell* **15**, 707-719 (2014).

117 Zhao, B. S. *et al.* m(6)A-dependent maternal mRNA clearance facilitates zebrafish maternal-to-zygotic transition. *Nature* **542**, 475-478 (2017).

118 Kasowitz, S. D. *et al.* Nuclear m6A reader YTHDC1 regulates alternative polyadenylation and splicing during mouse oocyte development. *PLoS Genet* **14**, e1007412 (2018).

119 Xu, K. *et al.* Mettl3-mediated m(6)A regulates spermatogonial differentiation and meiosis initiation. *Cell Res* **27**, 1100-1114 (2017).

120 Li, H. B. *et al.* m(6)A mRNA methylation controls T cell homeostasis by targeting the IL-7/STAT5/SOCS pathways. *Nature* **548**, 338-342 (2017).

121 Yoon, K. J. *et al.* Temporal Control of Mammalian Cortical Neurogenesis by m(6)A Methylation. *Cell* **171**, 877-889 e817 (2017).

122 Zhang, C. *et al.* m(6)A modulates haematopoietic stem and progenitor cell specification. *Nature* **549**, 273-276 (2017).

123 van der Hoeven, F. *et al.* Programmed cell death is affected in the novel mouse mutant Fused toes (Ft). *Development* **120**, 2601 (1994).

124 Gao, X. *et al.* The fat mass and obesity associated gene FTO functions in the brain to regulate postnatal growth in mice. *PLoS One* **5**, e14005 (2010).

125 Fischer, J. *et al.* Inactivation of the Fto gene protects from obesity. *Nature* **458**, 894-898 (2009).

126 Fawcett, K. A. & Barroso, I. The genetics of obesity: FTO leads the way. *Trends Genet* **26**, 266-274 (2010).

127 Cecil, J. E., Tavendale, R., Watt, P., Hetherington, M. M. & Palmer, C. N. An obesity-associated FTO gene variant and increased energy intake in children. *N Engl J Med* **359**, 2558-2566 (2008).

128 Boissel, S. *et al.* Loss-of-function mutation in the dioxygenase-encoding FTO gene causes severe growth retardation and multiple malformations. *Am J Hum Genet* **85**, 106-111 (2009).

129 Ho, A. J. *et al.* A commonly carried allele of the obesity-related FTO gene is associated with reduced brain volume in the healthy elderly. *Proc Natl Acad Sci U S A* **107**, 8404-8409 (2010).

130 Gerken, T. *et al.* The obesity-associated FTO gene encodes a 2-oxoglutarate-dependent nucleic acid demethylase. *Science* **318**, 1469-1472 (2007).

131 Jia, G. *et al.* Oxidative demethylation of 3-methylthymine and 3-methyluracil in single-stranded DNA and RNA by mouse and human FTO. *FEBS Lett* **582**, 3313-3319 (2008).

132 Fu, Y. *et al.* FTO-mediated formation of N6-hydroxymethyladenosine and N6-formyladenosine in mammalian RNA. *Nat Commun* **4**, 1798 (2013).

133 Wei, C.-M., Gershowitz, A. & Moss, B. N6, O2'-dimethyladenosine a novel methylated ribonucleoside next to the 5[prime] terminal of animal cell and virus mRNAs. *Nature* **257**, 251-253 (1975).

134 Adams, J. M. & Cory, S. Modified nucleosides and bizarre 5'-termini in mouse myeloma mRNA. *Nature* **255**, 28-33 (1975).

135 Wei, C. M., Gershowitz, A. & Moss, B. Methylated nucleotides block 5' terminus of HeLa cell messenger RNA. *Cell* **4**, 379-386 (1975).

136 Fu, Y. *Dynamic Regulation of Rna Modifications by AlkB Family Dioxygenases* Ph.D. thesis, The University of Chicago, (2012).

137 Muller-McNicoll, M. & Neugebauer, K. M. How cells get the message: dynamic assembly and function of mRNA-protein complexes. *Nat Rev Genet* **14**, 275-287 (2013).

138 Aas, A. *et al.* Nucleocytoplasmic Shuttling of FTO Does Not Affect Starvation-Induced Autophagy. *PLoS One* **12**, e0168182 (2017).

139 Gulati, P. *et al.* Fat mass and obesity-related (FTO) shuttles between the nucleus and cytoplasm. *Biosci Rep* **34**, e00144 (2014).

140 Sanchez-Pulido, L. & Andrade-Navarro, M. A. The FTO (fat mass and obesity associated) gene codes for a novel member of the non-heme dioxygenase superfamily. *BMC Biochem* **8**, 23 (2007).

141 Van Nostrand, E. L. *et al.* Robust transcriptome-wide discovery of RNA-binding protein binding sites with enhanced CLIP (eCLIP). *Nat Methods* **13**, 508-514 (2016).

142 Phizicky, E. M. & Hopper, A. K. tRNA biology charges to the front. *Genes Dev* **24**, 1832-1860 (2010).

143 Hopper, A. K. & Phizicky, E. M. tRNA transfers to the limelight. *Genes Dev* **17**, 162-180 (2003).

144 Liu, F. *et al.* ALKBH1-Mediated tRNA Demethylation Regulates Translation. *Cell* **167**, 816-828 e816 (2016).

145 Haag, S. *et al.* NSUN6 is a human RNA methyltransferase that catalyzes formation of m5C72 in specific tRNAs. *RNA* **21**, 1532-1543 (2015).

146 Sendinc, E. *et al.* PCIF1 Catalyzes m6Am mRNA Methylation to Regulate Gene Expression. *Mol Cell* **75**, 620-630 e629 (2019).

147 Akichika, S. *et al.* Cap-specific terminal N(6)-methylation of RNA by an RNA polymerase II-associated methyltransferase. *Science* **363**, eaav0080 (2019).

148 Maniatis, T. & Reed, R. The role of small nuclear ribonucleoprotein particles in pre-mRNA splicing. *Nature* **325**, 673-678 (1987).

149 Toh, J. D. W. *et al.* Distinct RNA N-demethylation pathways catalyzed by nonheme iron ALKBH5 and FTO enzymes enable regulation of formaldehyde release rates. *Proc Natl Acad Sci U S A* **117**, 25284-25292 (2020).

150 Boulias, K. *et al.* Identification of the m(6)Am Methyltransferase PCIF1 Reveals the Location and Functions of m(6)Am in the Transcriptome. *Mol Cell* **75**, 631-643 e638 (2019).

151 Conrad, T. & Ørom, U. A. in *Enhancer RNAs: Methods and Protocols* (ed Ulf Andersson Ørom) 1-9 (Springer New York, 2017).

152 Bolger, A. M., Lohse, M. & Usadel, B. Trimmomatic: a flexible trimmer for Illumina sequence data. *Bioinformatics* **30**, 2114-2120 (2014).

153 Corcoran, D. L. *et al.* PARalyzer: definition of RNA binding sites from PAR-CLIP short-read sequence data. *Genome Biol* **12**, R79 (2011).

154 Schick, S. *et al.* Dynamics of chromatin accessibility and epigenetic state in response to UV damage. *J Cell Sci* **128**, 4380-4394 (2015).

155 Kweon, S. M. *et al.* An Adversarial DNA N(6)-Methyladenine-Sensor Network Preserves Polycomb Silencing. *Mol Cell* **74**, 1138-1147 e1136 (2019).

156 Ferenc, K. *et al.* Intracellular and tissue specific expression of FTO protein in pig: changes with age, energy intake and metabolic status. *Sci Rep* **10**, 13029 (2020).

157 Liu, J. *et al.* Landscape and Regulation of m(6)A and m(6)Am Methylome across Human and Mouse Tissues. *Mol Cell* **77**, 426-440 e426 (2020).

158 Liu, J. *et al.* N(6)-methyladenosine of chromosome-associated regulatory RNA regulates chromatin state and transcription. *Science* **367**, 580-586 (2020).

159 Percharde, M. *et al.* A LINE1-Nucleolin Partnership Regulates Early Development and ESC Identity. *Cell* **174**, 391-405 e319 (2018).

160 Jachowicz, J. W. *et al.* LINE-1 activation after fertilization regulates global chromatin accessibility in the early mouse embryo. *Nat Genet* **49**, 1502-1510 (2017).

161 Buenrostro, J. D., Wu, B., Chang, H. Y. & Greenleaf, W. J. ATAC-seq: A Method for Assaying Chromatin Accessibility Genome-Wide. *Curr Protoc Mol Biol* **109**, 212921-21 2929 (2015).

162 Buenrostro, J. D., Giresi, P. G., Zaba, L. C., Chang, H. Y. & Greenleaf, W. J. Transposition of native chromatin for fast and sensitive epigenomic profiling of open chromatin, DNA-binding proteins and nucleosome position. *Nat Methods* **10**, 1213-1218 (2013).

163 Yan, F., Powell, D. R., Curtis, D. J. & Wong, N. C. From reads to insight: a hitchhiker's guide to ATAC-seq data analysis. *Genome Biol* **21**, 22 (2020).

164 Consortium, E. P. An integrated encyclopedia of DNA elements in the human genome. *Nature* **489**, 57-74 (2012).

165 Handoko, L. *et al.* CTCF-mediated functional chromatin interactome in pluripotent cells. *Nat Genet* **43**, 630-638 (2011).

166 Wang, Y. *et al.* N(6)-methyladenosine RNA modification regulates embryonic neural stem cell self-renewal through histone modifications. *Nat Neurosci* **21**, 195-206 (2018).

167 Ma, B. *et al.* Molecular characteristics of early-stage female germ cells revealed by RNA sequencing of low-input cells and analysis of genome-wide DNA methylation. *DNA Res* **26**, 105-117 (2019).

168 Pandey, R. R. *et al.* The mammalian cap-specific m6Am RNA methyltransferase PCIF1 regulates transcript levels in mouse tssues. *Cell Rep.* **32**, 108038 (2020).

169 Chen, H. *et al.* METTL4 is an snRNA m(6)Am methyltransferase that regulates RNA splicing. *Cell Res* **30**, 544-547 (2020).

170 Wuarin, J. & Schibler, U. Physical isolation of nascent RNA chains transcribed by RNA polymerase II: evidence for cotranscriptional splicing. *Mol Cell Biol* **14**, 7219-7225 (1994).

171 Abudayyeh, O. O. *et al.* RNA targeting with CRISPR-Cas13. *Nature* **550**, 280-284 (2017).

172 Kim, D., Langmead, B. & Salzberg, S. L. HISAT: a fast spliced aligner with low memory requirements. *Nat Methods* **12**, 357-360 (2015).

173 Li, H. *et al.* The Sequence Alignment/Map format and SAMtools. *Bioinformatics* **25**, 2078-2079 (2009).

174 Zhang, Y. *et al.* Model-based analysis of ChIP-Seq (MACS). *Genome Biol* **9**, R137 (2008).

175 Liao, Y., Smyth, G. K. & Shi, W. featureCounts: an efficient general purpose program for assigning sequence reads to genomic features. *Bioinformatics* **30**, 923-930 (2014).

176 Langmead, B. & Salzberg, S. L. Fast gapped-read alignment with Bowtie 2. *Nat Methods* **9**, 357-359 (2012).

177 Love, M. I., Huber, W. & Anders, S. Moderated estimation of fold change and dispersion for RNA-seq data with DESeq2. *Genome Biol* **15**, 550 (2014).

178 Shen, L. *et al.* diffReps: detecting differential chromatin modification sites from ChIP-seq data with biological replicates. *PLoS One* **8**, e65598 (2013).

179 Huang, Y. *et al.* Meclofenamic acid selectively inhibits FTO demethylation of m6A over ALKBH5. *Nucleic Acids Res* **43**, 373-384 (2015).

180 Tsao, H., Chin, L., Garraway, L. A. & Fisher, D. E. Melanoma: from mutations to medicine. *Genes Dev* **26**, 1131-1155 (2012).

181 Kleffel, S. *et al.* Melanoma Cell-Intrinsic PD-1 Receptor Functions Promote Tumor Growth. *Cell* **162**, 1242-1256 (2015).

182 Tudrej, K. B., Czepielewska, E. & Kozlowska-Wojciechowska, M. SOX10-MITF pathway activity in melanoma cells. *Arch Med Sci* **13**, 1493-1503 (2017).

183 Domanska, U. M. *et al.* A review on CXCR4/CXCL12 axis in oncology: no place to hide. *Eur J Cancer* **49**, 219-230 (2013).

184 Chatterjee, S., Behnam Azad, B. & Nimmagadda, S. in *Advances in Cancer Research* Vol. 124 (eds Martin G. Pomper & Paul B. Fisher) 31-82 (Academic Press, 2014).

185 Sharma, P., Hu-Lieskovan, S., Wargo, J. A. & Ribas, A. Primary, Adaptive, and Acquired Resistance to Cancer Immunotherapy. *Cell* **168**, 707-723 (2017).

186 Sherr, C. J. Principles of tumor suppression. *Cell* **116**, 235-246 (2004).

187 Chitsazzadeh, V. *et al.* Cross-species identification of genomic drivers of squamous cell carcinoma development across preneoplastic intermediates. *Nat Commun* **7**, 12601 (2016).

188 Gao, S. *et al.* Ubiquitin ligase Nedd4L targets activated Smad2/3 to limit TGF-beta signaling. *Mol Cell* **36**, 457-468 (2009).

189 Wang, Z. *et al.* NEDD4L Protein Catalyzes Ubiquitination of PIK3CA Protein and Regulates PI3K-AKT Signaling. *J Biol Chem* **291**, 17467-17477 (2016).

190 Ding, Y., Zhang, Y., Xu, C., Tao, Q. H. & Chen, Y. G. HECT domain-containing E3 ubiquitin ligase NEDD4L negatively regulates Wnt signaling by targeting dishevelled for proteasomal degradation. *J Biol Chem* **288**, 8289-8298 (2013).

191 Amm, I., Sommer, T. & Wolf, D. H. Protein quality control and elimination of protein waste: the role of the ubiquitin-proteasome system. *Biochim Biophys Acta* **1843**, 182-196 (2014).

192 Klionsky, D. J. Autophagy: from phenomenology to molecular understanding in less than a decade. *Nat Rev Mol Cell Biol* **8**, 931-937 (2007).

193 Moscat, J. & Diaz-Meco, M. T. p62: a versatile multitasker takes on cancer. *Trends Biochem Sci* **37**, 230-236 (2012).

194 Duran, A. *et al.* The signaling adaptor p62 is an important NF-kappaB mediator in tumorigenesis. *Cancer Cell* **13**, 343-354 (2008).

195 Wang, X. *et al.* m(6)A mRNA methylation controls autophagy and adipogenesis by targeting Atg5 and Atg7. *Autophagy* **16**, 1221-1235 (2020).

196 Wei, Y. *et al.* EGFR-mediated Beclin 1 phosphorylation in autophagy suppression, tumor progression, and tumor chemoresistance. *Cell* **154**, 1269-1284 (2013).

197 Gulati, P. *et al.* Role for the obesity-related FTO gene in the cellular sensing of amino acids. *Proc Natl Acad Sci U S A* **110**, 2557-2562 (2013).

198 Berulava, T. *et al.* Changes in m6A RNA methylation contribute to heart failure progression by modulating translation. *Eur J Heart Fail* **22**, 54-66 (2020).

199 Fan, W. *et al.* Keap1 facilitates p62-mediated ubiquitin aggregate clearance via autophagy. *Autophagy* **6**, 614-621 (2010).

200 Ran, F. A. *et al.* Genome engineering using the CRISPR-Cas9 system. *Nat Protoc* **8**, 2281-2308 (2013).

201 Aceto, N. *et al.* Tyrosine phosphatase SHP2 promotes breast cancer progression and maintains tumor-initiating cells via activation of key transcription factors and a positive feedback signaling loop. *Nat Med* **18**, 529-537 (2012).

202 Marinov, G. K. *et al.* From single-cell to cell-pool transcriptomes: stochasticity in gene expression and RNA splicing. *Genome Res* **24**, 496-510 (2014).

203 Adivarahan, S. *et al.* Spatial Organization of Single mRNPs at Different Stages of the Gene Expression Pathway. *Mol Cell* **72**, 727-738 e725 (2018).

204 Sun, H., Zhang, M., Li, K., Bai, D. & Yi, C. Cap-specific, terminal N(6)-methylation by a mammalian m(6)Am methyltransferase. *Cell Res* **29**, 80-82 (2019).

205 Dang, C. V. MYC on the path to cancer. *Cell* **149**, 22-35 (2012).

206 Zhu, T., Yong, X. L. H., Xia, D., Widagdo, J. & Anggono, V. Ubiquitination Regulates the Proteasomal Degradation and Nuclear Translocation of the Fat Mass and Obesity-Associated (FTO) Protein. *J Mol Biol* **430**, 363-371 (2018).

207 Hirayama, M. *et al.* FTO Demethylates Cyclin D1 mRNA and Controls Cell-Cycle Progression. *Cell Rep* **31**, 107464 (2020).

208 Yang, C. G. *et al.* Crystal structures of DNA/RNA repair enzymes AlkB and ABH2 bound to dsDNA. *Nature* **452**, 961-965 (2008).

209 Yu, B. *et al.* Crystal structures of catalytic complexes of the oxidative DNA/RNA repair enzyme AlkB. *Nature* **439**, 879-884 (2006).

210 Song, H. *et al.* SFPQ Is an FTO-Binding Protein that Facilitates the Demethylation Substrate Preference. *Cell Chem Biol* **27**, 283-291 e286 (2020).

211 Attig, J. *et al.* Heteromeric RNP Assembly at LINEs Controls Lineage-Specific RNA Processing. *Cell* **174**, 1067-1081 e1017 (2018).

212 Petti, E. *et al.* SFPQ and NONO suppress RNA:DNA-hybrid-related telomere instability. *Nat Commun* **10**, 1001 (2019).

213 Orecchini, E. *et al.* ADAR1 restricts LINE-1 retrotransposition. *Nucleic Acids Res* **45**, 155-168 (2017).

214 Slobodin, B. *et al.* Transcription Impacts the Efficiency of mRNA Translation via Co-transcriptional N6-adenosine Methylation. *Cell* **169**, 326-337 e312 (2017).

215 Bertero, A. *et al.* The SMAD2/3 interactome reveals that TGFbeta controls m(6)A mRNA methylation in pluripotency. *Nature* **555**, 256-259 (2018).

216 Huang, H. *et al.* Histone H3 trimethylation at lysine 36 guides m(6)A RNA modification co-transcriptionally. *Nature* **567**, 414-419 (2019).

217 Wu, C. *et al.* Interplay of m(6)A and H3K27 trimethylation restrains inflammation during bacterial infection. *Sci Adv* **6**, eaba0647 (2020).

218 Fustin, J. M. *et al.* RNA-methylation-dependent RNA processing controls the speed of the circadian clock. *Cell* **155**, 793-806 (2013).

219 Takahashi, J. S. Transcriptional architecture of the mammalian circadian clock. *Nat Rev Genet* **18**, 164-179 (2017).

220 Marzluff, W. F. & Koreski, K. P. Birth and Death of Histone mRNAs. *Trends Genet* **33**, 745-759 (2017).

221 Bertoli, C., Skotheim, J. M. & de Bruin, R. A. Control of cell cycle transcription during G1 and S phases. *Nat Rev Mol Cell Biol* **14**, 518-528 (2013).

222 Abakir, A. *et al.* N(6)-methyladenosine regulates the stability of RNA:DNA hybrids in human cells. *Nat Genet* **52**, 48-55 (2020).

223 Yang, X. *et al.* m(6)A promotes R-loop formation to facilitate transcription termination. *Cell Res* **29**, 1035-1038 (2019).

224 Zhang, C. *et al.* METTL3 and N6-Methyladenosine Promote Homologous Recombination-Mediated Repair of DSBs by Modulating DNA-RNA Hybrid Accumulation. *Mol Cell* **79**, 425-442 e427 (2020).

225 Zhang, Z. *et al.* Genetic analyses support the contribution of mRNA N(6)-methyladenosine (m(6)A) modification to human disease heritability. *Nat Genet* **52**, 939-949 (2020).

226 Akhtar, J. *et al.* m6A RNA methylation regulates promoter proximal pausing of RNA Polymerase II. *bioRxiv*, 2020.2003.2005.978163 (2020).

227 Li, Y. *et al.* N(6)-Methyladenosine co-transcriptionally directs the demethylation of histone H3K9me2. *Nat Genet* **52**, 870-877 (2020).

228 Chelmicki, T. *et al.* m6A RNA methylation regulates the fate of endogenous retroviruses. *Nature* doi:10.1038/s41586-020-03135-1 (2021).

229 Xu, W. *et al.* METTL3 regulates heterochromatin in mouse embryonic stem cells. *Nature* doi:10.1038/s41586-021-03210-1 (2021).

230 Molinie, B. *et al.* m(6)A-LAIC-seq reveals the census and complexity of the m(6)A epitranscriptome. *Nat Methods* **13**, 692-698 (2016).

231 McIntyre, A. B. R. *et al.* Limits in the detection of m(6)A changes using MeRIP/m(6)A-seq. *Sci Rep* **10**, 6590 (2020).

232 Zhang, Y. *et al.* MazF cleaves cellular mRNAs specifically at ACA to block protein synthesis in Escherichia coli. *Mol Cell* **12**, 913-923 (2003).

233 Li, X. *et al.* Base-Resolution Mapping Reveals Distinct m(1)A Methylome in Nuclear- and Mitochondrial-Encoded Transcripts. *Mol Cell* **68**, 993-1005 e1009 (2017).

234 Safra, M. *et al.* The m1A landscape on cytosolic and mitochondrial mRNA at single-base resolution. *Nature* **551**, 251 (2017).

235 Arango, D. *et al.* Acetylation of Cytidine in mRNA Promotes Translation Efficiency. *Cell* **175**, 1872-1886 e1824 (2018).

236 Yang, X. *et al.* 5-methylcytosine promotes mRNA export — NSUN2 as the methyltransferase and ALYREF as an m5C reader. *Cell Res* **27**, 606 (2017).

237 Liu, J. *et al.* Sequence- and structure-selective mRNA m5C methylation by NSUN6 in animals. *Natl Sci Rev*, nwaa273 (2020).

238 Xu, L. *et al.* Three distinct 3-methylcytidine (m(3)C) methyltransferases modify tRNA and mRNA in mice and humans. *J Biol Chem* **292**, 14695-14703 (2017).

239 Chen, Z. *et al.* Transfer RNA demethylase ALKBH3 promotes cancer progression via induction of tRNA-derived small RNAs. *Nucleic Acids Res* **47**, 2533-2545 (2019).

240 Li, X. *et al.* Transcriptome-wide mapping reveals reversible and dynamic N1-methyladenosine methylome. *Nat Cell Biol* **12**, 311 (2016).

241 He, C. *et al.* TET2 chemically modifies tRNAs and regulates tRNA fragment levels. *Nat Struct Mol Biol* (2020).

242 Shen, Q. *et al.* Tet2 promotes pathogen infection-induced myelopoiesis through mRNA oxidation. *Nature* **554**, 123-127 (2018).

243 Chen, H. *et al.* m(5)C modification of mRNA serves a DNA damage code to promote homologous recombination. *Nat Commun* **11**, 2834 (2020).

244 Wang, Y., Xiao, Y., Dong, S., Yu, Q. & Jia, G. Antibody-free enzyme-assisted chemical approach for detection of N(6)-methyladenosine. *Nat Chem Biol* **16**, 896-903 (2020).

245 Rubio, M. A. *et al.* Editing and methylation at a single site by functionally interdependent activities. *Nature* **542**, 494-497 (2017).

246 Ontiveros, R. J. *et al.* Coordination of mRNA and tRNA methylations by TRMT10A. *Proc Natl Acad Sci U S A* **117**, 7782-7791 (2020).

247 Ito, S. *et al.* Tet proteins can convert 5-methylcytosine to 5-formylcytosine and 5-carboxylcytosine. *Science* **333**, 1300-1303 (2011).

248 He, Y. F. *et al.* Tet-mediated formation of 5-carboxylcytosine and its excision by TDG in mammalian DNA. *Science* **333**, 1303-1307 (2011).

249 Wu, T. P. *et al.* DNA methylation on N(6)-adenine in mammalian embryonic stem cells. *Nature* **532**, 329-333 (2016).

250 Hao, Z. *et al.* N(6)-Deoxyadenosine Methylation in Mammalian Mitochondrial DNA. *Mol Cell* **78**, 382-395 e388 (2020).

251 Zhang, L. H. *et al.* The SUMOylated METTL8 Induces R-loop and Tumorigenesis via m3C. *iScience* **23**, 100968 (2020).

252 Liu, X. M., Zhou, J., Mao, Y., Ji, Q. & Qian, S. B. Programmable RNA N(6)-methyladenosine editing by CRISPR-Cas9 conjugates. *Nat Chem Biol* **15**, 865-871 (2019).

253 Wilson, C., Chen, P. J., Miao, Z. & Liu, D. R. Programmable m(6)A modification of cellular RNAs with a Cas13-directed methyltransferase. *Nat Biotechnol* **38**, 1431-1440 (2020).

254 Rauch, S. *et al.* Programmable RNA-Guided RNA Effector Proteins Built from Human Parts. *Cell* **178**, 122-134 e112 (2019).

255 Rafalska, I. *et al.* The intranuclear localization and function of YT521-B is regulated by tyrosine phosphorylation. *Hum Mol Genet* **13**, 1535-1549 (2004).

256 Guallar, D. *et al.* RNA-dependent chromatin targeting of TET2 for endogenous retrovirus control in pluripotent stem cells. *Nat Genet* **50**, 443-451 (2018).

257 Heard, E. & Martienssen, R. A. Transgenerational epigenetic inheritance: myths and mechanisms. *Cell* **157**, 95-109 (2014).

258 Daxinger, L. & Whitelaw, E. Understanding transgenerational epigenetic inheritance via the gametes in mammals. *Nat Rev Genet* **13**, 153-162 (2012).